The use of heat for subsurface flow quantification and understanding the subsurface heterogeneity

Behzad Pouladiborj

UNIVERSITÉ DE RENNES 1

THESE DE DOCTORAT DE

L'UNIVERSITE DE RENNES 1

ECOLE DOCTORALE N° 600
Ecole doctorale Ecologie, Géosciences, Agronomie et Alimentation
Spécialité : Sciences de la Terre et de l'Environnement

Par
Behzad POULADIBORJ

The use of heat for subsurface flow quantification and understanding the subsurface heterogeneity

Thèse présentée et soutenue à Rennes, 02/03/2021

Unité de recherche : UMR 6118 Géosciences Rennes

Rapporteurs avant soutenance :

Roger GUÉRIN	Professeur, Sorbonne Université
Abderrahim JARDANI	Maître de Conférences, Université de Rouen Normandie

Composition du Jury :

Président :	Philippe DAVY	Directeur de Recherche CNRS - Université Rennes 1
Examinateurs :	Mickaele LE RAVALEC	Professeur - Ifp Energies Nouvelles
	Roger GUÉRIN	Professeur, Sorbonne Université
	Abderrahim JARDANI	Maître de Conférences, Université de Rouen Normandie
	Patrick EGERMANN	Chef du Pôle Modèles Nouvelles Technologies - Storengy
Dir. de thèse :	Olivier BOUR	Professeur des universités – Université Rennes 1
Co-dir. de thèse :	Laurent LONGUEVERGNE	Directeur de recherche CNRS – Université Rennes 1

Acknowledgements

I am genuinely grateful for the chance to spend three wonderful years at the Observatoire des Sciences de l'Univers de Rennes (OSUR), where I learned how to practice hydrogeology and how to be a better friend to earth and water (although moral knowledge does not bring moral action). Though my life in Rennes was not always warm and bright like a breezy summer day by Saint-Malo Beach, it also was not always gloomy and dark as a biting winter night alone on Rue de la soif (La rue Saint-Michel). As much as those bright days reinforced my deep commitment to working hard and being optimistic, those gloomy days taught me to be aware of the fragility of human existence and the perilous nature of things that I used to take for granted. It was an uphill struggle, but it was all worth it.

First and foremost, I thank my supervisors Professor Olivier Bour and Dr. Laurent Longuevergne, for their unlimited and non-stop support from the first day I got the mail to join ITN-ENIGMA. It has been a privilege to work with you and learn a lot hydrogeology. You have always been caring and kind-hearted to me. I was so lucky to have you both as my supervisors.

I would also like to thank Professor Niklas Linde at the University of Lausanne for scientific collaboration and hosting me during the scientific visit to Lausanne.

My sincere thanks also go to Professor René Lefebvre, Dr. Daniel Paradis, Jean-Marc Ballard, Cynthia Lee and all people at INRS (Institut national de la recherche scientifique) for the scientific collaboration and kindly preparing their study site for our experiment. You did a great job.

I would also like to warmly thank Silixa Ltd for hosting me during the internship, Dr. Athena Chalari for the arrangement of the internship, Dr. Mahmoud Farhadiroushan for warmly welcoming me to Silixa, Dr. Veronique Mahue for involving me with data analysis and flow profiling and in the same team Dr. Sina Hafezi (lunchmate), Odam Ebokpo, Amer Khayyat. I'm also grateful to nice and kind friends I made at Silixa.

I'm also thankful to my friends in Rennes who made my stays a wonderful experience. A big thank to Quentin, Maxime (my office budy during the cold days with no heater in Room 121!), Thomas, Charlotte, Baptiste, Luca, Camille, Madeleine, Claire, Jean, Alexandre, Lucas, Meruyert, Alison, Nataline and everyone who I may have forgotten to mention. A big thank to Jérôme de La Bernardie for being so nice, friendly and helping me with experiments. I would also like to thank my old but gold friends, Doyi Koroush, Doyi Arash and Doyi Milad and Farhad Jan for their support whenever I was in need. My lovely friends in ENIGMA, Kevin, Justin, Lara, Richard, Álvaro, Alejandro, Anne-Karin, Satoshi, Gui, Joel, Peleg, Jorge, Veronika and Andrea who made the ENIGMA program a wonderful one.

Last but not least, I would like to deeply thank my parents, Hassan and Soraya, for their endless love and support throughout my life and many scarifications they did to provide me with the best opportunities to help me grow. Thanks to my lovely sister Bahare and cute nephew Niki, my brothers Javad and Babak for all the positive energy and helps.

This work has received funding from the European Union's Horizon 2020 research and innovation program under the Marie Sklodowska - Curie grant agreement number 722028 (ENIGMA ITN).

Rennes, le 12 Janvier 2021

Contents

Acknowledgements ..... **ii**

List of Figures **7**

List of Tables **9**

List of Equations **10**

Chapter 1 Introduction **12**

1.1 General introduction 13

1.1.1 Subsurface heterogeneity 14

1.1.2 Tools and techniques for the subsurface characterization 16

1.2 Inverse problem and hydraulic tomography 21

1.3 The use of heat for monitoring and characterization of subsurface media 25

1.3.1 Introduction 25

1.3.2 Fiber Optic Distributed Temperature Sensing (FO-DTS) 27

1.3.3 Borehole flow measurement 28

1.3.4 Groundwater flow measurement 32

1.3.5 Thermal tracer tomography 35

1.4 Research motivation and thesis outlines 36

Chapter 2 Individual and joint inversion of head and flux data by geostatistical hydraulic tomography 38

2.1 Abstract 39

2.2 Introduction 39

2.3 Methods 42

2.3.1 Inverse model 42

2.3.2 Principal Component Geostatistical Approach 43

2.3.3 Forward model 44

2.4 Numerical experiments 45

2.4.1 Setup of the synthetic test case 45

2.4.2 Hydraulic tomography using head and flux data 46

2.4.2.1 Boundary condition at the pumping borehole 46

2.4.2.2 Variance of *Y*-field and number of observation points 46

2.4.2.3 Performance Metrics 47

2.5 Results 47

2.5.1 Inversion of head data 47

2.5.2 Inversion of flux data 49
2.5.3 Joint inversion of flux and head data 51
2.6 Discussion 53
2.6.1 General findings 53
2.6.2 The effect of number of observations and variance 55
2.6.3 The effect of truncation order (*P*) on final inversion results 56
2.6.4 Implications for field implementations 57
2.7 Conclusion 58
Chapter 3 Reconstruction of the aquifer heterogeneity using joint inversion of the head and flux data: Application to a shallow granular aquifer 60
3.1 Introduction 61
3.2 Experimental setup 63
3.2.1 State of the art A-FO DTS experiment in shallow aquifers 63
3.2.2 The Saint-Lambert site 64
3.2.3 Previous hydraulic tomography experiments 65
3.2.4 Collection of hydraulic head data 66
3.2.5 Collection of A-FO DTS data 66
3.3 Methodology 68
3.3.1 Inversion of temperature profile to the water flux profile 68
3.3.2 Hydraulic tomography using PCGA 70
3.3.3 Groundwater flow modeling 71
3.4 Field data analysis 72
3.4.1 Temperature data acquired in FO-17 and FO-18 72
3.4.1.1 Temperature data quality check and calibration 73
3.4.1.2 Temperature data to flux profile 73
3.4.2 Head data in packer-isolated and open boreholes 76
3.4.3 Setup of the inverse model and hydraulic tomography 78
3.5 Preliminary results 78
3.5.1 Hydraulic tomography with pressure data 79
3.5.2 Hydraulic tomography jointly with flux and pressure data 81
3.6 Discussion and conclusions 83
3.6.1 General findings 83
3.6.2 Field application implications 83
3.6.3 Perspective works 84

Chapter 4 Modeling borehole flows from Distributed Temperature Sensing Data to monitor groundwater dynamics in fractured media 86

4.1 Abstract 87

4.2 Introduction 88

4.3 Flow model from the temperature profile 90

4.3.1 State of art 90

4.3.2 Heat transfer model 91

4.3.3 Inversion of temperature data and flow profiling 92

4.3.4 Numerical validation 93

4.3.4.1 Description of the numerical model 93

4.3.4.2 Synthetic test with two fractures 94

4.3.5 Sensitivity of the model to the different parameters 95

4.4 Hydrogeological setting 97

4.4.1 The Ploemeur-Guidel field site 97

4.4.2 Borehole PZ-26 97

4.5 Data acquisition and processing 98

4.5.1 Experimental setting 98

4.5.2 Data processing 99

4.5.2.1 FO-DTS calibration and processing 99

4.5.2.2 Heat-pulse flowmeter calibration 99

4.6 Field application 99

4.6.1 Spatio-temporal temperature variations 99

4.6.2 Flow rate calculations 102

4.6.2.1 Flow Profiling using Distributed Temperature Sensing (DTS) Data 103

4.6.2.2 Flow Profiling using Heat Pulse Flow meter (HPFM) 103

4.7 Discussion 107

4.7.1 Thermal parameters estimation 107

4.7.2 Added values and drawbacks of using FO DTS for field applications 108

4.7.3 Inferring groundwater dynamics from temperature data 109

4.8 Conclusions 110

4.9 Appendix A – Heat Transfer Model 111

4.10 Supplementary Materials 113

4.10.1 Introduction 113

4.10.2 Calculation Procedure 113

4.10.3 Automatic flowing zone detection 113
4.10.4 Linearization of the Ramey's equation 113
4.10.5 Inversion of Temperature data and flow profiling 114
4.10.6 Effect of the different parameters on temperature profile 114
4.10.6.1 Effect of geothermal gradient on the flowing water temperature 114
4.10.6.2 Effect of rock thermal conductivity on the flowing water temperature 115
4.10.6.3 Effect of flow time on flowing water temperature 116
4.10.7 Heat-Pulse flowmeter calibration curve 117
Chapter 5 Conclusions 118
5.1 Achieved results 119
5.2 Future developments 121
References 124

List of Figures

Figure 1-1: A schematic of a confined and unconfined aquifer. 13

Figure 1-2: Heterogeneous permeability distribution in SPE 10 comparative model. 14

Figure 1-3: Representation of a hydraulic tomography inverse problem..... 21

Figure 1- 4: Heat transfer mechanism based on the values of hydraulic gradient and hydraulic conductivity. 26

Figure 1-5 Representation of (a)single-ended and (b)double-ended configurations. 28

Figure 1-6: (a) Schematic of inner component of heat-pulse flow meter (b) typical response of heat pulse flow meter 29

Figure 1- 7: Illustration of the concept of deviation of passive temperature profile from the geothermal gradient as a signature of flow in the borehole..... 30

Figure 1-8: Schematic and plan views of the PVP.. 32

Figure 1- 9 Schematic of thermal tracer tomography..... 35

Figure 2-1: Schematic of the steps of using Active FO-DTS to infer a groundwater flux profile with depth 41

Figure 2-2: Reference *Y*-field..... 45

Figure 2- 3: Hydraulic conductivity field (variance 4) estimates for hydraulic head data 48

Figure 2-4: Hydraulic conductivity field (variance 4) estimates for flux data 50

Figure 2-5: Hydraulic conductivity field (variance 4) estimates from joint inversion 52

Figure 2-6: Diagonal element of the resolution matrix for. 55

Figure 2-7: Correlation coefficient versus number of observations for reference hydraulic conductivity fields 56

Figure 2-8: Estimated Y-field for differnet truncation order 57

Figure 3- 1 : Schematic of the steps of using Active FO-DTS to infer groundwater flux profile with depth..... 64

Figure 3-2: Geographical location of the Saint-Lambert site. 65

Figure 3-3: Horizontal hydraulic conductivity value from previous studies 66

Figure 3- 4: Schematic of the location of the boreholes and fiber optic cables. 67

Figure 3-5: Timeline of the experiment performed on the Saint-Lambert site. 67

Figure 3-6: Temperature evolution curve and characteristic times used to quantify flow 69

Figure 3-7: Temperature evolution curves in FO-18 cable. 72

Figure 3-8: Groundwater flux measured in two FO-cable locations..... 75

Figure 3-9: The values of thermal conductivity and flow obtained using characteristic time (t_d) for two points in FO-18. 76

Figure 3-10: Head data recorded in (a): borehole P17 and (b): P18 which are equipped with packers. Numbers in the legend corresponds to the elevation where sensors are placed. 77

Figure 3- 11: Y-field estimation using pressure data only..... 79

Figure 3- 12: Y-filed estimation uncertainty (standard deviation of the hydraulic conductivity estimate) 80

Figure 3- 13: Data fitting for inversion of pressure data only..... 80

Figure 3- 14: Y-field estimation using joint inversion of head and flux data 81

Figure 3- 15: Y-field estimation estimation using joint invesrion of head and flux data 82

Figure 3- 16: Data fitting for joint inversion of head and flux data 82

Figure 4-1 Diagram of the Control Volume used for heat transfer modelling inside the production borehole 92

Figure 4-2: Schematic of the numerical model and representation of the borehole with two fractures and three flowing sections 94

Figure 4-3: Comparison of flow rate used in the numerical model and flow rate calculated from the temperature data using the analytical approach 95

Figure 4-4: Global sensitivity analysis (Sobol method) performed for three parameters and the corresponding sobol indices including main effect and total effect. 96

Figure 4-5: Representation of borehole schematic 101

Figure 4-6: Comparison of three time-shots recorded temperature profile. 102

Figure 4-7: Comparison of flow rates estimated at different depth through DTS measurements and from HPFM measurements during different conditions 106

Figure 4-8 : Normalized RMSE error between predicted flow by DTS and measured flow rate at the surface..... 108

Figure S-1: Schematic of flow profiling procedure..... 114

Figure S-2: Effect of geothermal gradient on flowing water temperature drop versus depth travelled in the borehole 115

Figure S-3: Effect of rock thermal conductivity on flowing water temperature drop versus depth travelled in the borehole..... 116

Figure S-4: Effect of flow time on flowing water temperature drop versus depth travelled in the borehole..... 116

Figure S-5: Calibration curve obtained to calibrate the HPFM data 117

List of Tables

Table 2-1 Summary of the performance metrics for inversion of head data in the area of interest 49

Table 2-2 Summary of the performance metrics for inversion of flux data in the area of interest 51

Table 2-3 Summary of the performance metrics for joint inversion of head and flux data in the area of interest 53

Table 3-1 Location of pressure sensors and values of head drop recorded. 76

Table 3-2 Aquifer model and inversion parameters 78

Table 4-1 Fluid and Media Properties Used for Flow Profiling 102

Table 4-2 Contribution of each fracture to the total flow during ambient 1, ambient 2 and pumping conditions estimated from DTS data and measured by HPFM..... 104

List of Equations

Equation 1:1 – Darcy equation 14

Equation 1:2 – Relationship between permeability and hydraulic conductivity 14

Equation 1:3 – Relationship P-wave, bulk, shear moduli and bulk density 16

Equation 1:4 – Relationship S-wave, shear moduli, and bulk density 17

Equation 1:5 – Relationship between electrical conductivity and hydraulic conductivity proposed by Heigold et al. (1979) 17

Equation 1:6 – Inverse problem formulation 22

Equation 1:7 – posterior probability density function by Bayes theorem 22

Equation 1:8 – Assumption of geostatistical inversion 23

Equation 1:9 – model parameter in each iteration by geostatistical inversion 23

Equation 1:10 – System of the equation solved to obtain the trend function coefficient 23

Equation 1:11 – Three-dimensional heat transport equation in the aquifer 26

Equation 2:1 – Formulation of the inverse problem 42

Equation 2:2 – Posterior probability density function expressed by Bayes theorem 42

Equation 2:3 – model parameter at each iteration 43

Equation 2:4 – model parameter at each iteration 43

Equation 2:5 – Approximation of the terms used in geostatistical inversion by *P* number of principal components by PCGA 43

Equation 2:6 – posterior covariance matrix 43

Equation 2:7 – Resolution matrix 44

Equation 2:8 – groundwater flow equation 44

Equation 2:9 – Weighted root mean square error 46

Equation 2:10 - Frobenius norm calculated for ***Y*** estimates 47

Equation 3:1 – Characteristic times to obtain groundwater flux 68

Equation 3:2 – Temperature evolution tim during conduction-dominant period .. 69

Equation 3:3–general equation for temperature evolution with time 70

Equation 3:4 – Formulation of the inverse problem 70

Equation 3:5 – Posterior probability density function expressed by Bayes theorem 70

Equation 3:6 – model parameter at each iteration 70

Equation 3:7 – system of equation to find the trend matrix and coefficient 71

Equation 3:8 – Approximation of the terms used in geoststistical inversion by *P* number of principal components by PCGA 71

Equation 3:9 – posterior covariance matrix 71

Equation 3:10 – groundwater flow equation 71

Equation 3:11 – relationship between recorded temperature data, real temperature data and heat storage effect 73

Equation 4:1 – The moving fluid temperature inside the borehole 91

Equation 4:2 – Relaxation distance given by Ramey (1962) and Hassan & Kabir (1994) 92

Equation 4:3 – objective function for flow profiling 93

Equation 2:1 – Initial estimation of water velocity using linearized Ramey equation 93

Equation 4:5 – Energy balance for the fluid inside the borehole 111

Equation 4:6 – differential form of energy balance equation 111

Equation 4:7 – Enthalpy change as a function of pressure and temperature change 112

Equation 4:8 – Energy balance for fluid in terms of pressure change, velocity change, heat exchange with media 112

Equation 4:9 – Energy balance for the formation 112

Equation 4:10 – Ramey and Hassan & Kabir solutions 112

Equation 4:11 – Linearization of the Ramey's equation 114

Chapter 1 Introduction

1.1 General introduction

Groundwater is among the vital human resources constituting a major part of the planet's freshwater (Nriagu, 2019). Opposite to the surface water present in the rivers, lakes, and oceans, the groundwater (as the name also indicates) is present in the void spaces in the rocks beneath the ground. The aquifer is an underground geological structure storing groundwater and allowing its transmission through void spaces or fractures of the rocks constituting the aquifers. The aquifer may be bounded by impervious or semi-impermeable layers called aquitards, which have less or no ability to transmit water. The aquifers generally fall into three categories: (i) unconfined, (ii) semi-confined, and (iii) confined aquifers. In unconfined aquifers, no aquitard is present to isolate or protect the aquifer from above, and it is bounded (upper boundary) by water level. Recharge is easier in the unconfined aquifers, which are nevertheless less protected from pollution. Confined aquifers are in general bounded between two aquitards with water pressure being greater than atmospheric pressure in all places so that water level is higher than the roof of the aquifer. Drilling a borehole in a confined aquifer may result in naturally flowing water (artesian flow) if the groundwater pressure is high enough to reach the surface. Semi-confined aquifers (leaky aquifers) are overlain or underlain by a semi-pervious layer, through which flow into or out of the aquifer can take place.

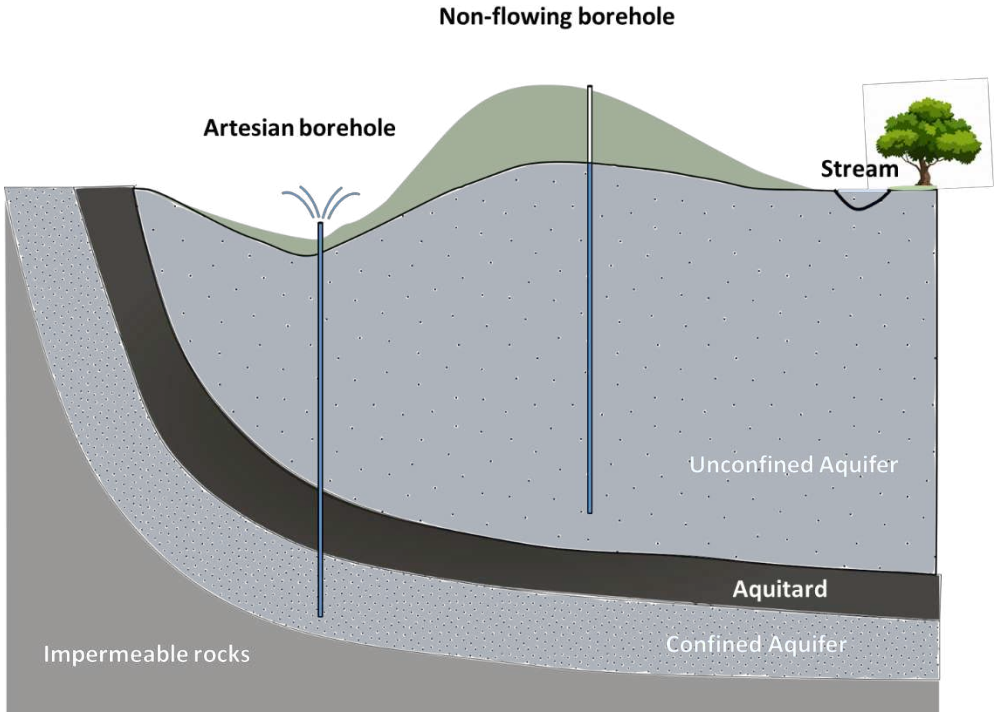

Figure 1-1: A schematic of a confined and unconfined aquifer.

The aquifers are characterized by specific properties that define the aquifer's ability to store groundwater (porosity) and transmit (permeability) it through the rocks' voids and fractures. The porosity is an intrinsic property of the rock, which describes the amount of empty space between grains to host water. The permeability defines how easily water can flow through the rocks in the aquifer (porous media). However, it is not the only parameter controlling the flow, and other parameters such as density, viscosity also play a role in the flow. All of these parameters are lumped into one parameter called hydraulic conductivity. In fact, permeability is only the porous media's property, while hydraulic conductivity also accounts for other parameters related to the fluid (viscosity and density of water) contributing to the flow. Darcy law explains the groundwater flow in the steady-state condition:

$$q = -K\frac{dh}{dl},$$

Equation 1:1 – Darcy equation

where, K is the hydraulic conductivity (L/T), $\frac{dh}{dl}$ is the hydraulic head gradient, and q is specific discharge (L/T). The permeability and hydraulic conductivity terms are related to each by Equation 1:2 given as following:

$$K = -k\frac{\rho g}{\mu},$$

Equation 1:2 – Relationship between intrinsic permeability and hydraulic conductivity

where k (L^2) is the intrinsic permeability, ρ (ML^{-3}) and μ ($ML^{-1}T^{-1}$) are water density and viscosity, respectively. g (L^2/T) also stands for gravitational acceleration. It is also worth pointing out that porosity plays no role during the steady-state flow as we do not find the porosity in the Darcy equation. However, during the transient state, not only the hydraulic conductivity but also storativity, which depends on porosity, aquifer thickness, and compressibility of fluids and solids, influence the flow. Storativity is a dimensionless measure of the volume of water that would be discharged from an aquifer per unit area of the aquifer and per unit reduction in hydraulic head.

1.1.1 Subsurface heterogeneity

Knowledge of aquifer hydraulic properties is of great importance for the management, optimization, and protection of groundwater resources. Due to the complex natural and geological processes that lead to forming the reservoirs and aquifers, the values and distribution of the hydraulic properties are mostly not the same and constant across the aquifer, i.e., the aquifers in general are not homogenous and are said to be heterogeneous. The aquifer heterogeneities firmly control the flow pattern (Freeze and Witherspoon, 1967), contaminant, solute transport (Bellin et al., 1992; Dagan, 1984; Fiori and Jankovic, 2012; Gelhar and Axness, 1983), mixing, and reactions (Dagan, 1987; Dentz et al., 2011; Gelhar and Gelhar, 1993; De Vriendt et al., 2020) as well as heat transport and storage (Sommer et al., 2013). The heterogeneity effect is particularly well pronounced in fractured media as the flow is localized in more or less connected fractures (Davy et al.,2006). It is worth noting that, in addition to heterogeneity, hydraulic properties might also be different in various directions, which is called anisotropy. As an example, hydraulic conductivity in the horizontal and vertical directions might be of different values. Figure 1-2 shows a heterogeneous distribution of the permeability in the SPE 10 comparative model (SPE 10 is a standard model provided by the Society of Petroleum Engineers (SPE) to assess and compare the different up gridding and upscaling approaches through a million-cell geological model).

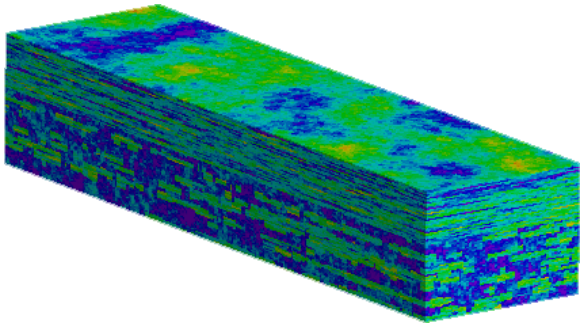

Figure 1-2: Heterogeneous permeability distribution in SPE 10 comparative model. The red color represents the high permeability region while the blue colors show the low permeability region

Even though the heterogeneity and its role are appreciated, seldom sufficient data are available to explicitly represent the geological heterogeneity data in groundwater models (De Marsily et al., 2005; Koltermann and Gorelick, 1996). Since long ago, there have been many approaches for dealing with heterogeneity. The earliest work would be attributed to the Dupuit (1857), who consciously or unconsciously applied the Darcy law to a natural medium by intuitively considering the media as a homogenous media (De Marsily et al., 2005). However, the most pronounced and pioneer work allowing accounting and estimation of the heterogeneity belongs to Theis (1935). He introduced a new well testing approach and the solution to the transient flow of the water in non-leaky confined aquifers that averages the hydraulic properties over the radius of investigation. In this approach, the heterogeneity is taken into account by an equivalent homogenous model. These equivalent homogenous models would help hydrogeologists develop well fields, adapt the exploitation to the resource, and solve local engineering problems (De Marsily et al., 2005).

The introduction of the numerical models empowered the hydrogeologist to move one step forward toward heterogeneity characterization. It led to considering the aquifer properties variable in the space and adapting to the model to the aquifers' geometry and boundary conditions. Considering several pumping tests, the initial approach was to allocate the average permeability obtained by the well-test to the grid where the borehole was located. The grids between boreholes were then interpolated from the adjacent wells, done through zoning, polynomial trending fit, and hand countering (De Marsily et al., 2005). This approach was one step forward to represent the heterogeneity compared to equivalent homogenous models but still insufficient for some applications such as enhanced oil recovery (water cut prediction) in oil and gas reservoirs and groundwater contamination transport models in the aquifers. The reason is simply that the water movement in the reservoirs during the enhanced oil recovery operation and the movement of contaminants are susceptible to the high permeability and low permeability regions and their distribution as they control the flow pattern. These flow patterns cannot be well explained by the averaged values obtained using the methods mentioned earlier. These limitations provoked more advanced studies following the introduction of sequential stratigraphy comprising advanced geological analysis of depositional environments, combined geophysics, and well logging to learn how to describe and represent them. It was a basis for developing other advanced approaches such as geostatistics (De Marsily et al., 2005). The geostatistics was developed for mining estimations by Matheron (1965) and was applied in hydrogeology by Delhomme (1979). The geostatistics and the spatial covariance definition imply that heterogeneity follows a structure obtained through the geostatistical analysis (experimental variogram). The variogram is a model that defines the spatial dependence of the variables and consists of two main elements, the range, which is the average size of heterogeneous bodies, and the sill that is the measure of the magnitude of the change in values of the property form one heterogeneous body to another. Geostatistical tools such as Kriging, provide an optimal method to estimate the properties compared to previously mentioned approaches (zoning, arbitrary interpolation, etc.) and not necessarily the best (De Marsily et al., 2005). Geostatistics has revolutionized dealing with heterogeneity and make better use of the data. However, geostatistics traditionally provides a continuous representation of the properties field, and it could not represent the abrupt changes in the properties such as facies and discontinuities. Novel geostatistical methods such as multiple statistics (MPS) provide an opportunity to capture and present such complex heterogeneity. The other approach would be based on the inversion tomographies in which the aquifer system's response and prior knowledge of the aquifer (could be the geostatistical information) are used to map the heterogeneity of the subsurface media. This approach, which is used in this thesis, is more detailed in the following subsection.

Although the real heterogeneity is more complicated to be presented by any model, generated heterogeneous models are closer to unattainable reality. It should be noted that heterogeneity should be dealt (De Marsily et al., 2005) and not to be ignored. Before dealing with heterogeneity, one would ask whether the heterogeneity matters and if it has a considerable impact on the application of the interest. For instance, it may be possible to use equivalent homogenous models of the aquifer for flow-related applications such as regional aquifer management, optimization of borehole discharges, and a large scale view of the heterogeneity would be sufficient. In contrast, the transport problems need to deal with heterogeneity in an appropriate scale as it dictates flow pattern and transport of contaminant, etc.

1.1.2 Tools and techniques for the subsurface characterization

There have been years-long efforts characterizing the aquifer using two main techniques, geophysical and hydraulic methods. Geophysical methods consist of non-invasive or minimally invasive approaches such as Seismic, Electrical Resistivity, Electro Magnetic, which measure wave velocity, and wave attenuation sent to the ground, electrical properties, and electromagnetic properties of the aquifer. The self-potential (SP) which is based on the measurement of natural occurrence of electrical field on the Earth's surface is also a passive geophysical approach. Traditionally, geophysical methods were applied to identify the subsurface structures, delineate aquifer boundaries, mapping fault zone, and water-saturated zones (Vanderborght et al., 2005). However, in recent years, much effort has been devoted to deriving the aquifer hydraulic properties (hydraulic conductivity, porosity, dispersivity) using the continuous measurement of geophysical properties. This area of research is called hydro-geophysics. Geophysical methods can measure spatially distributed of properties in the region where conventional hydrological wellbore methods fail to do sampling (Linde, 2005). In fact, hydro-geophysical methods can be utilized for three purposes: (i) hydrological mapping of subsurface architecture, (ii) estimation of subsurface properties, and (iii) monitoring of subsurface processes.

The seismic methods are based on analyzing the velocity and attenuation of propagating elastic waves generated by a seismic source (weight drops, hammer, explosive, air gun, thumper truck, electromagnetic pulse energy source, piezoelectric transducers, etc.). Seismic velocities depend on the subsurface properties such as porosity, grain texture, and their state variable (water saturation, etc.). The two main types of waves considered are primary (P-waves) and shear waves (S-waves). The P-waves are the fast compressional waves that pull or push the material in their moving direction. They are the first waves that arrive at seismic stations and can move through solids and fluids. The propagation velocity is dependent on bulk and shear moduli of a medium:

$$v_p = \sqrt{\frac{B + \frac{4}{3}G}{\rho_b}} ,$$

Equation 1:3 – Relationship P-wave, bulk, shear moduli and bulk density

where $B(MT^{-2}L^{-1})$, G $(MT^{-2}L^{-1})$ and ρ_b (ML^{-3}) are bulk, shear moduli, and bulk density, respectively. The bulk moduli is a measure of how resistant the substance is to compression. The shear moduli define the deformation due to a force applied parallel to the solid surface. On the other hand, S-waves do not depend on bulk moduli but the shear moduli.

$$v_s = \sqrt{\frac{G}{\rho_b}} ,$$

Equation 1:4 – Relationship S-wave, shear moduli, and bulk density

Seismic cross-hole tomography provides detailed information about the wave velocity structure in the area between two boreholes, which can be further used to estimate the inter-borehole hydraulic properties. The above-mentioned elastic moduli distribution, coupled with related petrophysical models, can be used to estimate the aquifer's hydraulic properties. For instance, Hyndman et al. (2000) developed an approach to establish the relationship between cross-hole seismic slowness and hydraulic conductivity. They applied their approach to an alluvial aquifer in California in which they combined the slowness from cross-hole seismic and hydraulic properties information obtained from cores, pumping and tracer tests. They found that slowness and hydraulic conductivity are positively correlated for that aquifer. They concluded that seismic slowness provides high-resolution information about the aquifer properties consistent with the local measurement of the hydraulic conductivity. However, this approach was limited by a variety of data requirements.

Electrical resistivity is one of the most used and oldest geophysical methods in aquifer characterization (Loke et al.,2011). Electrical resistivity tools are based on injecting electric current into the subsurface and measuring the media's bulk electrical property, which shows how strongly it opposes the electrical current flow. A low resistivity value would indicate that an electrical current would easily flow in the media. Most resistivity surveys use four electrodes arrangement, two electrodes (transmitter) to create an electrical circuit and two electrodes at some distance away from the current injection point, to measure the electrical potential difference (voltage). This allows the determination of apparent resistivity (resistivity of an equivalent uniform media). The measurement of electrical resistivity could be done by moving the whole setting laterally along the ground surface (called profiling) or by obtaining the electrical properties variation with depth at a single location using vertical electrical sounding (VES). In VES, four-electrode measurements could be made with progressively larger spacing, centered at the same position. The other survey approach is a cross borehole survey in which two current and measurement electrodes could be placed in the same well or one in each borehole to image the area between two boreholes. The electrical survey's ultimate purpose is to find the electrical resistivity or conductivity distribution in the subsurface. Once the distribution is determined, one would use the appropriate petro-physical relationship to convert distribution of electrical resistivity to water saturation by Archie's law (Archie, 1942) and also hydraulic conductivity (Heigold et al., 1979) or permeability (Börner et al., 1996; De Lima and Niwas, 2000; Purvance and Andricevic, 2000; Slater and Lesmes, 2002) by many proposed empirical relationship in the literature.

$$log\ \mathrm{K} \approx -1.28 + 0.93 \log \sigma_e,$$

Equation 1:5 – Relationship between electrical conductivity and hydraulic conductivity proposed by Heigold et al. (1979)

here, K is the hydraulic conductivity and σ_e ($L^{-3}M^{-1}T^{3}I^{2}$) is the electrical conductivity.

In electromagnetic methods, electromagnetic fields generated by a source (controlled transmitter coils, radio transmitters, telluric currents) are utilized to measure the electromagnetic properties of the subsurface media. Depending on the source employed, one may measure the time-domain or the frequency-domain. The measurement can be whether low frequency (1–100 kHz) including frequency-domain and time-domain or high frequency (10–1000 MHz) ground-penetrating radar (GPR). GPR data can also be collected in the time and frequency-domain. Low-frequency EM methods primarily characterize the subsurface in terms of electrical conductivity, while the GPR method measure analyzes dielectric permittivity. Low-frequency electromagnetic methods are best suited for detecting shallow conductive units (clay layers or saline water-saturated sediments) (Linde, 2005). Unlike electrical resistivity tools, electromagnetic tools do not require

contact with the ground. Estimation of water content in the unsaturated zone is one of the principal application of GPR (Alumbaugh et al., 2002; Binley et al., 2002, 2001; Huisman et al., 2003, 2002; Schmalholz et al., 2004; Schmalz and Lennartz, 2002) using proven petro-physical relationships. Variation of grain size, porosity, or in general, properties relevant to texture and hydraulic parameters leads to electromagnetic velocity attenuation in GPR, which means that GPR methods could be used to infer these properties. Furthermore, the lithology would be inferred as the high-velocity zones correspond to sand and gravel layers, while low-velocity regions correspond to clay and silt layers (Vanderborght et al., 2005). Groundwater table can also be understood by GPR as there would be a large contrast between saturated and unsaturated zones. Some works have reported GPR use for monitoring the contamination transport as the contaminants lead to weakness or absence of radar or where additional reflection may occur (Brewster and Annan, 1994; Davis and Annan, 1989; Francisca and Rinaldi, 2001).

Self-potential (SP) method is based on measuring the natural electrical potentials developed in the earth due to electrochemical interaction between minerals and subsurface fluids, electrokinetic processes from the flow of ionic fluids or thermoelectric mechanism from temperature gradient in the subsurface (Sharma, p.V., 1997). The exciting aspect of the SP method is that it is the only geophysical measurement directly sensitive to the groundwater flow (Jardani et al., 2007). The SP surveys are especially useful for localizing and quantifying the groundwater flow, pollutant plume spreading and estimating of the pertinent hydraulic properties of the aquifer (hydraulic conductivity, water table) (Jouniaux et al., 2009). Jardani et al. (2007), used SP measurement to map the Darcy velocity distribution of the groundwater. Their approach relies on the relation between streaming current density and Darcy velocity. They tested their approach to two synthetic model cases and they found reconstructed Darcy velocity distribution is in agreement with the reference one. Finally, they applied their approach to an infiltration test data and concluded that distribution of the Darcy velocities agrees reasonably well with the result inverted from the SP data. In another work, Jardani and Revil (2009) used SP and temperature data in geothermal field to invert the piecewise constant hydraulic conductivity distribution using a stochastic method and known facies. They applied their inversion scheme to a 2D synthetic case and found out joint inversion of temperature and SP data can be complementary since one is being measured in surface and one being measured in the borehole. They also successfully applied their approach to a geothermal field in Baja California and found the estimated permeabilities consistent with previous hydrogeological studies. Soueid Ahmed et al. (2014) performed a joint tomography of the head and SP data to reconstruct the hydraulic conductivity. They studied several synthetic case studies and found that adding SP data in case of limited number of head data can improve the estimation of hydraulic conductivity field. However, the successful addition of SP data requires precise estimation of electrical conductivity distribution.

Even though the geophysical measurement provides the continuous measurement of the subsurface properties and are less costly and time-consuming compared to hydraulic methods, the response of geophysical approaches must be accompanied by a petro-physical relationship to convert the geophysical responses to aquifer properties, highlighting their most significant drawback in characterizing aquifers' hydraulic properties. It is hard to define a petro-physical relationship, especially in complex media such as fractured rocks. Furthermore, the discrepancy in scale and resolution between geophysical and hydrogeological measurements makes it difficult to develop a petro-physical relationship linking geophysical parameters to hydraulic parameters (Chen et al., 2003).

On the other hand, in hydraulic methods, a hydraulic disturbance is created into the aquifer system, and the response of the aquifer is analyzed to quantify and map the hydraulic properties. The disturbance

can be made by a hydraulic head change, introducing solute or heat into the aquifer. The hydraulic head change may be attained by producing or injecting a fluid through boreholes in the aquifer or the tidal effect. Well-testing is a common approach for the creation of the hydraulic changes by subjecting the aquifer to one/series of pumping. The well-tests have three main objectives, (i) to observe the response of the aquifer to the hydraulic head change and further use it to characterize and determine the subsurface properties, (ii) evaluation of the hydraulic properties of the production well itself in order to design the exploitation scheme, and (iii) investigating the type of boundary conditions acting on the aquifer. The well-tests can be performed in different modes based on the desired perturbation:

(i) single well-test: the perturbation and monitoring are done in the same borehole.

(ii) interference test: the perturbation and monitoring are performed in different boreholes.

(iii) pumping test: the aquifer is disturbed by pumping whether using a single or interference well test. The injection test is the same as the pumping test, but the fluid is injected instead of being pumped. The pumping tests are typically conducted with a constant flow rate. However, tests with variable flow rates can also be interpreted.

(iv) step-drawdown test: a single well test with a series of successive constant pumping rates. This type of test is particularly performed to evaluate the properties of the groundwater production depending on the equipment of the well.

(v) Build up or recovery test: it follows the stop of the pumping test by observing the head's recovery at the pumping test or other monitoring points to the initial state.

(vi) constant head test: the head is maintained at the constant level, and water discharge is measured in the perturbation borehole. The head can also be measured in other observation boreholes.

(vii) slug test: the perturbation is a sudden change of the head in the perturbation borehole, and the response of the test in the borehole itself or other monitoring points are measured.

(viii) packer test: if any of the above tests are performed using packers to isolate the perturbation interval or monitoring interval.

Performing a series of pumping tests in an aquifer and recording the head change across the aquifer, one would use classical analytical solutions such as Thiem methods (1906), Theis non-equilibrium equation (1935), Hantush-Walton method (1962), and many others to estimate average hydraulic properties of the aquifer. However, this traditional pumping test analysis relies on the aquifer's homogeneity assumption and estimates the average value for hydraulic properties. Even though the analytical solutions do not provide information about the hydraulic properties distribution, they are still powerful tools to understand the general aquifers' characteristics and performance. On the other hand, the pumping test data could be used by hydraulic tomography inversion technique to map the values and hydraulic properties distribution. Hydraulic tomography is explained in detail in the following subsection.

The other hydraulic method that is conventionally used is based on injecting a distinguishable chemical compound called tracers into the aquifer. Tracers such as saline water, fluorescent dies, or noble gasses, etc., are injected into the aquifer by a defined pattern (pulse injection, etc.), and then the arrival time and concentration are observed in other points (Curtis et al., 1986; Freyberg, 1986; Jawitz et al., 2003; Ptak

and Schmid, 1996; Sudicky, 1986; Sutton et al., 2000). Tracers can be classified based on their interaction with media:

(i) conservative tracers which do not interact with media and thus they are carried passively with the water carrying them,

(ii) reactive tracers, which undergo a reaction or a biological process as the aquifer's moving water, is carrying them.

The combination of conservative and reacting tracer can provide insightful information about the aquifer's physical, chemical, and biological characteristics (Cao et al., 2020). The conservative tracers can be informative about the hydraulic properties, groundwater velocity, determination of recharge and discharge, and estimation of hydro-mechanical dispersivity. Some examples of conservative tracers are anions and bromide, dye tracers, stable isotope 18O, 2H, and rhodamine (Cao et al., 2020). Implementation of reactive tracer tests can provide useful information such as physicochemical aquifer properties (e.g., sorption capacity), water chemistry, and biological activity of the aquifer. Examples of reactive tracers are alcohols of varying chain length, such as 1-hexanol (Imhoff et al., 2003), fluorotelomer alcohols (Dwarakanath et al., 2016), sulfur hexafluoride (SF6) (Reid and Jaffé, 2013), and many others available in the literature.

Despite the valuable information provided by solute tracers, the implementation is expensive, and recovery of injected tracers as well as their detection is not simple and requires special instruments. Instead, heat can be an appropriate substitution for chemical tracers, and it also reveals some other thermal related aspects of the aquifer properties. Heat tracer is implemented by injection of heated or cold water and monitoring the temperature change in the injection borehole and other locations in the aquifer. Measurement of the aquifer temperature is much cheaper and easier due to commercially available thermometers and novel distributed temperature sensing tools compared to the chemical tracer detection tools. It has proven advantages over solute tracers for being environmentally friendly, available, easily measurable, and relatively inexpensive (Anderson, 2005). It also should be noted that each tracer reveals one aspect of the aquifer properties. For instance, Irvine et al. (2015), showed that solute tracer provides more understanding about the variance in velocity caused by aquifer heterogeneity while heat tracer provides a better approximation of the mean velocity. This is due to the fact that heat is not a conservative tracer, and the diffusivity of heat is much greater than the diffusivity of the solute tracers. Heat interacts more with the media by diffusing through the solid grains, which leads to more attenuated signals in monitoring points rather than the solute tracers.

In brief, geophysical methods provide continuous measurement and are less time consuming compared to hydraulic methods. Pressure-based methods require less time than tracer-based methods and provide information about the subsurface media's hydraulic properties while the data may not be as sensitive as chemical and heat tracer data to the heterogeneity. The pressure-based methods are easier to interpret and implement compared to the tracer-based methods.

In the following subsections, firstly, the inverse problems and one of the most favorable methods for hydraulic properties characterization, hydraulic tomography, is explained. Next, we review the heat-based methods for quantifying subsurface flow and characterization of subsurface media. We then introduce the Fiber Optic Distributed Temperature Sensor (FO-DTS), a novel tool that allows us to measure the temperature all along the fiber optic cable and used in our study. The final subsections are devoted to explaining the research objectives and thesis outlines.

1.2 Inverse problem and hydraulic tomography

The subsurface hydraulic properties are not readily accessible for measurement unless the core samples are taken from the ground by drilling boreholes or cone penetrating tests. In addition, core-based and laboratory measurement methods are time-consuming, expensive, and invasive to the aquifer. Furthermore, the information inferred from core-scale experiments would not represent the whole system (De Marsily et al., 2005). Thus, the hydraulic properties characterization methods rely on the estimation of the values and distribution using a limited number of data (Emsellem and De Marsily, 1971; Gavalas et al., 1976; Neuman, 1973). One way would be interpolating the measured hydraulic properties using geostatistical or stochastic methods. The common assumption is that hydraulic properties are stationary and log-normally distributed. A variogram model that describes the property's spatial continuity is created based on the available measured properties. Then, estimation methods such as ordinary kriging are employed to find the property's values and distribution.

Due to the scarcity of the hydraulic properties data, the inversion methods such as Hydraulic tomography are developed to estimate the hydraulic properties by the sparse number of data. Hydraulic tomography relies on the analysis of the aquifer response to a hydraulic change. The response is a function of hydraulic property values and distribution. Hydraulic tomography tries to find a solution for an inverse problem in which a set of model responses are used to estimate the model parameters. In a forward problem, the model parameters (**m**) and a mathematical model (*f(-)*), which is an approximation of real physic by mathematical terms, are used to predict the observable response data (**d**). While, in inverse problems, a set of observable response data (**d**) along with the mathematical model (*f (-)*) are used to estimate model parameters (**m**). For instance, in the hydraulic tomography problem, the observed hydraulic head changes in the aquifer (**d**) accompanied by a mathematical model (*f(-)*) describing the hydraulic changes as a function of hydraulic conductivity go through an inversion process to estimate the hydraulic property (**m**) values and distribution across the aquifer. The mathematical model used in hydraulic tomography is mostly based on the numerical models describing groundwater flow in the porous media. The numerical simulation predicts the aquifer response to a hydraulic change as a function of the hydraulic conductivity field, fluid properties, and boundary conditions imposed on the model.

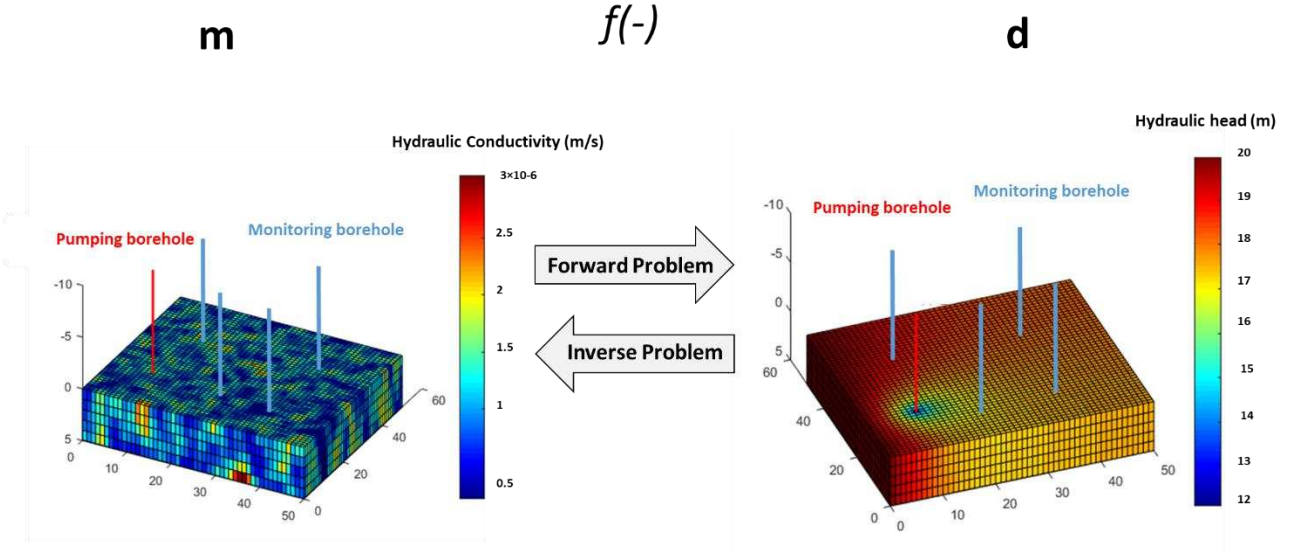

Figure 1-3: Representation of a hydraulic tomography inverse problem.

The inverse problem contained in hydraulic tomography can be formulated as follow. The terms used in the equation 1:6 are previously defined except η, which is the error associate with measurements.

$$\mathbf{d} = f(\mathbf{m}) + \eta$$

Equation 1:6 – Inverse problem formulation

From a mathematical point of view, the problem is ill-posed, and the solution is non-unique as limited number of observations are used to estimate a much larger number of the model parameters. Thus, additional information (prior model) is required for regularization and having physically meaningful results. From the probabilistic point of view, the solution of inverse problems is obtained by maximizing a posterior probability density function (maximizing the term in brackets), which is expressed using Bayes's theorem as follow

$$\pi_{\text{post}}(\mathbf{m}|\mathbf{d}) \propto \sim\exp\left[\frac{-1}{2}(f(\mathbf{m}) - \mathrm{d})\mathbf{C}_{\mathrm{d}}{}^{-1}(f(\mathbf{m}) - \mathbf{d}) + \frac{-1}{2}\left(\mathbf{m} - \mathbf{m}_{\text{prior}}\right)\mathbf{C}_{\mathrm{m}}{}^{-1}\left(\mathbf{m} - \mathbf{m}_{\text{prior}}\right)\right].$$

Equation 1:7 – posterior probability density function by Bayes theorem

where $\mathbf{C}_{\mathrm{d}}$ and $\mathbf{C}_{\mathrm{m}}$ are model properties and data covariance matrix, respectively. The prior model is denoted by $\mathbf{m}_{\text{prior}}$. The first term in equation 1:7 is the likelihood and the second term is the regularization. The inverse problem solution corresponds to best-fitting model properties, resulting in reproducing the observed data by the mathematical model while constraining the solution to some prior information to avoid unlikely and unrealistic solutions.

There are various techniques to solve hydraulic tomography problems. The two of the most important methods are the stochastic inverse method and geostatistical inverse methods. The stochastic inversion methods rely on the Sequential Successive Linear Estimator (SSLE) to map the hydraulic conductivity field (Yeh and Liu, 2000; Yeh and Zhang, 1996). The SSLE approach is similar to the co-kriging, which seeks mean parameter fields using point data and geological/hydrogeological structures (i.e., the spatial covariance and cross-variance of parameters and hydraulic heads) to condition the estimates (Berg et al., 2010). Co-kriging relies on the classical linear predictor theory that considers spatial correlation structures of flow processes (such as hydraulic head and velocity), subsurface hydraulic property, and cross-correlation between the flow processes and the hydraulic properties (Berg et al., 2010). SSLE is different from co-kriging because it uses a linear estimator based on differences between observed and simulated hydraulic heads successively to update both conditional means and covariance of the estimates.

Geostatistical inversion methods produce the first and second statistical moments of hydraulic variables, representing their most likely estimates and their uncertainty, respectively, conditioned on the available observations. Quasi-linear inversion approach has been developed and proposed by Kitanidis (1995). The geostatistical approach has been applied to many engineering disciplines such as contaminant source identification (Snodgrass and Kitanidis, 1997), tracer data inversion (Fienen et al., 2009; Nowak and Cirpka, 2006), hydraulic tomography (Cardiff et al., 2009; Cardiff and Barrash, 2011; Li et al., 2007, 2008). For the purposes of the studies presented in this thesis, the geostatistical inversion formulation and procedure are briefly explained. Geostatistical methods have been widely used to solve the hydrogeological inverse problems in which geostatistical information is used for regularization. This approach assumes that the model parameter field is random, auto-correlated with a certain correlation structure. The model parameter constitutes from a deterministic mean and a random fluctuation (Υ') about the mean and has the following properties

$$\mathbf{m} = \mathbf{X}\boldsymbol{\beta} + \mathrm{Y}' , \quad \text{(a)}$$

$$E(\mathbf{m}) = \mathbf{X}\boldsymbol{\beta} , \quad \text{(b)}$$

$$E[(\mathbf{m} - \mathbf{X}\boldsymbol{\beta})(\mathbf{m} - \mathbf{X}\boldsymbol{\beta})^T] = \mathbf{C}_{\mathrm{m}}(\theta) , \quad \text{(c)}$$

Equation 1:8 – Assumption of geostatistical inversion

where $\mathbf{m}$ is a vector of model properties, Y' is its random fluctuation, $\mathbf{X}$ is a matrix of trend function, $\boldsymbol{\beta}$ is the vector of trend coefficient. $\mathbf{C}_{\mathrm{m}}$ represent the model covariance matrix, characterized by geostatistical information (θ) about the field through a variogram. An iterative optimization process obtains the model parameters. The solution at $(i+1)^{th}$ iteration is obtained as:

$$\mathbf{m}_{\mathrm{i}+1} = \mathbf{X}\boldsymbol{\beta}_{\mathrm{i}} + \mathbf{C}_{\mathrm{m}}\mathbf{J}_{\mathrm{i}}\boldsymbol{\varepsilon}_{\mathrm{i}},$$

Equation 1:9 – model parameter in each iteration by geostatistical inversion

where $\boldsymbol{\beta}$ and $\boldsymbol{\varepsilon}$ are obtained by solving the following system of equations.

$$\begin{bmatrix} \mathbf{J}_{\mathrm{i}}\mathbf{C}_{\mathrm{m}}\mathbf{J}_{\mathrm{i}}{}^T + \mathbf{C}_{\mathrm{d}} & \mathbf{J}_{\mathrm{i}}X \\ (\mathbf{J}_{\mathrm{i}}\mathbf{X})^T & 0 \end{bmatrix} \begin{bmatrix} \boldsymbol{\varepsilon}_{\mathrm{j}} \\ \boldsymbol{\beta}_{\mathrm{j}} \end{bmatrix} = \begin{bmatrix} \mathbf{d} - f(\mathbf{m}_{\mathrm{i}}) + \mathbf{J}_{\mathrm{i}}\mathbf{m}_{\mathrm{i}} \\ 0 \end{bmatrix}$$

Equation 1:10 – System of the equation solved to obtain the trend function coefficient

here, $\mathbf{J}$ represents the Jacobian matrix sensitivity matrix of the measurements with respect to the model parameters. Calculation of Jacobian matrix for high dimensional problem requires great computational effort.

Hydraulic tomography is performed for two different aquifer states in which data are acquired, the steady-state (Cardiff et al., 2009; Huang et al., 2011; Li et al., 2008) and transient hydraulic tomography (Berg and Illman, 2011; Illman et al., 2009; Straface et al., 2007). In steady-state hydraulic tomography, the head or drawdown values when aquifer reaches steady-state condition are used for the inversion. In the transient hydraulic tomography, the head or drawdown values recorded during the transient period are used as the observation. Steady-state hydraulic tomography allows estimation of the hydraulic conductivity while using transient hydraulic tomography, estimation of storativity of the aquifer is possible in addition to the hydraulic conductivity. Transient or steady-state hydraulic tomography is accounted by the mathematical model in the inversion process. Furthermore, some authors have proposed oscillatory hydraulic tomography (Cardiff et al., 2013, 2009; Fischer et al., 2018) in which periodic pumping tests are used as a source for aquifer hydraulic state disturbance and pressure sensors are located in different places to record amplitude and change of the oscillating pressure signals. The recorded data accompanied by a proper model are used to find the hydraulic conductivity field.

Hydraulic tomography has been the subject of research for many years. Hydraulic tomography was first proposed as an equivalent to geophysical tomography by Neuman (1978) and further developed by Gottlieb and Dietrich (Gottlieb and Dietrich, 1995). The applicability of the hydraulic tomography was first tested by synthetic numerical studies (Yeh and Liu, 2000; Zhu and Yeh, 2005, 2006) followed by many laboratory works reported in the literature (Illman et al., 2010, 2008, 2007; Liu et al., 2002). Illman et al. (2010) used a sandbox aquifer to evaluate the performance of the hydraulic tomography. They estimated a hydraulic conductivity field using steady-state hydraulic tomography and then compared the drawdown observed and predicted by

the estimated hydraulic conductivity field for 16 independent pumping tests (these pumpings were not included in the hydraulic tomography). They also used kriging using 16 pumping points to estimate the hydraulic conductivity field. They found out that the hydraulic conductivity field obtained from kriging cannot accurately predict the drawdown for 16 independent pumping tests, while the hydraulic conductivity field obtained from hydraulic tomography provided an excellent prediction of the drawdowns. In another work, Liu et al. (Liu et al., 2007) tried to validate the transient hydraulic conductivity on a heterogeneous sandbox aquifer. They compared the hydraulic conductivity estimates from hydraulic tomography and estimates obtained from core samples, slug tests, single-hole analyses, cross-hole analyses, and unidirectional flow-through tests. They found that the sandbox's heterogeneity pattern can be delineated by core and the slug test, while hydraulic tomography provides considerably more details. The storage values determined by hydraulic tomography are close to those from single hole analysis and within the plausible range. The average of the hydraulic conductivity estimates from the cross-hole tests and analyses yields an averaged value close to the effective value determined from the uniform flow experiment or the mean value of the estimates from hydraulic tomography. Finally, they claimed that transient hydraulic tomography could yield the same quality hydraulic conductivity estimate with fewer pumping data than steady-state hydraulic tomography. In another important lab experiment, Illman et al. (2012) concluded that hydraulic conductivity estimated by Hydraulic tomography could remarkably improve the predictions of solute transport.

There have also been many field applications of hydraulic tomography applied to characterize fractured and alluvial aquifers (e.g., (Berg and Illman, 2012; Bohling et al., 2007; Bohling and Butler Jr, 2010; Cardiff et al., 2012; Cardiff and Barrash, 2011; Fischer et al., 2018, 2017; Huang et al., 2011; Liu et al., 2002, 2007; Michael Tso et al., 2016; Ni et al., 2009; Straface et al., 2007; Yeh and Liu, 2000; Yin and Illman, 2009; Zha et al., 2015; Zhu and Yeh, 2005). The promising results obtained from hydraulic tomography validate this approach's effectiveness for the subsurface media characterization compared to traditional aquifer characterization methods (Berg and Illman, 2015, 2011).

Despite the effectiveness of hydraulic tomography, it is still a costly and time consuming operation. Illman et al. (2012) compared the costs and benefits associated with heterogeneity characterization by hydraulic tomography and analysis of the core data through geostatistical analysis. They found that hydraulic tomography is costlier compared to the geostatistical analysis of high resolution hydraulic conductivity data. This higher cost is due to the capital cost of the equipment used for the hydraulic tomography. However, it should be noted that the equipment may be bought or reused in other sites, which compensate the cost paid over the equipment's life span. Despite the associated cost, hydraulic tomography better captures the important features of aquifer and aquitard and better predicts the aquifer's response to the pumping tests. This suggests that information from hydraulic tomography would be more trustable to design robust remediation operations in the aquifers. For this purpose, adding more measurements, in particular about the groundwater flows distribution, may be particularly useful and complementary for hydraulic tomography. This will be one of the main motivations of the work presented in this thesis.

1.3 The use of heat for monitoring and characterization of subsurface media

1.3.1 Introduction

From a thermodynamic point of view, heat is defined as a form of energy transferred (due to temperature difference) from/to an object by mechanisms other than thermodynamic work or transfer of matter. The concept of heat has been extensively used in hydrogeology. One of the oldest applications was the analogy used to derive Darcy flow law from Fourier's Law and the analogy that Theis (1935) used to solve the transient flow equation using the transient heat's analytical solution equation. The heat has also been recognized as a natural groundwater tracer, and its application is comprehensively reviewed by Anderson (2005), Saar (2011). Much attention is given to the use of natural temperature variation as a tool to characterize surface water/groundwater exchange (Conant Jr, 2004; Constantz et al., 2008; Doussan et al., 1994; Keery et al., 2007; Molina-Giraldo et al., 2011; Schmidt et al., 2006; Vogt et al., 2010) and groundwater recharge and discharge (Conant Jr, 2004; Ferguson et al., 2003). Groundwater flux in the fracture or faults can disturb the geothermal temperature distribution locally or regionally due to the advection of the heat by flow of water (Anderson, 2005; Deming and Investigators, 1993; Saar, 2011) and so the temperature can be indicative of a such a process. Temperature-depth profile is also used to estimate the aquifers' vertical heat flux, vertical groundwater flux, and thermal properties of the aquifers (Bredehoeft and Papaopulos, 1965; Frei et al., 2009; Lowry et al., 2007; Taniguchi et al., 2003; Vandenbohede et al., 2009). Some works indeed reported using the variation of the temperature for model calibration (hydraulic conductivity values) along with the head data (Bravo et al., 2002). The temperature data has also been used to determine spatial and temporal infiltration dynamics (Tabbagh et al., 2017) during the managed aquifer recharge (Herckenrath et al., 2012; Mawer et al., 2016; Racz et al., 2012), groundwater recharge (Cheviron et al., 2005) and monitoring of the soil water content (Bechkit et al., 2014). Considering the vast domain of temperature utilization in hydrogeology, the temperature is still underused (Anderson, 2005) and overlooked (Kurylyk and Irvine, 2019) tool in hydrogeology.

Heat transfer mechanism in porous media can be classified into two main categories:

(i) Conduction: transfer of energy inside or from a matter to adjacent matter in direct contact, which is explained by Fourier's law.

(ii) Convection: transfer of energy through the movement of a fluid (in our case, water). It should be noted that mostly advection and convection are interchangeably used. The convection can be present in porous media, provided a minimum permeability within the range of 5×10^{-17} to 10^{-15} m^2 (Saar, 2011). Rojstaczer et al. (2008) and Ferguson et al. (2006) have determined a minimum permeability value of 10^{-16} m^2 so that convection could have an effect on the temperature distribution.

Heat is transported in the porous media through conduction and convection. The movement of water controls the convective heat transfer, while conductive heat transfer is the only process occurring when water does not move. Conduction is controlled by the thermal conductivity and heat capacity of the rock and water. Thermal conductivity refers to the ability of a material to transfer heat through conduction. Heat capacity refers to the amount of heat required to be given to a substance to increase its temperature by a unit. This property in the unit mass or unit volume of the substance is called specific heat capacity and volumetric heat capacity, respectively. Thermal diffusivity is the ability of a substance to conduct thermal energy relative to

its ability to store energy and is calculated by dividing the value of thermal conductivity by the value of volumetric heat capacity. It provides information about the competition of heat transfer due to conduction and heat storage. The three-dimensional heat transport in the aquifer is given as follow (Domenico and Schwartz, 1998):

$$\frac{\lambda_e}{\rho c}\nabla^2 T - \frac{\rho_w c_w}{\rho c}\nabla.(Tq) = \frac{\partial T}{\partial t},$$

Equation 1:11 – Three-dimensional heat transport equation in the aquifer (Domenico and Schwartz, 1998)

where, T, λ_e, c, ρ, q, and t refer to temperature, effective thermal conductivity (taking into account rock and fluid), specific heat capacity, density, specific discharge, and time. The terms ρc and $\rho_w c_w$ are volumetric heat capacity of the rock-water matrix and water, respectively. The term $\frac{\lambda}{\rho c}$ also defines the thermal diffusivity of the rock-fluid matrix. In equation 1:11, all media properties are assumed to be constant. The first term in the above equation represents the transport of heat by conduction. The second term is the advection or convection term, which represents heat transport by water flow. Depending on the hydraulic conductivity and hydraulic gradient value, which defines the Darcy flux value in porous media, conduction and convection can be the dominant heat transfer process. For small Darcy flux values, only conduction occurs, while for larger values, both conduction and convection are present, but the role of convection might be more significant. Figure 1-4 shows the heat transport mechanism for a combination of hydraulic conductivity and hydraulic gradient (Ferguson et al., 2006) in different ranges. Note that, hydraulic gradient in the field ranges in general from 10^{-4} up to 10^{-1}.

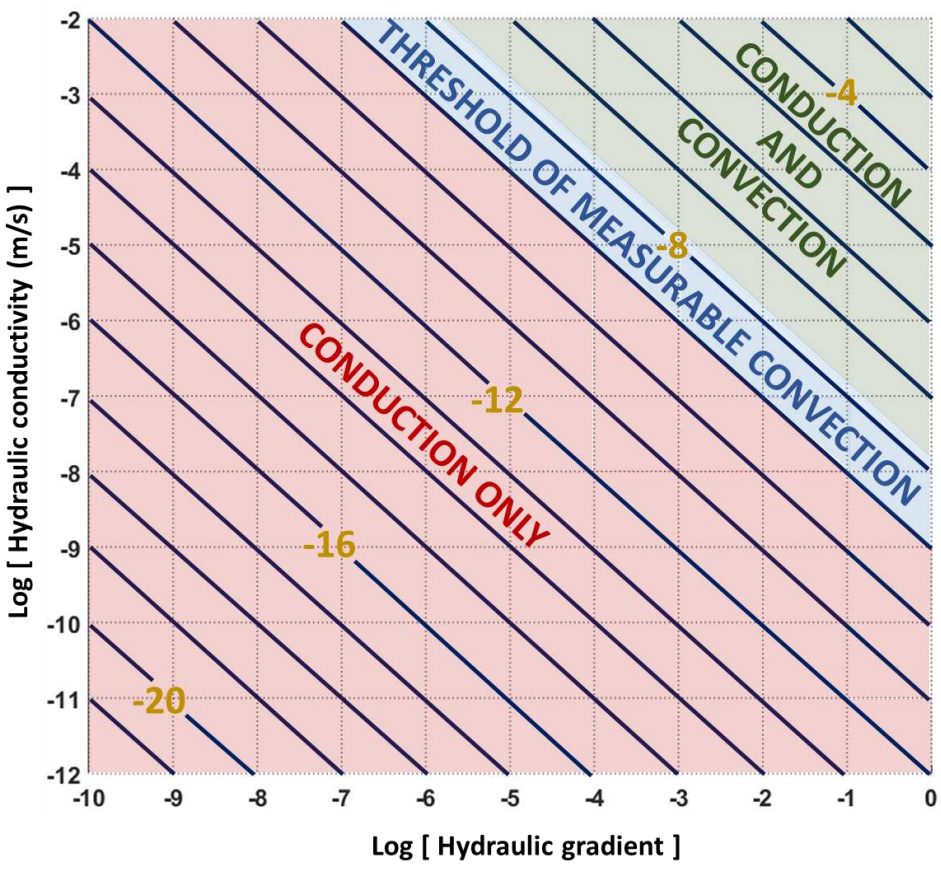

Figure 1- 4: Heat transfer mechanism based on the values of hydraulic gradient and hydraulic conductivity. The dark yellow number represents the log of Darcy flux (m/s) (Modified after Ferguson et al., 2006)

Measurement of the temperature is quite easy and inexpensive which can be carried out by deploying the temperature probes in the borehole (to obtain temporal temperature data in a fixed position) or performing logging (to obtain spatial temperature data) by lowering the temperature probe into the borehole and performing up and downhole surveys. Fiber optic DTS technology can measure the temperature profile both in space (along the fiber optic) and with time so it can be an appropriate substitution to the classical probes. Two main types of popular thermal tracer tests are active thermal tracer tests, where temperature anomalies are artificially induced, and passive thermal tracer tests, where the natural variability of temperature is targeted.

Considering the wide range of applications of using heat as a groundwater tracer in hydrogeology, from now on, we narrow our focus to using heat for subsurface flow quantification and subsurface media's tomography. The heat has been used to quantify flows within boreholes and the flow in aquifers. We first review the use of passive and active heat tracer to quantify the vertical borehole flow and the horizontal flow passing by the borehole. Next, we review the use of heat for the quantification of flow in the subsurface.

1.3.2 Fiber Optic Distributed Temperature Sensing (FO-DTS)

Fiber optic DTS technology can measure the temperature profile both in space (along the fiber optic) and with time so it can be an appropriate substitution to the classical temperature probes. Fiber Optic Distributed Temperature Sensing (FO-DTS) is a member of distributed family sensors, a technology allowing real-time measurement of the temperature, strain, acoustic, etc., in space and time along the FO-cables. FO-cables are thin (as thin as a human hair) flexible cables made up of pure glass (silica) consisting of two parts: the inner core (central part of FO cable in which majority of lights travel through this section) and outer cladding, which is a lower reflective index glass layer helping the light to be maintained within the core. A single or multiple layers of polymers are wrapped around the core and cladding for protection. The current DTS devices are able to have sampling measurement down to 12.5 cm (e.g., Silixa Ultima S), which is different from spatial resolution (Simon et al., 2020), and can measure temperature with a temperature resolution of 0.05 °C and even 0.01 °C depending on the sampling frequency. The length of the cable and thus temperature measurement can range from meters to kilometers. For cable lengths up to 2 or 5 km, one may measure the temperature (Silixa Ultima S) with a resolution of 0.05 °C or less, but for longer cables, the sampling measurement becomes every 0.5 m to 1 or 2 m depending on the instruments with the generally coarser temperature resolution.

The measurement starts by launching a short light pulse (by DTS unit) into the FO-cable, and as the light moves forward in the FO-cable, it colloids with the atoms of the fiber, energizing them and leading to the emission of lights traveling back to the light source at slightly shifted frequencies called Raman backscattered light. The name originates from Chandrasekhara Raman (1928), who was the first to discover the temperature dependency of these backscattered lights. The Raman backscattered lights, which have two wavelengths called Stokes and anti-Stokes, are recorded by the DTS unit. Keeping in mind that the velocity of light is constant (even in fiber optic), the time difference between launching the light into the fiber and return of the backscattered light determines the measurement's location in the FO-cable. The temperature value of backscattered light is dependent on the ratio of anti-Stoke to Stokes intensities.

The calibration is a prerequisite for successful and accurate measurement of temperature data. Calibration refers to determining the physical quantities that allow inferring temperature from DTS raw signal. Calibration avoids temperature readings to be affected mainly by offset (constant shift between measured and real

absolute temperatures) and slope issues (variation with the distance of DTS readings of a constant temperature). Commercially available DTS units have built-in calibration routines that use part of the cable in a known temperature environment. However, external reference temperature measurement would result in more precise temperature determination (Bense et al., 2016). This would be normally achieved by using a temperature probe in a bath of uniform and controlled temperature (cold and hot baths) assumed to have a constant temperature on the time scale (Constant bath temperature is not obligatory, and one would use varying temperature bath to calibrate for every time steps). The data obtained by external temperature probes are used in post-processing to determine the temperatures more accurately.

The FO-DTS measurement can be performed in different configurations, but the two most frequently used configurations are single-ended and double-ended (des Tombe et al., 2020). In the single-ended configuration, the temperature measurement is outward from the DTS unit to the end of the cable as the laser pulse only moves in one direction from the DTS unit toward the end of the cable. In the double-ended configuration, both ends of the fiber optic cable (U shape configuration) are connected to the DTS unit, and the temperature measurement is done in both directions. Figure 1-5 shows the single-ended and double-ended configurations. The double-ended configuration requires calibration mainly for offset, while single-ended requires calibration for offset and signal loss and gain.

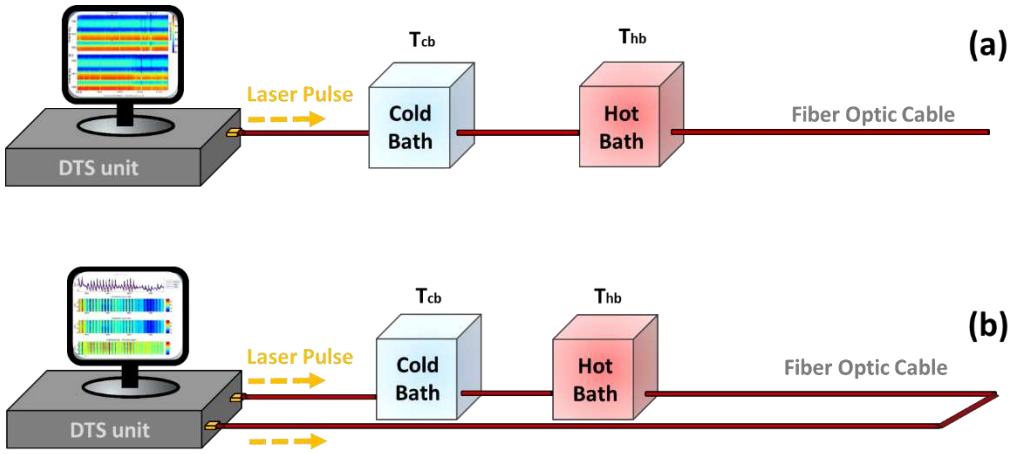

Figure 1-5 Representation of (a)single-ended and (b)double-ended configurations. The cold bath and hot bath are used to calibrate the temperature data acquired by FO-DTS

FO-DTS are employed in two different modes, namely, passive and active modes. In passive mode, the temperature along fiber optic cable is measured, while in active mode (also known as heat pulse method), heat is added to FO-cable by an element deployed inside the FO-cable or by using an additional heating cable. Active and passive temperature monitoring has found applications in hydrogeology, hydrology, and environmental sciences as well (Bense et al., 2016).

1.3.3 Borehole flow measurement

Some various non-thermal methods and tools allow for a measurement of vertical water velocity in the boreholes, such as heat-pulse flowmeter (Hess, 1986), electromagnetic flowmeter (Molz et al., 1994), and spinner or impeller flowmeter (Molz et al., 1989). Heat-pulse flowmeters are made up of a cylinder containing a heat source in the middle and two temperature sensors at each end of the cylinder. It is positioned stationary in the borehole, and flowing water is diverted to the cylinder. A packet of water is being heated and moving with flowing water upward or downward. The sensors monitor the temperature and time of the heated peak recorded and used to calculate water velocity. It should be noted that this approach may not be

classified as a heat-based method since water is just locally heated to have a signature of the travel time between the heating source and the sensors. The electromagnetic flowmeters work based on Faraday's Law of Electromagnetic Induction, which states that voltage induced by a conductor moving through a magnetic field is directly proportional to the conductor's velocity. This tool contains two coils that generate an electromagnetic field perpendicular to the flow, and the voltage that is measured is proportional to the water velocity. It should be noted that the fluid passing through the electromagnetic field must be a conductor (like water with salinity), and it cannot be applied for hydrocarbons. The spinner flowmeters use an impeller that rotates as it collides with the flowing water. The higher the velocity, the faster the rotation of the spinner. The spinner rotation is recorded and then converted to fluid velocity. Note that heat-pulse and electromagnetic flowmeters can be used to measure ambient flows, while impellers are generally used only when pumping in the observation borehole (Young and Pearson, 1995).

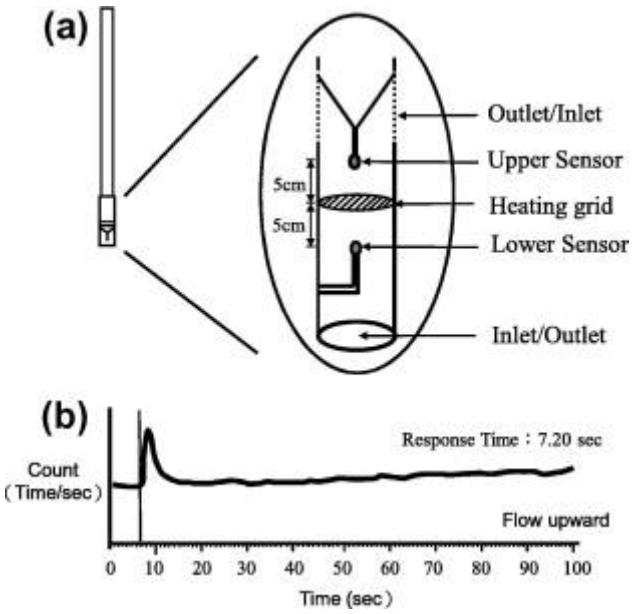

Figure 1-6: (a) Schematic of inner component of heat-pulse flow meter (b) typical response of heat pulse flow meter (modified after Lee et al., 2012)

There are also some methods that are used to estimate horizontal groundwater velocities in boreholes. In these methods, the horizontal water velocity is measured inside the borehole and then converted to specific water discharge away from the borehole by correcting the borehole effect (Masciopinto and Palmiotta, 2014). However, uncertainties arise in the correction of the borehole effect. It requires proper modelling of borehole and aquifer, information about the aquifer's hydraulic conductivity, filter pack, screen, and radius of annular filter pack, well screen, etc. Examples of methods used for horizontal groundwater velocity measurement in the boreholes are (i) Acoustic Doppler velocimeter (ADV), (ii) scanning colloidal borescope flowmeter (SCBFM), and (iii) fluid-conductivity logging system (FCLS). The ADV uses acoustic signals emitted at a specific rate per second to track the particle entrained in the flow and calculate the 3D groundwater velocity vector (Wilson et al., 2001). The SCBFM utilizes a camera, magnifier lens, and illumination source to track naturally buoyant colloid inside the water. The visual recordings are then used along with computer algorithms to compute groundwater velocity and direction (Bayless et al., 2011). FCLS measures the sequential profile of fluid conductivity and uses a computer algorithm to estimate the groundwater velocity. FCLS are not able to measure the groundwater flow direction and can only measure the magnitude. A comprehensive comparative study of different methods used for horizontal groundwater velocity in the boreholes is provided by Bayless et al. (Bayless et al., 2011).

Furthermore, the point dilution test (Drost et al., 1968) is also a common method proposed to estimate horizontal groundwater velocities. It relies on introducing a tracer in the borehole and tracking the tracer's dilution with time. A very simple analytical solution can explain the tracer's dilution through an exponential decay, relating the dilution rate to the groundwater velocity. Different tracers are used, such as radioisotopes or isotopes (Drost et al., 1968; Ronen et al., 1986; Wurzel, 1983), dyes or fluorescent dyes (Gutiérrez et al., 1997; Lewis et al., 1966; Novakowski et al., 1995; Pitrak et al., 2007; Sale et al., 2007), salts or brines (Hall, 1993; Hatfield et al., 2004; Moore et al., 1992; Novakowski et al., 2006; Riemann, 2002; West and Odling, 2007), and deionized water (Paillet and Pedler, 1996; Tsang et al., 1990). There is also an extension of the point dilution tests called Finite Volume Point Dilution Method (FVPDM), allowing temporal monitoring of the groundwater velocity (Brouyère et al., 2008). The last non-thermal method mentioned here is the Passive Flux Meter (PFM), a permeable cylinder sorbing the dissolve organic and inorganic contamination of the water inside the borehole. After a specific period, PFM is removed, and contaminant mass absorbed is used to calculate the time-averaged contaminant fluxes (Klammler et al., 2006). A groundwater flux profile can be obtained by performing the point dilution test in different depths in the borehole with packers to isolate the borehole segments and avoid vertical movement of the water (Palmer, 1993). It is worth noting that point dilution is applicable to both porous (Piccinini et al., 2016) and fractured (Jamin et al., 2015) aquifer. However, there are certain limitation associated with this approach as the measurement is quite time consuming, the special equipment required to perform the test which may not be cheap and readily available and the fact that it provides local (point) measurement or integrated measurement (over a borehole interval) rather than discrete points along the borehole.

The works on the concept of using passive temperature profile in the flowing borehole as a tool for quantification of vertical flow dates back to nearly sixty years ago (Edwardson et al., 1962; Lesem et al., 1957; Moss and White, 1959). The principal concept in using passive temperature for flow quantification is that the temperature profile with depth would follow the geothermal gradient unless there is an advection caused by flow, which disturbs the geothermal equilibrium.

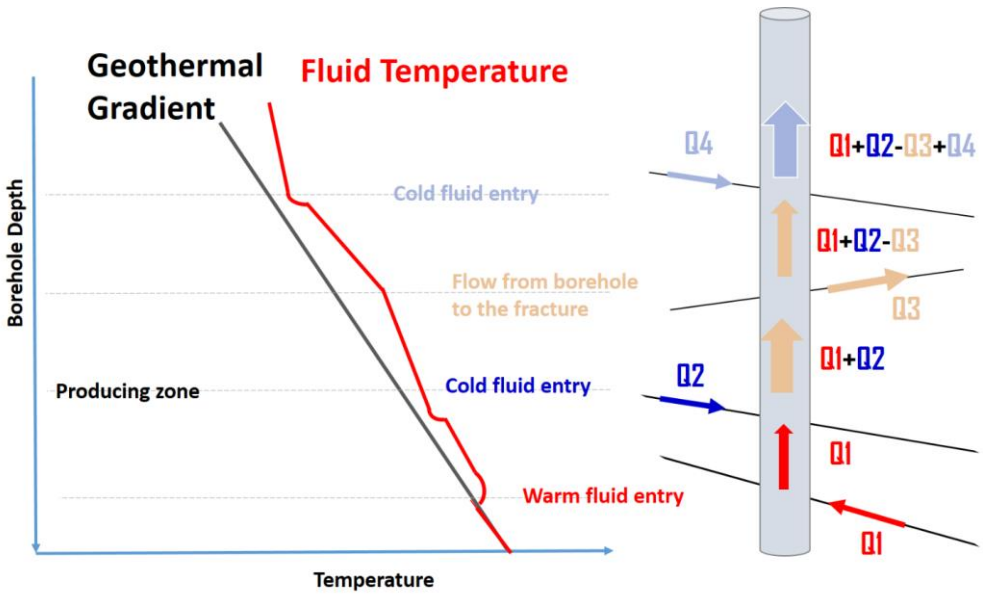

Figure 1- 7: Illustration of the concept of deviation of passive temperature profile from the geothermal gradient as a signature of flow in the borehole

The pioneering work in this area belongs to Ramey et al. (Ramey Jr., 1962). He proposed a simple analytical solution to predict the temperature profile of single-phase fluid in an injection well as a function of the media's thermal properties and fluid velocity in the borehole. Later his model was successfully applied to production wells (Horne and Shinohara, 1979). The model considers steady-state heat transfer inside the borehole while heat transfer from the borehole to the surrounding formation is governed by transient radial conduction. Ramey considered the borehole as a line source and the surrounding earth as an infinite sink in which heat diffusion only occurs in the horizontal plane and vertical heat diffusion is negligible. In Ramey's model, no inflow or outflow of the fluid from formation to the borehole or vice versa is considered, and the fluid temperature moving inside the borehole is a function of the depth, thermal properties of the borehole and surrounding earth, and also time. A time function is also introduced, which accounts for the temporal heat transfer behavior in the formation. Later Satter (1965) and Sagar et al. (1991) extended Ramey's model to two-phase flow by considering the effect of the kinetic energy and Joule Thompson effect caused by pressure change along the borehole. Hagoort (2004) examined Ramey's model applicability and found out that it can provide an excellent approximation except for the early times when the calculated temperature is overestimated. Hasan and Kabir (1994) further developed Ramey's model. They proposed a new approximate solution for transient heat transfer in the formation and incorporating both convective and conductive heat transport for the borehole/formation system. Hassan and Kabir's model used an appropriate inner boundary condition (finite wellbore) for wellbore/formation heat transfer and demonstrated the importance of including the convective heat transfer. Later, Kabir et al. (1996) proposed a model using energy, mass and momentum balance, and different fluid entries to the borehole. In their model, entry fluid temperature is assumed to be the geothermal temperature of the entry point inside the wellbore. Afterward, Hasan et al. presented many works incorporating hydrodynamic of different flow patterns and well geometry (Hasan et al., 2002; Hasan and Kabir, 2005). In one of their most general works, a robust analytical steady-state model is presented, including wellbore inclination, varying geothermal gradient, and Joule-Thomson effect by dividing the borehole into uniform sections thermal properties and inclinations (Hasan et al., 2009). The limitation of this approach is that the solution is not applicable in production zones. The majority of the works reporting the use of temperature flowing temperature profile for vertical flow profiling belongs to oil and gas wells (Hossain and Abu-Khamsin, 2012; Izgec et al., 2010; Kabir et al., 2008; Wang et al., 2008). However, the same concept has also been used in hydrogeology as well, as shown by Klepikova et al. (2011) who used a numerical model showing the water temperature profile's dependency in the borehole to its velocity. They inverted the temperature profile to a flow profile using the numerical simulator, not Ramey's equation. They validated their approach in a fractured borehole with the different entry of water to the borehole. The heat pulse flow meter recorded the flow profile, and a thermometer recorded the temperature profile by lowering it into the borehole. The temperature profile was inverted to the flow profile using a numerical simulator and was in good agreement with the flow profile obtained by the heat pulse flow meter.

Read et al. (2014) developed a method for quantifying the borehole's vertical flow based on active heating and distributed temperature sensing. They used two parallel fiber optic cables kept fixed adjacent to each other at a known distance. One cable is heated while the other cable measures the passive temperature. The principle is based on the temperature difference between the heating cable and fiber-optic distributed temperature sensing, which is a function of the vertical fluid velocity. They proposed an analytical solution relating the temperature difference to vertical flow velocity, which was used to invert the temperature difference profile to the borehole's flow profile. They applied their approach to a fractured borehole in Brittany, France. They found a good agreement between flow estimated by their approach and flow measured by the

heat pulse flow meter. Maldaner et al. (2019) used active fiber-optic distributed sensors in the sealed fractured borehole to quantify the fractured media's natural flow. They sealed the borehole with a flexible inflatable liner and placed an active fiber optic DTS between the liner and the fractured medium. Using a numerical simulator, they found a relationship between thermal conductivity calculated from the temperature evolution with time (apparent thermal conductivity) and those obtained by the numerical simulator for different flow values. They found that in no-flow regions, calculated thermal conductivity values agree well with laboratory measurement of thermal conductivity. Finally, they quantified the flow along the borehole using the established relationship. Recently, Munn et al. (2020) applied the previous approach to monitoring the fracture flow change once the borehole is subjected to pumping. They found out that this approach can effectively quantify the changes in the fracture flow.

1.3.4 Groundwater flow measurement

The quantification of the flow inside the porous media requires deploying the tool directly inside the media. There are not many non-thermal methods reported in the literature. Among them, Point Velocity Probe (PVP) (Devlin et al., 2009; Labaky et al., 2009, 2007) is introduced, measuring the groundwater flux on a centimeter scale. The method is based on mini tracer tests performed around a cylinder's perimeter in close contact with the aquifer. With one injection port and two or more tracer detectors on the cylinder's perimeter, one can measure the time required for the tracer to travel from the injection port to the detector and find the groundwater velocity. PVPs can be made of inexpensive materials and be deployed in multi arrays to find the groundwater velocity in space and time (Walter and Devlin, 2017). It is reported that PVPs can also find the velocity direction with an uncertainty of ± 8° on the direction angle (Devlin et al., 2009).

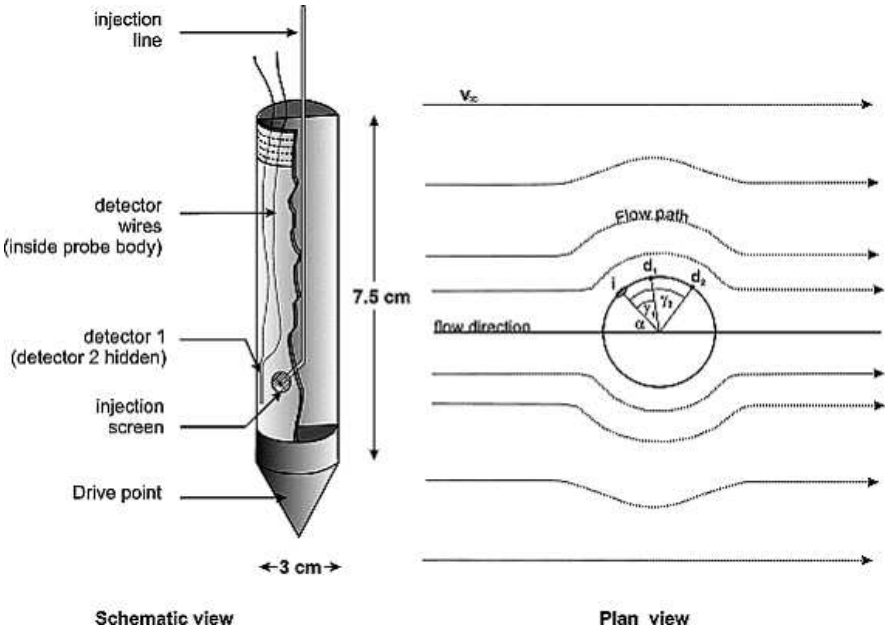

Figure 1-8: Schematic and plan views of the PVP. Flow travels around the probe body, picking up tracer at the injection port, i, and delivering it to two detectors, d1 and d2. Knowing the angles γ1 and γ2, apparent velocities averaged up to the detectors can be converted to the average linear velocity in the aquifer away from the probe, v_∞. In addition, the angle from the injection port to the average flow direction, α, can be calculated (modified after Labaky et al., 2009).

In this context, much attention has been given to active and passive thermal methods as the temperature is ubiquitous, easy to measure by available and inexpensive temperature probes, which can also be deployed directly to the ground. The concept of the geothermal gradient plays an important role in understanding the

subsurface flow using passive temperature. By definition, the geothermal gradient is the increase in the subsurface temperature with respect to the increase in the depth due to the heat produced in the earth and coming to the surface. The source of heat is mostly from naturally occurring radioactive elements inside the earth. It can be generally said that subsurface temperature deviation from the geothermal gradient can be indicative of the subsurface flow (Reiter, 2001). In application to quantify the vertical flow in stream bed exchange, passive temperature surface and subsurface temperature fluctuation is acquired to infer the water flux using the solution to convective-conductive equations (Constantz et al., 2002; Naranjo and Turcotte, 2015; Taniguchi et al., 2003; Rau et al., 2010; Stallman, 1965; Vogt et al., 2010). The convection-conduction equation (Equation 1:11) is linearized, and 1D steady-state flow is assumed from which the mass flux is related to the temperature change. Bredehoftand and Papadopulos (1965) presented an analytical solution for 1D steady-state heat transfer considering vertical flow with top and bottom boundary conditions at a constant temperature. Following this work, there has been some works offering modification for the solution. Stallman (1965) used sinusoidal fluctuation at the surface and constant temperature at very deep instead of constant temperature. Mansure and Reiter (1979) and Reiteret al. (1989) showed that the estimate of steady-state vertical flow could be obtained by using the plots of temperature gradient versus temperature in which the slope is proportional to multiplication of the vertical flux and media's thermal properties. Soon it was realized that the effect of horizontal flow could not be ignored when using the passive temperature profile to estimate the vertical flux. The effect of the horizontal flux on the estimation of vertical flux was taken into account by the analytical solution proposed by Lu and Ge (Lu and Ge, 1996). Later, Roshan et al. (Roshan et al., 2012) proposed an analytical solution for a 2-D heat transfer model considering the horizontal flow. They found out that ignoring the horizontal groundwater flux will result in a -60% to 250% error in estimating the vertical groundwater flux.

For the quantification of the horizontal flow, Stallman (1963) solved the 1D steady-state heat transfer equation (the steady-state form of Equation 1:11) with only horizontal flow components to find the effect of horizontal groundwater flow on the temperature profile with depth. As it is previously explained, the estimation of vertical and horizontal flux from passive temperature data may produce a significant error if one element of the flux is ignored. As an alternative to the passive temperature data, active heat tracing has been proposed and used for estimation of the horizontal groundwater flux. In this approach, a heater and temperature probes are embedded in porous media. The continuously injected heat subjected to groundwater flow will lead to temperature time series in temperature probes. The time series and analytical solutions to the advection-diffusion problem can infer the magnitude of the flux. Some works suggest using multiple arrangements of temperature probes to understand the flow direction as well. One of the earliest works belongs to Campbell et al. (1991), who designed the dual probe heat pulse sensors that comprise one temperature sensor and one heating element kept at a fixed distance. Many works then used this tool and modified the approach analysis approach (Basinger et al., 2003; Bristow, 1998; Heitman et al., 2003; Welch et al., 1996). However, the dual probe heat pulse was not applicable to flow quantification and was used to estimate thermal conductivity, thermal capacity, and volumetric water content of unsaturated soils. Ren et al. (1999) then modified the dual probe heat pulse sensors by adding another probe to the opposite side of the first temperature probe (at the same distance), leaving the heating element in the middle. Then he used the modified tool in a column with saturated soil imposed on different water fluxes (Ren et al., 2000). He used a dimensionless parameter called maximum temperature drop to relate the temperature drop between probes and flux. He found the approach reasonably accurate even though the errors increased with an increase in flow rate. Wang et al. (2002) proposed a relationship between the temperature change between upstream and downstream temperature probes and the media's flow and thermal conductivity. Since then, many works

have reported modifying the devices and approaches to quantify groundwater fluxes in the subsurface (Hopmans et al., 2002; Gresswell. 2009; Lewandowski et al., 2011). To investigate three-dimensional flow, Ballard (1996) also invented a tool consisting of a heating cylinder and an array of 30 temperature probes and deployed them permanently in an unconsolidated aquifer to measure groundwater flow velocity and directions. He found the fluxes' values and direction and the media's thermal properties using a mathematical model. Angermann et al. (2012a, 2012b) used a heating cylinder with 24 temperature sensors to investigate the flow magnitude and direction. They also proposed an algorithm to enhance the interpretation of heat pulse sensor results. They successfully applied it to a field site in the UK. They found out this approach can provide useful insight into the water flow directions and magnitudes. Recently, Banks et al. (2018) proposed a novel instrument with three heat sources and 56 temperature sensors to capture three-dimensional flow direction and magnitude. They used the instrument in the field and in a sand tank with numerous controlled hydraulic conditions to validate the method. They concluded that this approach could capture all three components of the flow field around the observation points. Despite all developments and advances in creating heat pulse instruments, their application is still limited to very shallow depths and in most cases for local measurements.

The introduction of active fiber-optic distributed temperature sensors provides new opportunities as a tool to measure groundwater fluxes profile along the cable. Fiber optic cables can be deployed using the direct push method to a higher depth (tens of meters) than other instruments reviewed previously. Bakker et al. (2015) performed a thermal tracer test by inserting six fiber optic and heating cables with one-meter spacing vertically into an unconsolidated aquifer in the Netherland. The active test was performed for four days, and temperature data recorded in fiber optic cables were used to estimate the horizontal groundwater flux and direction. Using this approach, they estimated the value and direction of the groundwater velocity and thermal conductivity and media heat capacity. Des Tombes et al. (2019) proposed an analytical solution to estimate the groundwater flux using a heating cable and fiber optic cable buried separately and vertically into the ground. They used their analytical solution to the data set obtained at two different sites. At the first site, a managed aquifer recharge, the fiber-optic cables were inserted 15 m deep at various locations. In the second site, the fiber optic cables were inserted up to the depth of 45 m. They used their analytical solutions with data obtained in these two sites and found the flux profile versus depth. Recently, Simon et al. (2021) validated numerically and experimentally using an analytical solution to obtain the groundwater fluxes (specific discharges). We proposed a graphical approach to obtain the groundwater flux using active fiber-optic distributed temperature sensors in which the heating element is embedded inside the fiber optic cable. The graphical approach is based on several characteristic times that can be used with other thermal parameters to estimate the groundwater flux. It is shown that the temperature evolution recorded by fiber optic cable consists of three main stages, heating storage period, conduction-dominant, and advection-dominant. In the very first moments of the heating, the heat is stored in the cable, which must be corrected to be further used to infer the groundwater flux. In the conduction-dominant period, the heat-transfer from the cable to surrounding media is governed by conduction, while in advection-dominant, the temperature becomes stable as the heat transfer is governed by advection. In the conduction-dominant period, the slope in the plot of temperature change versus the natural logarithm of time permits to derive the thermal conductivity of the saturated porous media. We finally validated their approach in a laboratory controlled flow aquifer and found the excellent agreement between fluxes imposed and fluxes estimated from the temperature data. Being validated, the method can now be used to achieve distributed groundwater fluxes measurements in sandy aquifers.

1.3.5 Thermal tracer tomography

The most common practice for using heat in subsurface tomography involves stressing the aquifer with a heat signal (Dirac pulse signal, Step signal, etc.) by injecting heated water into the aquifer and monitoring arrival heat pulses in other locations across the aquifer. One can discern the arrival of heat to a particular location by measuring the temperature with time and establish a temperature breakthrough curve. Breakthrough curves are characterized by their shape (dictated by the heat injection signal), their breakthrough time (the time when the peak of the breakthrough curve is observed), and the attenuation due to the heat exchanged between heated water and rock's matrix (de La Bernardie et al., 2018). The transport of heat is linked to the groundwater movement through the preferential paths and the media's thermal characteristics. The temperature evolution curves obtained at different aquifer locations coupled with a mathematical model describing the conductive-advective heat transport in subsurface media undergo an inversion process to estimate the aquifer's hydraulic properties.

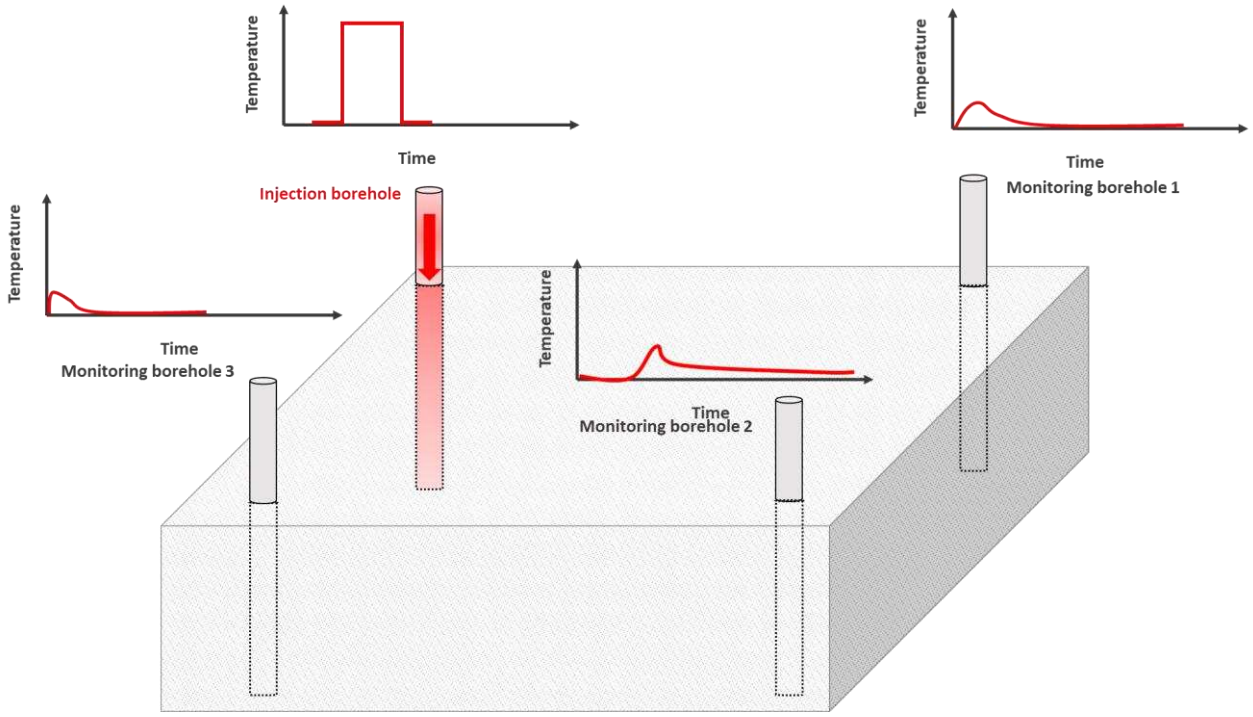

Figure 1- 9 Schematic of thermal tracer tomography

The thermal tracer tomography has been the subject of few studies both in porous and fractured media. Doro et al. (Doro et al., 2015) proposed a heat tracer experimental design and its field application to sandy gravel, the alluvial aquifer in Lauwisen Hydrogeological Research Site. They used a dipole forced gradient flow and three-level injection system to inject heated water in the middle and ambient water in the above and below sections. They claimed that their results agree well with previous works on delineating the hydraulic properties of the site. Klepikova et al. (2016) also performed a thermal tracer test tomography at an alluvial aquifer in the Hermalle-sous-Argenteau site in Belgium. They also injected a dye tracer simultaneously with heat and monitored the evolution of temperature and dye concentration in the injection well and closely spaced monitoring wells. They found out that temperature evolution curves were contrary to their expectation of a layered aquifer, explained by unequal lateral and vertical heat transport. They also observed a complex heat plume that is due to lateral and vertical heterogeneity of the aquifer. A temperature-induced

water density effect was also noted due to the high temperature of injected water. They finally performed a point-based inversion approach to find the main preferential path by using temperature breakthrough curves. They concluded that thermal heat tracer could be a promising approach for the characterization of subsurface media. In another work, Somogyvari et al. (2016) developed the travel time-based thermal tracer tomography and applied (Somogyvári and Bayer, 2017) this approach to a series of thermal tracer tests performed on a shallow alluvial sandy gravel aquifer in the Widen field site in northeast Switzer-land. They performed repeated thermal tracer tests with distributed temperature monitoring to obtain multi-source, multi-observation tomographic data. The heated water was injected through a double packer system as a forced hydraulic gradient condition was established. The obtained breakthrough curves and travel time-based tomography were used to estimate the hydraulic conductivity tomogram. They found that their results agree well with previously reconstructed aquifer hydraulic conductivity tomograms. They concluded that thermal tracer tomography would be a potential approach for resolving the structures and hydraulic conductivity field in heterogeneous aquifers sensitive to the borehole flow. A limitation was nevertheless due to the attenuation of the signal that required short distances between the injection borehole and the monitoring boreholes (Somogyvari et al. 2017).

There are not many works reported on using the thermal tracer for subsurface tomography in fractured media. Klepikova et al. (2011) presented a tomography approach based on using the fractured boreholes' passive temperature profile. They showed a close relationship between the borehole flow profile and the borehole's passive fluid temperature profile. They used a numerical model to invert the temperature profile to the flow profile. They experimentally validated the proposed approach using temperature data and flow data measured by a heat pulse flow meter. Next, they proposed a three-step inversion approach (Klepikova et al., 2014) to use temperature profiles in the fractured borehole to estimate the transmissivity and connectivity of preferential flow paths in fractured boreholes. In the first step, they determined fracture zones, and then temperature profiles are inverted to flow profiles, and finally, flow tomography is applied to the flow profile obtained in the previous step. They applied the proposed approach to field data obtained in a fractured aquifer in Ploemeur in the northwest of France. They found the calculated fractures transmissivity and their connections correspond well with previous information about the site obtained by geophysical data and other flowmeter tests.

1.4 Research motivation and thesis outlines

In the previous section, we show that active FO-DTS is a promising tool that can provide flux measurement with great spatial resolution over depth. Compared to the classical hydraulic tomography practices, which rely on a few hydraulic head measurements, A-FO DTS may provide a new interesting source of data that can be useful and sensitive to the transport processes. However, using this new source of data requires an understanding of the advantage and disadvantages compared to hydraulic head data. Chapter 2 describes the advantage of measuring and quantifying the flux data in porous media to reconstruct the aquifer's heterogeneity. We use a synthetic numerical model to show that subsurface flux data, which can be measured by active fiber-optic distributed temperature sensors, convey important information about the aquifer's heterogeneity. The numerical model is used to simulate the hydraulic tomography tests in which head data and flux data are measured in different locations. Then obtained head data and flux data undergo the inversion process, independently and jointly. The results show that flux data, whether used independently or jointly with head data, can better capture the aquifer heterogeneity than the cases that head data is solely used, especially for a very limited number of data points. As the number of measurements increases, the final inversion result would be independent of the data type.

Chapter 3 presents a real field application of the methodology developed in Chapter 2. The first objective was to test the feasibility of a field experiment designed for hydraulic tomography, including active FO-DTS for measuring fluxes. We thus describe the hydraulic tomography test performed on a shallow sandy gravel aquifer at Saint-Lambert site close to Quebec City. This sandy aquifer has been already used for hydraulic tomography experiments, and the availabilities of the direct-push methods at INRS makes possible the installation of the FO specifically designed for active DTS measurements. In this hydraulic tomography test, both head and flux data are measured and used to estimate the values and distribution of the hydraulic conductivity. Head data are recorded both in four open boreholes and two boreholes equipped by packers. Two active fiber optic cables buried in the aquifer by the direct push method measure the flux data. It is worth pointing out that to the best of our knowledge, this hydraulic tomography test is the first of its kind and has never been performed. Obtained head and flux data are used within a geostatistical inversion scheme to map the heterogeneity.

It would be interesting to apply the same approach for the fractured media. However, the application of the direct-push method to deploy the FO cable is currently limited to the shallow unconsolidated aquifer and cannot be used in crystalline rocks. In this case, the only opportunity to measure flux in the fractured media would be to access the media through the boreholes. Maldaner et al. (2019) and Munn et al. (2020) attempted to measure the groundwater flux by using A-FO DTS between the formation and liner. However, the current spatial resolution is too large, for precisely measuring the fracture flow. Furthermore, in the fractured media, the flow varies greatly, and local groundwater flux measured at the borehole scale may not be an appropriate representation of the media's flow. Thus, in order to counteract these challenges, we suggest measuring the vertical borehole flows using the passive temperature data by extending the work of Klepikova et al. (2011) and also employing the analytical solutions provided by Ramey (1962) and Hassan& Kabir (2002).

Chapter 4 describes how passive heat can allow monitoring the dynamic of subsurface flow in the fractured boreholes. The monitoring process requires real-time measurement of passive temperature data along the borehole attained by fiber-optic distributed temperature sensing. Each recorded temperature profile is converted to the flow profile along the borehole, and fracture contributions are determined. This chapter shows the added value of using temperature for real-time flow quantification in fractured boreholes, enabling us to capture the dynamic change in the aquifer's hydraulic state and fractures' contribution to the total flow.

Finally, Chapter 5 summarizes this work's key findings and contributions and presents recommendations for future researches and development. This thesis comprises five chapters, with three core chapters (Chapters 2, 3, and 4) written as stand-alone manuscripts submitted or in preparation for possible publications in peer-reviewed journals.

Chapter 2 Individual and joint inversion of head and flux data by geostatistical hydraulic tomography

This chapter is in preparation for a possible publication in Advances in Water Resource

This paper has been prepared in collaboration with Dr. Niklas Linde from the University of Lausanne. The paper investigates the relative merit of groundwater flux data in comparison to typical head data used within geostatistical hydraulic tomography.

Behzad Pouladi [1*], Niklas Linde[2], Laurent Longuevergne[1], Olivier Bour[1]

1 Univ Rennes, CNRS, Géosciences Rennes, UMR 6118, 35000 Rennes, France.
2 University of Lausanne, Institute of Earth Sciences, Lausanne, Switzerland

2.1 Abstract

The hydraulic conductivity distribution is a key control on groundwater flows in aquifers. Hydraulic tomography is a state of the art method for inferring hydraulic conductivity fields using head data. Here, a numerical model is used to simulate a steady-state hydraulic tomography experiment by assuming a Gaussian hydraulic conductivity field (also constant storativity) and generating the head and flux data in different observation points. We employed geostatistical inversion using head and flux data individually and jointly to better understand the relative merits of each data type. For the typical case of a small number of observation points, we find that flux data provide a better resolved hydraulic conductivity field compared to head data when considering data with similar signal-to-noise ratios. In the case of a high number of observation points, we find the estimated fields to be of similar quality regardless of the data type. A resolution analysis for a small number of observations reveals that head data averages over a broader region than flux data and flux data can better resolve the hydraulic conductivity field than head data. The inversions' performance depends on borehole boundary conditions, with the best performing setting for flux data and head data are constant head and constant rate, respectively. However, the joint inversion results of both data types are insensitive to the borehole boundary type. Considering the same number of observations, the joint inversion of head and flux data does not offer advantages over individual inversions. By increasing the hydraulic conductivity field variance, we find that the resulting increased non-linearity makes it more challenging to recover high-quality estimates of the reference hydraulic conductivity field. This paper's finding would be useful for future planning and design of hydraulic tomography tests comprising the flux and head data.

KEYWORDS: hydraulic tomography, groundwater flux, geostatistical inversion, principal component geostatistical analysis (PCGA), resolution analysis

2.2 Introduction

Knowledge of hydraulic conductivity distributions is of great importance for the management of water resources (Liu et al., 2020), solute transport prediction (Yeh, 1992; Jiménez, 2015) and designing remediation of contaminated sites (Fakhreddine et al., 2016). A variety of geophysical (Kowalsky et al., 2004; Revil et al., 2012; Slater, 2007) and hydraulic methods (Brauchler et al., 2003; Yeh and Liu, 2000; Zhu and Yeh, 2005), including tracer-based measurements (Doro et al., 2015; Jiménez et al., 2016; Somogyvári and Bayer, 2017), have been developed and employed for characterizing hydraulic properties (Lochbühler et al., 2013). In hydraulic flow methods, head data responses to hydraulic perturbations (pumping, tidal fluctuation, etc.) are measured at different locations across the aquifer. The recorded head data are then used to estimate the spatial distribution of hydraulic conductivity (K) and storativity. A distinct advantage of hydraulic methods for imaging purposes is that the hydraulic response of an aquifer is directly related to its hydraulic parameters described by flow equations (Fakhreddine et al., 2016), while in most geophysical methods, the hydraulic properties are inferred from other estimated physical properties, thereby, requiring petro-physical relationships. For convenience, we define $Y=\log(K)$ and use it afterward.

Hydraulic tomography has received considerable attention and has been the subject of many theoretical and numerical (Fienen et al., 2008; Luo et al., 2020; Yeh and Liu, 2000; Zha et al., 2018; Zhu and Yeh, 2005), laboratory (Illman et al., 2008, 2010; Liu et al., 2002, 2007; Yin and Illman, 2009; Zhao et al., 2016), and field studies (Berg and Illman, 2015, 2013, 2011; Bohling et al., 2007; Brauchler et al., 2013, 2011, 2010, 2003; Cardiff et al., 2009, 2013; Cardiff and Barrash, 2011; Fischer et al., 2017; Gottlieb and Dietrich, 1995; Huang et al., 2011; Klepikova et al., 2013; Kuhlman et al., 2008; Paradis et al., 2016, 2015; Sun et al., 2013;

Tosaka et al., 1993). However, hydraulic tomography based on pressure data has limitations. One is inherent to the underlying potential field physics as measured head data are spatially averaged due to the diffusive nature of pressure disturbances created during the test (Bohling and Butler Jr, 2010). This averaging results in tomographic estimates displaying a high degree of smoothing compared to the actual underlying aquifer properties. This smearing of the reconstructed hydraulic conductivity field may lead to degraded predictions for transport problems. Another limitation appears in applying hydraulic tomography in high conductivity aquifers as hydraulic tests lead to small drawdown values, implying high relative uncertainty of the measured head perturbations and correspondingly low signal-to-noise ratio data. Adding other types of non-redundant data in hydraulic tomography can help to better image the subsurface (Mao et al., 2013; Yeh et al., 2015). In this regard, Zha et al. (2014) demonstrated the usefulness of flux data (specific discharge) for hydraulic tomography in a 2D synthetic fractured media mimicking a field site in Mizunami, Japan. In their model, fracture elements (assumed as linear features) were given a *Y*-value of 1, while a value of -1 and -2 was assigned to elements representing the rock matrix and low permeable fault zones, respectively. Then seven steady-state pumping tests were simulated, and obtained head and flux data were used to estimate the *Y*-field. Estimated mean, variance, and correlation length of the *Y*-field were applied as prior information to the inversion model. Using the cross-correlation approach, they showed that even if the head and flux would be measured at the same location, they contribute differently to the *Y*-field's construction. Their synthetic work showed that using flux data with head data improves the estimation of *Y*-field values and the fracture distribution. In another study, Tso et al. (2016) performed numerical test studies on a 3D model identical to the one at the North Campus Research site in Waterloo, Canada. They simulated pumping in this porous aquifer, obtaining head data and flux data in different locations. Then, head and flux data were subjected to inversion, considering different prior information. They showed that using flux data jointly with head data in hydraulic tomography can enhance hydraulic conductivity estimates. Furthermore, they found out that the estimated hydraulic conductivity field is less affected by an inadequate prior model when non-redundant data such as flux are used.

Up to some recent developments, measuring groundwater fluxes in the field was limited to local and tedious measurements. The most popular technique for quantifying groundwater flux in the field was based on dilution tests (Drost et al., 1968; Jamin et al., 2015; Schneider et al., 2019), where the dilution of an injected tracer inside a screened borehole or within packers permits to measure the horizontal groundwater flux. Nevertheless, boreholes disturb the flow field and affect the measurements; hence, the measured values may not represent the real flux values. Recently, the advent of Fiber Optic Distributed Temperature Sensors (FO-DTS) lead to new possibilities for measuring groundwater discharge with unprecedented spatial and temporal resolutions (des Tombe et al., 2019; Simon et al., 2021)

FO-DTS is a distributed sensor family member that allows measurement of temperature all along the fiber optic cable. FO-DTS can be employed in both passive and active modes. In passive mode, only the fiber optic cable's temperature is measured, while in active mode, a heat source is added to the fiber optic cable by using a heating element located very close to the FO cable or by using a heating fiber optic cable. Active-DTS have been developed for instance, for measuring borehole flows (Read et al., 2014), wind speed (Sayde et al., 2015), or for characterizing groundwater fluxes in fractured media (Maldaner et al., 2019). It has recently also been used for measuring groundwater discharge in sedimentary aquifers; the FO cable being deployed successfully by the direct-push method (Bakker et al., 2015; des Tombe et al., 2019). In this case, the buried cable is in direct contact with the ground with the minimum subsurface perturbation compared to natural conditions. Simon et al. (2021) showed that active-DTS might be used for measuring both thermal conductivities and groundwater fluxes on a large range of values with excellent accuracy. The experiment's

principle, which is described in figure 2-1, consists of monitoring the temperature evolution with time, which is a function of the surrounding area's thermal properties (porous medium) and groundwater fluxes that limit the temperature rise. Typically, the slope of the temperature rise in the conduction regime is inversely proportional to thermal conductivity, while the greater the groundwater fluxes, the lower the temperature at stabilization (figure 2-1). The temperature evolution with time may be easily interpreted to estimate groundwater fluxes through an analytical solution or by using a graphical analysis (Simon et al., 2021). It is worth noting that the application of A-FO DTS for flux measurements is currently limited to shallow and unconsolidated aquifers due to limitations in deployment by the direct push method.

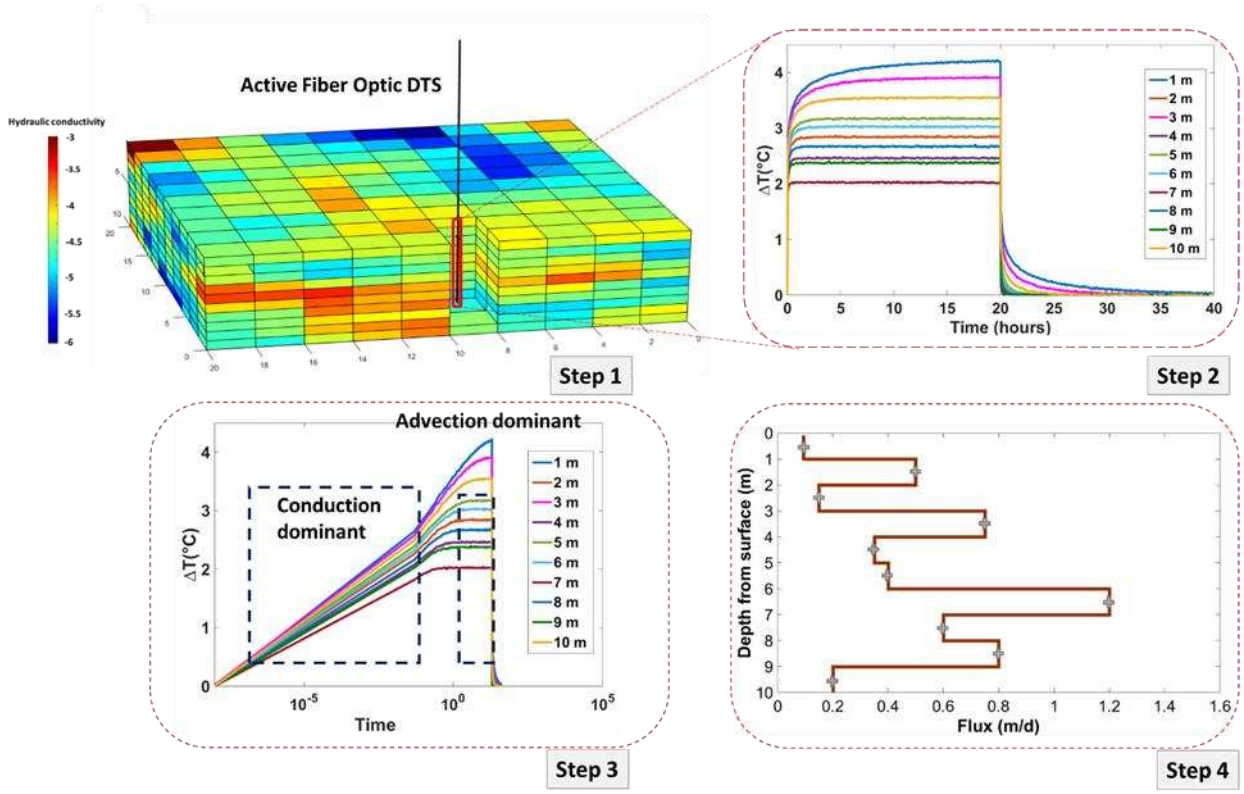

Figure 2-1: Schematic of the steps of using Active FO-DTS to infer a groundwater flux profile with depth. (Step 1) An Active fiber Optic Cable is deployed vertically into the ground in close contact with the formation. (Step 2) The cable is heated (active mode), and the cable temperature during the heating (first 20 hours) and cooling periods (from 20 to 40 hours) is measured. Each curve corresponds to one-point measurement along the FO-cable. (Step 3) In semi-logarithmic plot, the slope of the temperature profile is used to estimate the thermal conductivity while the temperature at stabilization is dependent on groundwater fluxes (Simon et al., 2021). (Step 4) Measured temperature data along the fiber optic cable are converted to a flux profile with depth, with each "+" sign indicate one datum.

New advances in distributed sensing of groundwater flux make it an appealing data source for independent inversion or joint inversion with hydraulic head. This work assumes that groundwater fluxes can be inferred from the above-mentioned techniques at a given spatial resolution and accuracy. Using a geostatistical hydraulic tomography approach, we then address the benefits and drawbacks of using either head or flux data individually or jointly. More specifically, we address the following questions.

(1) Considering equal numbers and distributions of flux and head data, which data type leads to the best reconstruction of hydraulic conductivity?

(2) How does the number of observations affect the inversion results?

(3) How does inversion performance for the different data types vary with the hydraulic conductivity field variance?

The paper is structured into six sections. Section 2 presents the geostatistical inversion method and the forward model employed. In section 3, we describe the hydraulic conductivity test model used for our analysis. In sections 4 and 5, we present and discuss the main results, respectively, and section 6 concludes the paper

2.3 Methods

The Principal Component Geostatistical Approach (PCGA) is a computationally-efficient geostatistical inversion method. PCGA uses the main principal components of the prior model covariance matrix for model parameterization and corresponding estimates of the Jacobian (sensitivity matrix). The resulting model reduction from a model of many gridded elements to the number of retained principal components leads to smaller matrices to invert and fewer sensitivities to estimate, implying less computational costs than full inversions. This method has been employed extensively in recent years (Fakhreddine et al., 2016; Fischer et al., 2017; Kang et al., 2017; Lee et al., 2018; Soueid Ahmed et al., 2016). In this study, we use PCGA combined with the Matlab Reservoir Simulation Toolbox (MRST) that simulates fluid flow in porous media (forward model) to perform inversion of head and flux data.

2.3.1 Inverse model

Inferring properties of subsurface media (storage, hydraulic conductivity) from error-contaminated and sparse observed data (head data, flux data, etc.) is an inverse problem and can be formulated as follow:

$$\mathbf{d} = f(\mathbf{m}) + \eta,$$

Equation 2:1 – Formulation of the inverse problem

where **d**, f (-), **m,** and **η** refer to measured data, forward model, model parameters and errors, respectively. The forward model refers to a non-linear operator solving a set of differential equations numerically or analytically to describe the relationship between model parameters and data. From a mathematical point of view, the inverse problem is ill-posed and the solution is non-unique, implying that additional information (e.g., a prior model) is required to obtain unique and physically-meaningful results. Here, the subsurface is described as a multi-Gaussian stationary field with known statistical properties and a superimposed deterministic trend. In the presence of a multivariate Gaussian prior model and error distribution, it is common to formulate the inverse problem in terms of an exploration of the maximum a posteriori (MAP) estimate and its variance. In such a setting, the solution of the inverse problem is obtained by maximizing a posterior probability density function (maximizing the term in bracket) expressed by using Bayes's theorem as follow:

$$\pi_{\text{post}}(\mathbf{m}|\mathbf{d}) \sim \exp[\frac{-1}{2}(f(\mathbf{m}) - \mathbf{d})\mathbf{C}_{\text{d}}^{-1}(f(\mathbf{m}) - \mathbf{d}) + \frac{-1}{2}(\mathbf{m} - \mathbf{m}_{\text{prior}})\mathbf{C}_{\text{m}}^{-1}(\mathbf{m} - \mathbf{m}_{\text{prior}})]$$

Equation 2:2 – Posterior probability density function expressed by Bayes theorem

where $\mathbf{C_m}$ and $\mathbf{C_d}$ are the a priori model covariance and data covariance matrix, respectively.

Geostatistical methods have been widely used and proven to be efficient for hydraulic tomography purposes (Illman et al., 2015). The iterative optimization process obtains the model parameters. The solution at $(i+1)^{th}$ iteration is calculated as:

$$\mathbf{m}_{i+1} = \mathbf{X}\boldsymbol{\beta}_i + \mathbf{C}_{\mathrm{m}}\mathbf{J}_i{}^T\boldsymbol{\varepsilon}_i\,,$$

Equation 2:3 – model parameter at each iteration

where **X** is a known matrix, and **β** is an unknown vector used to determine linear trends that is inferred along with **ε** by solving the system of equations below. Here **J** represents the Jacobian matrix that is the sensitivity of the forward model output (at observation points) with respect to the unknown model parameters.

$$\begin{bmatrix} \mathbf{J}_i\mathbf{C}_{\mathrm{m}}\mathbf{J}_i{}^T + \mathbf{C}_{\mathrm{d}} & \mathbf{J}_i\mathbf{X} \\ (\mathbf{J}_i\mathbf{X})^T & 0 \end{bmatrix} \begin{bmatrix} \boldsymbol{\varepsilon}_i \\ \boldsymbol{\beta}_i \end{bmatrix} = \begin{bmatrix} \mathbf{d} - f(\mathbf{m}_i) + \mathbf{J}_i\mathbf{m}_i \\ 0 \end{bmatrix}$$

Equation 2:4 – model parameter at each iteration

2.3.2 Principal Component Geostatistical Approach

Calculating the Jacobian matrix (**J**) used in equations 2:3 and 2:4 for high-dimensional problems often requires a very high computational effort. Lee and Kitandis (2014) proposed the Principal Component Geostatistical Approach (PCGA), which uses a low-rank approximation of the prior covariance via principal component analysis and avoids forming the Jacobian explicitly by using a finite difference approximation (equation 2:5 (d)) for products of the Jacobian matrix and eigenvalues (equations 2:5 (b) and (c)). This results in a faster inversion process of high accuracy, provided that a sufficient number of principal components are retained. The terms that are used for geostatistical inversion in equation 2:4 are approximated through the *P* largest principal components as follow:

$$\mathbf{C}_{\mathrm{m}} \approx \mathbf{C}_{\mathrm{m}P} = \sum_{\mathrm{ii}=1}^{P} (\boldsymbol{\varsigma}_{\mathrm{ii}})(\boldsymbol{\varsigma}_{\mathrm{ii}})^T, \qquad \text{(a)}$$

$$\mathbf{J}_{\mathrm{i}}\mathbf{C}_{\mathrm{m}} \approx \mathbf{J}_{\mathrm{i}}\mathbf{C}_{\mathrm{mP}} = \mathbf{J}_{\mathrm{i}} \sum_{\mathrm{ii}=1}^{P} (\boldsymbol{\varsigma}_{\mathrm{ii}})(\boldsymbol{\varsigma}_{\mathrm{ii}})^T = \sum_{\mathrm{ii}=1}^{P} (\mathbf{J}_{\mathrm{i}}\boldsymbol{\varsigma}_{\mathrm{ii}})(\boldsymbol{\varsigma}_{\mathrm{ii}})^T, \qquad \text{(b)}$$

$$\mathbf{J}_{\mathrm{i}}\mathbf{C}_{\mathrm{m}}\mathbf{J}_{\mathrm{i}}{}^T \approx \mathbf{J}_{\mathrm{i}}\mathbf{C}_{\mathrm{mP}}\mathbf{J}_{\mathrm{i}}{}^T = \sum_{\mathrm{ii}=1}^{P} (\mathbf{J}_{\mathrm{i}}\boldsymbol{\varsigma}_{\mathrm{ii}})(\mathbf{J}_{\mathrm{i}}\boldsymbol{\varsigma}_{\mathrm{ii}})^T, \qquad \text{(c)}$$

$$\mathbf{J}_{\mathrm{i}}\boldsymbol{\varsigma}_{\mathrm{ii}} \approx \frac{1}{\delta}[f(\mathbf{m}_{\mathrm{i}} + \delta\boldsymbol{\varsigma}_{\mathrm{ii}}) - f(\mathbf{m}_{\mathrm{i}})]\,. \qquad \text{(d)}$$

Equation 2:5 – Approximation of the terms used in geostatistical inversion by *P* number of principal components by PCGA

Here, $\mathbf{C}_{\mathrm{m}P}$ is a rank-*P* approximation of the model parameter covariance matrix. The $\mathbf{C}_{mP}$ and Jacobian matrix products required for the inversion (equation 2:4) are given by equations 2:5 (b) and (c). The choice of the finite difference interval δ is addressed by Lee and Kitandis (2014).

The diagonal entries of the posterior covariance matrix ($\mathbf{v}_{jj}$) are often presented as the estimation of the variance and can be calculated without explicit construction of **v** (Lee and Kitanidis, 2014)

$$\mathbf{v}_{jj} = \mathbf{C}_{\mathrm{m}\,jj} - \begin{bmatrix} (\mathbf{JX})_j \\ \mathbf{X}^T \end{bmatrix}^T \begin{bmatrix} \mathbf{J}\mathbf{C}_{\mathrm{m}}\mathbf{J}^T + \mathbf{C}_{\mathrm{d}} & \mathbf{JX} \\ (\mathbf{JX})^T & 0 \end{bmatrix}^{-1} \begin{bmatrix} (\mathbf{JX})_{\mathrm{j}} \\ \mathbf{X}_{\mathrm{j}}{}^T \end{bmatrix},$$

Equation 2:6 – posterior covariance matrix

where $\mathbf{C}_{mjj}$ represents the j^{th} diagonal entry of the model covariance matrix and $(\mathbf{JX})_j$ is the j^{th} column of the product **JX**.

Once the model parameters are determined, it is desirable to perform a resolution analysis by obtaining the resolution matrix (**R**), which can be seen as a low pass filter that maps the true model parameters to the estimated model parameters (e.g., Alumbaugh and Newman, 2000). Each model parameter during the inversion is estimated from the averaging of other model parameters adjacent to the one of interest. The components of **R** can be interpreted as weights (each row in the resolution matrix) of the average of true model parameters for estimating each model parameter (Day-Lewis et al., 2005). The ideal resolution matrix would be an identity matrix that would imply that all model parameters are resolved perfectly. The deviation of the diagonal element from the identity matrix reveals the degree of averaging and smoothness. Thus, plotting diagonal elements of the resolution matrix in their corresponding blocks is indicative of the degree of smoothness. The diagonal elements of the resolution matrix (equation 11) inform the extent to which each estimated parameter is resolved independently.

The resolution matrix (**R**) is obtained by equation 2:7(b), which requires recovering the Jacobian matrix (**J**) from the previously calculated product (equation 6) and low rank-approximation of the covariance matrix ($\mathbf{C}_{mP}$);

$$\mathbf{m}^{\text{estimate}} = \mathbf{R}\mathbf{m}^{\text{true}} \ , \qquad \text{(a)}$$

$$\mathbf{R} = (\mathbf{J}^{\mathrm{T}}(\mathbf{C}_{\mathrm{d}})^{-1}\mathbf{J})^{-1}(\mathbf{J}^{\mathrm{T}}(\mathbf{C}_{\mathrm{d}})^{-1}\mathbf{J}). \qquad \text{(b)}$$

Equation 2:7 – Resolution matrix

2.3.3 Forward model

The incompressible fluid flow module of MRST (Lie, 2019) was used to simulate steady-state groundwater flow. It is used to calculate head and flux values at different points across a confined aquifer. Starting from the mass conservation law on a control volume, introducing the Darcy law, assuming incompressible fluid flow and steady-state condition, the final form of the equation reads:

$$-\nabla.[\boldsymbol{K}(\mathbf{w}).\nabla h(\mathbf{w})] = \mathbf{q}(\mathbf{w}) \, ,$$

Equation 2:8 – groundwater flow equation

subjected to the following constant head boundary conditions across external boundaries:

$$h{=}h_{\mathrm{D}} \quad \text{for} \quad \vec{\mathbf{w}} \in \Gamma_{\mathrm{a}}$$

Here, **w**= (*x, y, z*), *K* (L/T), *h* (L), and **q** [L/T] represent the hydraulic conductivity, head and fluid source or sink (inflow or outflow of fluid per volume at certain locations), respectively. Γ_a represents Dirichlet boundaries. The above equations are solved numerically to calculate the head values at grid points across the aquifer. The MRST uses the two-point flux approximation scheme (Lie, 2019) to calculate the Darcy flux in each grid.

2.4 Numerical experiments

2.4.1 Setup of the synthetic test case

To assess the information content of hydraulic head and groundwater flux data for the reconstruction of heterogeneous aquifers, a stationary multi-Gaussian log-hydraulic conductivity field is generated, resulting in the field, shown in figure 2-2. The generated aquifer is 550 m in length, 550 m in width and 5 m in depth. The aquifer is discretized into 110 × 110 × 1 in x-, y-, z- directions and corresponding block sizes are 5 m × 5 m × 5 m, respectively. The aquifer is assumed to have one layer (in order to reduce the complexity of analysis of the results and fairly compare the advantages and drawbacks value of each type of data), and the log-hydraulic conductivity field has a multi-Gaussian distribution. The area of interest is chosen in the middle of the aquifer, away from the boundaries, to reduce the boundaries' effect on the inversion. All boundaries are set to a constant head equal to 350 m.

The correlation length used for generating the *Y*-field is 75 m and 45 m for *x*- and *y*-directions, respectively. The same field (same heterogeneity structure) with different variances of 0.5, 1, 2, and 4 are generated to assess the effect of variance and number of observations on the inversion results. The mean Y_{mean} is -3.57 for all cases, but the *Y*-fields variance and ranges are different for different experiments.

We use a five-spot setup with a central borehole (P1) and four boreholes (P2, P3, P4 and P5) on the corners of the area of interest (bounded by white dashed lines in figure 2-2). Other monitoring points are also considered between the boreholes, as shown by asterisk symbols. The aquifer is subjected to a series of pumping experiments in each borehole. Two different boundary conditions in the borehole, namely, constant rate and constant head, are considered. When simulating pumping in one borehole, the head and flux values are recorded in other boreholes and monitoring points. The acquired flux and head data are noise-contaminated before being used to estimate the *Y*-field.

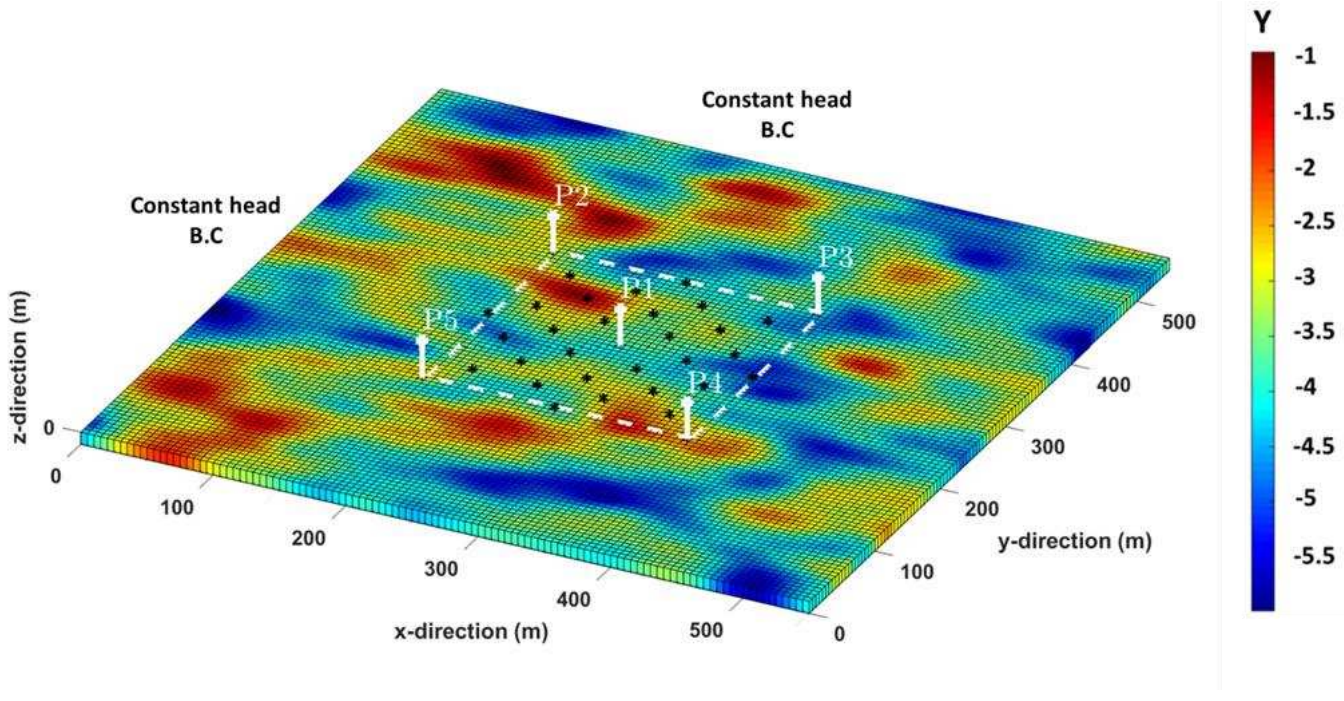

Figure 2-2: Reference *Y*-field (variance 4), borehole (P1 to P5), and monitoring locations (asterisks). All boundaries are set to the constant head. The white dash-lines crossing the side boreholes define the area of interest.

2.4.2 Hydraulic tomography using head and flux data

Our numerical inversion experiments aim to compare the relative merits of each data type and analyze how borehole boundary conditions (constant head or constant rate), the variance of the Y-field, and the number of observations affect the inversion results. The observational data are generated using the reference hydraulic conductivity field, and a normally distributed error is added to the observations. The standard deviations of these errors are different in all cases. The errors' standard deviations were chosen to be in a realistic range while ensuring the same initial signal-to-noise ratio of 38 for all cases defined by running the code using Y_{mean}. The resulting measurement errors range from 0.05 to 0.013 (m) for the head and 0.055 to 0.01 (m/day) for the flux.

PCGA with previously mentioned geostatistical parameters are used for the inversion. The truncation order (p-rank) of the prior covariance matrix is chosen as 400 out of 12100. Based on the recommendation by Lee et al. (2016), the truncation order (P), which results in the relative Eigenvalue error below 0.01 would be sufficient to capture most of the covariance matrix structure. The relative Eigenvalue error is defined as the ratio of first to $(P+1)^{th}$ Eigenvalue. We have chosen P to be more conservative than having a ratio of 0.01. For *Y*-field with variance 4, the first Eigenvalue is 1411.47, while the 401st Eigenvalue is 0.047 giving the ratio of 3.25×10^{-5}.

The inversion starts with a constant value of Y_{mean} and continues until the root mean square error between observed and simulated measurement, normalized with the error standard deviation (weighted root mean square error), defined in equation 2:9 reaches a value close to one or after ten iterations.

$$\mathrm{WRMSE}=\sqrt{\frac{\frac{1}{N}\sum_{1}^{N}(\mathbf{d}\text{-}f(\mathbf{m}^{\mathrm{estimate}}))^2}{\sigma^2}}\ ,$$

Equation 2:9 – Weighted root mean square error

here *N* is the number of observations and σ is the absolute value of the error's standard deviation.

2.4.2.1 Boundary condition at the pumping borehole

Hydraulic tomography is simulated considering two different borehole boundary conditions, constant rate (the borehole is being pumped with constant flow rate) and constant head (the head in the borehole is kept constant). Note that the external boundary conditions do not change and are kept fixed. The pumping rates used in the model are 2400, 4000, 1750, 5000, and 3800 (m3/day) for P1, P2, P3, P4, and P5, respectively. The equivalent constant head borehole boundary conditions are 324, 340, 300, 329, and 336 (m) for P1, P2, P3, P4, and P5, respectively

2.4.2.2 Variance of *Y*-field and number of observation points

The effect of the *Y*-field variance is also investigated by considering four different variances (0.5, 1, 2, and 4). Furthermore, a different number of observation points are used to assess their impact on the final inversion results. The observation points are distributed symmetrically in the aquifer. The minimum number of observation points considered is the boreholes (4 observation points) and the maximum are boreholes plus points in the middle shown by asterisk symbols (32 observation points).

2.4.2.3 Performance Metrics

To evaluate each data type's performance in estimating ***Y***, we use the Frobenius norm and scatter plots of estimated versus reference ***Y*** for each case. The Frobenius norm for the vector of difference between the reference ***Y*** and estimated ***Y*** is:

$$\mathrm{Norm}^{\mathrm{Fr}}=\sqrt{\sum_{1}^{N}\left|\mathbf{Y}_{\mathrm{reference}}-\mathbf{Y}_{\mathrm{estimated}}\right|^{2}}$$

Equation 2:10 - Frobenius norm calculated for ***Y*** estimates

Furthermore, the correlation coefficient between reference ***Y*** and estimated ***Y*** values and their corresponding slope lines are calculated.

2.5 Results

2.5.1 Inversion of head data

First, the head data is individually inverted to obtain the Y-field. Here, the results are presented once 4 observation points (only the observations in the boreholes), 8, 16 and 32 observation points are used. For each case, two different borehole boundary conditions are considered, constant rate and constant head. Figure 2-3 shows the estimated Y-field with a variance of 4, and Table 2-1 represents the performance metrics.

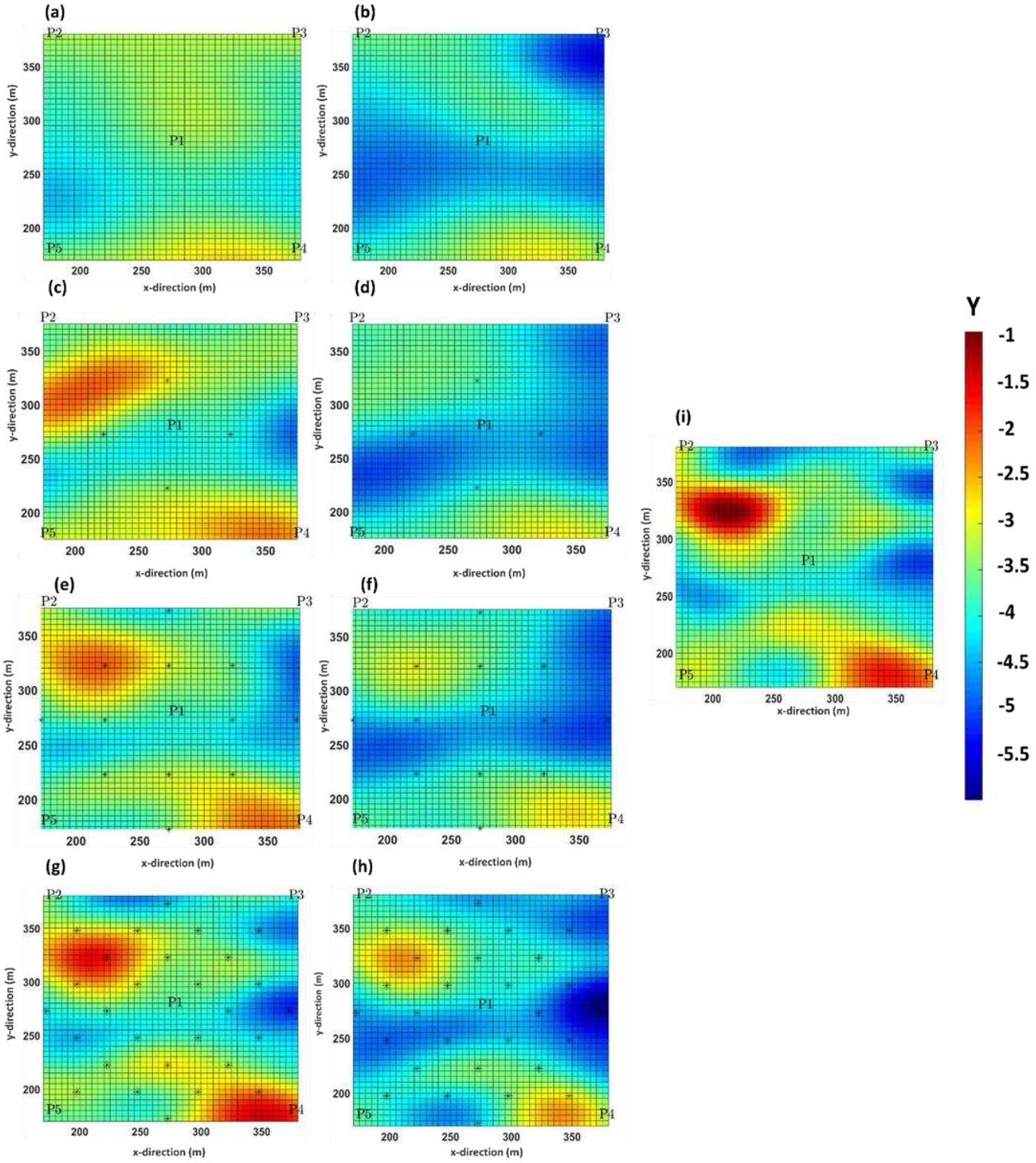

Figure 2- 3: Hydraulic conductivity field (variance 4) estimates for hydraulic head data: **(a)** inversion result for 4 observations point and constant rate B.C., **(b)** inversion result for 4 observations point and constant head B.C., **(c)** inversion result for 8 observations point and constant rate B.C., **(d)** inversion result for 8 observations point and constant head B.C., **(e)** inversion result for 16 observations point and constant rate B.C., **(f)** inversion result for 16 observations point and constant head B.C., **(g)** inversion result for 32 observation points and constant rate B.C., **(h)** inversion result for 32 observation points and constant head B.C. **(i)** reference Y-field

Table 2-1: Summary of the performance metrics for inversion of head data in the area of interest

Variance	Boundary Condition	Number of observations	Frobenius norm	Correlation coefficient	Slope	Final WRMSE
4	Constant Rate	4	68.4	0.27	0.13	1.19
		8	48.27	0.75	0.62	1.05
		16	30.4	0.9	0.76	0.97
		32	23.47	0.94	0.95	1.1
	Constant Head	4	85.5	0.49	0.32	1.00
		8	75.15	0.68	0.48	0.96
		16	61.9	0.82	0.67	1.26
		32	54.90	0.9	0.93	1.23

For all cases considered, we find that changing borehole boundary condition from constant rate to constant head deteriorates the Y-field estimation as the Frobenius norm listed in Table 2-1 increases from 68.4 to 85.5, 48.27 to 75.15, 30.4 to 61.9 and 23.47 to 54.90 for 4, 8, 16 and 32 observation points, respectively. Comparing figures 2-3(a) to 3-3(h) with the reference *Y*-field (figure 2-3 (i)) also show that cases with constant rate boundary conditions resemble more reference *Y*-field. The use of constant head borehole boundary condition results in an underestimation of *Y*-field values and the mean value of *Y*-field. For instance, in the case of 4 observation points, the mean value of the estimated *Y*-field is around -4 for constant head boundary condition while it is -3.45 for constant rate boundary condition. The mean value for reference *Y*-field is -3.57.

Adding more observations leads to better results. This is reflected in the improvement of the correlation coefficient from 0.27 to 0.94 for constant rate borehole boundary condition and from 0.49 to 0.93 for constant head boundary condition. The increase of slope from 0.13 to 0.95 and from 0.32 to 0.93 for constant rate and constant head boundary conditions further certifies the previous statement.

2.5.2 Inversion of flux data

This subsection presents the results of individual inversion of flux data. Figure 2-4(a) to (i) show the Y-field estimates for 4, 8, 16 and 32 observation points subjected to constant rate and constant head borehole boundary conditions. Table2-2 summarizes.

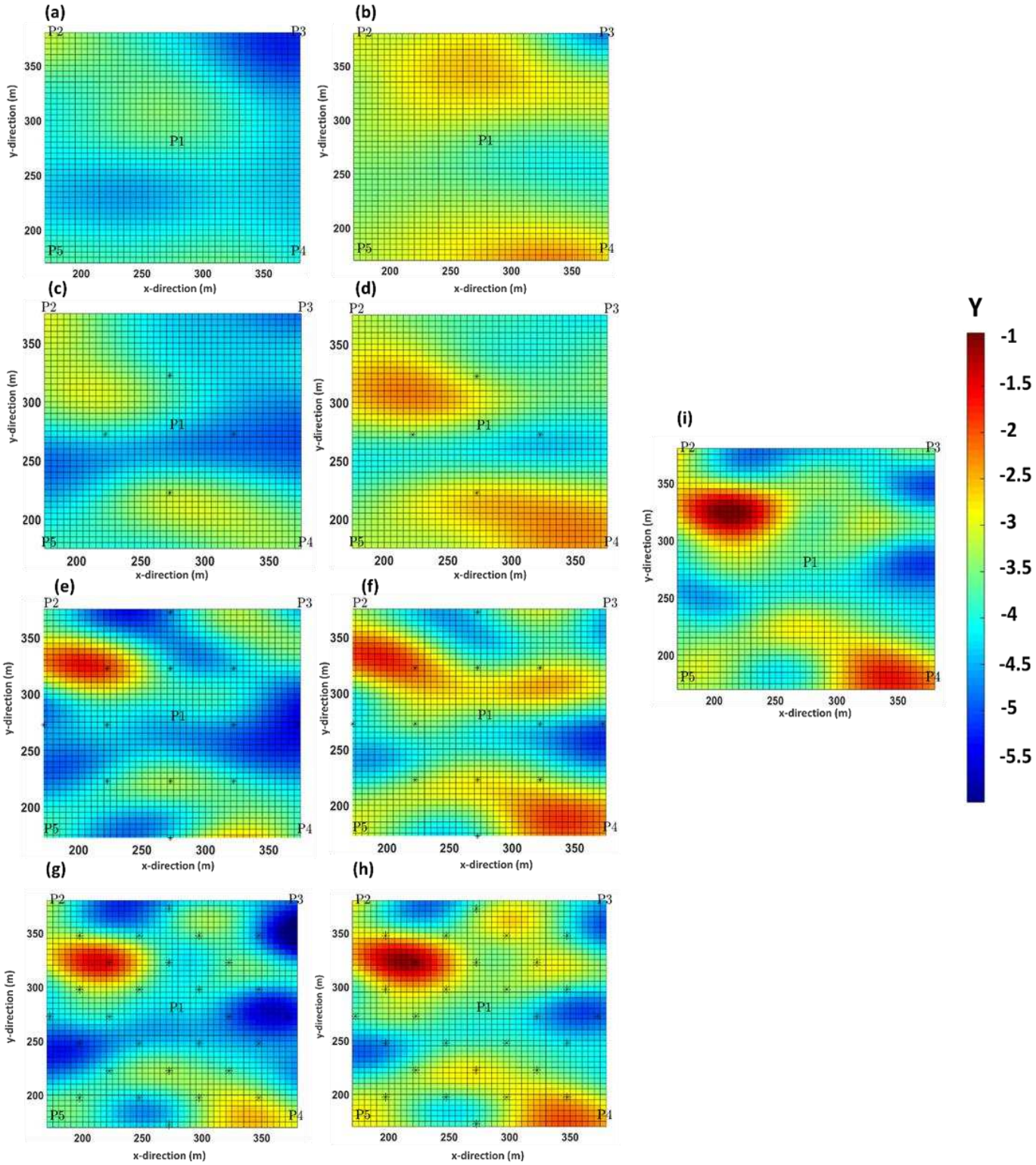

Figure 2-4: Hydraulic conductivity field (variance 4) estimates for flux data: (a) inversion result for 4 observations point and constant rate B.C., (b) inversion result for 4 observations point and constant head B.C., (c) inversion result for 8 observations point and constant rate B.C., (d) inversion result for 8 observations point and constant head B.C., (e) inversion result for 16 observations point and constant rate B.C., (f) inversion result for 16 observations point and constant head B.C., (g) inversion result for 32 observation points and constant rate B.C., (h) inversion result for 32 observation points and constant head B.C., (i) reference Y-field

Table 2-2: Summary of the performance metrics for inversion of flux data in the area of interest

Variance	Boundary Condition	Number of observations	Frobenius norm	Correlation coefficient	Slope	Final WRMSE
4	Constant Rate	4	81.2	0.45	0.22	1.31
		8	65.61	0.76	0.56	1.19
		16	62.2	0.79	0.77	1.34
		32	53.6	0.9	0.90	2.12
	Constant Head	4	64.53	0.53	0.29	1
		8	47.7	0.77	0.61	1
		16	44.72	0.8	0.81	0.95
		32	32.03	0.92	0.91	1.45

Contrary to head data, we find that constant head boundary conditions provide a better *Y*-field estimate when considering flux data. The better performance of the constant head (with respect to constant rate) boundary condition is seen, for instance, by comparing the values of the Frobenius norm given in Table 2-2. For the case of 4, 8, 16, and 32 observation points, the Frobenius norm decreases from 81.2 to 64.53, 65.61 to 47.7, 62.2 to 44.7, and from 50.51 to 32.03, respectively. Using constant rate boundary condition for the flux data results in an underestimation of the *Y*-field mean. Considering the case with 4 observation points, the estimated *Y*-field's mean value with the constant rate boundary condition is around -4 while it is around -3.4 for the constant head boundary condition.

Comparing the values of Frobenius norm for the head and flux data given in Table 2-1 and Table 2-2 reveals that for a small number of observations (4 observation points), using flux data with constant head boundary condition gives a better *Y*-field estimate compared to head data with constant rate boundary condition as the Frobenius norm decreases from 68.4 to 64.53. This improvement is further supported by an increase in the correlation coefficient from 0.2744 to 0.446 and slope as it increases from 0.127 to 0.22. Note however that for a larger number of observations, no improvements are observed.

2.5.3 Joint inversion of flux and head data

The results obtained by joint inversion of flux and head data are provided in Figure 2-5 (a) to (e) that show the *Y*-field estimate for 8, 16, 32, and 64 observations subjected to the constant head and constant rate borehole boundary conditions. The inversion metrics are outlined in Table 2-3. It should be noted that we have two measurements (head and flux) for each point shown leading to 64 observations for 32 observation points for instance.

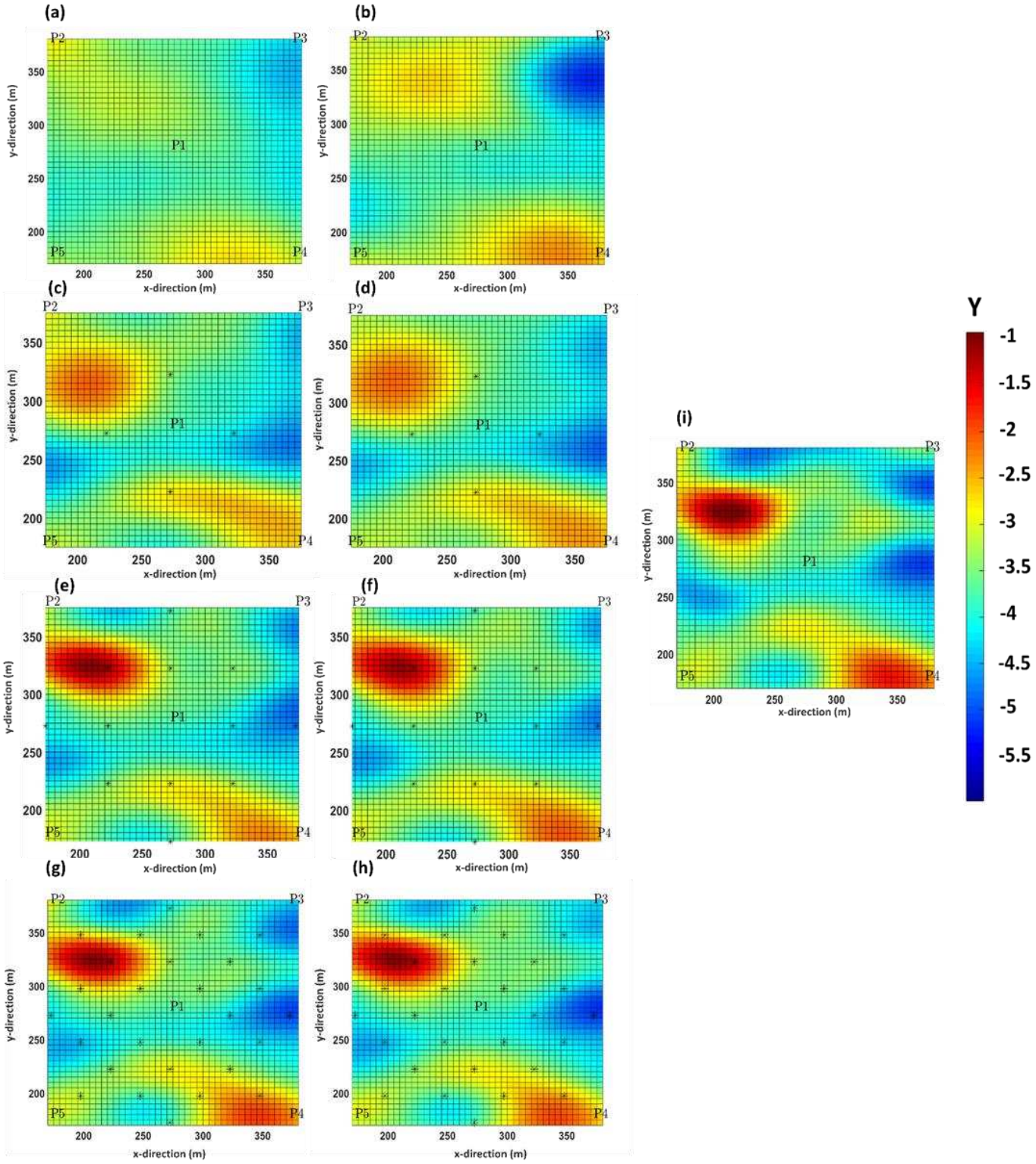

Figure 2-5: Hydraulic conductivity field (variance 4) estimates from joint inversion: **(a)** inversion result for 8 observations point and constant rate B.C., **(b)** inversion result for 8 observations point and constant head B.C., **(c)** inversion result for 16 observations point and constant rate B.C., **(d)** inversion result for 16 observations point and constant head B.C., **(e)** inversion result for 32 observations point and constant rate B.C., **(f)** inversion result for 32 observations point and constant head B.C. **(g)** inversion result for 64 observation points and constant rate B.C., **(h)** inversion result for 64 observation points and constant head B.C., **(i)** reference Y-field

Table 2-3: Summary of the performance metrics for joint inversion of head and flux data in the area of interest

Variance	Boundary Condition	Number of observations	Frobenius norm	Correlation coefficient	Slope	Final WRMSE
4	Constant Rate	8	51.8	0.7	0.34	0.8
		16	39.7	0.82	0.68	1.24
		32	24.44	0.94	0.92	2.25
		64	22	0.96	0.98	1.13
	Constant Head	8	53.97	0.64	0.51	1.1
		16	38.34	0.84	0.74	1.13
		32	27.38	0.93	0.92	1.5
		64	21.71	0.95	0.97	1.65

Considering constant head boundary condition, the Frobenius norm for the 8, 16, 32 and 64 observations, is 51.8, 39.7, 24.44 and 22, respectively, while for it is 53.97, 38.34, 27.38 and 21.71 for constant rate boundary condition. It is evident that for equal number of observations, the Frobenius norm are close to each other which suggests that changing of the borehole boundary condition does not significantly affect the results of joint inversion.

The joint inversion results (Table 2-3) does not demonstrates any improvement compared to the individual inversions (Tables 2-1 and 2-2) when considering the same number of observations. The joint result lies between head and flux data inversion result. For 8 observations, the minimum Frobenius norm obtained for head, flux and joint inversion are 48.27, 47.7 and 51.8, respectively. For 16 observations, the minimum Frobenius norm obtained for head, flux and joint inversion are 30.4, 44.72 and 38.34, respectively while it is 23.47, 32.03 and 24.44 for 32 observations. However, it should be noted that the comparison is made for the same number of observations and not for the same number of observation points. For the same number of observation points, it is clear that joint inversion has double number of observations compared to sole inversion of head and flux which leads to better estimate of hydraulic conductivity field.

2.6 Discussion

2.6.1 General findings

Considering the results of all 96 inversion cases, we find that inversion of flux data (with appropriate borehole boundary condition) leads to better resolved *Y*-field estimates then when considering head data. Nevertheless, the quality of the inversion results is strongly dependent on the type of boundary condition used in the borehole. The results in Tables 2-1 and 2-2 suggest that it is more suitable to use constant rate boundary condition for head data and constant head boundary condition for the flux data as reflected in Frobenius norms' values. The reason is that if the observation is head data and the borehole boundary is set

to constant head, the model response (head) will have less sensitivity to change of *Y*-field values. The same argument is also valid for the flux data.

The effect of the boundary is essential for proper experimental design. The experimental designs should ensure that once head data are intended to be used for the inversion, wells must be pumped at a constant rate while for the inversion of the flux data, the head in the borehole should be kept fixed. Other borehole boundary conditions lead to an underestimation of hydraulic conductivity values. However, for the joint inversion of both data, the type of borehole B.C. does not play a significant role.

Tso et al. (2016) and Zha et al. (2014) have stated that joint inversion of head and flux data results in better estimation of *Y*-filed in the porous and fractured media compared to the head data. However, joint inversion of both data does not offer any advantage over the individual inversion of the flux and head data when considering an equal number of observations. In fact, in this study, we showed that for a constant signal-to-noise-ratio the inversion performance for each type of data depends largely on the number of observations. For a small number of observations, the flux data provides a superior *Y*-field estimate compared to inversion of head data, while for the higher number of observations, all data types perform almost the same. However, if we would be able to measure flux and head data at the same location, then for the same number of observation points, joint inversion of flux and head data provide better estimate of *Y*-field as the number of observations are doubled. Furthermore, we showed the importance of borehole boundary conditions for hydraulic tomography experiment design based on the type of data intended to be used and acquired. It is worth mentioning that we do not see significant differences for a high number of observations comparing inversion results of flux and head data. In the following, we also show the integrative nature of head data and the fact that flux data can better resolve the *Y*-field for small number of observations through performing resolution analysis. Resolution analysis for the case of the variance of 4 and 4 measurement points demonstrates that flux data can better resolve the hydraulic conductivity field compared to head data (figure 2-6). Figure 2-6 shows the diagonal elements of the resolution matrix (calculated in the final inversion iteration) for head data, flux data, and joint inversion of both data are plotted on their corresponding blocks, respectively.

Considering the best ***Y***-field estimates obtained for the head (constant rate boundary condition) and flux (constant head boundary condition) data for calculating the resolution matrices, as shown in figure 2-6 (a) and 2-6 (d), it can be stated that model parameters (hydraulic conductivity values) are poorly resolved by head data while much better resolved when flux data are used. This is manifested by comparing both the values and coverage area of non-zero elements larger than 0.005. It is evident that once the head data are used for the inversion, the degree of smoothing and averaging is higher compared to the case in which the flux data are used. It is worth noting that using the constant head boundary condition for head data can better resolve the *Y*-field heterogeneity structure than the constant rate boundary condition, even though it underestimates the *Y*-field values. Comparing figure 2-6 (a) and 2-6 (b) and the correlation coefficient in Table 2-1 certifies this statement. The correlation coefficient increases from 0.27 to 0.49 when a constant head boundary condition is used instead of a constant rate boundary condition.

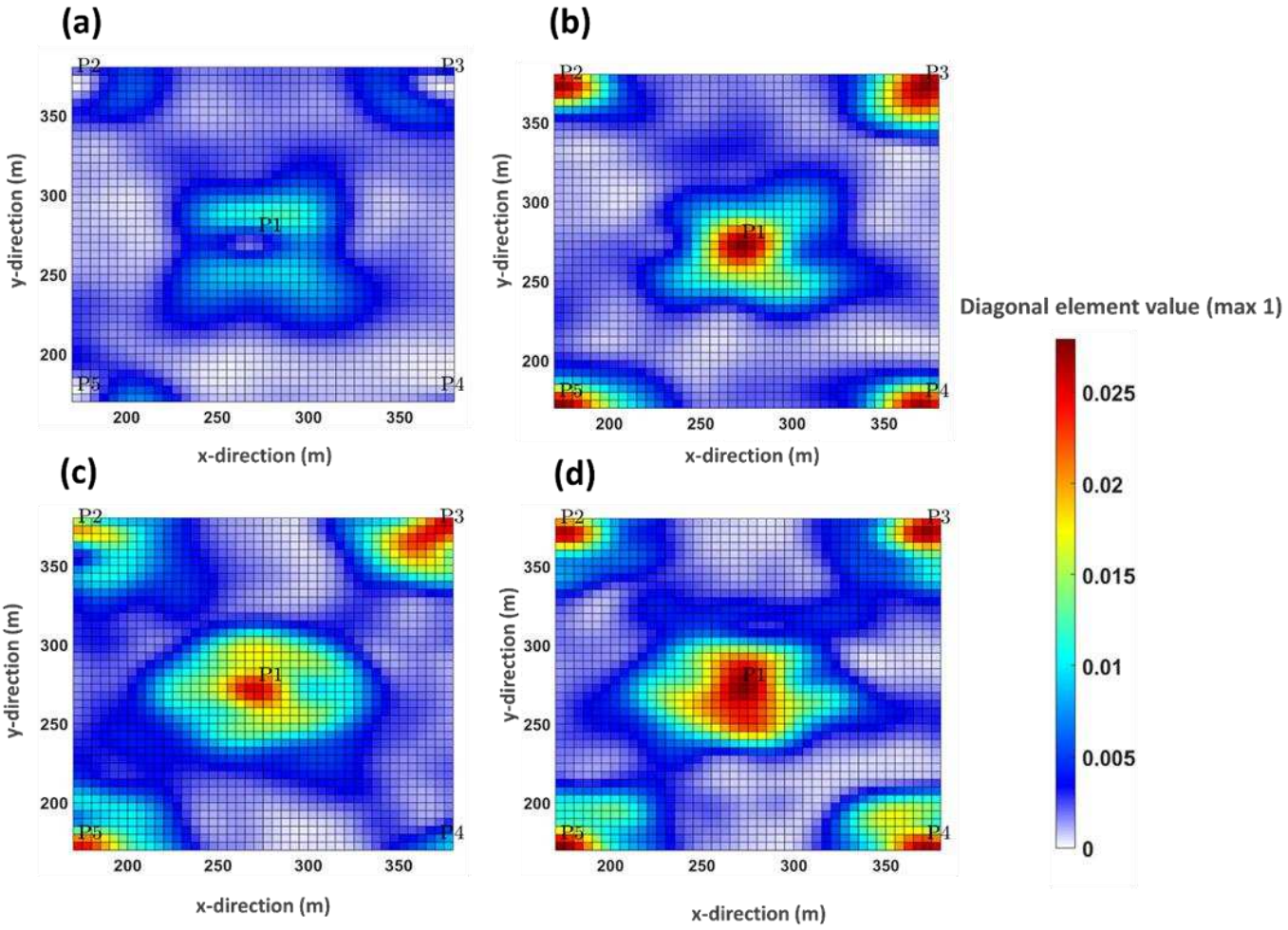

Figure 2-6: Diagonal element of the resolution matrix for **(a)** Y-field obtained by inversion of head data (4 observation - borehole boundary is set to constant rate), **(b)** Y-field obtained by inversion of head data (4 observation - borehole boundary is set to constant head), **(c)** Y-field obtained by inversion of flux data (4 observation - borehole boundary is set to constant head), **(d)** Y-field obtained by inversion of flux data (4 observation - borehole boundary is set to constant rate).

2.6.2 The effect of number of observations and variance

Figures 2-7 (a) to (d) show the correlation coefficient (between estimated Y-filed and reference Y-field) versus the number of observations for different type of data and borehole boundary conditions. Blue, red and gray color show the results for head data, flux data and joint inversion of both data, respectively. The data with constant rate borehole boundary condition is marked with solid line while the data with constant head borehole boundary condition is shown by the dashed line.

It can be seen in Figures 2-7 (a) to (d) that as the number of observations increases, the correlation coefficient also increases for all types of data and boundary conditions. For a small number of observations, flux data are superior to head data. The difference between the correlation coefficient of flux and head data is the strongest for a small number of observations, while the difference gradually decreases as the number of observations increases and at a high number of observations, they converge. This is a consequence of the decreasing distance between data points as the number of observations increases, thereby decreasing the radius of averaging. It is worth noting that no added value is observed for joint inversion of both data unless it makes the inversion independent of the type of the borehole boundary condition.

The variance of the hydraulic conductivity field affects the final values of the correlation coefficient. The higher the variance, the lower the correlation coefficient (especially for a small number of observations), and also the more challenging it is to reach a WRMSE close to 1. It is worth mentioning that having a higher number of observations, it would be more challenging to converge to the true values.

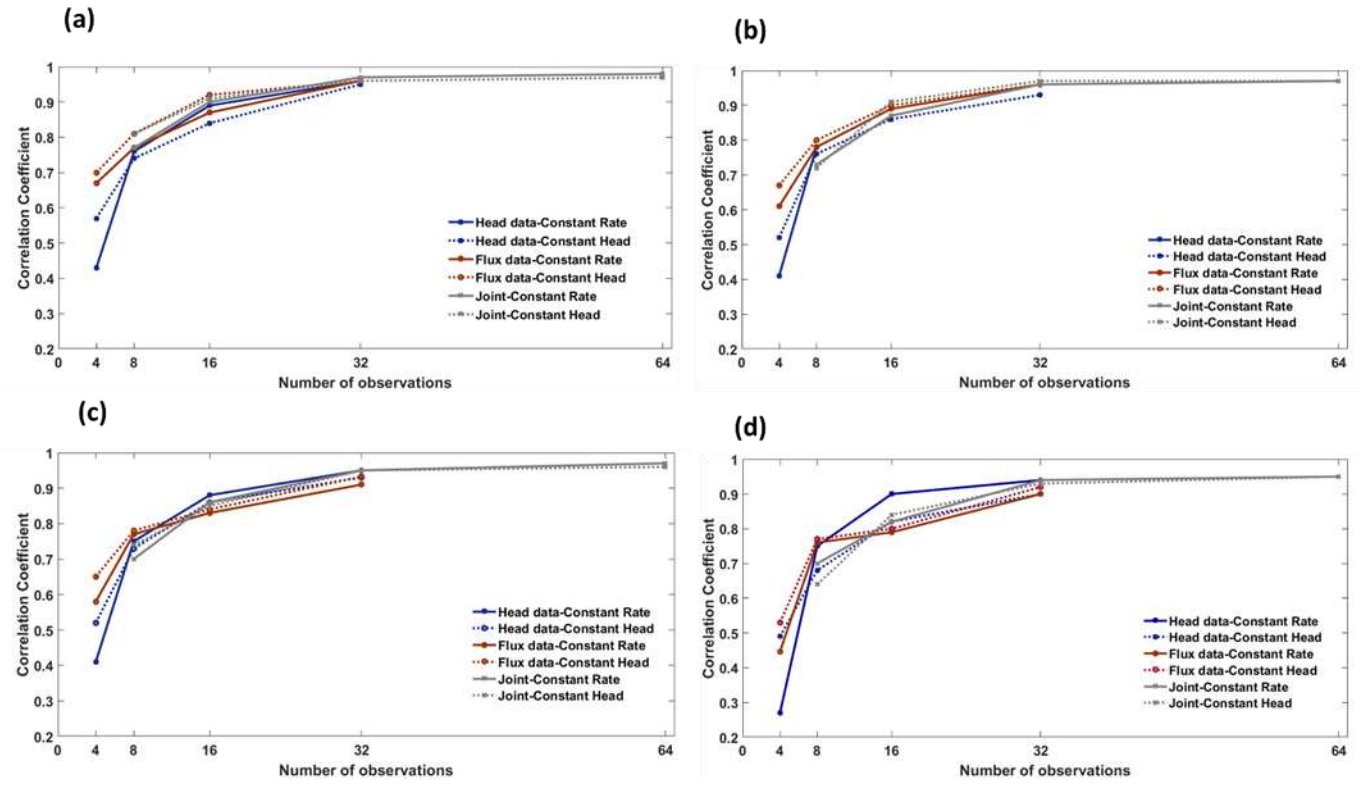

Figure 2-7: Correlation coefficient versus number of observations for reference hydraulic conductivity field with **(a)** variance=0.5, **(b)** variance=1 **(c),** variance=2 **(d),** variance=4

2.6.3 The effect of truncation order (P) on final inversion results

One of the inversion cases (variance of 4, 32 observation points, joint inversion of head and flux data) was chosen to investigate the effect of truncation order (P) on the final inversion result. Inversions were performed using truncation orders of 25, 50, 100, 200, 400, 800, and 1600. The inversions were performed on a server with one Terabyte (1 Tb) memory, 4 processors (Intel Xeon CPU E7-4850 v4 @ 2.10 GHz) and 40 cores in parallel mode. Figure 2-8 shows the *Y*-field estimated for each P value, the effect on the correlation coefficient, and elapsed time for each geostatistical iteration. For a truncation order of 25, we capture an overly smooth version of the true model with a correlation coefficient of 0.84. By setting the truncation order to 50, 100, and 200, the correlation coefficient increases to 0.88, 0.91, and 0.94, respectively. The truncation order of 400 (used in our study) with a correlation coefficient of 0.96 is a turning point beyond which increasing the truncation order does not significantly improve the correlation coefficient. So, the truncation order leads to improvement of *Y*-field reconstruction up to some points and after this point, it is only the computational time that increases. The computational time increased exponentially for large P values but could be decreased by being less stringent to the final inversion results. The truncation order would be chosen based on the degree of heterogeneity and the computational resource available. It would help perform inversion using a different number of principal components to ensure the proper choice of the number of principal components.

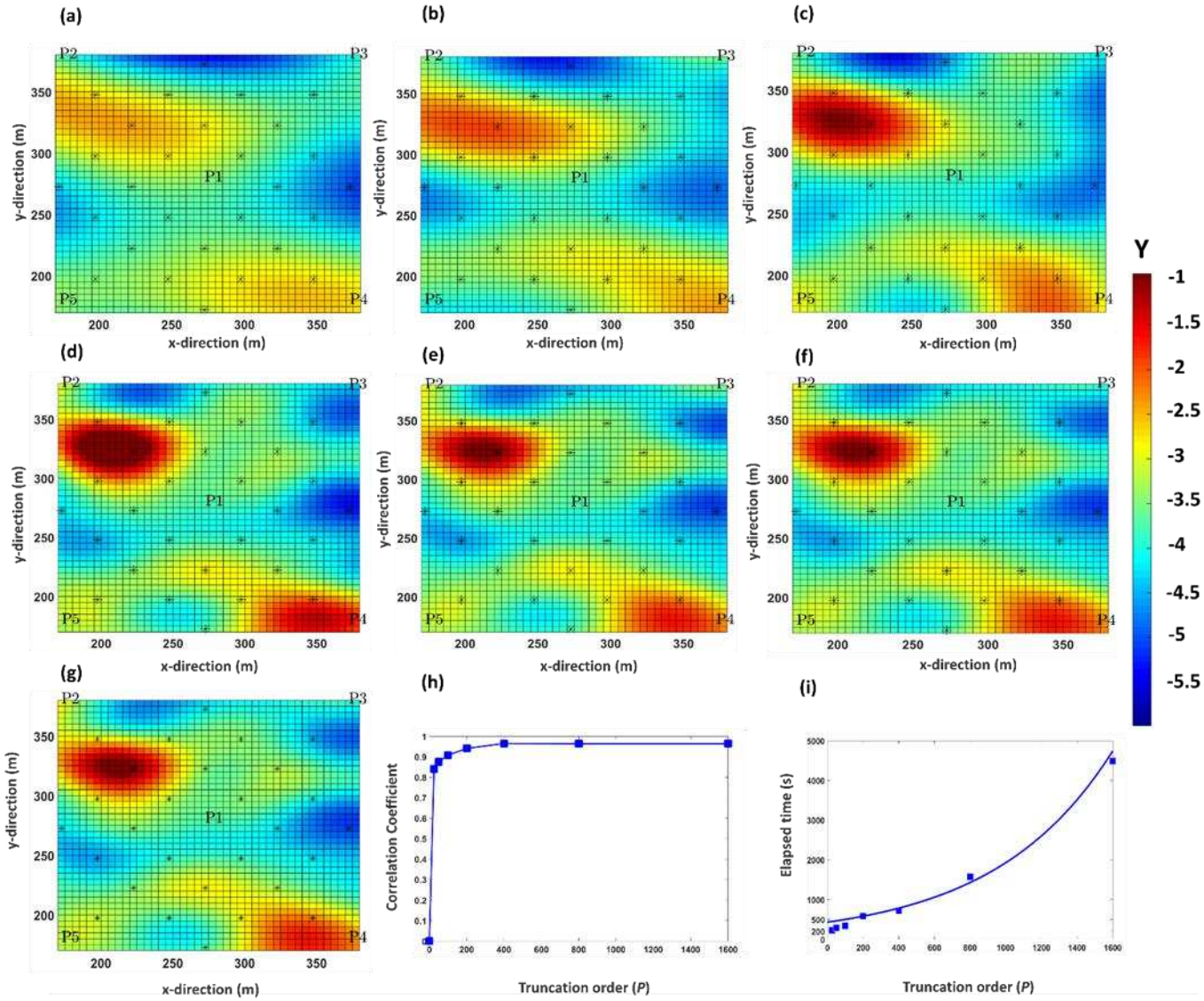

Figure 2-8: Estimated Y-field for truncation order of **(a)** 25, **(b)** 50, **(c)** 100, **(d)** 200, **(e)** 400, **(f)** 800, **(g)** 1600. **(h)** Correlation coefficient versus truncation order **(i)** elapsed time per one iteration versus truncation order

2.6.4 Implications for field implementations

Our results highlight the added value of using the flux data individually or jointly with head data in hydraulic tomography to achieve an enhanced reconstruction of the hydraulic conductivity field compared to using head data alone. This improvement is particularly pronounced when considering a small number of observations, a more likely setting for field applications. However, using only flux data requires setting the borehole B.C. to constant head, which is feasible (using pumps whose rates are controlled with water level) but would be more challenging than pumping at a constant rate during the field experiments. However, measuring the flux data during pumping (with constant rate) and joint inversion of both data would be quite feasible and removes the limitation of the borehole boundary condition. Moreover, for the same number of observation points, by doubling the number of measurements, joint inversion should significantly increase

the quality of the inversion, especially for a small number of observations points. Moreover, if one could measure the head and flux data at the same location, by doubling the number of observations, Y-field estimate would be significantly improved with minimum number of observation points and minimum invasion to the aquifer.

2.7 Conclusion

We used a numerical model representing a one-layer heterogeneous aquifer along with a geostatistical inversion approach (PCGA) to assess the information content of head and flux data. We investigated the cases of having a different number of observation points and different hydraulic conductivity variances (with the same field structure). We found that for a small number of observation points, using flux data reproduces a closer *Y*-field to reference *Y*-field compared to head data. Furthermore, by increasing the number of observation points, the effect of the type of data vanishes, and all converge to the same results as the sampling distance between points becomes smaller. For the same number of observation points, if we are able to measure the head and flux data at the same location, joint inversion of head and flux data provides an improved estimate compared to the inversion of sole head or flux data due to double number of observation. This means that even if, the head and flux data are measured at the same location, it still provides useful information about the media.

We also found out that the type of borehole boundary conditions used in the tomography and modeling affects the inversion results. The appropriate boundary condition for head and flux data is constant rate and constant head while joint inversion of both data is independent of the boundary type. Inappropriate selection of borehole boundary conditions may result in an underestimation of the K field values.

Measuring flux data during a hydraulic tomography experiment is now feasible, especially for shallow sandy aquifers where active Distributed Temperature Sensing can be deployed using direct push method to install the fiber optic cables into the sediments (des Tombe et al., 2019). Since the inversion is particularly sensitive to the number of measurements, groundwater fluxes measurements by active DTS can be particularly useful since it may provide a large number of measurements thanks to the high spatial resolution of fiber optic temperature measurements (Simon et al., 2021). Moreover, it can be also particularly useful in aquifers where the head drop due to the pumping is small, but there may be high groundwater fluxes. This should lead to interesting developments of hydraulic tomography experiments in the near future.

Acknowledgments

This work has received funding from the European 'Union's Horizon 2020 research and innovation program under the Marie Sklodowska - Curie grant agreement number 722028 (ENIGMA ITN). In our work we relied on the PCGA implementation in python (pyPCGA) by Lee et al. (2016) that is available on GitHub (https://github.com/jonghyunharrylee/pyPCGA/). We would like to appreciate SINTEF for providing free access to the Matlab Reservoir Simulator Tool (MRST) which is available on the SINTEF website (https://www.sintef.no/projectweb/mrst/).

CRediT authorship contribution statement

Pouladi, B.: Writing - original draft, Writing - review & editing, Methodology, Conceptualization, Software, Formal analysis, Investigation. **Niklas Linde**: Conceptualization, Methodology, Supervision, Writing - original draft, Writing - review & editing. **Laurent Longuevergne**: Supervision. **Olivier Bour**: Writing - review & editing, Conceptualization, Writing - review & editing.

Declaration of Competing Interest

The authors declare that they have no known competing financial interests or personal relationships that could have appeared to influence the work reported in this paper.

Chapter 3 Reconstruction of the aquifer heterogeneity using joint inversion of the head and flux data: Application to a shallow granular aquifer

This chapter provides provisional results of a paper in preparation

The paper in preparation is made in collaboration with Dr. René Lefebvre from INRS (Québec), Dr. Daniel Paradis from Geological survey of Canada and Dr. Niklas Linde from the University of Lausanne. In this paper, we describe the first hydraulic tomography experiment conducted including the groundwater flux data.

Behzad Pouladi[1*], Olivier Bour[1], René Lefebvre[2], Daniel Paradis[3], Niklas Linde[4], Jean-Marc Ballard[2], Jérôme de La Bernardie[1], Laurent Longuevergne[1], Nataline Simon[1]

1 Univ Rennes, CNRS, Géosciences Rennes, UMR 6118, 35000 Rennes, France.
2 Institut national de la recherche scientifique, Centre Eau Terre Environnement, Québec, QC, Canada
3 Natural Resources Canada, Geological Survey of Canada, 490 rue de la Couronne, Québec, QC, Canada, G1K
4 University of Lausanne, Institute of Earth Sciences, Lausanne, Switzerland

3.1 Introduction

Characterizing and quantifying subsurface media properties are essential for the successful investigation of subsurface processes. The hydraulic conductivity field is the main parameter controlling groundwater flow (Zinn and Harvey, 2003) and the contamination transport path (Jim Yeh, 1992) in the aquifers. The characterization methods of hydraulic conductivity generally fall into two categories, geophysical and hydraulic methods. In geophysical methods such as Ground Penetrating Radar (GPR) (Hyndman et al., 2000; Doetsch et al., 2012) and Electrical Resistivity Tomography (ERT), radar pulses and electrical currents are used to measure properties (permittivity and electrical conductivity) related to hydraulic parameters by petrophysical relationship. On the other hand, hydraulic methods such as hydraulic tomography (Yeh and Liu, 2000) and tracer-based methods (Jiménez et al., 2016), rely on the analysis of the aquifer response to a hydraulic perturbation (pumping, tide, tracer injection, etc.) imposed to the aquifer. The advantages of geophysical methods are that they are non-invasive (applied from the surface) or minimally invasive (applied from the borehole), require less time for the operation while the biggest drawback is the petro-physical relation required to infer hydraulic parameters from estimated geophysical parameters. However, in hydraulic methods, the aquifer response is mechanistically related to the media's hydraulic properties, which can be explained through a set of equations. This makes hydraulic methods more preferable when it comes to the estimation of hydraulic properties, especially for predicting contaminant transport which requires an accurate characterization of hydraulic conductivity distribution.

Hydraulic tomography has been long used for the characterization of the subsurface media and has been the subject of many theoretical (Lee and Kitanidis, 2014; Yeh and Liu, 2000; Zhu and Yeh, 2005), laboratory (Liu et al., 2007; Zhao et al., 2016) and field studies (Berg and Illman, 2013, 2011; Bohling et al., 2007; Cardiff et al., 2009; Cardiff and Barrash, 2011; Fischer et al., 2017). In hydraulic tomography, the aquifer undergoes series of pumping, and the head pulses are observed in the boreholes or other observation points across the aquifer. The observed head variations along with a numerical model (describing the aquifer response to the pumping) are then used to map the hydraulic conductivity distribution and values through an inversion process. Even though, hydraulic tomography is a proven approach for the estimation of hydraulic parameters, there are certain limitations associated with it. One limitation stems from the underlying physic in which the measured head variations are spatially averaged because of the diffusive nature of head perturbation in the aquifer. This leads to a high degree averaging of the reconstructed hydraulic conductivity field compared to the real field. The other limitation emerges in the hydraulic tomography tests performed in the aquifers with high values of hydraulic conductivity where small head drops would result in a low signal to noise ratio. This would imply using other types of hydraulic data to improve hydraulic tomography. Few works address the inclusion of the flux data in hydraulic tomography to improve the imaging of the hydraulic conductivity field. Zha et al. (2014) included the flux data in hydraulic tomography for a 2D synthetic fractured aquifer model and found out that it helps better characterization of the fracture distribution and their hydraulic conductivity values. Tso et al. (2016) performed hydraulic tomography for a 3D synthetic aquifer and compared two cases in which head data alone and jointly with flux data were used. They found out that flux data provide non-redundant information about subsurface heterogeneity and joint inversion of flux and head data improves the estimation of the hydraulic conductivity field. Recently, Pouladi et al. (2021, in preparation) performed hydraulic tomography in a 2D model. They found out that inversion of the flux data leads to a higher resolution hydraulic conductivity field compared to head data especially for low number of observation points. They also found that steady state hydraulic tomography using head or flux data is dependent on borehole boundary condition used. For head data the best borehole setting is constant rate while for flux the data, the best setting is constant head. Joint inversion of both data is insensitive to the type of boundary

condition. It should be noted that joint inversion of head and flux data offers no advantage over the sole inversion of head and flux data considering an equal number of observations.

Subsurface flux measurement has long been an interest for hydrogeologists. Available techniques for quantifying groundwater flux generally fall into two categories based on the measurement conditions: (i) they are measured inside the borehole or (ii) they are measured by tools buried in the formation. In the first family of methods, water flux passing through the borehole are measured. For instance, the colloidal borescope measures the horizontal groundwater flow inside the borehole (Kearl, 1997) and is based on the analysis of pictures of colloid propagation by water passing through a well. Another more common alternative comes from bore-hole dilution tests (Drost et al., 1968; Jamin et al., 2015; Schneider et al., 2019), relying on the dilution of a tracer injected inside a screened borehole or within a double packer system. Other approaches, such as acoustic Doppler flow meter, fluid-conductivity of the logging system (Bayless et al., 2011), or temperature logging (Reiter; 2001) can also provide some estimation of the horizontal groundwater fluxes.

Nevertheless, boreholes disturb the flow field and affect the measurements; hence, the measured values may not represent the real flux values (unless proper modeling of underlying measurement physics is done). To over-come this challenge, the following methods require burying of the tool in the ground such that it is in close contact with the formation. However, this may limit its application to shallow and unconsolidated formations. These methods are either temperature-based (Ballard, 1996; Banks et al., 2018) and rely on relating the measured signal associated to heat propagation due to the flux or tracer-based (Devlin et al., 2009; Labaky et al., 2009) by relating the flux to the dissipation of a tracer (like saline tracer). The advent of Fiber Optic Distributed Temperature Sensors (FO-DTS) has revolutionized the capability of measuring and monitoring the temperature over large distances with unprecedented spatial, temporal, and temperature resolutions. FO-DTS is a distributed sensor family member that allows measurement of temperature along the fiber optic cable. FO-DTS can be employed in both passive and active modes. In passive mode, only the fiber optic cable's temperature is measured, while in active mode (A-FO DTS), heat is added to the fiber optic cable by a heating element located very close to the FO cable or within the cable. In A-FO DTS the temperature evolution with time is a function of the surrounding area's thermal properties (porous medium) and also groundwater flux passing around the FO cable (Bakker et al., 2015; des Tombes et al., 2019; Simon et al., 2021). Thus, by measuring the temperature evolution with time during an A-DTS FO experiment, it is now possible to measure groundwater fluxes at an excellent accuracy along a FO cable previously inserted in an aquifer (Simon et al., 2021). The flux profile data is of particular interest in heterogeneous aquifers as it provides information with an excellent spatial resolution (Simon et al., 2020), while head data would give an average value at greater scale, even when packers are used. It is worth noting that the application of A-FO DTS for flux measurements is currently limited to shallow and unconsolidated aquifers due to limitations in deployment by the direct push method (Bakker et al., 2015).

Motivated by the results of Pouladi et al. (2020, in preparation), we present here a hydraulic tomography experiment performed in a shallow granular aquifer using head and flux data. To our knowledge, this is the first hydraulic tomography field study that uses joint inversion of flux and head data. The paper is structured in 7 sections. In section 2, we describe the experimental site and settings used for the hydraulic tomography experiment and A-DTS measurements. In section 3, we explain the inversion of the acquired temperature profile to infer the flux profile as well as the model developed for the aquifer. In section 4, the flux data and head data acquired are presented. Section 5 and 6 are devoted to explaining the hydraulic tomography results obtained and the discussion, respectively. The last section concludes the work.

3.2 Experimental setup

3.2.1 State of the art A-FO DTS experiment in shallow aquifers

The first step for conducting the A-FO DTS experiment comprises inserting the FO cable into the ground by the direct push method (Bakker et al., 2015; des Tombe et al., 2019). Direct-push technology is a suitable substitute for drilling-based operations in which a hollow rod with a conical head is pushed into the unconsolidated formation (Butler Jr et al., 2002). FO cables are placed inside the rod, attached to the conical head and pushed into the aquifer. Once the desired depth is reached, the hollow rod is retrieved and the FO is left inside the ground (Bakker et al., 2015). Direct-push technology is advantageous since the buried cable is in direct contact with the ground with the minimum subsurface perturbation compared to natural conditions. Furthermore, it is low cost, simple to operate, and it allows inferring additional information such as local hydraulic conductivity during the deployment (Bakker et al., 2015; Butler Jr et al., 2002). Once the FO cables are deployed in the aquifer, it is then possible to utilize A-FO DTS and follow the temperature evolution over the time that is a function of the surrounding area's thermal properties (porous medium) and groundwater flux passing around the FO cable. Among the first applications, Bakker et al. (2015) and des Tombe et al. (2019) showed the feasibility of groundwater fluxes measurements (specific discharges) in shallow sandy aquifers. More recently, Simon et al. (2021), using a laboratory sandbox, showed that heat propagation comprises three steps: FO cable heat storage effect during the first minutes, conduction-dominant during a more or less long period, and advection-dominant period at late times when relevant. In particular, we showed that after a proper correction for the heat storage effect induced by the FO cable, thermal conductivities and groundwater fluxes along the FO cable can be obtained with an excellent accuracy from measurements during the conduction-dominant period (the slope of temperature curve in natural logarithm coordinate) and from the temperature evolution curve at late times by using analytical solutions and graphical approaches. Figure 3-1 (a) to (c) schematically show how A-FO DTS can be used to infer groundwater fluxes. Note that groundwater fluxes correspond to specific discharges or Darcy fluxes. In step 1, the FO DTS cable is buried vertically by the direct push method within the aquifer. Then, part of the FO cable embedded in the aquifer is electrically heated for a few hours or days by passing an electrical current through the metal cable materials (red rectangle). Next, the temperature evolution for each section along the cable is measured and corrected for the heat storage effect and the water background temperature (step 2). The typical temperature rise follows a logarithmic evolution with time characteristic of the conduction regime until the temperature stabilizes when the heat produced is fully dissipated (Simon et al., 2021). The temperature in the conduction-dominant period (the slope in natural logarithmic scale) can be used to estimate thermal conductivity along the cable (step 3). Finally, the temperature profile at a given time can be converted to the flux profile using analytical solutions and graphical approaches (step 4) (Simon et al., 2021). Typically, for the same thermal conductivity, the greater the groundwater fluxes, the lower will be the temperature at stabilization.

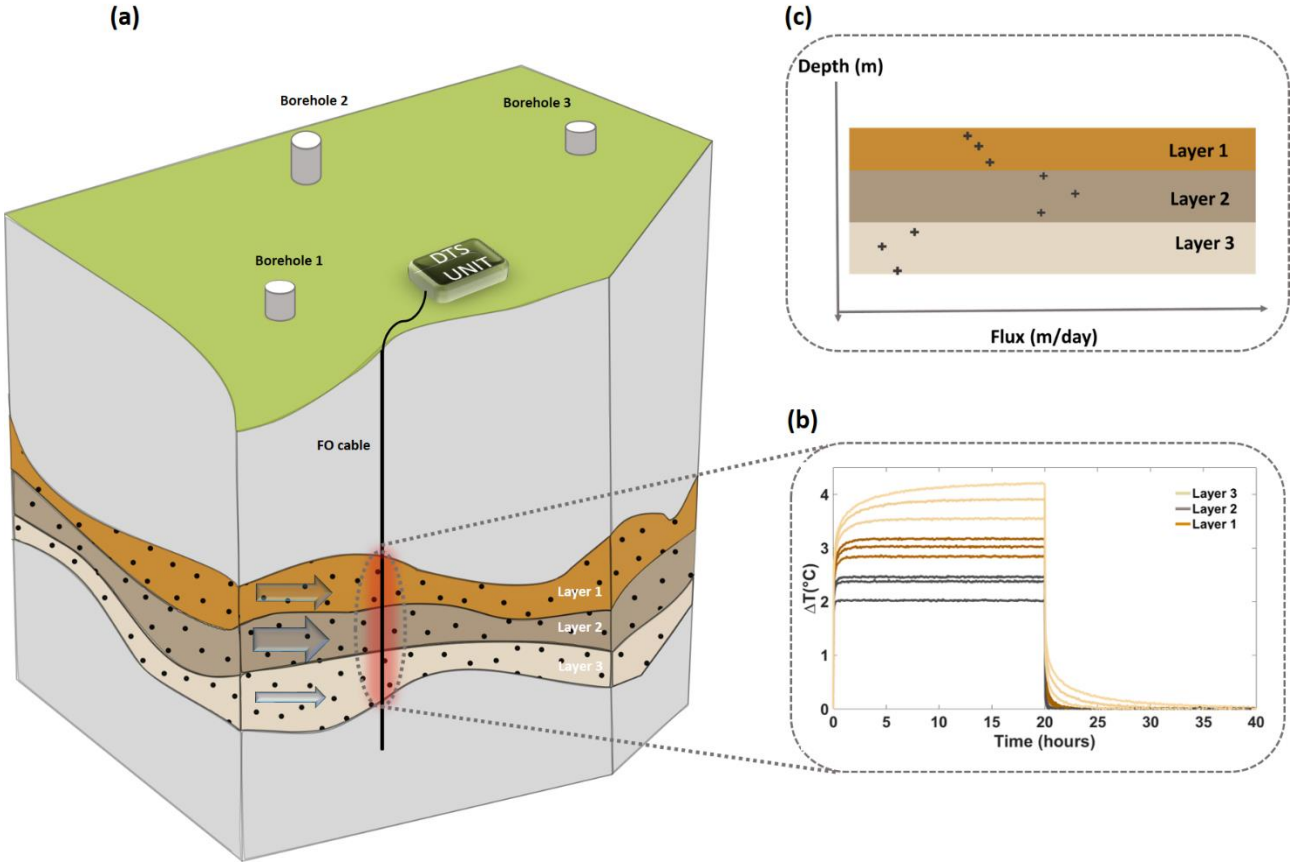

Figure 3- 1: Schematic of the steps involved in using Active FO-DTS to infer groundwater flux profile with depth-(step a) Active Fiber Optic Cable is deployed vertically into the ground so that it is in close contact with the formation. (step b) The cable is heated (active mode) and cable temperature during the heating (here 20 hours) and cooling periods is measured. Each curve corresponds to one measurement point or one section in the FO-cable, whose length depends on the experiment's spatial resolution (Simon et al., 2020). (step c) Measured temperature data along the fiber optic cable are converted to flux profile with depth.

3.2.2 The Saint-Lambert site

The hydraulic tomography field study was performed on a shallow granular aquifer at Saint-Lambert experimental site located 40km south of Quebec City, Canada. This 12 km2 aquifer hosts a decommissioned sanitary landfill and has been subjected to numerous field experiments such as the GPR surveys, cone penetrometer tests (CPT), soil moisture resistivity (SMR), fluid sampling as well as multilevel slug tests (Paradis et al., 2014, 2015, 2016; Tremblay et al., 2014; Ruggeri et al., 2014). The surficial sediments consist primarily of Late Quaternary sandy and silty sediments that were deposited in the receding Champlain Sea, which was an arm of the Atlantic Ocean that had invaded the St. Lawrence Valley at the time of the last deglaciation (Paradis et al., 2016). This littoral and sublittoral depositional environment resulted in superposition of long (>100 m) inter-digitized sand and silt strata with fine vertical and lateral intratarsal transitions in grain-size as a result of changing energy levels along Champlain Sea shorelines (Paradis et al., 2014). Figure 3-2 shows the site's geographic location and the relative position of the boreholes in the site. This site has been chosen since it was previously subjected to HT experiments. It was also a convenient site as the direct-push tool was possible and available to bury the FO cables in this shallow aquifer.

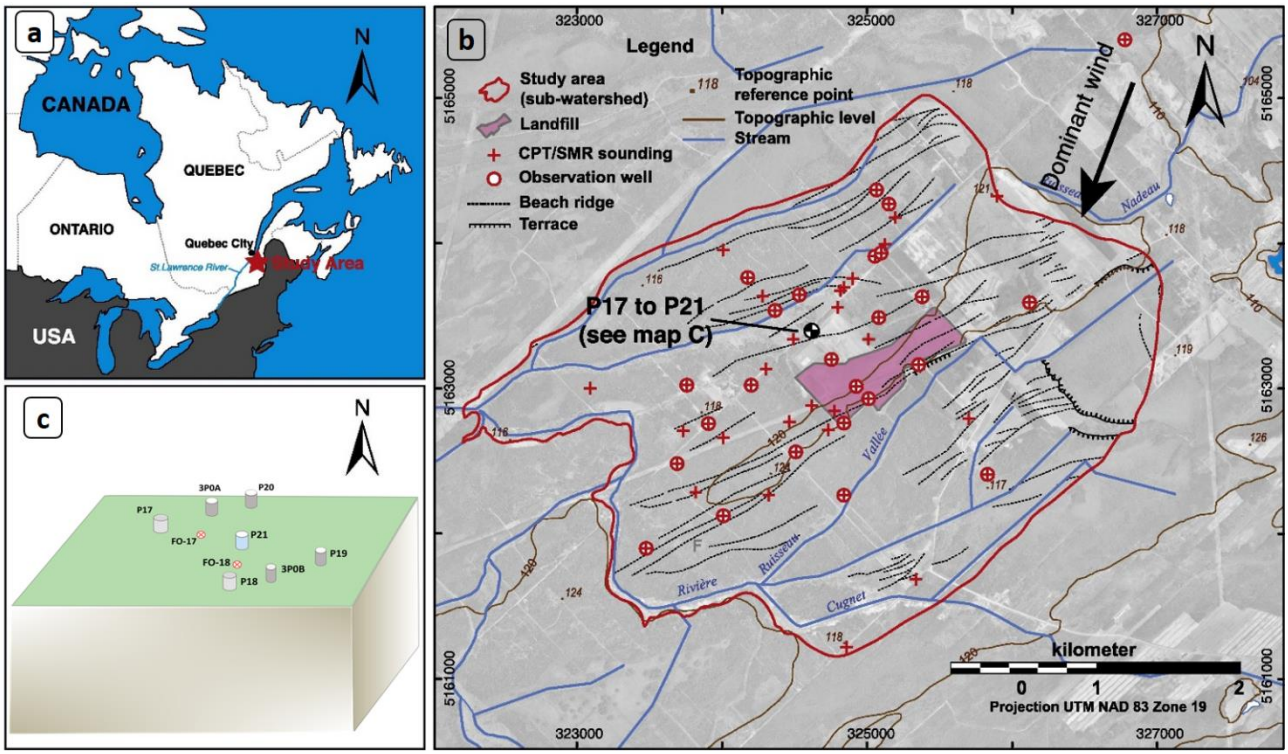

Figure 3-2: (a): Geographical location of the Saint-Lambert site, (b): location of the testing site within the sub-watershed enclosing the former sanitary landfill, (c): Relative position of the boreholes (Modified after Paradis et al., 2016).

3.2.3 Previous hydraulic tomography experiments

In two of the most important study works done on the Saint-Lambert site, Paradis et al. (2014) used machine learning technique to find a statistical relationship between CPT/SMR data and horizontal hydraulic conductivity (measured by slug test), vertical hydraulic conductivity and porosity (obtained by sediment sample testing). They found that applying this approach allowed them to identify the hydrofacies and estimate the hydraulic properties consistent with hydraulic tests. In another work, Paradis et al. (2016) performed a transient slug test to assess its efficiency for estimation of horizontal and vertical hydraulic conductivity as well as porosity. Their results showed that the transient slug test could estimate the hydraulic properties consistent with previous studies. Furthermore, they shown that this approach could capture small scale heterogeneities that induce K-anisotropy at larger scales, difficult to quantify through conventional hydraulic tests. Figure 3-3 (a) shows the values of horizontal hydraulic conductivity by CPT test at borehole P17 and the horizontal hydraulic conductivity obtained through transient slug tests. For convenience let's consider $\boldsymbol{Y}=\log(\boldsymbol{K})$.

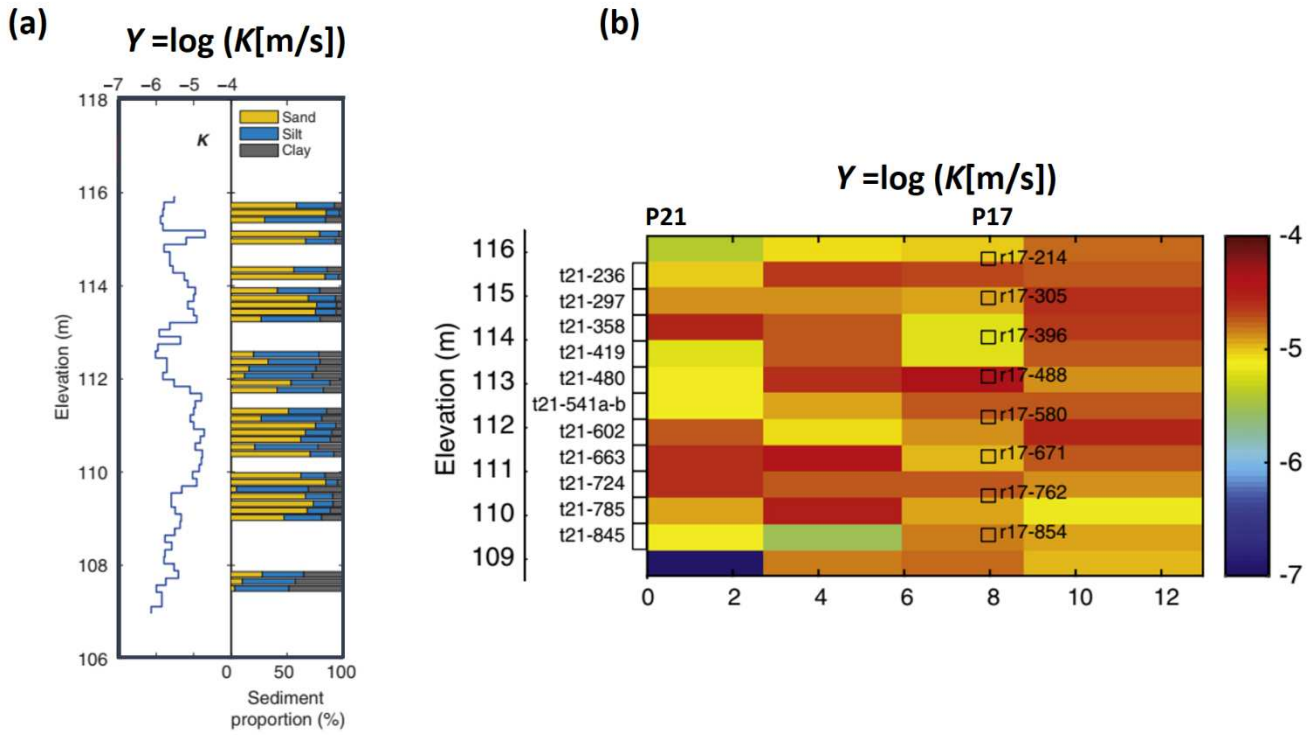

Figure 3-3: Horizontal hydraulic conductivity value (a) at borehole P17 by CPT and (b) between P21 and P17 obtained by transient slug test hydraulic tomography. (Modified after Paradis et al., 2014, 2016.)

3.2.4 Collection of hydraulic head data

The tomography site consists of 7 boreholes with the pumping borehole (P21) in the center and six other boreholes on the side. Two screened boreholes were equipped with the packers (P17 and P18) to monitor the head and temperature in discrete intervals isolated by the packers. The head and temperature were also monitored in the other four open boreholes, P19, P20, 3P0A, and 3P0B. The screened boreholes have a diameter of 5.1 cm and were developed to ensure adequate hydraulic contact between the screens and formation without any sand-pack. This is important for the successful implementation of good quality hydraulic tomography test and data acquisition. The aquifer was subjected to continuous pumping for 88 hours at a constant rate of 10 lit/min and hydraulic heads in 8 discrete intervals in the observation boreholes (P17 and P18), four other side boreholes (P19, P20, 3P0A, and 3P0B), were monitored. The borehole P21 is fully screened for around 7.5m (until the elevation of 109.5m), and pumping is performed on the whole depth of borehole P21.

3.2.5 Collection of A-FO DTS data

Two FO cables were installed vertically by a direct push drilling technique at mid-point between the central pumping well (P21) and P17 and P18, named FO-17 and FO-18, respectively. Figure 3-4 shows the location of the boreholes and buried fiber optic cables. The FO cables were buried two months before the start of the experiment to ensure that the formation well surrounds the cable after installation. The FO cables are designed by Brugg Kabel AG, Switzerland, with a 3.8 mm diameter and protected by steel armoring and a polyamide jacket. Silixa-XT was used as the DTS unit to monitor the temperature using a double-ended configuration. In order to calibrate the DTS unit, around 13 m of FO-cable (FO-17 and FO-18) for both channels was placed in the hot bath and cold bath (filled with a mixture of ice and water). Both baths were equipped with PT 100 probes and RBR Solo T probe, which record the temperature during the experiment

with an accuracy of 0.1°C and 0.002°C, respectively. As soon as the pumping started, FO-DTS measurement also started in parallel in passive mode to collect the aquifer temperature data for 19 hours with a nominal spatial sampling of 25 cm and a temporal acquisition frequency of 10 seconds. Then, by analyzing the piezometric heads and ensuring that steady-state condition was achieved, the pumping was held at the same rate, but the heat was injected into fiber optic cables (active mode) for around 45 hours. After this period, pumping and heating were stopped. It must be noted that the whole experiment took about 92.5 hours (around four days). However, we face some technical incidents with the power-controller that led to deviation from the initially planned experiment. Nevertheless, it was possible to accomplish 28 hours of heating during pumping (figure 3-5) and provide sufficient data to be analyzed.

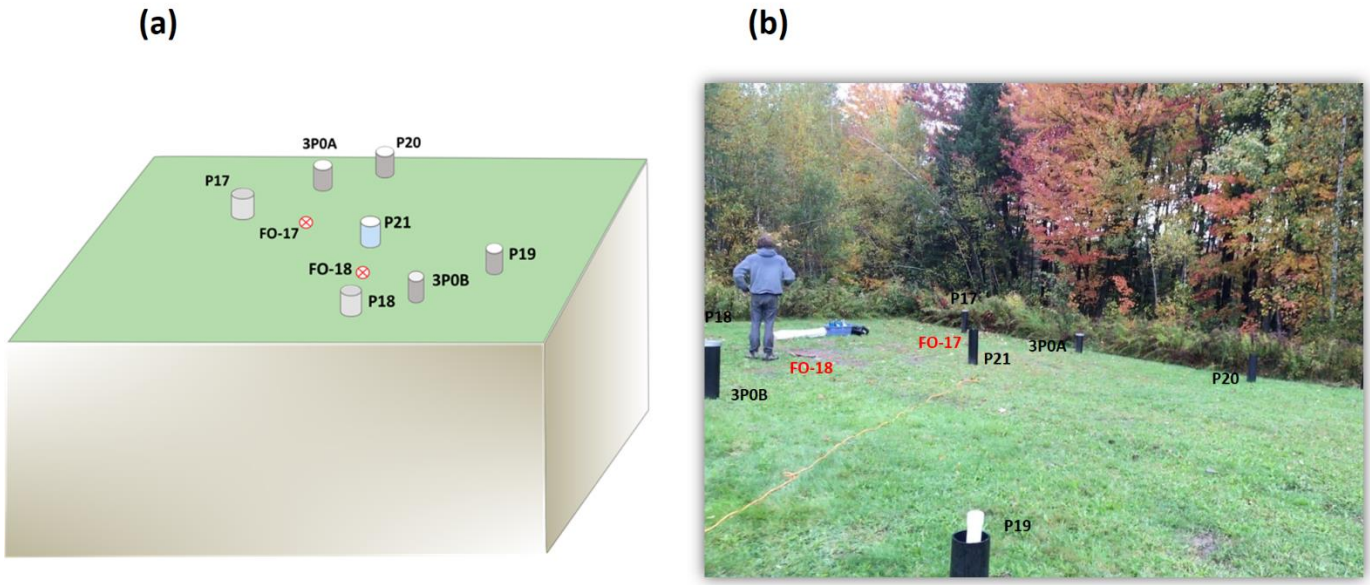

Figure 3- 4: (a): Schematic of the location of the boreholes and fiber optic cables. The pumping borehole (P21) is located in the center and shown in blue color. Grey caps show the two observation boreholes with packers (P17, P18), while the white cap shows the other four open observation boreholes (P19, P20, 3P0A, 3P0B). (b): Experimental site image

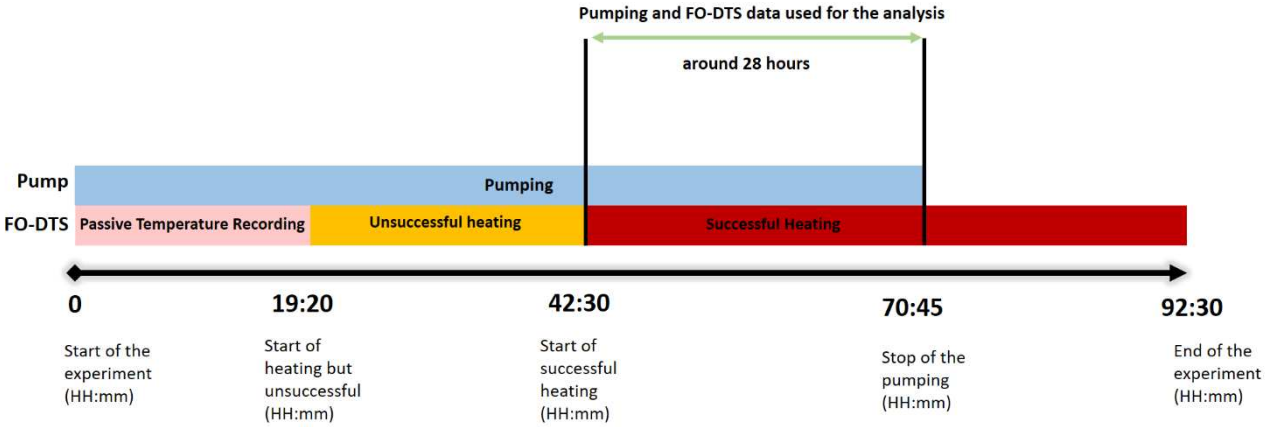

Figure 3-5: Timeline of the experiment performed on the Saint-Lambert site. The top blue bar shows pumping, which started from the beginning of the experiment and performed continuously for 88 hours (unwanted stop due to a sudden power shortage). The bottom bar shows the FO-DTS, which recorded passive temperature data for around 19 hours, followed by an unsuccessful attempt to heat the FO-cable (caused by technical problem) and a successful start of heating at 42:30, which lasted for around 50 hours.

3.3 Methodology

In the current section, the methods used to analyze the temperature and head data are explained. In the first subsection, we describe how the fiber optic cable's temperature data are converted to the flux profile. Next, the principal component geostatistical approach (PCGA) (Lee and Kitanidis, 2014) and geostatistical inversion used in this paper are explained. The final subsection is devoted to explaining the numerical model created in Matlab Reservoir Simulation Toolbox (MRTS) (Lie, 2019) to simulate the aquifer.

3.3.1 Inversion of temperature profile to the water flux profile

In Simon et al. (2021), we showed that in the very first moments of heating, the temperature increases as the heat is stored inside the fiber optic cable due to its heat capacity. In the conduction-dominant period, heat is transported from the fiber optic cable to the surrounding media by the conduction heat transfer mechanism, while in the convection-dominant period, the effect of convection is more pronounced and may lead to temperature stabilization. The slope of the temperature in the semi-log plot during the conduction-dominant period allows to estimate the media's thermal conductivity (eq 3.1a). The temperature evolution graphs by several characteristic times depending on the flux and thermal properties of the media and water. The characteristic times are (t_d), corresponding to the time when the conduction-dominant period ends, (t_s), the time when 99% of the stabilization temperature is reached, and (t_i), which is the time of intersection between the conduction and advection regime (see Simon et al., 2021 for more details).

$$\lambda = \frac{Q}{4\pi s}, \qquad \text{(a)}$$

$$t_d = \frac{1}{2q^2}\frac{\lambda}{\rho c}, \qquad \text{(b)}$$

$$t_s = \frac{4\,\lambda}{q^2}\frac{\rho c}{{\rho_w}^2{c_w}^2}, \qquad \text{(c)}$$

$$t_i = \frac{2.24\,\lambda}{q^2}\frac{\rho c}{{\rho_w}^2{c_w}^2}. \qquad \text{(d)}$$

Equation 3:1 – Characteristic times that permit to estimate groundwater fluxes (q) (Simon et al., 2021)

where Q, λ, q and s represent the injected heat power (W/m), the thermal conductivity of the rock(W/m/K), the groundwater flux (or Darcy flux) (m/s), and the slope of the line in the conduction-dominant period on a semi-log plot, respectively. Here ρc and $\rho_w c_w$ are the volumetric heat capacity of the saturated media and water, respectively. The characteristic times could be used to quantify the value of water flux measured graphically. Figure 3-6 shows the temperature evolution curve with different periods and corresponding characteristic times for a synthetic data set.

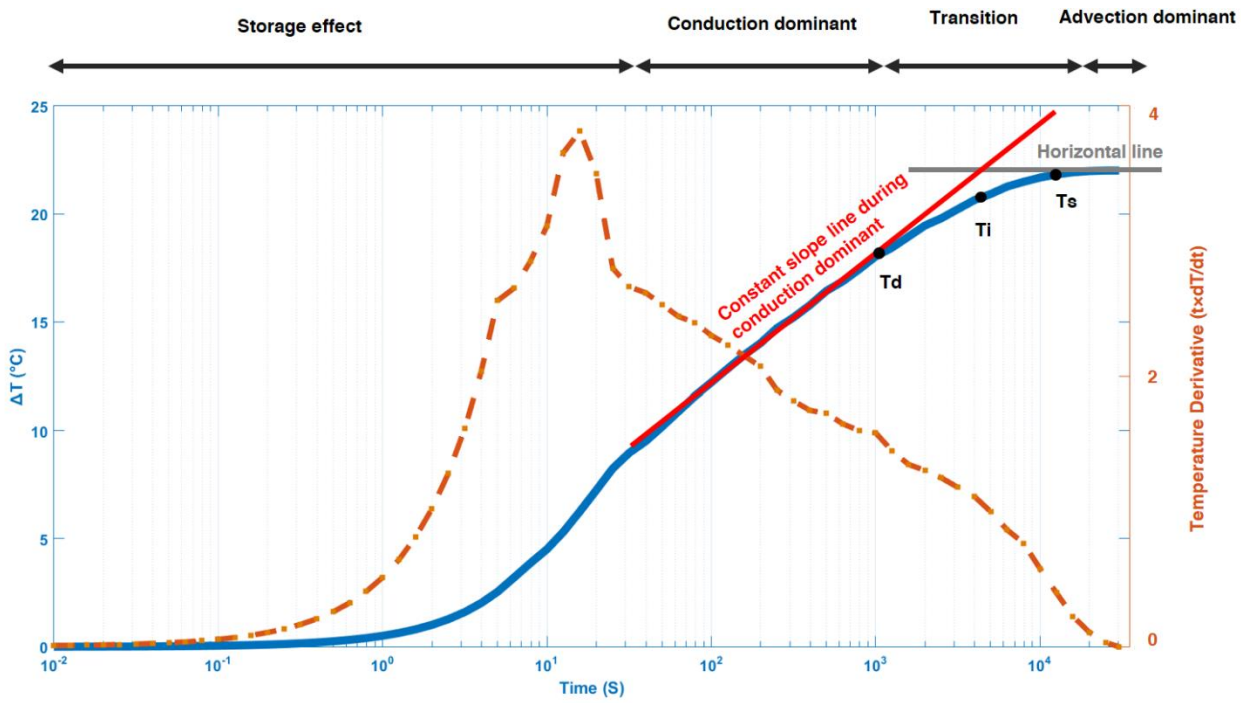

Figure 3-6: Temperature evolution curve and characteristic times used to quantify the flow (modified after Simon et al., 2021)

In order to invert the temperature profile to flux profile, first, the slope of the temperature evolution curve in the conduction-dominant period on a semi-log plot is identified. Next, equation 3:1 (a) is used to estimate rock thermal conductivity. Then, each of the characteristic times mentioned above (depending on the availability and detectability) can be employed to estimate the flux values independently. It should be noted that flux estimation requires knowledge of the rock and water's volumetric heat capacity. We do not expect much variation in the heat capacity of water, but the rock's heat capacity would vary based on the type of rock and also dependent on the porosity value. Geological information about the aquifer would help define a plausible range for the rock heat capacity in order to estimate flux within an uncertainty range.

Furthermore, one can also use the following equations which describe the temperature trend during conduction dominant (Blackwell, 1954; Marsily, 1976) and during the whole period (Carslaw and Jaeger, 1959), respectively, to find the value of the flux:

$$\Delta \mathbf{T}_{\text{conduction}} \approx \frac{Q}{4\pi\lambda} \ln\left(\frac{\lambda}{\rho c r^2}\mathbf{t}\right),$$

Equation 3:2 – Temperature evolution with time during conduction dominant period (Simon et al., 2021)

where $r = \sqrt{x^2 + y^2}$ is the distance between the heat source and FO cable. The equation describing the temperature change for the whole period (except the early times associated with the heat storage in FO cable) is given as follow:

$$\Delta \mathbf{T} = \frac{Q}{4\pi\lambda} \times exp\left(\frac{qx}{2\lambda}\rho c\right) \times W\left(\frac{r^2 \rho c}{4\mathbf{t}\lambda}, \frac{rq}{2}\frac{\rho_w c_w}{\lambda}\right) \qquad \text{(a)}$$

$$W(\alpha, \beta) = \int_{\alpha}^{\infty} \frac{1}{\psi} exp\left(-\psi - \frac{\beta^2}{4\psi}\right) d\psi, \qquad \text{(b)}$$

Equation 3:3 – general equation for temperature evolution with time (Carslaw and Jaeger., 1959)

The above equation and the measured temperature data can be used to estimate the flux for each section along the A-FO DTS by minimizing the following objective function:

$$\text{objective function} = \sum \sqrt{|\Delta \mathbf{T}_{\mathrm{A-FODTS}} - \Delta \mathbf{T}_{\mathrm{calculated}}|^2}$$

where, $\Delta \mathbf{T}_{\mathrm{A-FODTS}}$ and $\Delta \mathbf{T}_{\mathrm{calculated}}$ are temperature evolution measured by the A-FO DTS and the equation. It must be noted that, $\Delta \mathbf{T}_{\mathrm{A-FODTS}}$ must be corrected for the heat storage effect before being used to estimate the flux (q).

3.3.2 Hydraulic tomography using PCGA

Estimating the hydraulic conductivity from a limited number of data represents an inverse problem in which a set of error-contaminated observation data (**d**) is used to infer the model parameters (**m**). A mathematical model (f (-)) describing the problem's physic by mathematical terms relates the model parameters to observation data. The forward problem is formulated as follow:

$$\mathbf{d} = f(\mathbf{m}) + \eta,$$

Equation 3:4 – Formulation of the inverse problem

where **d**, f (-), **m** and **η** refer to measured data, forward model, model parameters and errors, respectively. Due to the small number of observations compared to the unknowns, the problem is ill-posed and underdetermined and would have a non-unique solution. The solution would be obtained by maximizing the posterior probability density function ($\pi_{post}(\mathbf{m}|\mathbf{d})$) which is written by using Baye's theorem as follow

$$\pi_{\mathrm{post}}(\mathbf{m}|\mathbf{d}) \sim \exp[\frac{-1}{2}(f(\mathbf{m}) - \mathbf{d})\mathbf{C}_{\mathrm{d}}{}^{-1}(f(\mathbf{m}) - \mathbf{d}) + \frac{-1}{2}(\mathbf{m} - \mathbf{m}_{\mathrm{prior}})\mathbf{C}_{\mathrm{m}}{}^{-1}(\mathbf{m} - \mathbf{m}_{\mathrm{prior}})]$$

Equation 3:5 – Posterior probability density function expressed by Bayes theorem

where $\mathbf{C_m}$ and $\mathbf{C_d}$ are the a priori model covariance and data covariance matrix, respectively. In practice, the term in the bracket is maximized. The first term in the bracket is the likelihood and the second term is prior information. The solution obtained by maximizing the posterior probability density function corresponds to the model parameters that best estimates the observed data while is constrained to prior information to have a plausible and meaningful solution (Carrera and Neuman 1986a).

Geostatistical inversion is one of the methods that is used extensively for hydraulic tomography (Illman et al., 2015). In this approach, prior information is provided by the geostatistical information. The model parameter in each iteration is obtained as follow:

$$\mathbf{m}_{i+1} = \mathbf{X}\boldsymbol{\beta}_i + \mathbf{C}_{\mathrm{m}}\mathbf{J}_i{}^{T}\boldsymbol{\varepsilon}_i,$$

Equation 3:6 – model parameter at each iteration

here $\mathbf{X}$, $\boldsymbol{\beta}$ is trend matrix and trend coefficient, respectively. The multiplication of the trend matrix and trend coefficient defines the mean of the model parameter field. $\mathbf{C_m}$ is the prior model covariance, **J** represents the Jacobian matrix, which is the sensitivity of the observation to the change of model parameters. $\boldsymbol{\varepsilon}$ is a parameter which is obtained along with $\boldsymbol{\beta}$ by solving the following system of equations:

$$\begin{bmatrix} \mathbf{J}_i\mathbf{C}_{\mathrm{m}}\mathbf{J}_i{}^T + \mathbf{C}_{\mathrm{d}} & \mathbf{J}_i\mathbf{X} \\ (\mathbf{J}_i\mathbf{X})^T & 0 \end{bmatrix} \begin{bmatrix} \boldsymbol{\varepsilon}_i \\ \boldsymbol{\beta}_i \end{bmatrix} = \begin{bmatrix} \mathbf{d} - f(\mathbf{m}_i) + \mathbf{J}_i\mathbf{m}_i \\ 0 \end{bmatrix}$$

Equation 3:7 – system of equation to find the trend matrix and coefficient

The computation of Jacobian matrix has always been a challenge specially for large number of unknowns. Lee and Kitanidis (2014), proposed the PCGA method which forms low rank approximation of prior covariance matrix by principal components analysis and skips direct calculation of Jacobian matrix and its products used in equation 3:7. PCGA reduces the inversion computational time while preserving the most of the model parameter characteristics provided that proper number of principal component is chosen. Considering *P* number of principal components, the terms used in the equation 3:7 is approximated by:

$$\mathbf{C}_{\mathrm{m}} \approx \mathbf{C}_{\mathrm{m}P} = \sum_{\mathrm{ii}=1}^{P} (\boldsymbol{\varsigma}_{\mathrm{ii}})(\boldsymbol{\varsigma}_{\mathrm{ii}})^T, \qquad \text{(a)}$$

$$\mathbf{J}_{\mathrm{i}}\mathbf{C}_{\mathrm{m}} \approx \mathbf{J}_{\mathrm{i}}\mathbf{C}_{\mathrm{mP}} = \mathbf{J}_{\mathrm{i}} \sum_{\mathrm{ii}=1}^{P} (\boldsymbol{\varsigma}_{\mathrm{ii}})(\boldsymbol{\varsigma}_{\mathrm{ii}})^T = \sum_{\mathrm{ii}=1}^{P} (\mathbf{J}_{\mathrm{i}}\boldsymbol{\varsigma}_{\mathrm{ii}})(\boldsymbol{\varsigma}_{\mathrm{ii}})^T, \qquad \text{(b)}$$

$$\mathbf{J}_{\mathrm{i}}\mathbf{C}_{\mathrm{m}}\mathbf{J}_{\mathrm{i}}{}^T \approx \mathbf{J}_{\mathrm{i}}\mathbf{C}_{\mathrm{mP}}\mathbf{J}_{\mathrm{i}}{}^T = \sum_{\mathrm{ii}=1}^{P} (\mathbf{J}_{\mathrm{i}}\boldsymbol{\varsigma}_{\mathrm{ii}})(\mathbf{J}_{\mathrm{i}}\boldsymbol{\varsigma}_{\mathrm{ii}})^T, \qquad \text{(c)}$$

$$\mathbf{J}_{\mathrm{i}}\boldsymbol{\varsigma}_{\mathrm{ii}} \approx \frac{1}{\delta}[f(\mathbf{m}_{\mathrm{i}}+\delta\boldsymbol{\varsigma}_{\mathrm{ii}})\text{-}f(\mathbf{m}_{\mathrm{i}})]\,. \qquad \text{(d)}$$

Equation 3:8 – Approximation of the terms used in geostatistical inversion by *P* number of principal components by PCGA

where, $\mathbf{C}_{mP}$ is a rank-*P* approximation of the model parameter covariance matrix. The $\mathbf{C}_{mP}$ and Jacobian matrix products required for the inversion (equation 3:8) are given by equations 3:8 (b) and (c). The choice of the finite difference interval δ is addressed by Lee and Kitanidis (2014). The posterior covariance matrix is calculated as follow:

$$\mathbf{v}_{jj} = \mathbf{C}_{\mathrm{m}\,jj} - \begin{bmatrix} (\mathbf{JX})_j \\ \mathbf{X}^T \end{bmatrix}^T \begin{bmatrix} \mathbf{J}\mathbf{C}_{\mathrm{m}}\mathbf{J}^T + \mathbf{C}_{\mathrm{d}} & \mathbf{JX} \\ (\mathbf{JX})^T & 0 \end{bmatrix}^{-1} \begin{bmatrix} (\mathbf{JX})_{\mathrm{j}} \\ \mathbf{X}_{\mathrm{j}}{}^T \end{bmatrix},$$

Equation 3:9 – posterior covariance matrix

where $\mathbf{C}_{mjj}$ represents the j^{th} diagonal entry of the model covariance matrix and $(\mathbf{JX})_j$ is the j^{th} column of the product **JX**.

3.3.3 Groundwater flow modeling

The incompressible fluid flow module in MRST (Lie, 2019) is used to create a numerical model corresponding to forward mathematical models used for the inversion. The model is used to calculate the head and flux data at different points across the aquifer. The steady-state flow of incompressible fluid is formulated as follow:

$$-\nabla.[\boldsymbol{K}(\mathbf{w}).\nabla h(\mathbf{w})] = \mathbf{q}(\mathbf{w})\,,$$

Equation 3:10 – groundwater flow equation

subjected to no-flux condition at the side and bottom boundaries, and head-dependent flux at the surface (leaky-layer). In the head-dependent flux boundaries, which are also called the mixed boundary, the rate of flux fed to the system varies according to the head change in the boundary elements. Note that in this aquifer system, the water is being fed into the system from the top layer as the head drops in the aquifer due to the pumping.

$$-\mathbf{q}.\mathrm{n} = 0, \text{for } \vec{\mathbf{w}} \in \Gamma_a$$

$$\mathrm{C}(h_{\mathrm{ref}} - h) = \mathrm{q}_0, \text{ for } \vec{\mathbf{w}} \in \Gamma_b$$

here, $\mathbf{w}$ = (*x, y, z*), $\boldsymbol{K}$ (L/T), h (L), and $\mathbf{q}$ [L/T] represent the coordinates, hydraulic conductivity, head and fluid source or sink (inflow or outflow of fluid per volume at specific locations), respectively. Γ_a and Γ_b represent Dirichlet and Cauchy boundaries. In order to define the the rate of transfer through leaky-layer two parameters are needed, C (L^2/T) which accounts for the transmissivities of the leaky-layer and h_{ref} (L) which is reference head at the top of the layer. q_0 (L^3/T) represent the rate of the fluid fed into the system.

3.4 Field data analysis

In this section, we explain processing of the temperature data recorded during the heating period and how they are converted to the flux profile. We also present the pressure drops recorded in different boreholes. Final subsection is devoted to explain the model and parameters used for inversion of the flux and pressure data.

3.4.1 Temperature data acquired in FO-17 and FO-18

Figure 3-7 shows the raw temperature evolution curve obtained during the heating period in FO-18 cables. This temperature is corrected for the background temperature of the aquifer recorded during the passive measurement.

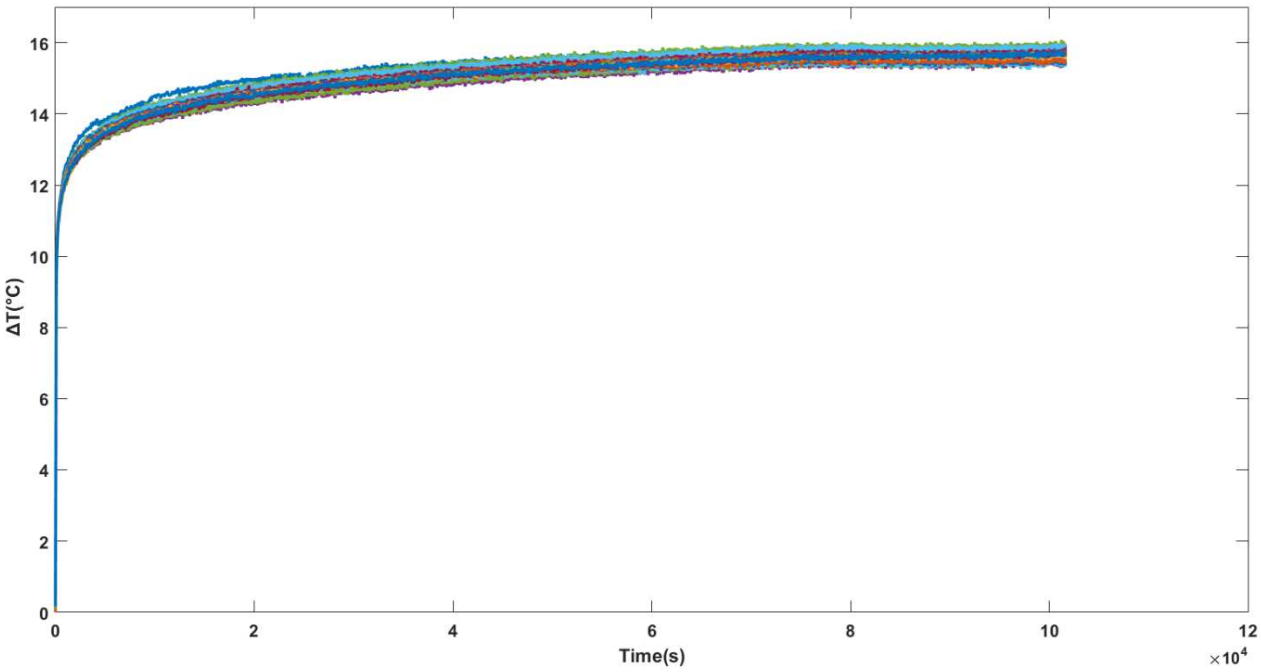

Figure 3-7: Temperature evolution curves in FO-18 cable. Each colour corresponds to one point along the FO cable. Different colors correspond to different points along the FO-cable

3.4.1.1 Temperature data quality check and calibration

The quality of the temperature data acquired by FO-DTS was assessed by comparing the FO section immersed in the hot and cold bath with the RBR solo temperature data. DTS unit performs an internal calibration (using PT-100 temperature as reference temperature) and it was found out the temperature data was imperfectly calibrated due to the malfunctioning of PT-100 in hot and cold baths. So we used the temperature data recorded by RBR solo in hot and cold bath as the reference temperature to improve calibration. For the calibration, we relied on the code developed by des Tombe et al. (2020) who provide a code allowing double end calibration with post-processing. The calibrated data were then used to quantify the flux at different depths. Nevertheless, figure 3-7 shows that the temperature difference and evolution between the different data points is relatively small, even at the end of the heating period. Therefore, one excepts small difference in groundwater fluxes measurements with depth.

3.4.1.2 Temperature data to flux profile

The temporal temperature evolution data obtained by FO-17 and FO-18 during the heating period (measured every 25 cm along the heating cable) is converted to the flux using equations 3:1 to 3:3. As already explained, the inversion of the temperature measured in each segment to the flux data comprises three steps:

(i) Finding the thermal conductivity value (λ) from the slope of temperature evolution data during the conduction-dominant period in semi-log plot and equation 3:2.

(ii) Correction of the fiber optic storage effect. In the early times of heating, FO temperature data increases due to heat storage in the FO cable and does not represent the temperature evolution that is only due to the conductive and advective heat exchanges with porous media. All of the equations presented so far are valid neglecting the effect of the fiber optic cable itself. The following relationship holds (Simon et al., 2021; Del Val et al., in press):

$$\Delta\mathbf{T}_{\mathrm{A-FODTS}} = \Delta\mathbf{T}_{\mathrm{PorousMedia}} + \Delta\mathbf{T}_{\mathrm{FO}}\ ,$$

Equation 3:11 – relationship between recorded temperature data, the temperature evolution associated with heat exchanges with the porous media and the temperature increase due to heat storage in the fiber-optic cable

One can use equation 3:2 to generate $\Delta\mathbf{T}_{\mathrm{PorousMedia}}$ during the conduction-dominant period by using thermal conductivity (λ, obtained in previous step) and assuming a proper volumetric heat capacity of the saturated media (ρc). The difference between generated $\Delta\mathbf{T}_{\mathrm{PorousMedia}}$ and $\Delta\mathbf{T}_{\mathrm{A-FODTS}}$ during the conduction-domiant period is almost equal to $\Delta\mathbf{T}_{\mathrm{FO}}$. So the whole temperature data can be corrected for obtained $\Delta\mathbf{T}_{\mathrm{FO}}$.

(iii) The temperature data corrected in previous step is used to infer the groundwater flux profile using equation 3:3 and the objective function defined previously.

Figure 3-8 shows an example of the correction of the $\Delta\mathbf{T}_{\mathrm{A-FODTS}}$ and finding $\Delta\mathbf{T}_{\mathrm{FO}}$ and $\Delta\mathbf{T}_{\mathrm{PorousMedia}}$. The black curve shows the temperature data recorded by FO cable at one point. The blue curve shows the corrected temperature data for FO cable storage effect and the red curve shows the temperature matched to infer the value of groundwater flux at this point.

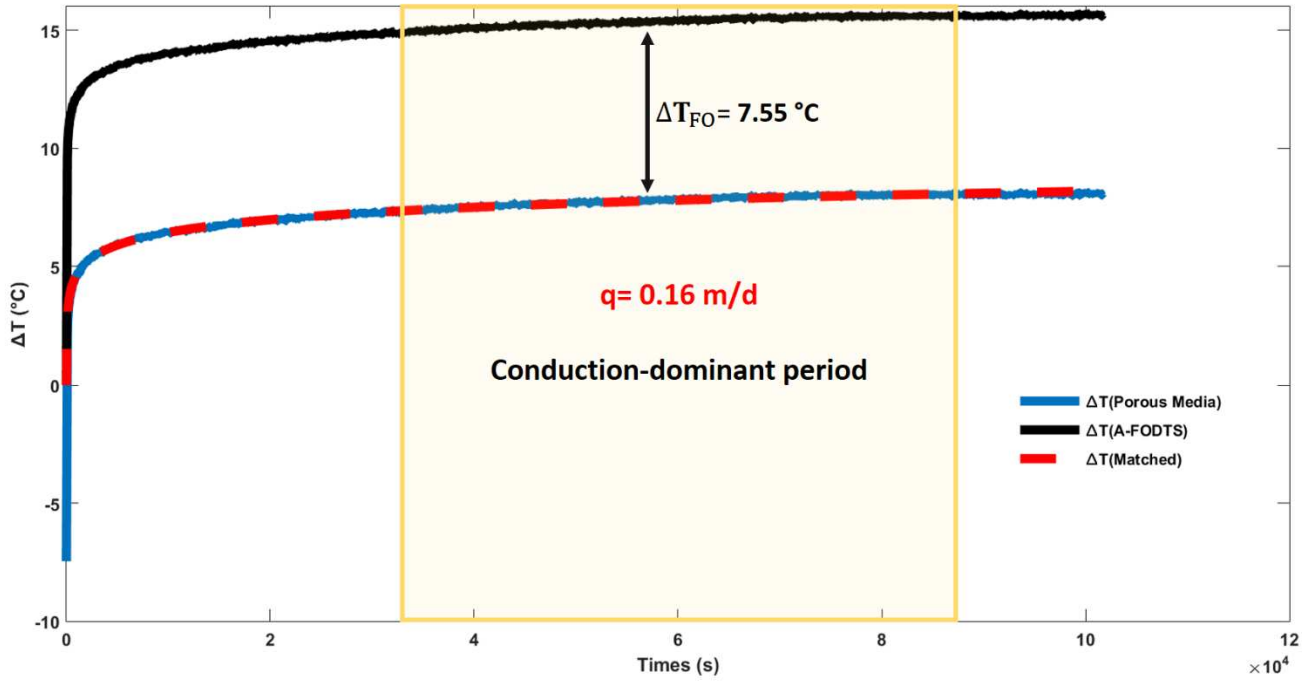

Figure 3- 8: An example illustrating the correction of acquired temperature data for FO cable storage effect and matching the corrected temperature data to infer groundwater velocity.

The three steps mentioned above are repeated for all data points, and thus, the flux profile with depth is obtained. It should be noted that measurements are performed every 25 cm (sampling resolution) along the FO-cable, while the spatial resolution can be much larger. Simon et al. (2020) used the same FO cable in a laboratory controlled experiment and found out the spatial resolution varies from 0.5 to 0.8 m depending on the DTS unit used. Thus we upscaled every two groundwater flux values into one value by averaging the two successive flux values. This reduces the number of observations, but this is more consistent with the effective spatial resolution in the field (Simon et al., 2020). Figure 3-8 shows the flux profile obtained in FO-17 and FO-18 by using the equations and the three-step procedure explained.

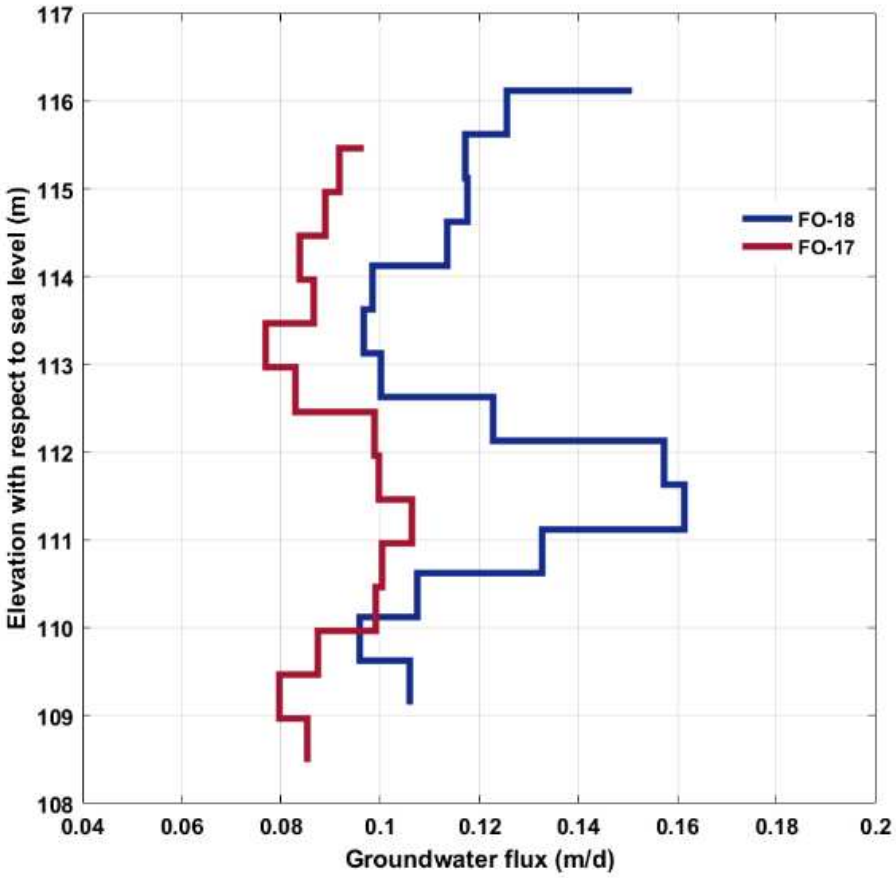

Figure 3-9: Groundwater flux measured in two FO-cable locations (FO-17 and FO-18)

Figure 3-9 shows that as expected, the range of estimated groundwater flux variation is small. Considering uncertainties in the measurements, some of the difference may not be significant. Nevertheless, we can see almost the same trend for groundwater fluxes profile estimated from FO-17 and FO-18. The trend is also consistent with hydraulic conductivity trend previously presented in figure 3:3(a). In figure 3:3(a), we see a high conductivity region bounded between the elevation of 113 and 109 m for borehole P17 which can be also seen in flux profile derived by FO-17 as well.

To further check the consistency of the results, we also used the characteristic time t_d to quantify the value of the flow for few points in FO-18. Due to relatively low values of the hydraulic conductivity in this site, we expected low value of water flux and long time to reach steady-state condition. Due to technical problems already discussed, it was not possible to heat long enough to reach temperature stabilization. Thus, we could only detect the end of conduction-dominant period. Figure 3-8 shows two examples, one with high flux (at 111.5m) and the other with low flux (at 113 m) on the FO-18. The values of high flow and low flow obtained by using characteristic time td are 0.18 (m/d) and 0.13 (m/d) while the values obtained by computer code for high and low flows are 0.16 (m/d) and 0.1 (m/d), respectively. Thus, the estimation of groundwater fluxes using the analytical method (figure 3.9) seems to be consistent with the estimation provided by characteristic times (figure 3.10).

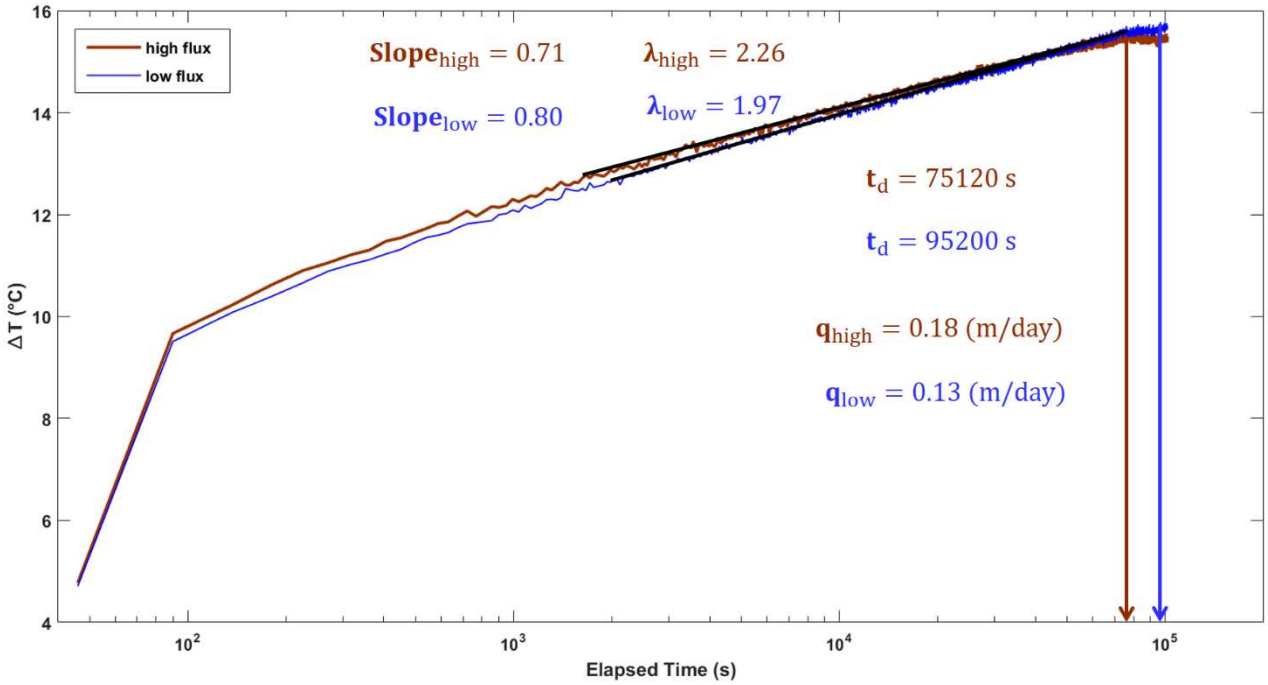

Figure 3-10: The values of thermal conductivity and flow obtained using characteristic time (t_d) for two points in FO-18.

It should be noted that end of conduction-dominated time (t_d) determination is possible for the point with higher groundwater flux value (red curve) while it is more challenging for the point with low groundwater flux value (blue curve). This is due to the fact that for low flux point, it takes longer to depart from the conduction-dominant period compared to high flux point. The fact that data are noisy makes it more complicated to detect this point. Nevertheless, we can see that the groundwater flux values obtained from characteristic times are almost in the same range as the values obtained by using the equations and three steps explained. For the rest of the work we assume that the groundwater flux profile obtained is valid and represents the real groundwater flux in the aquifer so that it can be used in the inversion process to test the information content of these data.

3.4.2 Head data in packer-isolated and open boreholes

The boreholes P17 and P18 are equipped with packers to isolate and measure the head in different intervals. Four pressure sensors are located in different intervals in P17 and P18. Each of other four open boreholes are also equipped with one pressure sensor. Table 3-1 presents the location and position of the pressure sensors and also the value of the head drop as the system reaches steady-state.

Table 3-1: Location of pressure sensors and values of head drop recorded

Borehole name	Elevation of the sensor with respect to sea level (m)	Head drop (m)
P17	114.53	0.1
P17	113.63	0.35
P17	112.46	0.32
P17	111.29	0.39
P18	115.49	0.12
P18	114.62	0.22
P18	113.75	0.46
P18	112.24	0.49

P20	112.93	0.54
P19	113.63	0.2
3P0A	112.76	0.29
3P0B	113.28	0.48
P21	-	1.95

The recorded head data by different sensors for two boreholes with packers (P17 and P18) are shown in figure 3-11. Each curve corresponds to one pressure sensor that is employed in the elevation mentioned.

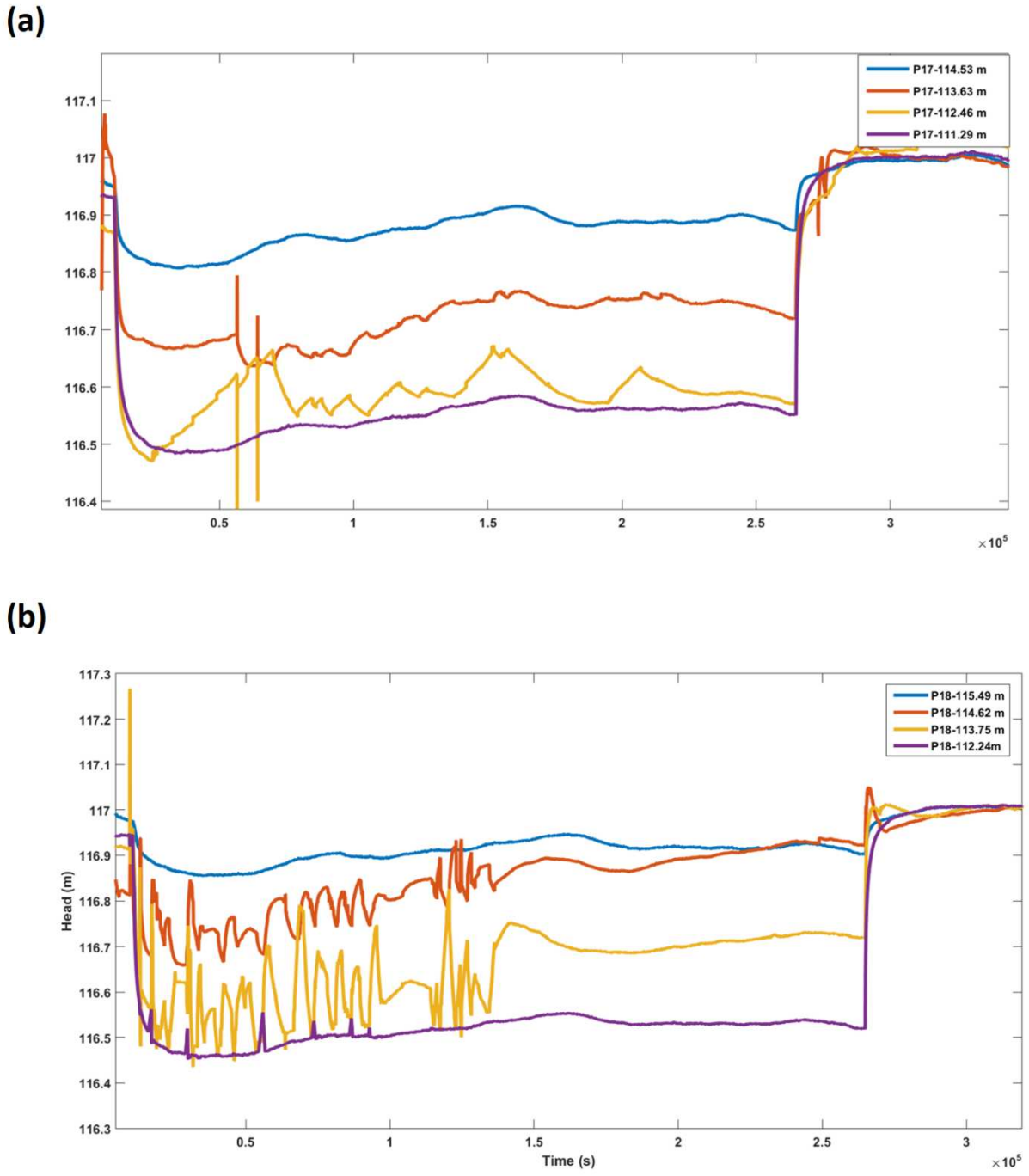

Figure 3-11: Head data recorded in (a): borehole P17 and (b): P18 which are equipped with packers. Numbers in the legend corresponds to the elevation where sensors are placed.

It is worth mentioning that we can see data are not perfectly recorded and we see fluctuations in the middle of the pumping for two successive sensors both in P17 and P 18 which might be related to technical issues with the pressure sensors or the packer setup. The values of the head drop reported in Table 3-1 is the average of the head drop over the time, once water level has more or less stabilized.

3.4.3 Setup of the inverse model and hydraulic tomography

The PCGA inversion algorithm was implemented in python coupled with MRST in Matlab as the forward model. The 3-D aquifer model is 112.5 m in length, 112.5 m in width, and 11.5 m in depth, discretized to 75×75×23 in x-, y- and z- directions with the block size of 1.5 m × 1.5 m × 0.5 m, respectively. The pumping borehole is located at the middle of the aquifer, far away from the boundaries to reduce the boundary effect on the inversion. Figure3-4 shows the relative location of the boreholes. The model simulates the steady-state head drop at the borehole locations. All side and bottom boundary conditions are set to no flow, while the upper boundary condition is considered as the head-dependent flux. This type of boundary was previously recognized by the pumping tests performed at the site. Furthermore, based on figure 3-11, we see that upper layers have higher head than lower layers which would support our assumption of head-dependent flux boundary condition at the surface (leaky layer). To simulate this boundary, a constant head value of 117 m was applied to the upper face of the first layer and first layer properties were also considered unknown values. It should be noted that two assumptions are made, (i): the vertical flow of the water passing through the heated FO cable does not affect the results significantly, (ii): the vertical hydraulic conductivity in each grid block is equal to 0.1 of its horizontal hydraulic conductivity. We relied on the data obtained from cone penetration tests performed at different aquifer locations to extract the geostatistical information about the site, which are further used in the inversion algorithm. The “variogramfit” written in Matlab by Schwanghart (2021) was used to fit a model to the experimental data. The fitted variogram model is Gaussian with the range of 7 m in horizontal direction and 2m in vertical direction with value of 0.2 for sill. Table 3-2 summarizes model and inversion parameters.

Table 3-2: Aquifer model and inversion parameters

Parameters	Value
Aquifer model dimension	112.5×112.5×11.5 (m)
Number of grids	75×75×23
Covariance Kernel	Gaussian
Prior variance	0.2
Correlation length (x, y, z)	7, 7, 2 (m)
Measurement error (STD)	0.01 (m), 0.01 (m/d)
Number of principal components (*P*)	1200

3.5 Preliminary results

The inversion is performed once with pressure data and once jointly with pressure and flux data. The inversion was performed on a server with one Terabyte (1 Tb) memory, 4 processors (Intel Xeon CPU E7-4850 v4 @ 2.10 GHz) and 50 cores in parallel mode. Each geostatistical iteration took around 8 hours. The inversion started with a homogenous distribution of the *Y*-field with value equal to -5. The number of principal component (*P*) used for the inversion is 1200. However, additional inversion with P=2000 was tested and

it was found that the estimation accuracy did not change significantly while the run time per one geostatistical iteration increased from 7 hours to 20 hours. In the following, we first show the inversion results with pressure only and then present the result for joint inversion of the pressure and flux data.

3.5.1 Hydraulic tomography with pressure data

The best estimate of the Y-field estimation when using only pressure data is presented in figure 3-12. The uncertainty of the estimated Y-field is also shown in figure 3-13. The degree of fitting observed head drop versus simulate head drop is shown in the figure 3-14. Figure 3-12 predicts low conductivity region for shallow layers and a moderate conductivity region in the middle of the aquifer. It should be noted that for layers below 109.5 m, estimates have a high uncertainty due to the fact the pressure data are only available above this depth (boreholes are screened up to here).

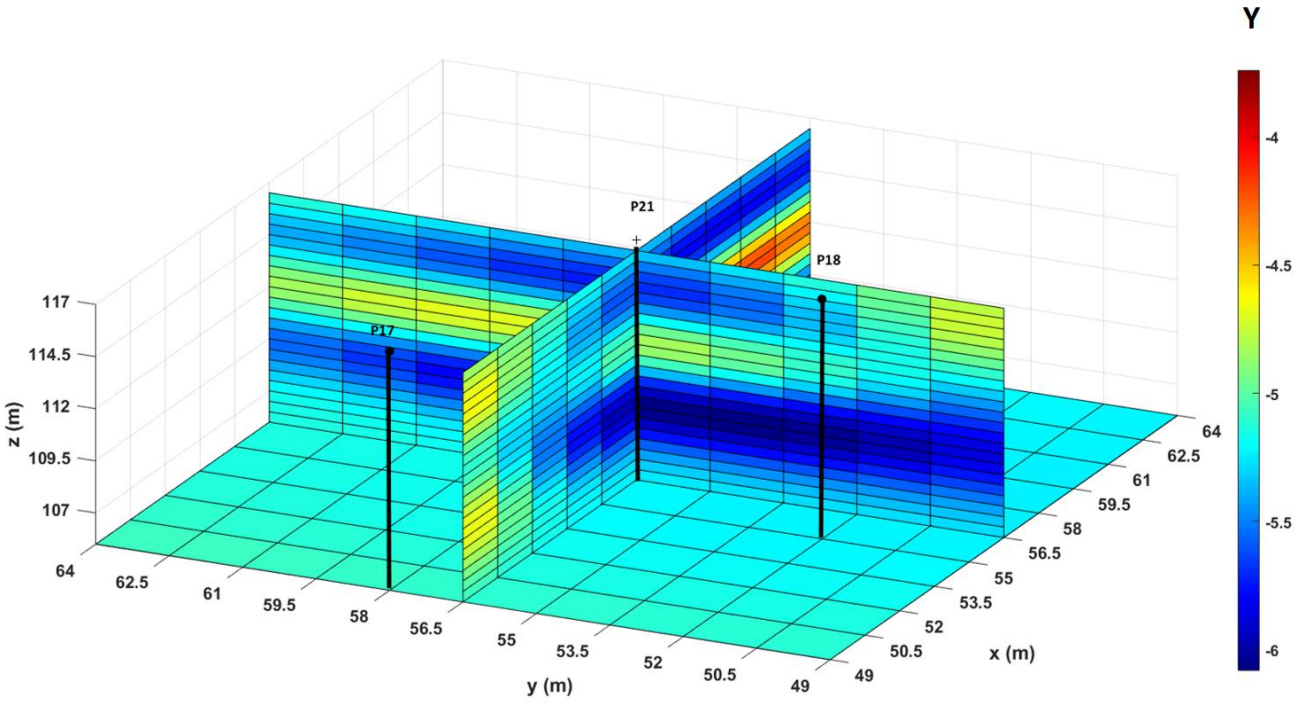

Figure 3-12: Y-field estimation using pressure data only

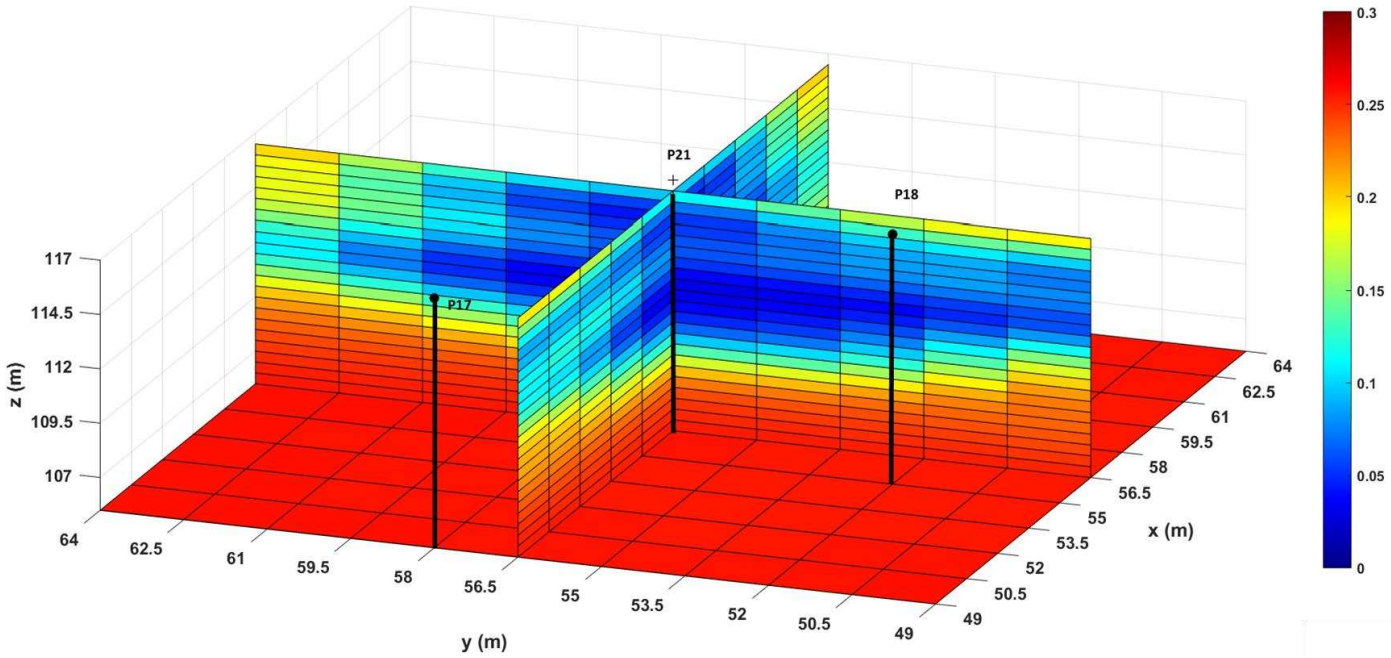

Figure 3-13: Y-filed estimation uncertainty (standard deviation of the hydraulic conductivity estimate)

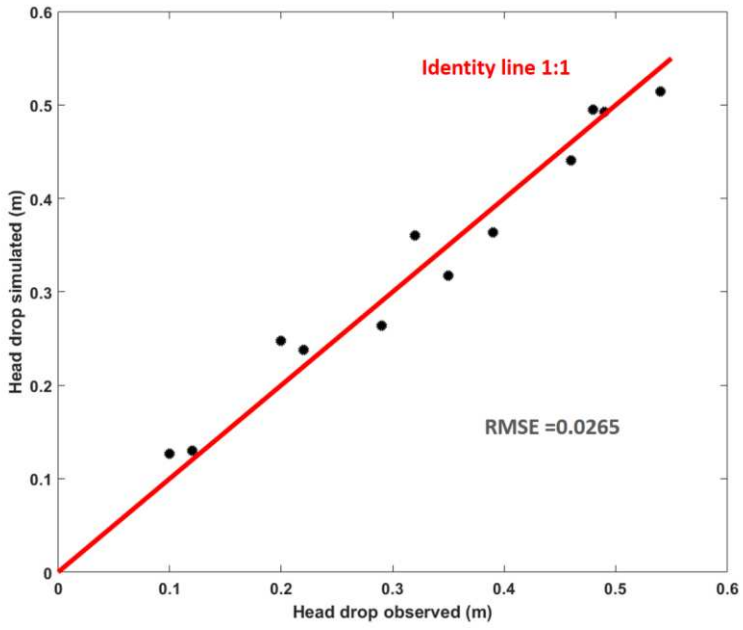

Figure 3-14: Data fitting for inversion of pressure data only

Furthermore, it worth noting that the hydraulic conductivity trend which was shown in figure 3-3 (a) for borehole P17 by cone penetration test can also be seen in the hydraulic conductivity map shown in figure 3-13 at P17 location. Figure 3-14 also shows that observed head drop data are satisfactorily reproduced by the simulation.

3.5.2 Hydraulic tomography jointly with flux and pressure data

Figure 3-15 shows the *Y*-field estimate using joint head and flux data. Using flux data along in addition to head data can lead to more detailed hydraulic conductivity map. This is certainly due to a higher number of observations which lead to constrain more the model, but also to the availability of regular flux data even at lower depths, below the bottom of borehole screens.

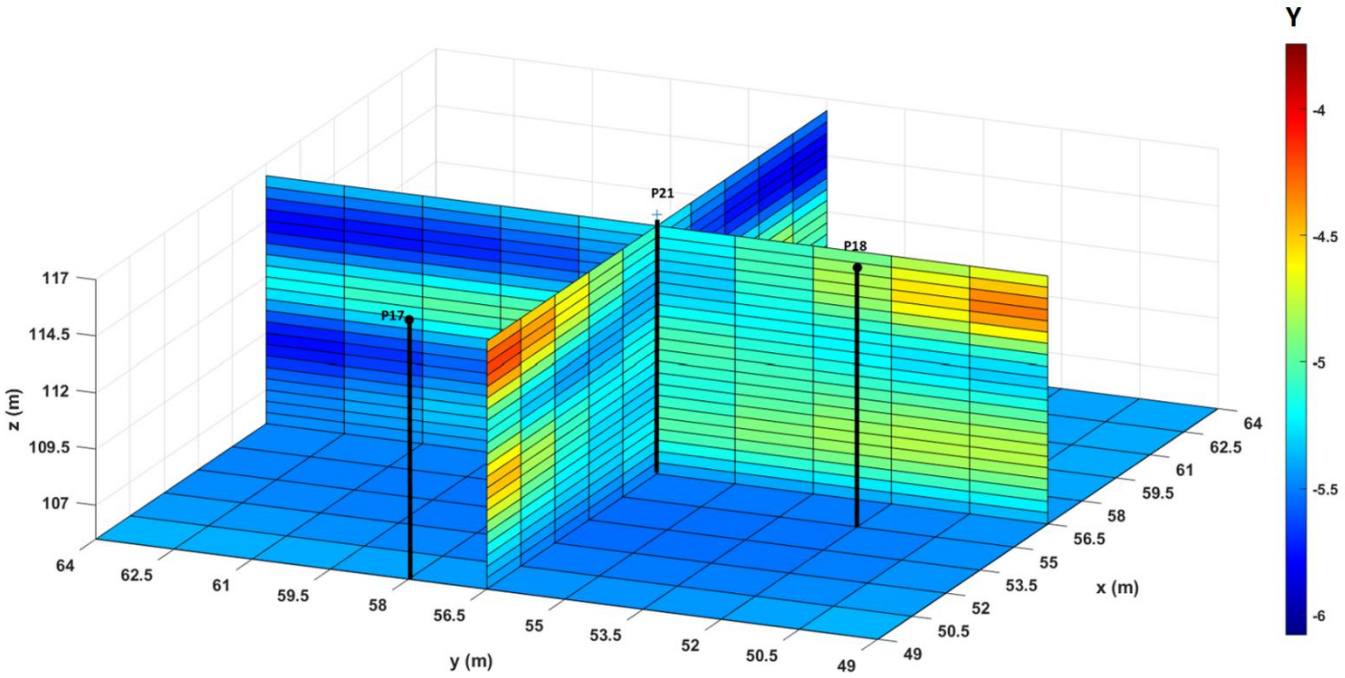

Figure 3- 15: Y-field estimation using joint inversion of head and flux data

It can be seen that for layers below 109.5m, we do not see the low hydraulic conductivity region that we were previously observing. Furthermore, at P17 location, the hydraulic conductivity trend is the same as hydraulic conductivity obtained by pressure data only (figure 3-12) and also the hydraulic conductivity estimated by cone penetration test shown in figure 3-3(a).

Figure 3-16 shows the uncertainty associated with the *Y*-field estimation by joint inversion of head and flux data.

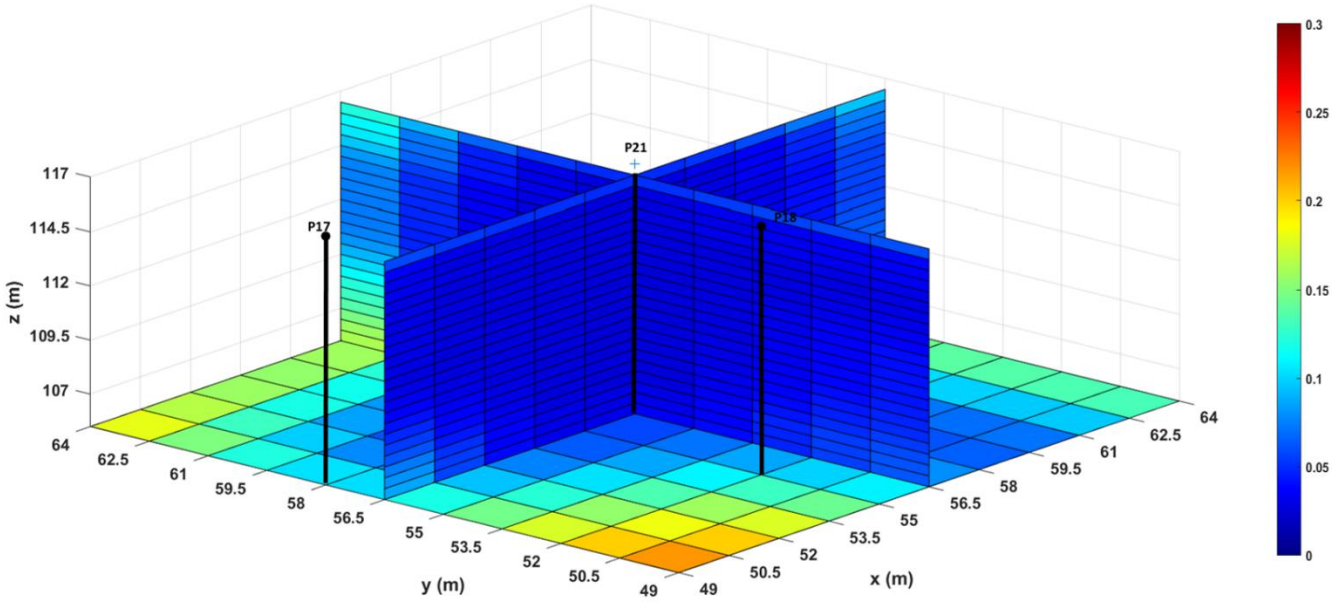

Figure 3- 16: Y-field estimation uncertainty (standard deviation of the hydraulic conductivity estimate) using head and flux data

We clearly observe that including the groundwater flux profile in the inversion reduced the Y-field estimation uncertainty, which is not the case for inversion with pressure data only. The advantage of groundwater flux measured by A-FO DTS is that using a single measurement point, we can obtain many observations along the cable and constrain more the inversion model, which is not easily achieved by pressure sensors.

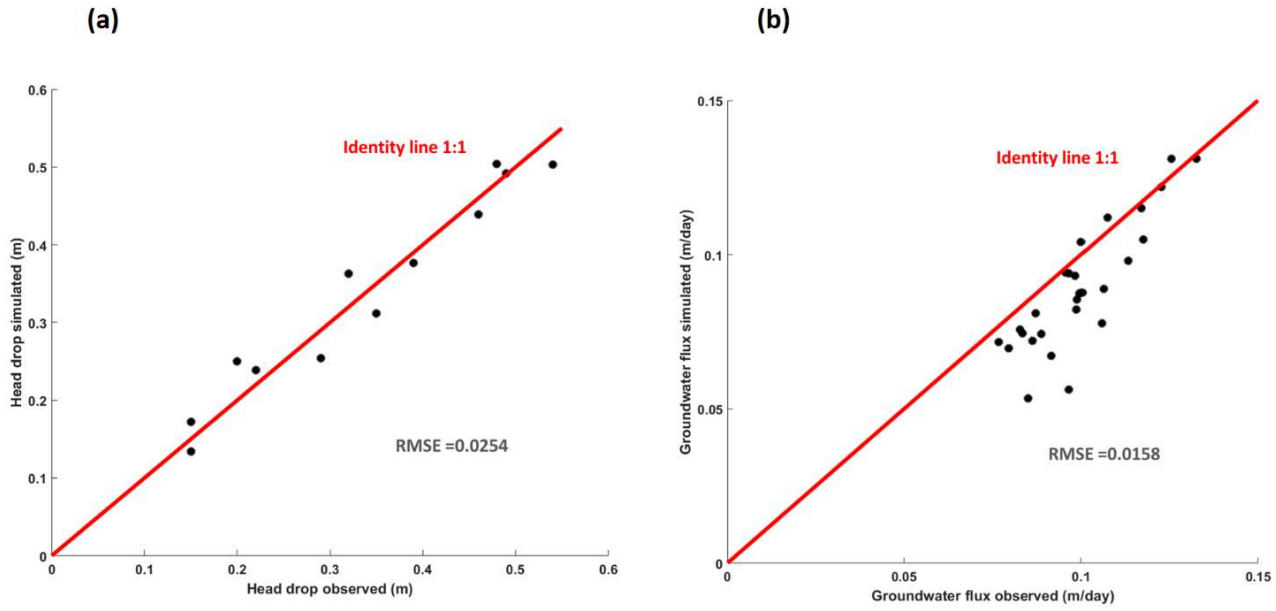

Figure 3- 17: Data fitting in the joint inversion for (a): head data and (b): flux data

Figure 3-17 shows the fitting of the head drop and head drop simulated. It can be seen that reproducing the observed flux data is more challenging compared to the head data, especially for small flux values.

3.6 Discussion and conclusions

3.6.1 General findings

In the current work, a novel hydraulic tomography approach using groundwater flux profile and head data is presented. The Saint-Lambert site near Quebec-city which hosts a decommissioned landfill sanitary is chosen to perform the hydraulic tomography experiment. The groundwater flux profile is measured by Active FO-DTS cable which were buried vertically into the shallow granular aquifer by use of direct-push method two months before the start of the experiment to ensure the maximum contact of the formation with the buried cable. The aquifer has 7 boreholes, one in the middle and 6 others on the side. The aquifer is subjected to the pumping through the central borehole and head is measured in 4 open boreholes and two boreholes equipped with packers. After 19 hours of pumping and making sure steady-state hydraulic condition is reached, heat is added to the fiber optic cable to start A-FO DTS mode in the two buried FO cables. The effective heating period for FO cables which can be used for flow profiling, is around 28 hours which was not sufficient to reach temperature stabilization (advection-dominant period). The temperature data obtained during heating period are quality-checked, calibrated and then used to infer the groundwater flux along the FO cable. The head data recorded during the steady-state hydraulic condition period is used for hydraulic tomography. The result of *Y*-field estimate using head data present some trends of moderate and low hydraulic conductivity regions. However, the uncertainty of the *Y*-estimate is high below a certain depth where boreholes are not screened and no data is provided. On the other hand, inversion of both flux and head data jointly results in a more detailed heterogeneity structure thanks to the inversion of the groundwater flux profile. We can also see that uncertainty of the estimation has been also reduced in the zones where head data could not have been provided due to the limitation with borehole depths. The groundwater flux profile measured by FO cables provides many observations by a single measurement point, which minimizes the subsurface intrusion for collecting data while providing valuable information about the subsurface. The density of information provided by FO cables is harder to be obtained by head data, which many packers and many pressure probes to be utilized.

3.6.2 Field application implications

This novel experiment relies on using FO cables to measure the groundwater flux profile. FO cables are embedded inside the rod of the direct-push tool and inserted into the ground. It is important to leave the cable in the ground for sometimes to let the formation surround the cable perfectly. This is done to have the FO cable in close contact with the formation and reduce the disturbance of the formation and also the flow field. Observations with FO cables are beneficial in the sense that FO cable disturbs less the media. One more point is the proper design and planning of the experiment. The proper heating time must be chosen based on the expected groundwater flow velocity in the aquifer which would be calculated by the knowledge from the aquifer hydraulic conductivity range and also induced hydraulic gradient by pumping. Sufficient heating period is required to achieve a trustable and easily interpretable results. Some guides about the required heating time based on groundwater velocity is provide by Simon et al. (2021). As the last point, based on the experiment design, if the plan lasts for many hours, you must think of additional and emergency power supply for pump, DTS and heat pulse system in case of sudden power shortage. It is also strongly recommended to use extra accurate temperature probes for calibration and quality check of acquired temperature data by FO-DTS.

3.6.3 Perspective works

This work assumes that the vertical flow is negligible while it is evident by having a leaky-layer at the top, water is charged vertically into the aquifer, which also may affect the response of the temperature evolution with time. A numerical model is required to how effective it is and whether it shall be taken into account. Another main assumption is the vertical conductivity value, which is considered to be 0.1 of its horizontal conductivity. For such a system in which water is being charged from the top layer to the aquifer, the vertical hydraulic conductivity plays an important role. So in the next step, we will also assume the vertical hydraulic conductivity as unknown and estimate its values and distribution.

ACKNOWLEDGMENTS

This work has received funding from the European Union's Horizon 2020 research and innovation program under the Marie Sklodowska - Curie grant agreement number 722028 (ENIGMA ITN). We would like to thank Cynthia Lee, Benyamin Shariatinik and Aymen Nefzi for their help during the experiment.

Chapter 4 Modeling borehole flows from Distributed Temperature Sensing Data to monitor groundwater dynamics in fractured media

This chapter has been submitted for possible publication in Journal of Hydrology

This paper has been prepared at University of Rennes 1 and we benefited from H+ Plomeur observatory site. In this paper,we show how distributed temperature sensing data in the borehole can be used to quantify the contribution of each fracture to the flow in the borehole and capture the dynamic response of the aquifer with time.

Behzad Pouladi[1*], Olivier Bour[1], Laurent Longuevergne[1], Jérôme de La Bernardie[1], Nataline Simon[1]
1 Univ Rennes, CNRS, Géosciences Rennes, UMR 6118, 35000 Rennes, France.

4.1 Abstract

Fractured aquifers are known to be very heterogeneous with complex flow path geometries. Their characterization and monitoring remain challenging despite the importance to better understand their behavior at all spatial and temporal scales. Heat and, correspondingly, temperature data have gained much interest in recent years and are often used as a tracer for characterizing groundwater flows. In the current work, a fast computer code has been developed using Ramey and Hassan & Kabir analytical solutions which converts the temperature profile to the flow rate profile along the borehole. The method developed has been validated through numerical simulations. A global sensitivity study recognizes the media thermal properties as the most influential parameters. For testing the method in the field, fiber-optic distributed temperature sensing (DTS) data were used to monitor the dynamic behavior of fractured aquifers at the borehole scale at the Ploemeur-Guidel field site in Brittany, France. DTS data were used to infer the flow rates in the different sections of a fractured wellbore (flow profile) and calculate the contribution of each fracture to the total flow. DTS data were acquired for about three days in three different hydraulic conditions corresponding to two different ambient flow conditions and one pumping condition. Flow profiling using distributed temperature data matches satisfactorily with results from heat-pulse flow metering performed in parallel for cross-checking. Moreover, flow profiling reveals the daily variations of ambient flow in this fractured borehole. Furthermore, it shows that during ambient flowing conditions, shallow and deep fractures contribute roughly equally to the total flow while during the pumping condition, the deepest fractures contribute more to the total flow, suggesting a possible reorganization of flow and hydraulic heads depending on the hydraulic conditions. The advantage of the proposed method (DTS data and proposed framework) is that it requires less time and effort and provides real-time monitoring of complex fracture interactions and recharge processes in fractured media. Thus, this method allows for a full analysis of the system's temporal behavior with a simple and fast analytical model. Furthermore, thanks to its narrow width, DTS can be used and installed in boreholes while heat-pulse flow metering may lead to head losses in the borehole and may not always be possible depending on some borehole conditions. One of the limitations the approach proposed is the proper knowledge of the thermal properties of media required to infer the flow rate from the temperature. Nevertheless, surface rate measurement can be useful to constrain these properties and reduce the flow profiling uncertainty. Thus, the method proposed appears to be an interesting and complementary method for characterizing borehole flows and groundwater dynamics in fractured media.

KEYWORDS: Fractured media, Borehole Flow, Flow Profiling, Distributed Temperature Sensing (DTS), Heat-Pulse Flow Metering (HPFM).

Nomenclature

Variables

w: Mass rate

H: Enthalpy

v: Fluid velocity

g: Gravitational constant

z: Depth

K_e: Thermal conductivity of the formation

c_p: Specific heat capacity

C_J: Joule-Thomson coefficient

f (t_d): Time function

L: Relaxation distance

Q: Heat

T_f: Fluid temperature

T_{ei}: Initial earth temperature

t_d: Dimensionless flow time

t: flow time

GG: Geothermal gradient

U_t: Overall heat transfer coefficient

p: Fluid pressure

r_{wb}: Borehole radius

4.2 Introduction

Crystalline rocks or basement are often characterized by a very low rock or matrix permeability but a relatively high fracture per-meability, which may enhance flow within aquifers (Roques et al., 2016). Thus, in such low permeability media, fractures are usually controlling flow within the aquifer through a network of more or less connected permeable fractures (Hsieh, 1998; Le Borgne et al., 2006). This makes flow characterization very challenging given the fact that flows are highly localized in a few frac-tures and may span few orders of magnitude depending on fracture permeability (Berkowitz, 2002; Novakowski et al., 2006). Among the established and numerous methodologies used for estimating fractured media hydraulic properties (Berkowitz, 2002; Day-Lewis et al., 2017), vertical borehole flow profiling has been developed to characterize fracture connectivity and hydraulic properties (Paillet, 1998; Le Borgne et al., 2006; Day-Lewis et al., 2011). The common practice for flow measurements is per-formed by using an impeller (Keys, 1990); heat-pulse flow meter (Hess, 1986; Paillet et al., 1987; Le Borgne et al., 2006), or elec-tromagnetic flowmeter (Molz et al., 1994). The two latter methods are particularly interesting for quantifying the relative contribution of the different fractures in ambient conditions to characterize how hydraulic head varies with depths within the borehole (Paillet, 1998). Alternatively, point dilution tracer tests allow obtaining a direct measurement of local groundwater fluxes or Darcy fluxes (Drost et al., 1968; Klotz et al., 1980; Pitrak et al., 2007; Novakowski et al. 2006; Jamin et al. 2015). Nevertheless, the re-quirement to perform classical dilution tests between packers for characterizing fractured media is a major issue that limits its use in the field.

Some other indirect methods have been developed to characterize borehole flows like for instance dissolved oxygen alteration (Vitale and Robbins, 2017), solute tracers (Michalski and Klepp, 1990), or from the analysis of the temperature profile (Klepikova et al., 2014). Temperature-based methods have been used for a long time in fractured rock hydrology (Silliman and Robertson, 1989; Keys, 1990). The main hypothesis is to assume that if heat advection occurs, due to fracture or borehole flows, the temperature profile should deviate from geothermal gradient that is controlled by heat conduction (Anderson, 2005). Thus, any anomaly or deviation from geothermal gradient can be used to infer fracture locations in the borehole and fracture connectivity (Silliman and Robertson, 1989; Keys, 1990; Pehme et al., 2010; Chatelier et al., 2011). In addition, Klepikova et al. (2011) recently showed that it is possible to deduce vertical flows in a borehole from temperature profiles that present a temperature gradient lower than the geothermal gradient. Their methodology was based on a numerical model of flow and heat transfer at the borehole scale and validated through the use of temperature profiles measured in different hydrogeological conditions. The method has been then extended successfully to propose a three-step inversion approach in which temperature profiles inside the boreholes are used to infer borehole flows and the inter-borehole fracture connectivity and transmissivity (Klepikova et al., 2014). Meyzonnat et al. (2018) proposed another approach based on the borehole scale heat budget, which is used for qualitative and quantitative interpretation of depth-temperature data to infer water origin and position of water inflows.

The emergence and promising advances of new temperature sensing technologies such as Distributed Temperature Sensors (DTS) which allows recording temperature along fiber-optic cables at an unprecedented spatial and temporal resolution, encouraged few authors to develop this technology for fractured rock hydrology (Read et al., 2013). In particular, few authors developed tempera-ture tests, where temperature anomalies are artificially induced, for the characterization of borehole flows in fractured aquifers. For instance, Leaf et al. (2012), Sellwood et al. (2015) and Read et al. (2015) used the injection of hot water or an electrical heater to infer water direction and velocities in a borehole in ambient and hydraulically stressed conditions. Read et al. (2014) used distributed temperature sensing (DTS) in combination with an electrically heated DTS cable to quantify vertical flows in a borehole. The temperature difference between a heating and non-heating cable was used to infer the fluid velocity variations with depths in the borehole. Coleman et al. (2015) proposed another approach in which a combination of Active DTS (A-DTS) tests with flexible liners was used to locate groundwater flow zones in a fractured aquifer. Recently, Maldaner et al. (2019) and Munn et al. (2020) extended this previous work to quantify depth-discrete flows during natural or artificial conditions in a sealed borehole using A-DTS.

Even though these methodologies are generally used to infer hydraulic properties of fractures either in ambient or hydraulically stressed conditions, but, to the best of our knowledge, they are not used for monitoring temperature variations in ambient conditions to detect some possible flow variations through time. Usually, flow in fractured media is characterized at a given time scale, assuming that such a characterization is representative of boundaries conditions. Some approaches at monthly or yearly time scales are common for studying annual recharge (Jimenez-Martinez et al, 2013), but are generally based on hydraulic head variations through time that is very integrative. Flow variations may reveal the sensitivity of the aquifer to changes in boundaries conditions that may be associated with groundwater recharge, tides, or other processes. Characterizing possible changes in boundaries conditions may be very useful since borehole flows are classically used to infer the distribution of fracture transmissivity along the borehole (Paillet, 1998; Le Borgne et al., 2006; Day-Lewis et al., 2011). Being able to monitor flow changes may also allow infer-ring characteristic response times of fractured media at varying depths. Such changes through time may also be crucial for characterizing mixing and biochemical reactivity in fractured media (Bochet et al., 2020).

Here, we are addressing the use of temperature data to monitor groundwater flows variations through time. We propose using fiber-optic DTS for continuously monitoring temperature data at a short time scale and for inferring borehole flow changes all along the borehole. To provide real-time monitoring of flows at different depths, we are using a framework based on analytical solutions for converting temperature data into flows, which can be much faster compared to numerical simulators while providing satisfactory results. Due to the high frequency of recorded temperature data, a fast interpretation framework is indeed required to capture the dynamic response of the media. In this paper, we intend to show: (i) the potential of using a simple analytical model to infer borehole flows from temperature data, (ii) the advantage and limitations of using DTS data for borehole flow metering (a potential substitute for conventional methods like heat pulse flow meter), and (iii) the potential information that the methodology provides to better characterize groundwater dynamics over time and space.

In the following section, we present the theory of the heat transfer model and describe Ramey's and Hassan Kabir's solutions for the flow profiling problem (Ramey, 1962; Hasan and Kabir, 1994). The calculation procedure used in the proposed framework is described in supplementary materials, and a numerical model is used to validate the proposed framework. Then, after having described the field site, the final section of the manuscript describes an application of the approach for monitoring the hydraulic response of a fractured borehole at the Ploemeur-Guidel field site located in Brittany, France.

4.3 Flow model from the temperature profile

4.3.1 State of art

In petroleum engineering, the works on the concept of flowing well temperature profile prediction date back to nearly sixty years ago (Edwardson et al., 1962; Lesem et al., 1957; Moss and White, 1959) but the pioneering work belongs to Ramey (1962). He proposed a simple analytical solution to predict the temperature profile of single-phase water in an injection well. Later, his analytical model was successfully applied to production wells (Horne and Shinohara, 1979). The model considers steady-state heat transfer inside the borehole while heat transfer from the borehole to the surrounding formation is governed by transient radial conduction. He considered the borehole as a line source and the surrounding earth as an infinite sink in which heat diffusion only occurs in a horizontal plane and vertical heat diffusion is negligible. In Ramey's analytical model, inflow or outflow of the fluid from formation to the borehole or vice versa is not directly considered. However, the inflow/outflow from the borehole can be inferred by estimating the flow, above and below the production/thief zone. The difference will indicate whether the zone is acting as inflow or outflow. The fluid temperature moving inside the borehole is a function of the depth, thermal properties of the borehole, surrounding earth, and also flow time. A time function is introduced to account for the temporal heat transfer behavior in the formation. Later Satter (1965) and Sagar et al. (1991) extended Ramey's model to two-phase flow by taking into account, the effect of the kinetic energy and Joule Thompson effect caused by pressure change along the borehole. Hagoort (2004) examined Ramey's model applicability and found out that it can be an excellent approximation except at early times when the calculated temperature is overestimated.

Hasan and Kabir (1994) further developed Ramey's model. They proposed a new approximate solution for transient heat transfer in the formation as well as incorporating both convective and conductive heat transport for the wellbore/formation system. In Hassan and Kabir's model, they used an appropriate inner boundary condition (finite wellbore) for wellbore/formation heat trans-fer and demonstrated the importance of including the convective heat transfer. Later, Kabir et al. (1996) proposed a model using energy, mass and momentum balance and including different fluid inflows to the borehole. Afterward, there have been many publications by Hassan et al. incorporated the hydrodynamic of different flow patterns and well geometry (2007, 2002). In one of his most general works, a robust analytical steady-state model is presented which includes wellbore inclination, varying geother-mal gradient, and Joule-Thomson effect by dividing the borehole into sections of uniform thermal properties and inclinations (Ha-san et al., 2009). The limitation of this approach is that the solution is not applicable in production zones (in front of production zones) but rather in stable flowing zones above and below the production zone.

Ramey (1962) and Hassan and Kabir's (1996) models were mostly applied for applications implying multiphase flows in petroleum engineering, CO2 sequestration or geothermal energy development. However, Hasan & Kabir's and Ramey's solutions can be ap-plied for hydrological applications. In such a case, the physics of flow and temperature exchanges must be simplified for single-phase flow. No specific assumption would limit the application of these solutions to hydrology. Silva et al. (2019) recently validated Ramey's solution experimentally for a range of water flow rates similar to our application in the field. Using a laboratory proto-type, they obtain very good agreement between flow rate measurements derived from temperature profiles using Ramey's model with imposed flow rates (Silva et al., 2019). Preto et al. (2019) investigated the reason for nonlinearity in the recorded geothermal gradient in the upper part of a deep wellbore which could not be explained by the variability of measured thermal properties of sediments and rocks. They also used Ramey's equation to see if the vertical flow of warm fluid in the upper part can explain this discrepancy between measured and modeled geothermal temperature. They estimated the vertical flow velocity and concluded that this discrepancy can be explained by the infiltration of warm fluid transported from depth by

fractures (Preto et al., 2019). In this work, the use of Hasan & Kabir's solution for converting temperature profile into flow profile is validated numerically (section numerical validation) and also experimentally by cross-checking the estimated flow rates with measured flow rates by a heat pulse flow meter.

Emergence and promising advances of new temperature sensing technologies such as Distributed Temperature Sensors which allows recording of high spatial and temporal temperature has also encouraged researchers to use these data type in petroleum engineering (Ouyang and Belanger, 2004; Kluth and Naldrett, 2009; Wang, 2012; Kabir et al., 2012; Nuñez-Lopez et al., 2014), especially for flow profiling inside boreholes and characterization of the unconventional reservoirs (Luo et al., 2020a; 2020b). These types of data can provide real-time monitoring of the system which may be very useful, especially when the system is subjected to different natural and artificial hydrological process variations. However, real-time, transient analysis of DTS data may not be practically favorable due to the computational time and resources required. In one of the recent works, Alemán et al. (2018) have used machine learning techniques for flow profiling and calculation of the fracture flow rate using temperature data to assess the effectiveness of the hydraulic fracturing operations in oil and gas wells.

4.3.2 Heat transfer model

This subsection is devoted to briefly explaining the heat transfer model developed by Ramey (1962) and Hasan & Kabir (1994) used in the current paper. We have provided more explanation of the derivation of equations in Appendix A. We encourage those who are interested in the detailed derivation of the analytical model to refer to works published by these authors as given in the references.

Considering a flowing volume of water in the jth section of the wellbore between z and z-dz (figure 4-1), both models assume steady-state heat transfer inside the wellbore and transient radial heat transfer from the borehole to the formation. Writing up the energy balance for the control volume, assuming radial heat transfer from the fluid to the surrounding earth, solving the two equations jointly with proper initial and boundary conditions (see Appendix A), we come up with the following equation which describes fluid's temperature profile (T_f) along a vertical borehole depth, z.

$$\mathbf{T_f} = \mathbf{T_{ei}} - \frac{\left[1 - e^{(\mathbf{z}-z_j)L_r}\right]}{L_r}\left(GG - \frac{g}{c_p}\right) + [\mathbf{T_{fj}} - \mathbf{T_{eij}}]e^{(\mathbf{z}-z_j)L_r},$$

Equation 4:1 – The moving fluid temperature inside the borehole

Here, T_{ei} is the initial earth temperature (the temperature at geothermal gradient), T_{fj} and Teij are fluid temperature and initial earth temperature at the fluid entry point to the borehole (z_j), respectively. Also, GG, g and c_p represent the geothermal gradient, gravitational acceleration, and specific heat capacity of water, respectively. Furthermore, L_r is called the relaxation distance. This is the distance required by the fluid to be traveled so as the fluid temperature gradient becomes parallel to the geothermal gradient. The relaxation distance depends on fluid velocity and the thermal properties of the fluid and media.

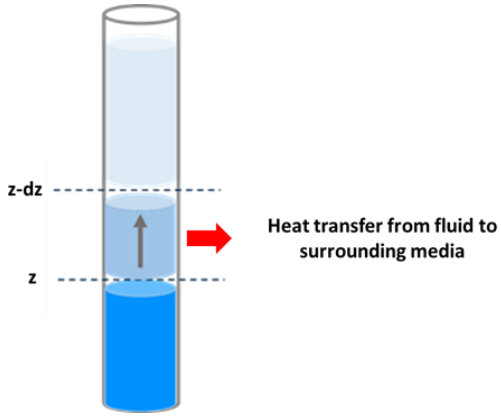

Figure 4-1 Diagram of the Control Volume used for heat transfer modelling inside the production borehole. Heat is either advected by fluid flow or conducted radially in the surrounding media.

The formula for L_r in Ramey and Hassan Kabir equations are essentially the same but proposed for different boundary conditions assumed for solving the set of equations. Ramey considered the borehole as a line source while Hassan and Kabir defined the borehole as a finite radius boundary condition. However, both solutions converge at late times.

$$L_r^{\text{Ramey}} = \frac{wc_p f(t_d)}{2\pi\lambda_e}, \quad \text{(a)}$$

$$L_r^{\text{Hassan \& Kabir}} = \frac{wc_p}{2\pi}\left[\frac{\lambda_e + U_t f(t_d)}{r_{wb} U_t \lambda_e}\right], \quad \text{(b)}$$

$$t_d = \frac{\lambda_e t}{{r_{wb}}^2}, \quad \text{(c)}$$

$$f(t_d) = ln(1 + 1.7\sqrt{t_d}), \quad \text{(d)}$$

Equation 4:2 – Relaxation distance given by Ramey (1962) and Hassan & Kabir (1994)

In the above equations, λ_e, r_{wb}, w, c_p are thermal conductivity of the rock, borehole radius, fluid mass rate, and fluid specific heat capacity, respectively. Also t is the flow time, td is dimensionless flow time defined in the equation (4). Flow time refers to the time that the borehole has been producing and heat being transferred from the fluid to the surrounding media. The dimensionless time function is shown by f (t_d) accounts for unsteady-state heat transfer to the formation. Furthermore, Ut is the overall heat transfer coefficient which is explained comprehensively in Appendix A. Various forms of formulas for f (t_d) existing in the literature, has been studied and compared by Satman and Tureyen (2016). They suggested that the dimensionless time function by Kutun et al. (2014) as given in equation 4:2 (d) would be sufficiently accurate for engineering purposes for most values of flow time. This approach is frequently used in petroleum engineering as well as in geothermal reservoir (Nian et al., 2018; Song et al., 2018; Wang., 2019). In the following, we demonstrate its applicability in hydrology by performing numerical validation and also showing its field application.

4.3.3 Inversion of temperature data and flow profiling

In this section, we explain how distributed temperature data (acquired along the borehole), are used to obtain the water velocity (and consequently water flow rate) in different sections of the borehole. Assuming proper knowledge of the water and media thermal properties (geothermal gradient, the thermal conductivity of the rock, flow time, etc.), L_r is determined so as the recorded distributed temperature data matches the predicted distributed temperature data by minimizing the following objective function. This objective function is the root mean square error normalized by the temperature measurement error variance (temperature accuracy) and minimization continues until the objective function converges to values close to one which means the prediction is within the error level.

$$\text{objective function}=\sqrt{\frac{\frac{1}{N}\sum_{1}^{N}(\mathbf{T}_{\text{recorded}}-\mathbf{T}_{\text{predicted}})^2}{\sigma_{\text{error}}{}^2}}\ ,$$

Equation 4:3 – objective function for flow profiling

where n and σ_{error} are the number of recorded temperature data and error of recorded temperature data, respectively. Once L_r is determined, we use the Hassan & Kabir equation for the relaxation distance given by equation 4:3 to calculate the water mass and thus flow rate and water velocity. It should be noted we use equation 4:3 as it applies to more general cases. In early times, the wellbore is not acting as a line source, so that Ramey's assumption is not satisfied. However, both equations (equations 4:2 (a) and (b)) can also be used to calculate the water flow rate and both should yield the same results for the large flow time and small borehole radius (large values of t_d) as the condition becomes closer to the line source assumption for the borehole.

The minimization process starts with an initial guess L_r. To speed up the minimization process, we need to provide an initial guess close to the final value. For this reason, we use the linearized form of the equation 4:1 (please see supplementary materials). Using $L_r{}^{Ramey}$ proposed by Ramey, we obtain the following simple equations to estimate the water velocity. This gives us most of the time, a fairly close initial guess to the final solution. The initial guess is given as follow:

$$\left.\frac{d\mathbf{T}_{fj}}{d\mathbf{z}}\right|_{z=zj}=(\mathbf{T}_{fj}-\mathbf{T}_{eij})\times L_r{}^{Ramey} \qquad \text{(a)}$$

$$v_{initial}=\frac{2\pi\lambda_e}{\rho_w c_p f(t_d)}\times\left[\frac{(\mathbf{T}_{fj}-\mathbf{T}_{eij})}{\left.\frac{d\mathbf{T}_{fj}}{d\mathbf{z}}\right|_{z=zj}}\right], \qquad \text{(b)}$$

Equation 4:4 – Initial estimation of water velocity using linearized Ramey equation

Here, ρ_{water} and $v_{initial}$ are water density and an initial guess for water velocity, respectively. The above equation simply states that the fluid velocity is not dependent on the absolute value of the temperature but rather on the spatial change of fluid temperature along the borehole. It should be noted that for multiple flowing zones (different j sections) i.e. zones with different water flow rates in the borehole, we repeat the same procedure explained above. Once the water flow rate in all zones is determined, the contribution of each fracture to the total flow can be inferred from deducing the flow rates in consecutive zones.

4.3.4 Numerical validation

4.3.4.1 Description of the numerical model

A numerical model describing heat transfer of moving fluid from the borehole to the surrounding area has been developed using the finite element-based software COMSOL Multi-physics® v. 5.4. (2018). The model mimics an artesian borehole in which, flow from the bottom of the borehole and flow from different fractures contribute to the total upward flow. This model is used in the following, to first validate the approach and secondly, evaluate the accuracy of the proposed framework. The model calculates fluid temperature profile along the borehole given the thermal properties of the fluid and the media as well as fluid velocity. Then, the generated temperature profile is used to back-calculate the fluid velocity in the borehole by inversion of generated temperature data (using the aforementioned analytical solutions and calculation procedure by the computer code developed). By comparing the given fluid velocity in the model and the one estimated from temperature data, we can evaluate the accuracy of the methodology. The model has been

created for cases where one, two, and three fractures are crossing the wellbore although it could be generalized to more complex cases with more fractures crossing the borehole. In this section, only the case of two fractures is shown, but similar results were obtained with one or three fractures.

It can be argued that the thermal effect of the fluid flow inside a fracture on the temperature distribution in the rock matrix away of the borehole (which consequently affects the fluid temperature inside the wellbore) may not be significant. Thus, to reduce the computational complexity associated with including fractures in the model, the borehole is divided into different sections and different fluid velocity is given to each section as shown in figure 4-2. This mimics the presence of fractures and their contribution to the total flow in the borehole. Figure 4-2 represents the numerical model schematic, meshing, and representation of physic used to model the effect of fracture in the borehole (for a case of two fractures). In the model, the outer radius and height of the aquifer are considered to be 100 m while the borehole radius is chosen as 0.07 m. The mesh size is small around the borehole while being larger moving away toward the boundaries.

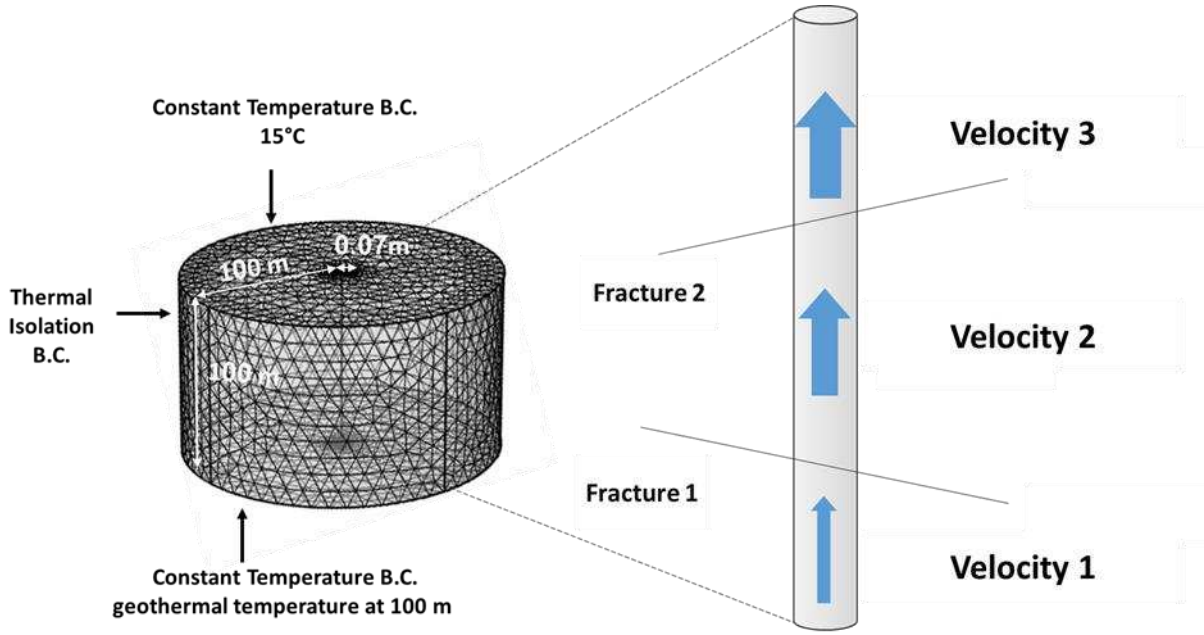

Figure 4-2: Schematic of the numerical model and representation of the borehole with two fractures and three flowing sections

4.3.4.2 Synthetic test with two fractures

In this part, it is assumed an artesian borehole in which two fractures are crossing the wellbore at the depths of 100 m and 70 m contributing to the total flow of water. There is a flow from the bottom of the borehole (velocity 1) and two fractures are also contributing to the total flow. The water and rock specific heat capacities are respectively fixed to 4180 and 750 (J/kg×°C) while water and rock densities are respectively 1000 and 2560 (kg/ m3). The geothermal gradient used in the model is 0.016 (°C/ m), as proposed by Klepikova et al. (2011) for the same site chosen for the application (see section 3). However, the choice of these parameters in the numerical model does not affect the results as they are supposed to be known (the same parameter are used in the computer code). The outer boundary conditions are taken to be thermal isolation. The surface and bottom boundary conditions are respectively set to a constant temperature of 15°C and the geothermal temperature at 100 Sm.

The difference between the flow rate used in the model and flow rate inferred from the temperature by the analytical approach defines the error. Analysis of the results for a different number of fractures, flow rate as well as a different range of flow time, indicate that errors are less than 10%, even for a very low

flow rate which may not be measurable by conventional flow meters. The flow rates tested range from 5.42 lit/min to 542.88 lit/min for different flow time ranging from one day to several weeks. As an example, the best and worst estimate for the case of 5 lit/min are 5.43lit/min and 4.98lit/min corresponding to 9% and 1% errors. For the case of 542.88 lit/min, the best and worst estimates are 541.12 lit/min and 494 lit/min and their associated errors are almost zero and 9%, respectively. These errors are very reasonable errors considering the errors of measurements from flowmeters that also range classically within 10% or more (Paillet et al 1998). Considering reasonable such errors allow validating the use of the analytical model for converting temperature data into flow profile. In figure 4-3, we show the flow used in the numerical model (to generate temperature) versus the estimated flow rate (estimated from the temperature using the analytical solution). It should be noted that here we only show the cases with the highest errors (worst estimates) and we still see the good agreement. It is worth mentioning that the source of this error could be the limitation of analytical solutions (due to their assumption during the derivation) in capturing the real physics of the problem but it still provides satisfactory results.

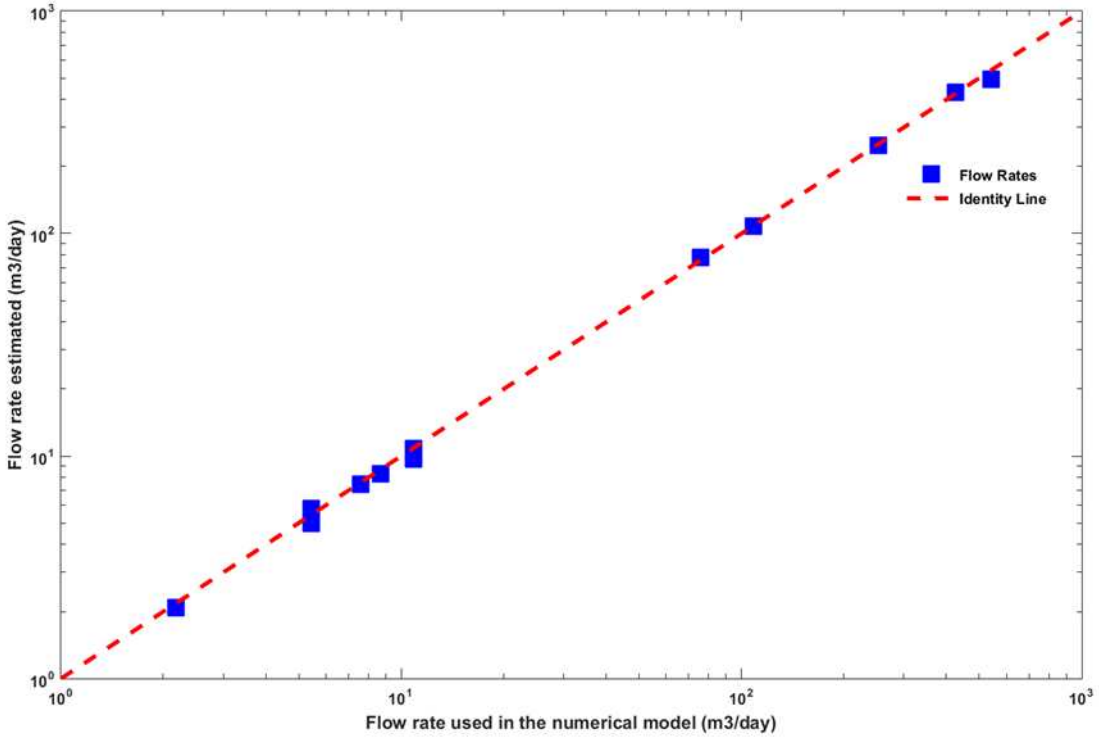

Figure 4-3: Comparison of flow rate used in the numerical model and flow rate calculated from the temperature data using the analytical approach

4.3.5 Sensitivity of the model to the different parameters

The analytical model being validated, we investigate here the sensitivity of the model to the different parameters. In the supplementary materials, some simulations are presented to investigate the respective impact of the different parameters. For the hydrological application considered, we found that the three most important parameters are the geothermal gradient, the thermal conductivity of the rock, and the flow time (by order of importance). Indeed, as heat is continuously exchanged between borehole and media with time, near-wellbore region will equilibrate toward fluid's temperature and heat transfer rate decreases. In fact, the geothermal gradient and flow time determine the driving force while the thermal conductivity of the rock controls the heat transfer rate.

To complement this analysis, a global sensitivity analysis has been performed using the Sobol method available in the safe MATLAB toolbox (Pianosi et al., 2015). It allows determining the importance of

the most influential parameters on the calculated flow rate. In a global sensitivity analysis, all parameters are varied simultaneously over the entire parameter space, which leads to simultaneously evaluating the relative contributions of each individual parameter and the interactions between parameters to the model output variance. To date, several types of global sensitivity analyses have been developed. However, variance decomposition based Sobol sensitivity analysis is so far one of the most powerful techniques. Sobol sensitivity analysis intends to determine how much of the variability in model output depends on each of the input parameters, either upon a single parameter or upon an interaction between different parameters. In order to understand how the output variance can be attributed to individual input variables and the interaction between each of the input variables, the total-order, first-order (main effect), second-order, and higher-order sensitivity indices are calculated to accurately reflect the influence of the individual input and their interactions. The first order Sobol index (main effect), explains the contribution of parameter alone to the output, while the total index (total effect) reflects the relative importance of one input variable and all its interactions with other variables. Here, the first-order Sobol index values are 0.66, 0.027, and 0.06 for the geothermal gradient, the thermal conductivity of the rock and flow time while the total Sobol index are 0.97 0.74 and 0.57, respectively. Figure 4-4, shows and compares the values of these indices. We see that the geothermal gradient is the most significant variable taking into account both its main effect and its interaction with other parameters. Rock thermal conductivity and flow time have a very small main effect. However, their impact on the total variance is notably high (high values of total effect) due to their interaction with other parameters. This means that uncertainty in flow profiling can be significantly reduced by proper measurement of the geothermal gradient which may not be difficult to estimate in comparison to the other parameters. The geothermal gradient can be measured in the wells with stagnant water inside, ensuring no cross-flow in a borehole section. In such boreholes, the change of stagnant water temperature with respect to the depth reflects the value of the geothermal gradient (assuming that water has stayed long enough in the borehole to reach thermal equilibrium with the surrounding media). However, in case of no or little, knowledge of thermal properties, we will show in section 6.1, how to estimate these parameters for flow profiling application using a measured flow rate.

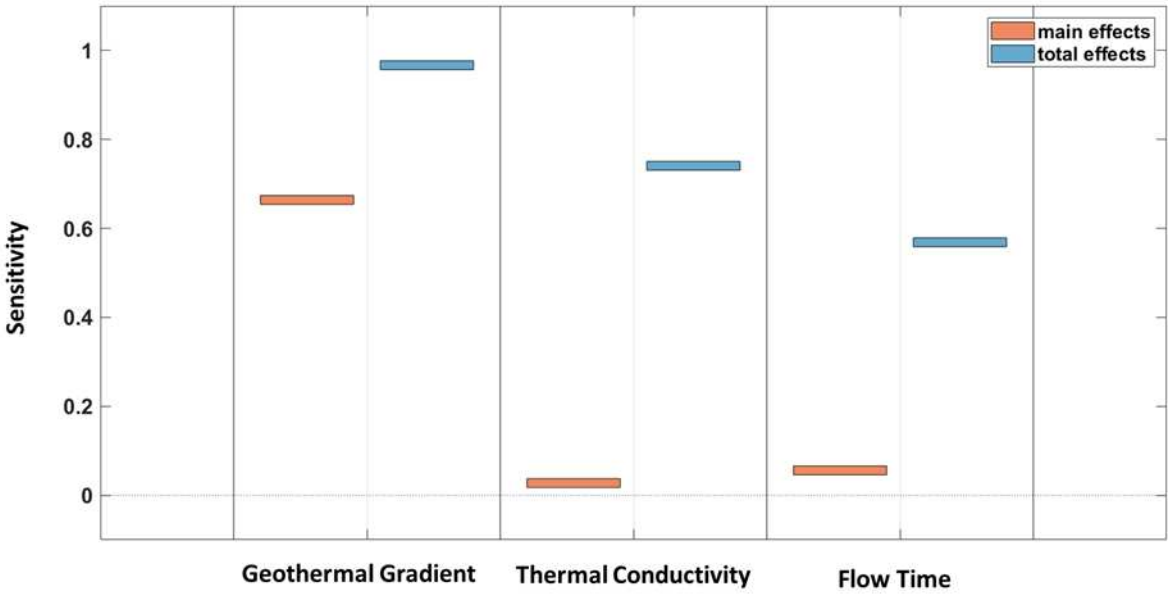

Figure 4-4: Global sensitivity analysis (Sobol method) performed for three parameters and the corresponding sobol indices including main effect and total effect. The main effect represents the contribution of parameter alone while the total effect represents its interaction with other parameters.

4.4 Hydrogeological setting

4.4.1 The Ploemeur-Guidel field site

The field site of Ploemeur-Guidel is a coastal aquifer located in Brittany, France, which provides one million cubic meters of drinking water annually to a nearby town. The mean annual precipitation is about 800 mm while the mean annual evapotranspiration is about 500 mm. Although the site is located in crystalline rocks composed of granite and micaschists, the good connectivity and high hydraulic conductivities of large-scale faults provide water supply since 1991 (Le Borgne et al., 2006). The structural analysis combined with geophysical data (Touchard, 1998; Ruelleu et al., 2010) revealed that the most productive boreholes are located at the intersection of two main tectonic features: a low-angle fault zone between granite and micaschist dipping about 30° to the north, and dextral fault zones regularly spaced and striking north 20°. Compared to other bedrock aquifers in Brittany, this aquifer is outstandingly productive. Although hydraulic properties are highly variable in space, especially at small scales, the large-scale transmissivity of the site varies between 10^{-3} to 10^{-2} m2/s (Le Borgne et al., 2006; Jimenez-Martinez et al, 2013). The site has been the subject of numerous experiments and studies, which include but are not limited to geophysical imaging, residence times modeling, water chemistry monitoring (Ruelleu et al., 2010; Leray et al., 2012; Roques et al., 2018). The Ploemeur-Guidel hydrogeological observatory (http://hplus.ore.fr/en/ploemeur) is a part of both the H+ network of hydrogeological sites (http://hplus.ore.fr/en/) and the French Critical Zone network OZCAR (http://ozcar-ri.org/) (Gaillardet et al., 2018). All data used in this study can be found on the H+ database (de Dreuzy et al., 2006; http://hplus.ore.fr/en/).

4.4.2 Borehole PZ-26

Among the numerous boreholes available, borehole PZ-26 was chosen to apply the approach experimentally. PZ-26 is an artesian borehole located near a small stream and very close to a wetland area fed by groundwater and which is the aquifer's outlet. The flow rate at the top of the well is varying depending on the seasons. It is maximum after groundwater recharge which occurs in winter in general, while the flow rate is minimum in autumn, just before the start of groundwater recharge. Thus, borehole PZ26 is an artesian well where flows are strongly sensitive to hydraulic changes through time. This sensitivity to hydraulic changes motivated the installation of temperature monitoring through FO-DTS hoping to record flow changes within the borehole through time. Note also that the development of microbial communities that can be observed locally at some fracture intersections up to 60 meters deep in this borehole, is strongly related to flows within the borehole (Bochet et al., 2020). Indeed, the developments of these microbial hotspots appear due to intermittent oxic–anoxic fluid mixing in relation to flow dynamics in the borehole, (Bochet et al., 2020). According to a simple mechanistic model of fluid flow and mixing in fractures, the authors showed that such microbial hotspots are sustained by the mixing of fluids with contrasting redox chemistries at fractures intersections and that meter-scale changes in near-surface water table levels could cause intermittent oxygen delivery through deep fractures (Bochet et al., 2020). Thus, temperature monitoring using FO-DTS was considered a promising tool for monitoring flow changes along the borehole to better understand flow dynamics and microbial communities development. Although the analysis of microbial communities development is beyond the scope of the present study, and the fact that flow profiling from temperature monitoring is an indirect method for estimating borehole flows, the advantages of FO-DTS borehole are to provide flow profiling all along the borehole without leading to head losses in the boreholes nor using multi-packers that are complex to use and may strongly alter microbial hotspot developments.

PZ 26 is a 6 inches' diameter open borehole where about a dozen permeable and producing fractures have been identified thanks to optical and flowmeter borehole logging (Bochet et al., 2020). Despite

the borehole's depth, only mica-schists dipping slightly towards the north have been encountered in the borehole. The deepest fractures were found the most productive (below 94m). Fractures in this borehole inherit two different orientations; North-West oriented and East oriented fractures. Note that the golden color shown on the borehole schematic in figure 4-5, for depths above 59 meters, corresponds to iron-oxide precipitation that results from the mixing of oxygen-containing surface water and iron-rich deep water. The value of the transmissivity of the productive fractures above 94m in this borehole ranges from 10^{-4} to 5.10^{-4} m2/s measured by borehole flowmetry (Bochet, 2017).

4.5 Data acquisition and processing

4.5.1 Experimental setting

Distributed Temperature was continuously monitored along the borehole during about three days thanks to a Fiber-Optic Distributed Temperature Sensing (FO-DTS) installed in the borehole PZ-26. The fiber-optic cable designed by Brugg Kabel AG, Switzerland has a 3.8 mm diameter and is protected by steel armoring and a polyamide jacket. It contains four multimode fiber-optics that were spliced together to make a connection between two fiber-optics. Such splicing allowed double-ended measurement calibration following Van de Giesen et al. (2012). The spliced endings were protected by 3-D printed casings filled with epoxy. The end of the cable was easily installed at the bottom of the borehole so that the cable was installed all along the borehole without any tension. DTS data were recorded using a DTS XT unit (Silixa) with a spatial sampling of 25 cm. The cable metering made it possible to associate a depth to each measured temperature. The acquisition frequency was set to every one minute in a double-ended configuration which allows temperature monitoring at a high temporal frequency.

During the three days of temperature monitoring (implemented in late October 2018, just before groundwater recharge), some hydraulic changes in the borehole were clearly observed from the variation of flow rate at the top of the borehole that was increased by a factor of around two during the first night of monitoring. Tidal variations or atmospheric pressure changes could not explain this hydraulic response but more likely due to water level changes associated with the hydrological cycle and groundwater recharge. As we shall see in the following sections, these flow rate changes were also associated with temperature variations in the borehole. In addition to monitoring natural hydraulic changes, a small pump (MP1- Grundfos) was installed in the first meters of the borehole at nearly the end (from 12:30 to 15:30 on the third day of the experiment) of the temperature monitoring period to increase the flow rate. This allows us to test the methodology used to monitor borehole flow changes in the borehole for three different conditions. Thus, throughout the monitoring period, the system was subjected to two different naturally occurring ambient conditions and one pumping condition (pumping flow rate around 40 l/min). For cross-validation of the flow profiling determined from temperature measurements, the flow has been also measured at different depths with a Heat-Pulse Flowmeter (HPFM, Geovista) (Le Borgne et al., 2006) to well capture the flow variations along the borehole. HPFM is composed of an electrical resistance acting as a heat generator and two thermistors below and above the resistance. The resistance generates a heat-pulse, and the travel time of the thermal breakthrough peak is recorded by one of the thermistors. The measured travel time is inversely proportional to the flow and the localization of the thermistor measuring the plume gives the direction of the flow. Note that a calibration process is used and described in the following to estimate the flow rate from travel time measurements. For each point measured by HPFM, we record the travel time at least three times to be able to quantify the uncertainty associated with the HPFM measurement. The mean standard deviation for travel time for ambient 1, ambient 2 and pumping hydraulic conditions are 1.92, 0.73 and 0.17 seconds corresponding to mean uncertainty of 1.1 lit/min, 2.45 lit/min and 2.92 lit/min. This mean uncertainty in flow measurement (dF) is obtained by taking the differential of both sides in the fitting equation (figure S5 in

supplementary materials) and using the mean uncertainty in the measured travel time as the uncertainty (dt) in travel time estimation. However, the uncertainty of the measurements is also defined locally at each point. The mean, and standard deviation of recorded travel times (at each point) are used to find the average flow rate and corresponding uncertainty.

4.5.2 Data processing

4.5.2.1 FO-DTS calibration and processing

The laser backscattered signal conversion to temperature was done directly by the DTS unit using the double-ended calibration procedure (Van De Giesen et al., 2012). Due to the double-ended configuration, four coil sections of fiber-optic were installed before and after entering the borehole, in two baths filled with water at ambient temperature (15°C) and with wetted ice (0°C). To assess the accuracy and resolution of the temperature data recorded by DTS, few RBR temperature sensors with a temperature accuracy of 0.002 °C were also used in different locations, including the calibration baths (cold and ambient baths). One additional RBR solo T was set up to the top of the borehole in the water to check the calibration. A comparison of the temperature data recorded by DTS and RBRs reveals that the mean absolute error is around 0.05 °C and the maximum error was found to be 0.1 °C by DTS. Recorded temperature data normally inherits noises. Removing the noise from the data is essential for a successful interpretation and flow. Temperature inflection points, which may represent the fluid's entry and consequently defining the production zones, should not be mistaken with local noise in the temperature at that location.

Smoothing was performed on time and not on space as details on the temperature variations in space are used for flow profiling and detection of the possible fracture locations. The locally Weighted Smoothing (LOESS) method (Cleveland, 1979) has been chosen to perform smoothing the data. LOESS uses locally weighted linear regression to smooth the data. It is weighted in the sense that a weighted function is defined within a span (window). Then a smoothed curve is obtained through a set of data defined by this dynamic span. The choice for value of span is critical to make sure that smoothing is effective and over-averaging will not happen which may result in losing resolution and dilution of the information (Moreno et al., 2014). Considering and trying the different spanning value for the smoothing process, we finally came up with a spanning of 10% of data. This means that moving smoothing window contain 10% (around 5 hours of recorded temperature data) of all observed temperature, each time it performs smoothing.

4.5.2.2 Heat-pulse flowmeter calibration

Parallel to recording distributed temperature data, heat-pulse flow metering was performed in all three different flowing condition periods. For all tested points (depths) in the borehole, at least three measurements were done to reduce the measurement uncertainty following Paillet's methodology (1998). To calibrate heat-pulse data, we recorded the travel time just above all fractures and below the casing in the upper meters of the borehole, where the flow rate is maximum. At this location, the borehole wall is relatively smooth, and measurements were made for different pumping flow rates that were precisely measured from the timing to fill a large bucket (figure S5 in the supplementary materials). The calibration has been used to convert travel times to flow rate assuming that borehole diameter is constant all along the borehole.

4.6 Field application

4.6.1 Spatio-temporal temperature variations

Figure 4-5 shows the Spatio-temporal representation of DTS data after smoothing. On the left, a schematic of the borehole and location of the fractures are presented. The bottom horizontal scale gives the

timing of different events (ambient 1, ambient 2 and pumping). The temperature scale is provided on the right of the figure. A blue rectangle presents the time range corresponding to approximately each event. The white vertical lines correspond to the three-time shots chosen for temperature data to represent the three different hydraulic conditions (figure 4-6). These time shots from smoothed temperature data were then used for flow profiling.

Considering figure 4-5, we can observe temperature variations happens in a relatively small range during the three days of the experiment, between 14° up to 15.8 °C, the highest temperature being observed at the greatest depths. Nevertheless, some changes can be clearly associated with different hydraulic conditions (ambient 1, ambient 2, and pumping). Hence, the temperatures are relatively stable from the beginning of the experiments up to 9 am in day 2. This period of time corresponds to the first natural conditions encountered at the beginning of the experiment. Then from 9 am up to 11 am, an increase in temperature seems to happen at all depths. This is difficult to define precisely the limits, but the temperature seems more or less stable from 11 am (second day) up to 9 am (third day), which corresponds to the second natural conditions encountered. During that period of time, the flow rate at the top of the borehole was approximate twice the one measured during ambient 1. Then, during the last hours of the experiment, pumping was started from around 12:30 (day 3) for three hours up to 15:30. This pumping period is associated with a clear increase in temperature. It is worth noting that a natural temperature variation (probably flow rate increase as the temperature isotherm moves to upper depth compared to ambient 2 condition) could be observed from around 10 a.m. to 12 a.m. in the third day just before the pumping. However, as the pumping starts, the temperature isotherms move to lower depths and the pumping condition temperature profile becomes dominant and stable.

These temperature variations with time may also be observed at a given depth for the different hydraulic conditions (ambient 1, ambient 2, and pumping). For instance, consider the yellow isotherm corresponding to the temperature of 15.1°C. It can be seen that this isotherm in ambient 1 condition reaches the depth of 70 m while in ambient 2 and pumping conditions in which flow rates are higher respectively, this isotherm is observed at 60 m and 20m, respectively. This means that as the fluid velocity increases, the fluid retains its energy more as it has less time to exchange heat with surrounding media. Furthermore, in front of fracture at 75m, a green horizontal line in ambient 1, and a yellow horizontal line in ambient 2 and pumping conditions can be observed. This suggests a cold water inflow into the borehole. Similar inflows can be observed for fractures at 29 and 95 meters, although temperature contrasts seem weaker. The locations of fractures are shown on the depth axis and it can be observed that many fracture locations correspond to temperature variations of the fluid.

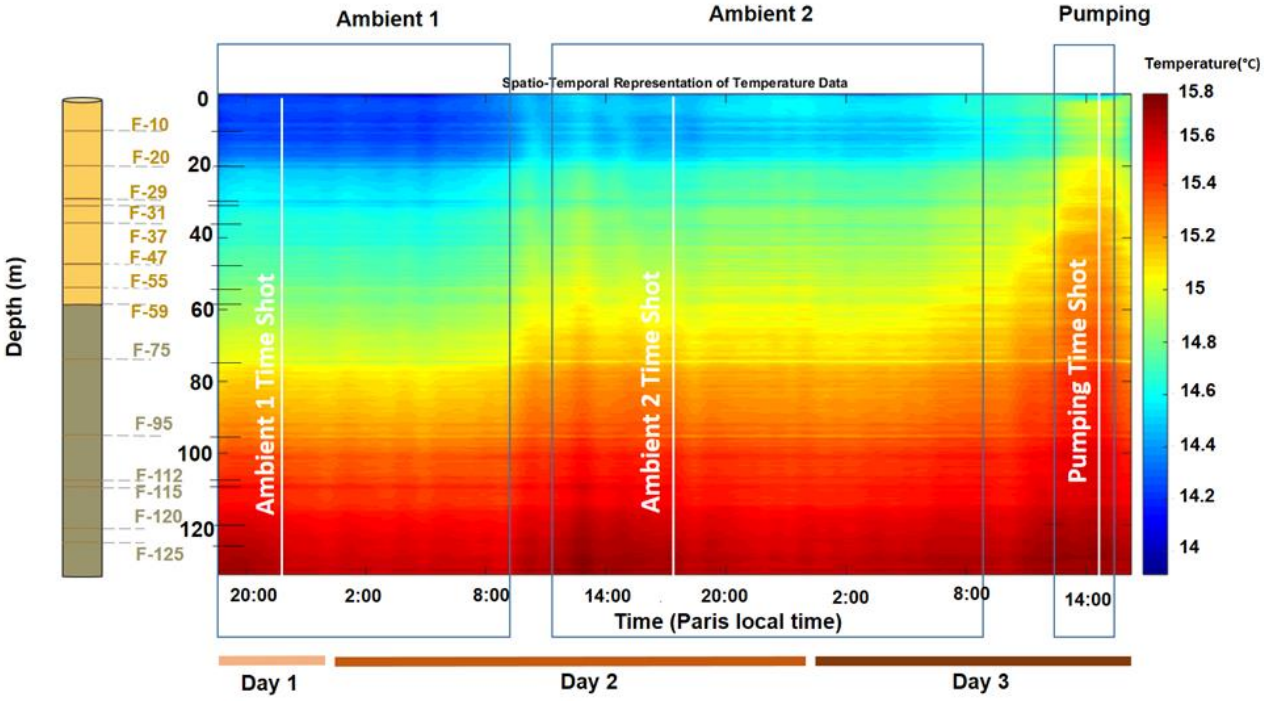

Figure 4-5: Representation of borehole schematic (left) with the position of the different fractures identified and Spatio-temporal temperature data (smoothed) recorded in borehole PZ-26 during the three different hydraulic conditions. The colour scale for temperature is provided on the right of figure.

The great advantage of FO-DTS is to provide full temporal monitoring that allows us to easily define some representative times of the different hydraulic conditions encountered. Thus, three-time shots from the DTS data representing three different flowing conditions (hydraulic conditions) were chosen to perform flow profiling in the borehole. Vertical white lines in figure 4-5 represent these three-time shots. Because heat-pulse flow metering typically lasts a few hours, the time shots were chosen to be in the middle of the heat-pulse flow metering operation and ensuing these time shots lies within a stable temperature period. This results in a fair comparison between results obtained by heat-pulse flow metering and flow profiling done by using DTS data (The temperature profile is chosen from smoothed data). Figure 4-6 shows the three-time shots chosen for flow profiling (distributed temperature with depth). The blue, orange and yellow curves represent ambient 1, ambient 2, and pumping conditions, respectively. It can be seen that increasing the flow rate results in less changes of temperature with depth. This happens because, for a fixed borehole length, higher the fluid velocity (rate), there will be less residence time for the fluid to do the heat exchange with the surrounding rock. This can be also seen in figure 4-5 when comparing the same color spectrum for different depths. For example, the isotherm of red color in ambient 1 is in lower depth rather than ambient 2 and finally pumping condition. This means in the pumping, the fluid has conserved more of its energy compared to two other conditions. It is important to mention that prior knowledge of the fractures' locations is essential for the interpretation of the temperature profile. However, in the case of no previous knowledge, finding the locations on the temperature profile where there is a heating (water coming to the borehole is colder with respect to the fluid in the borehole) or cooling (water coming to the borehole is hotter with respect to the fluid in the borehole) peak allow to infer the possible locations of the inflows. It must be noted that noise can create the same peaks but they are not stable with time while peaks corresponding to fluid inflows (with different temperatures) should persist at all times. It is worth mentioning that we see a sharp decrease in flowing water temperature at around 20m, possibly due to the introduction of cold surface water.

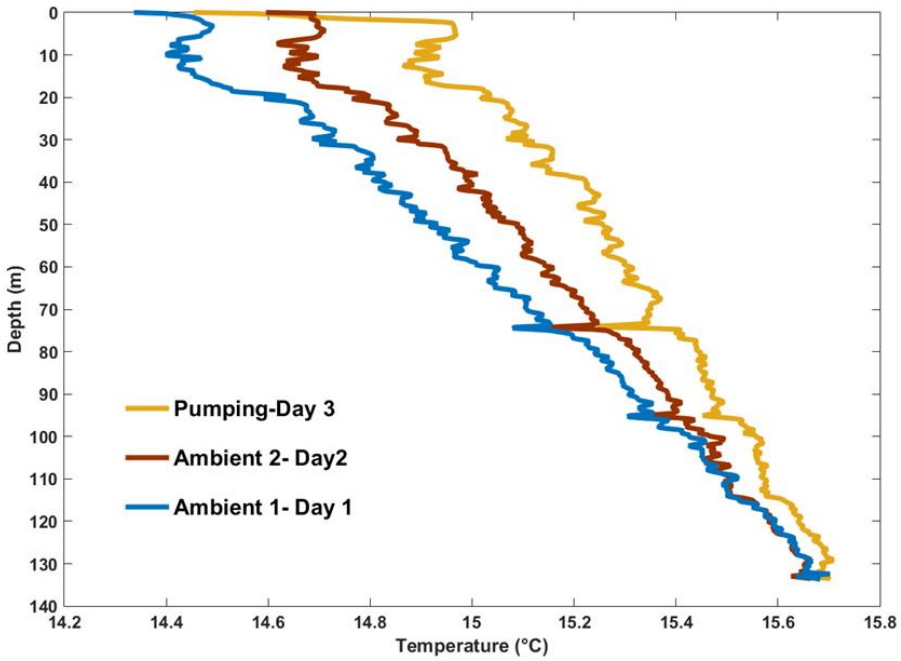

Figure 4-6: Comparison of three time-shots recorded temperature profile (smoothed) corresponding to the 3 different flowing conditions (ambient 1, ambient 2 and pumping).

4.6.2 Flow rate calculations

Flow profiling using temperature data is quite dependent on proper knowledge of media thermal parameters and the flow history of the well (how flow rate varies with time which is used to calculate the flow time). In general, flow changes over time are not considered and media thermal properties are chosen at "known" constants. We implemented a full sensitivity analysis that is described in section 6. Here, we present and compare flow results obtained (1) by using the parameters suggested by Klepikova et al., (2011), who also did measurements/estimations of thermal parameters on the same site and (2) results obtained using the optimum values found by matching the manually measured surface flow rate to surface flow rates predicted by DTS (see section 6.1). However, it should be noted that these values may not necessarily represent realistic parameter values but mostly parameters obtained by tuning of surface flow rate predictions to surface flow rate measurements. These parameter values will be discussed in section 6. Although the parameter sensitivity will be discussed in section 6, this provides an idea of the results' sensitivity depending on the parameters chosen. All parameter values used for flow rate estimations are given in Table 4-1. The explanation of the used parameters is also given in section 6.1.

Table 4-1: Fluid and Media Properties Used for Flow Profiling

Density of the rock (kg/ m3)	Heat capacity of the rock (J/kg×°C)	Thermal conductivity of the fluid (W/m×°C)	Heat capacity of water (J/kg×°C)	Thermal diffusivity of the fluid (m2/s)	Rock thermal conductivity (W/m×°C)		Geothermal gradient (deg°C/m)		Flow time (day) for ambient1, ambient2, pumping (respectively)	
					Optimum value	Klepikova et al. (2011)	Optimum value	Klepikova et al. (2011)	Optimum value	Klepikova et al. (2011)
2560	790	0.59	4190	1.41 E-7	5.8	2.4	0.013	0.016	7,7,5	6,3,1

4.6.2.1 Flow Profiling using Distributed Temperature Sensing (DTS) Data

Recorded temperature data along with previously mentioned values for fluid and media properties are used to find the flow rate in different sections of the borehole. During ambient 1 condition, major active flowing fractures that are identified are fractures below 115m, 115m, 95m, and 55m and 35 m (figure 4-7a). On figure 4-7, the locations of the main fractures, that are taken from the study by Bochet et al. (2020), are shown by the horizontal dashed lines. It should be noted that fracture at 75m is contributing to the total flow with the entry of fluid with notably different temperatures, as it can be seen in Figure 4-5. However, its flow contribution is small and integrated with the fracture at 55m. The manually measured surface rate is around 7 l/min. The value of each fracture's estimated or measured flow rate is shown in figure 4-7(a) and quantified in Table 4-2.

Ambient 2 condition occurred on the second day of the experiment as it was also observed at the site where the surface flow rate increased significantly. The measured surface flow rate is about 15.7 l/min. The analysis shows that major active flowing fractures are fractures below 115m, and fractures at 115m, 95m, 75m, 55m, and 35 m. The estimated individual contributions to the total flow are given in table 4-2. The value of the flow rate from each fracture is shown in figure 4-7(b). Note that the two main contributing fractures seem to be the fracture at 35 and 55 meters deep.

Pumping started at noon of the third day (from 12:30 to 15:30) with rate of 40 lit/min. Pumping continued for three hours to let the fluid temperature stabilize in the borehole by extracting the fluid that already existed in the borehole. Figure 4-5 shows that except at the very early times, temperature during the pumping period is almost stable, which was also a criterion to choose a proper time shot for the pumping period. Major active fractures, discerned by DTS are fractures below 115m, and at 115m, 95m, 75 and 55m and 35m. The value of each fracture's flow rate can be observed in figure 4-7(c) and is given in Table 4-2. Note that fractures at 95 and 115 m are the most productive fractures in that case. Note that the uncertainty associated with the estimation of borehole flows using DTS data stems from the uncertainty in the thermal parameters chosen. Defining a probable range of thermal parameters results in an uncertainty of the flow estimated.

4.6.2.2 Flow Profiling using Heat Pulse Flow meter (HPFM)

Heat-pulse flow metering in ambient 1 flowing condition was performed for a total of 12 points up to the depth of 62 m. It was not possible to do deeper measurements as the flow was too small, resulting in high variability of the recorded travel time with a large increase in the uncertainty of flow rate. Based on the analysis and interpretation of recorded travel time, fractures below 60m, 55m, and 35 m contribute to the total flow. Figure 4-7(a) compares the cumulative flow rate estimated by DTS data and heat-pulse flow meter with their associated error levels. Considering the uncertainties of both measurements, it seems that both estimates agree fairly well. The cumulative flow rate measured by HPFM is 4.28 l/min for flow below F-55 and also fractures below F-115. Fracture contributions estimated both from DTS and HPFM are given in Table 4-2 for comparison.

In ambient 2, a total of 10 measurement points were acquired up to the measured depth of 118m. Based on the analysis and interpretation of recorded travel times, fractures below 115m, and fractures at 115m, 95m, 55m, and 35 m contribute to the total flow. Figure 4-7(b) compares the cumulative flow rate estimated by DTS data and heat-pulse flow meter. Considering uncertainties, both estimates agree fairly well also in that case. The measured flow rate is shown and compared in Table 4-2.

During pumping, a total of 9 points were acquired up to the measured depth of 118m. Based on the analysis and interpretation of recorded travel times, fractures below 115m, and fractures at 115m, 95m,

75m, 55m, 35 m, 20m, and 12 m contribute to the total measurable flow. Figure 4-7(c) compares the cumulative flow rate estimated by DTS data and heat-pulse flow meter. It is interesting to note that fracture at 55 (F-55), one of the major producing fractures in ambient conditions, experiences a decrease in contribution during the pumping. This point will be discussed in the next section. It must be noted that in this case, the discrepancy between flow rate estimated by DTS and HPFM flow rate estimation can be mainly attributed to the fact that the selected flowing zone for interpretation of DTS data may not have been well established. Due to the increased velocity of the fluid in pumping, the distance required by the fluid to be traveled to establish a reliable flowing zone is longer and disturbed by introducing fluid into the borehole by other active fractures. It can also be observed that DTS cannot predict the rate in regions where the flowing zone is not established due to the high density of permeable fractures or inflows i.e., regions above 30 m. The measured flow rate is shown in figure 4-7(c) and compared in Table 4-2. Although more discrepancies may be observed in that case, flow rate estimates from DTS data agree relatively well with HPFM measurements.

Table 4-2 Contribution of each fracture to the total flow during ambient 1, ambient 2 and pumping conditions estimated from DTS data and measured by HPFM (note that for ambient 1 condition, F-55 and F-75 are merged together). As explained in the text, flow rates estimated from DTS data are calculated by using (1) the parameters suggested by Klepikova et al., (2011), and (2) the optimum values found by matching the manually measured surface flow rate to surface flow rates predicted by DTS (see section 6.1 and estimated parameters columns in the table below).

Fractures	**Ambient 1**			**Ambient 2**			**pumping**		
	Estimated flow rate from DTS data		Measured flow rate from HPFM	Estimated flow rate from DTS data		Measured flow rate from HPFM	Estimated flow rate from DTS data		Measured flow rate from HPFM
	Using estimated parameters	Using Klepikova et al. (2011) parameters		Using estimated parameters	Using Klepikova et al. (2011) parameters		Using estimated parameters	Using Klepikova et al. (2011) parameters	
F-37 and above	1.8 l/min (25%)	1.7 l/min (24%)	1.58 l/min (22%)	4.12 l/min (27%)	5 l/min (33%)	3.38 lit/min (21.5%)	6.5 lit/min (17%)	8 lit/min (19%)	6.4 lit/min (17.5%)
F-55	1.4 l/min (19%)	1.4 l/min (20%)	1.51 l/min (20%)	3.9 l/min (25%)	3.9 l/min (25%)	3.5 l/min (22.5%)	0.5 lit/min (1.2%)	1.3 lit/min (3%)	0.8 l/min (2%)
F-75				1 l/min (6 %)	0.8 l/min (5%)	1.52 l/min (10%)	1 l/min (8 %)	2 lit/min (5%)	1.5 l/min (4%)
F-95	1.54 l/min (20%)	1.7 l/min (24%)	4.28	2.92 l/min (19 %)	2.6 l/min (17%)	2.46 l/min (16%)	13.35 lit/min (35%)	14.5 lit/min (35%)	9.5 l/min (24.5%)

F-115	1.9 l/min (26%)	1.7 l/min (24%)	l/min (58%)	2.93 l/min (19%)	2.35 l/min (15%)	1 l/min (6%)	12.25 lit/min (32%)	11.1 lit/min (26.5%)	10.6 l/min (27%)
Below F-115	0.7 l/min (10%)	0.5 l/min (8%)		0.62 l/min (4%)	0.65 l/min (5%)	3.68 l/min (23.4%)	5.25 lit/min (13.5%)	4.7 lit/min (11.5%)	9.6 lit/min (25%)

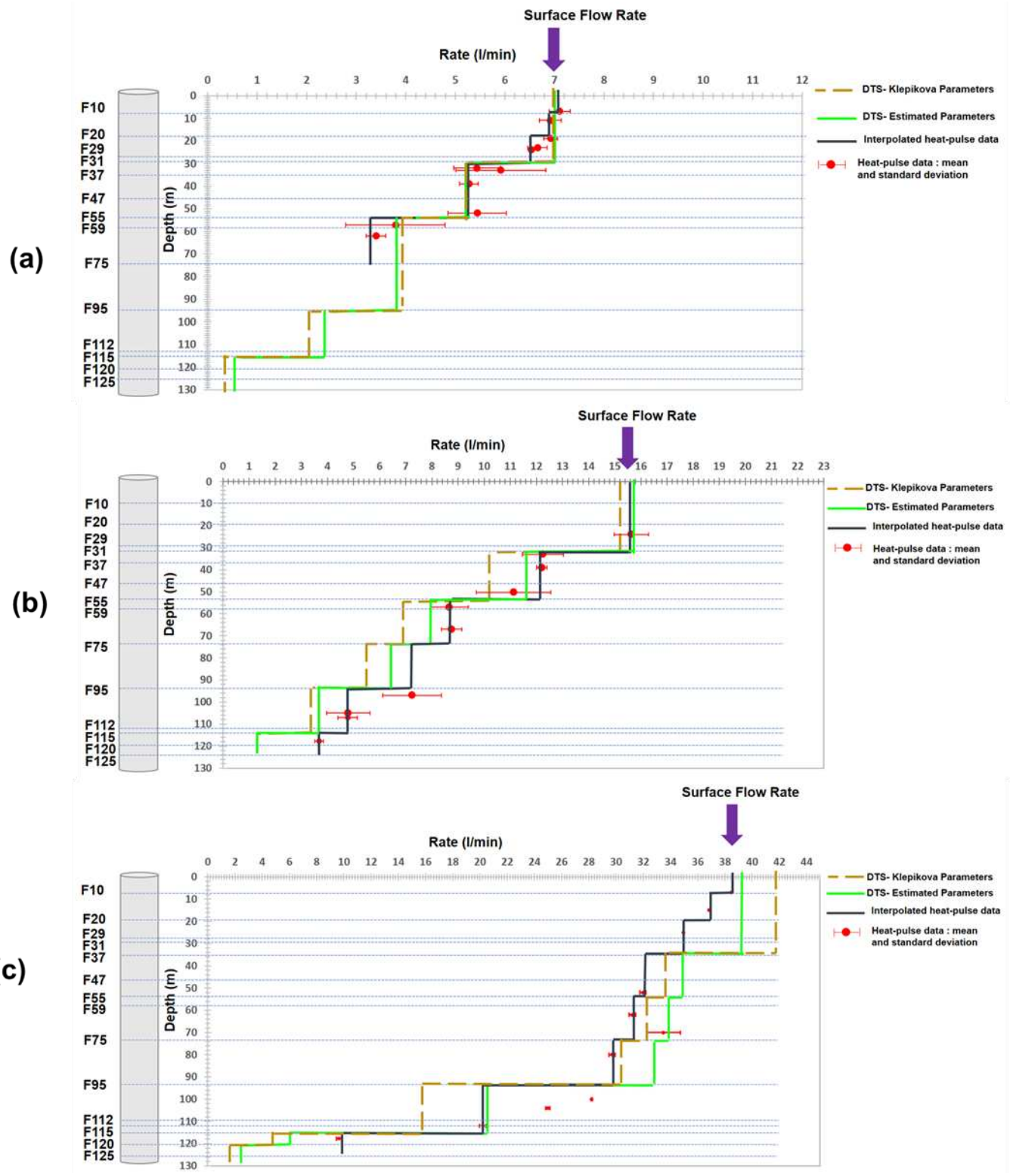

Figure 4-7: Comparison of flow rates estimated at different depth through DTS measurements and from HPFM measurements during ambient 1 (a), ambient 2 (b) and pumping (c) conditions. Green solid line shows flow profiles obtained by using estimated parameters from a sensitivity analysis (table 4-1) while brown dashed line shows flow profiles using Klepikova et al. (2011) parameters. Red dots show the measured flow rates by HPFM and their associated uncertainty in the measurement

Analysis of DTS data for flow profiling along with heat-pulse flow metering, show that there is a general agreement between flow measurements by HPFM and flows inferred from DTS data. Comparing two ambient conditions, we see the high daily flow variations, which depend on different hydraulic conditions imposed on the system. During ambient conditions, half of the flows (56% in ambient 1 and 42% in ambient 2) are coming from the deep fractures (F-95 and below) and the other half coming from fractures above F-95. However, during the pumping, more than half of the flows (around 75%) is supplied from deep fractures (F-95 and below) and the rest is provided by other fractures. This can also be seen in figure 4-6 as the bottom-hole temperature has shifted slightly toward higher values during pumping which implies that water is provided from deeper depth. As we will address this point in the discussion, this is important as it gives an insight into the system's behavior during ambient and pumping conditions since surface water and deep water contain different amounts of oxygen which may explain the essence of reactions that may happen in the borehole.

4.7 Discussion

4.7.1 Thermal parameters estimation

To perform successful flow profiling from temperature data, an estimate of the thermal properties values and the flow time is required. This subsection describes the cases (i) when we know the thermal properties but flow time is unknown and (ii) when thermal properties and flow time are all unknown. We estimate the unknown properties by using a measured flow rate at the surface which permits constraining the estimated flow at the surface and, therefore the unknown properties from the available temperature data.

In case that we have previous knowledge of geothermal gradient and rock thermal conductivity, we need to know the flow time to perform flow profiling from the temperature data. The flow time takes into account the superposition of antecedent conditions. However, for a continuously flowing system with a daily variable flow rate, if the history of the flow is not recorded, then it is not straightforward to suggest a time and it can be used as a tuning parameter by matching the measured surface flow to estimated surface flow. In the present case, Klepikova et al., (2011) have reported values of 0.016 °C/m and 2.4 W/m×°C for geothermal gradient and rock thermal conductivity, for the same site. However, the value of flow time (which is required for the flow profiling) is unknown. We determine the optimum flow time for each flowing condition to solve this issue, using the aforementioned thermal properties values and other required parameters (Table 4-1) by matching the estimated surface flow rate by DTS and measured surface rate. In fact, here the flow time is used as a tuning parameter. The optimum flow times for ambient 1, ambient 2, and pumping conditions obtained are respectively 6 days, 3 days, and 1 day. This means that for ambient 1 condition, in order to reach the current thermal condition (to observe the same temperature trend in fluid along the borehole), it is needed to have a continuous flow of 7 lit/min (ambient 1) for 6 days. These individual flow times can be seen as a tuning parameter to calculate the flow rate. The results of using these parameters for flow profiling are presented in Table 4-2 and figure 4-7 and corresponds to the columns “using Klepikova et al. (2011), parameters.

However, in the case of no previous knowledge on thermal properties of the media as well as the flow time, we may estimate them all by matching the DTS-predicted surface flow rate and measured flow rate (flow rate at the surface) for all flowing conditions (ambient 1, ambient 2 and pumping). For doing so, we considered a uniform distribution for the geothermal gradient (0.01 to 0.03 deg°C/m), the rock thermal conductivity (2 to 6 W/m×°C), and the flow time (1 day to 365 days). The obtained optimum parameters for geothermal gradient and rock thermal conductivity are 0.013 (°C /m), 5.8 (W/m×°C), respectively. Consequently, the optimum flow time for ambient 1, ambient 2, and pumping are 7 days, 7 days, and 5 days. The flow estimates using these sets of parameters are given in Table 4-2 and figure 4-7 (“estimated parameters”).

It must be noted that these estimated values may not necessarily reflect the real values but they can be used for estimation of flow from temperature data within an acceptable range of error. It worth noting that Klepikova (2013) has reported values of thermal conductivities ranging from 1.731 (W/m×°C) to 3.42 (W/m×°C) for the mica-schist and 2.98 (W/m×°C) to 4.061 (W/m×°C) for the granite measured in the lab for rocks from the same geological site.

To discuss in more detail, the effect of the choice of the different parameters, figure 4-8 presents results obtained using two values of flow time (1 day and 182 days) on the range of optimum thermal property values. Every point in this figure shows the average normalized error (with respect to standard deviation) of estimated surface flow by temperature data using the corresponding geothermal gradient (on the x-axis) and thermal conductivity (on the y-axis) for 1 day and 182 days flow time. The dark blue region shows the range of values for a set of geothermal gradient and rock thermal conductivity with minimum error.

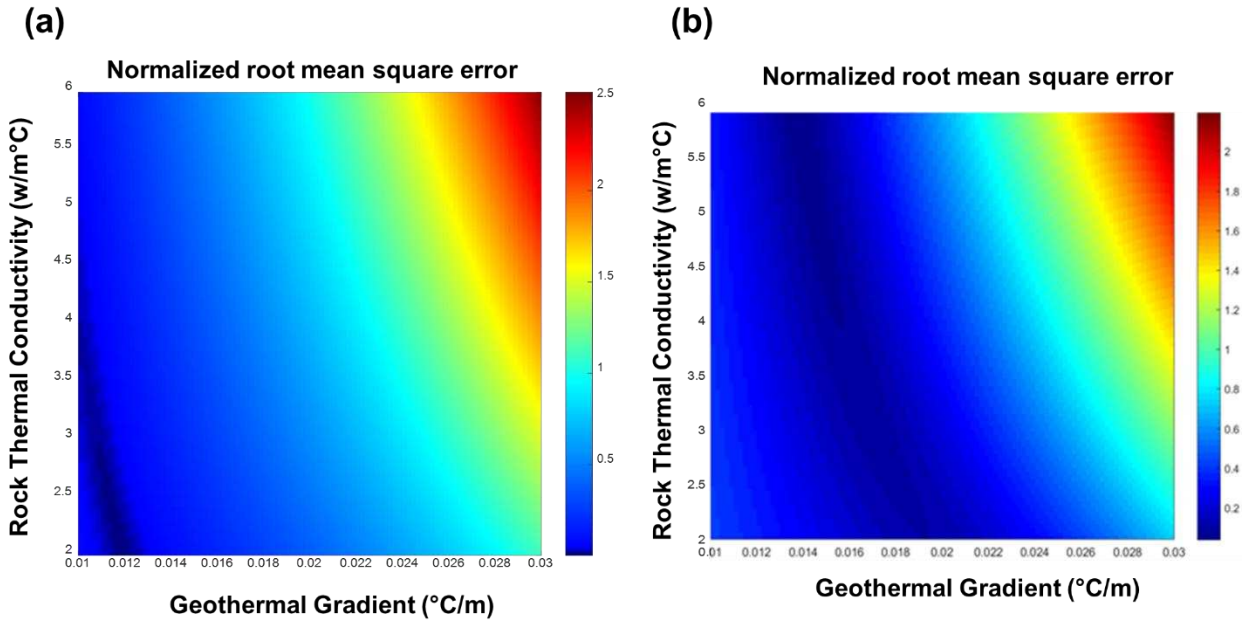

Figure 4-8 : Normalized RMSE error between predicted flow by DTS and measured flow rate at the surface at (a) one-day flow time (b) six-months flow time

Figure 4-8 shows that the estimated flow rate is clearly more sensitive to the geothermal gradient rather than rock thermal conductivity (considering a fixed flow time). This has been also confirmed by the global sensitivity analysis performed in section 2.5. Secondly, it shows that for two different flow times, there are sets of thermal parameters that can result in the same small estimation errors regardless of the fact that whether they present real values or not. It must be noted that as long as the purpose of thermal parameter and flow time estimation is flow profiling, regardless of their values (whether they present real values or not), they can be used for estimation of flow from the temperature data. This would be an issue if the analysis was to be used to determine either thermal gradient or conductivity but since that is not the goal, then not knowing them exactly is not crucial. This is reflected in Table 4-2 and figure 4-7 as we used two sets of different parameters (Kelipikova and optimized set of parameters) and we end up with a close estimation of the flow (by two sets of parameters) from the temperature data to the flow measured by HPFM.

4.7.2 Added values and drawbacks of using FO DTS for field applications

In the classical approaches, the temperature sensors record the temperature profile by pulling in and out the temperature probes or recording the temperature in a fixed position with time. For instance,

Klepikova et al. (2011; 2014) used temperature logging to infer the borehole flows with application to quantify inter-borehole connectivity and fracture transmissivity. The use of FO DTS has many advantages compared to classical probes. First, the introduction of DTS technology led to having both spatial and temporal information at the same time with data accessible during monitoring. This may be of great help for interpreting temperature signals during transient events or when groundwater dynamics cannot be fully understood by comparing simply two times shots. Moreover, using a fiber optic cable avoids fluid mixing in the borehole that can occur when logging the temperature probe. It also avoids generating head losses in the borehole, which may occur with the use of temperature probes or flowmeters.

There have been already previous attempts to use DTS for borehole flow metering. For instance, Read et al. (2014) showed that the temperature difference between a heated cable and a non-heated cable can be used to quantify the vertical flows in the borehole like a distributed flowmeter. However, this approach may not be appropriate for long term monitoring as it requires more complex equipment to ensure continuous heating. Furthermore, the calibration of this method for low flow rate, in particular for ambient conditions, is challenging and uncertain (Read et al., 2014). Some other attempts like Leaf et al. (2012), Sellwood et al. (2015) and Read et al. (2015) used the injection of hot water or an electrical heater to infer water direction and velocities in the borehole in ambient and hydraulically stressed conditions. However, these methods provide more accurate results close to the heating source and were not used for continuous monitoring. More recently, Selker and Selker (2018) used a distributed borehole heater to investigate water movement within and near wells, but the methodology proposed requires specific heating cables. In comparison, our field installation just requires monitoring temperature with a DTS unit. Although field DTS units having low electrical consumptions are currently developed, this may still be the main limitation in some field cases. Nevertheless, using distributed temperature data is beneficial since it is easy to install in the field, it leads to a minimal disturbance of borehole natural conditions and provides real-time data acquisition.

4.7.3 Inferring groundwater dynamics from temperature data

In the present study, we proposed a simple approach based on an analytical model to infer borehole flows from temperature data. Using a numerical model for inversion of temperature data may be indeed computationally expensive for some models while here we have substituted it with very fast and reasonably accurate analytical solutions. In addition, using DTS data, we addressed the temporal changes in temperature and showed the potential of using these types of data for capturing the dynamic response of the fractured media. One main challenge associated with this approach is having proper knowledge of the media's thermal properties. However, we showed that measuring the surface flow rate in the case of an artesian borehole can be of great help to obtain the proper value of thermal properties for flow profiling by constraining the calculated flow to measured flow at the surface. Another limitation comes from the scale of observation which remains limited to the borehole scale. Nevertheless, we have shown in the previous section how FO DTS can be used to infer flow variations and monitor the transient nature of the fracture system.

Once the flow from each fracture is estimated, it can be easily used to calculate the transmissivity of each fracture if the borehole transmissivity is known (Paillet, 1998; Day-Lewis et al., 2011). Considering the value of 5×10^{-3} m^2/s for the total transmissivity, that has been reported by Bochet et al. (2020) from a pumping test in the same borehole, the fractures transmissivities at different depths are estimated to vary between 10^{-4} and 1.7×10^{-3} m^2/s. Note that here, we observe roughly the same proportion of flow coming from the different fractures between ambient1 and ambient2 conditions. Nevertheless, in pumping conditions, the flow coming from the fracture at 55 meters is smaller than in ambient conditions. This is confirmed by the interpretation of DTS data and also by HPFM measurements which show that during pumping, the flow is produced mainly by fracture at 95 and 115m (figure 4-7). This is quite surprising since the head in the

borehole is lower for pumping conditions compared to ambient conditions and should therefore lead to an increase of flow coming from F-55. This suggests that the different inflows cannot be analyzed independently and that fracture F-55 is possibly somehow connected to complex fracture networks so that the inflow observed at 55 m in some conditions may be greatly dependent on the head distribution in the fracture network. This may have some implications when using classical borehole flowmetry to infer fracture transmissivity (Paillet, 1998; Day-Lewis et al., 2011). This may also explain some intermittent fluxes observed from fracture F-55, which provides at specific times, water enriched with Oxygen that is at the origin of bacterial development (Bochet et al., 2020). Long-term temperature monitoring may provide a better imaging of this intermittent behavior in groundwater dynamics.

4.8 Conclusions

In the current work, DTS data were used to calculate flows in different sections of the borehole and consequently quantify the flow from each producing fracture during the different hydraulic conditions. To be able to use temperature data for real-time flow profiling, a computationally fast tool is proposed to transform temperature profile to flow profile. This tool employs an analytical solution by Hassan & Kabir (1994) and Ramey (1962) for flow profiling. Comparing the results obtained from heat-pulse flow metering and DTS shows that the framework can estimate the flow rate with a good accuracy where there is a well-established fluid temperature profile. Results confirm the general agreement between flow rates estimated by DTS and flow rates measured by HPFM. During ambient 1 and ambient 2 flowing conditions, it seems that the repetition of flow measurements along the borehole is different but difficult to catch with heat-pulse flow metering while DTS flow profiling can be very convenient and useful in ambient conditions. However, one of the challenges of using the current approach is the proper knowledge of the thermal properties of media required to infer the flow rate from the temperature. In case of a lack of knowledge of the media's thermal properties, surface rate measurement can be useful to constrain the model and reduce the flow profiling uncertainty.

The use FO DTS data to monitor the dynamic behavior of a fractured system at the borehole scale has many advantages. It allowed us to capture changes in the flow inside the borehole once hydraulic conditions of the system changed naturally (from ambient 1 to ambient 2) and artificially (from ambient 2 to pumping). DTS data in PZ26 has many interesting aspects to note. Firstly, some fractures may be easily detected through temperature trace when there is a sufficient temperature contrast between the water exiting from the fracture and the water inside the borehole. Secondly, it shows its ability for monitoring daily borehole flow variations of flow at different temporal scales. Such a possibility opens a new window for real-time monitoring of complex fracture interactions and recharge processes in fractured media.

The advantage of the proposed method (DTS data and proposed framework) compared to conventional methods (such as heat-pulse flow meter) is that it requires less time and effort and it provides continuous monitoring appropriate for detecting rapid changes. Also, distributed sensors are made of fiber-optics and due to their narrow diameters, they can be used where there is a risk or limitation with the utilization of other tools of larger diameters. Furthermore, another interesting aspect of the DTS is that it provides spatial and temporal temperature data which can be used to do real-time monitoring and understanding the change in the state of the system with time (monitoring the dynamics of the system). In the present case, results show that fractures contribution varies significantly depending on hydraulic conditions. Beyond the transient nature of this fractured aquifer, this has also some consequences on mixing and reactivity occurring inside the borehole. Indeed, some Oxygen rich fractures like the fracture at 55 meters deep, appear to be characterized by varying borehole inflows and possible intermittent fluxes which may be due to complex interactions with others fractures. By inferring borehole flow variations, temperature could be thus a possible proxy for characterizing mixing at the borehole scale.

CRediT authorship contribution statement

Pouladi, B.: Conceptualization, Methodology, computer code development, Investigation, Writing - original draft, editing. **Bour, O**.: Methodology, Investigation, Writing - review & editing, Supervision. **Longuevergne, L**.: Methodology, - review & editing, Supervision. **La Bernardie, J**.: Investigation, review & editing. **Simon, N**.: Investigation

Declaration of Competing Interest

The authors declare that they have no known competing financial interests or personal relationships that could have appeared to influence the work reported in this paper.

Acknowledgments
This project has received funding from the European Union's Horizon 2020 research and innovation program under the Marie Sklodowska-Curie Grant Agreement No 722028 (ITN project ENIGMA). This work is also part of the ANR project EQUIPEX CRITEX (grant ANR-11-EQPX-0011) from which we received financial support. We thank very much the SNO H+ (Réseau National de sites Hydrogéologiques) for field and technical support.

The data presented in this paper are available and accessible through the following link at the database of the French National Network for Hydrogeological sites:

(http://hplus.ore.fr/en/pouladi-et-al-2021-joh-data).

The computer code will be also available upon request to any of the authors.

4.9 Appendix A – Heat Transfer Model

Let's consider a control volume inside the borehole spanning from the depth z to z-dz (figure 4-1), assuming that we have steady-state heat transfer inside the wellbore and transient heat transfer to the formation, energy balance for wellbore is written as follow:

[energy entering the control volume] = [energy out of the control volume]

$$[(\mathrm{wH})_{\mathrm{z}} - (\mathrm{wH})_{\mathrm{z-dz}}] + \frac{1}{2}[(\mathrm{wv}^2)_{\mathrm{z}} - (\mathrm{wv}^2)_{\mathrm{z-dz}}] + [(\mathrm{z})(\mathrm{wg})_{\mathrm{z}} - (\mathrm{z}-\mathrm{dz})(\mathrm{wg})_{\mathrm{z-dz}}] = \mathrm{Qdz}$$

Equation 4:5 – Energy balance for the fluid inside the borehole

Dividing by dz and w, then evaluating the expression as dz tends toward zero, we have,

$$\frac{d\mathrm{H}}{d\mathrm{z}} + \mathrm{v}\frac{d\mathrm{v}}{d\mathrm{z}} - \mathrm{g} = \frac{\mathrm{Q}}{\mathrm{w}},$$

Equation 4:6 – differential form of energy balance equation

where H, g, v, Q and w, are enthalpy of the fluid, gravity acceleration, fluid velocity, heat transfer from the fluid to surrounding media and fluid mass rate, respectively. The above equation states that change in Enthalpy of the fluid in the wellbore plus fluid gravitational and kinetic energy terms equal to heat transfer between the fluid and surrounding area per unit of the flowing fluid mass. Assuming that no phase change occurs in the fluid, enthalpy can be written as the following form in terms of measurable parameters, fluid's Temperature (T_f), and Pressure (p).

$$d\mathrm{H} = \left(\frac{\partial \mathrm{H}}{\partial \mathrm{T_f}}\right)_{\mathrm{p}} d\mathrm{T_f} + \left(\frac{\partial \mathrm{H}}{\partial \mathrm{p}}\right)_{\mathrm{T}} d\mathrm{p} = \mathrm{c_p} d\mathrm{T_f} - \mathrm{c_p c_j} dp,$$

Equation 4:7 – Enthalpy change as a function of pressure and temperature change

where c_p and c_J are Specific Heat Capacity of Water and Joule-Thompson coefficient. Specific heat capacity defines the amount of energy required for a unit to increase the water temperature. The Joule-Thompson coefficient defines the change in the temperature of fluid when subjected to the pressure change process. It can be a positive value (mostly for gases at moderate pressure), resulting in temperature drop or negative values (mostly for liquids) and increasing temperature.

Using equation (3) in equation (2) and rearranging the terms, the following form is obtained:

$$\frac{d\mathrm{T_f}}{dz} = \mathrm{c_j}\frac{d\mathrm{p}}{dz} + \frac{1}{\mathrm{c_p}}\left[\frac{\mathrm{Q}}{\mathrm{w}} + \mathrm{g} - \mathrm{v}\frac{d\mathrm{v}}{dz}\right], \qquad -\infty < x < \infty$$

Equation 4:8 – Energy balance for fluid in terms of pressure change, velocity change, heat exchange with media

Writing up the energy balance for the formation leads to the following equation:

$$\frac{\partial^2 \mathrm{T_e}}{\partial \mathrm{r}^2} + \frac{1}{\mathrm{r}}\frac{\partial \mathrm{T_e}}{\partial \mathrm{r}} = \frac{\mathrm{c_p}\rho_e}{\lambda_\mathrm{e}}\frac{\partial \mathrm{T_e}}{\partial \mathrm{t}}, \qquad -\infty < x < \infty$$

Equation 4:9 – Energy balance for the formation

where T_e, C_e, ρ_e and λ_e are rock temperature, rock heat capacity, rock density, and rock thermal conductivity, respectively.

Different methods and solutions are proposed by authors to solve the aforementioned equations. These solutions are based on some assumptions on the real physics of the problem. One of the most critical ones is the boundary condition between the wellbore and the surrounding earth. Authors have considered constant heat flux or constant temperature boundary conditions at the wellbore/earth interface while none of them generally explains the heat transfer problem as neither heat flux condition nor constant temperature condition remain constant (Satman and Tureyen, 2016). However, both solutions converge at long times. The other assumption is about the borehole. Ramey has considered the borehole as a line source while Hasan & Kabir have considered a finite radius for the borehole. Ramey's solution is most suitable for cases when conduction becomes the main heat loss mechanism which happens in low flow conditions. It has been reported that Ramey's solution is accurate except in early times (Hagoort, 2004) when heat flow in the wellbore is controlled by convection and when the assumed conditions are not met. The Ramey and Hasan and Kabir solutions are given in equations (A-6) to (A-10), respectively.

$$\mathbf{T_f} = \mathbf{T_{ei}} - \frac{\left[1 - \mathrm{e}^{(\mathbf{z}-\mathrm{z_j})\mathrm{L_r}}\right]}{\mathrm{L_r}}\left(\mathrm{GG} - \frac{\mathrm{g}}{\mathrm{c_p}}\right) + [\mathbf{T_{fj}} - \mathbf{T_{eij}}]\mathrm{e}^{(\mathbf{z}-\mathrm{z_j})\mathrm{L_r}}, \tag{a}$$

$$\mathrm{L_r}^{\mathrm{Ramey}} = \frac{\mathrm{wc_p}f(\mathrm{t_d})}{2\pi\lambda_e}, \tag{b}$$

$$\mathrm{t_d} = \frac{\lambda_\mathrm{e}\mathrm{t}}{\mathrm{r_{wb}}^2}, \tag{c}$$

$$f(\mathrm{t_d}) = ln(1 + 1.7\sqrt{\mathrm{t_d}}), \tag{d}$$

$$\mathrm{L_r}^{\mathrm{Hassan\ \&\ Kabir}} = \frac{\mathrm{wc_p}}{2\pi}\left[\frac{\lambda_\mathrm{e} + \mathrm{U_t}f(\mathrm{t_d})}{\mathrm{r_{wb}U_t}\lambda_\mathrm{e}}\right], \tag{e}$$

Equation 4:10 – Ramey and Hassan & Kabir solutions

Here L_r is called relaxation distance. This is the length required by the fluid to be traveled so as the fluid temperature becomes parallel to the geothermal temperature. A dimensionless time function $f(t_d)$ is introduced, accounting for change of heat transfer coefficient with time. Various forms of time functions existing in the literature have been studied and compared by Satman and Tureyen (2016). They suggested that dimensionless time function by Kutun et al. (2014) as given in equations (11) and (12), would be sufficiently accurate for engineering purposes for all values of heat flow time. Other terms used in the above equations are given in nomenclature.

4.10 Supplementary Materials

4.10.1 Introduction

The supplementary Material section includes sections, figures, and equations that are not included in the manuscript but would help to understand this study. Section 1 describes the computer code's calculation procedure to convert the temperature profile to the flow profile. The overall procedure is shown schematically in Figure S1. Section 2 shows the effects of the geothermal gradient, rock thermal conductivity, and flow time on the fluid temperature drop versus depth. The effects are shown through figures S2 to S4. Finally, in section 3, which is composed of only figure S5, we show the calibration curve and uncertainty calculation for the Heat Pulse Flow Meter (HPFM).

4.10.2 Calculation Procedure

Here, we describe the computer script procedure to perform flow profiling using previously defined analytical solutions. The analytical solutions predict the fluid temperature profile inside the borehole given the fluid's thermal properties, surrounding media, flow time, and fluid velocity inside the borehole. Flow time refers to the time that fluid has been flowing in the borehole without the change of the flow rate. Assuming that the fluid and surrounding media's thermal properties are well defined, the problem now becomes an inverse problem in which fluid velocity must be determined so as the calculated fluid temperature profile aggress with observed temperature profile. We have developed a computer code that receives the distributed temperature data, the media's thermal properties and the fluid and flows time, and performs flow profiling. The description of the computer code is given as follows.

4.10.3 Automatic flowing zone detection

The calculation process starts with the identification of the producing (mixing) and flowing zone as the aforementioned solutions are only applicable to flowing zones. The flowing zones are chosen based on previous knowledge of users but in case of lack of this knowledge, the computer script suggests some potential location of the producing zone. The logic behind this suggestion is the fact that fluids introduced into the boreholes mostly have a different temperature than the fluid temperature in the borehole, which causes a local peak in the recorded temperature profile. Furthermore, in oil and gas wellbores where fluids are compressible and upon entry, they experience a sharp pressure drop, this temperature peak is seen and known as the Joule-Thompson cooling/heating effect. Using the piecewise temperature gradient, local sharp change of derivative value corresponds to the temperature peak and consequently entry of the fluid and thus producing zone.

4.10.4 Linearization of the Ramey's equation

Providing a realistic initial solution close to the final solution makes the calculation procedure fast enough to allow real-time flow profiling. This initial solution is based on the linearization of Ramey's equation

which simply states that fluid mass rate inside the borehole is linearly approximated by thermal properties of the media and fluid, flow time, the temperature difference between fluid and surrounding earth as well as established fluid temperature gradient. Starting from Ramey's equation (6) and taking the derivative of fluid temperature with respect to depth, the mass rate is expressed as follows in equation 14 and can be used along the fluid density to calculate the fluid flow rate.

$$\left.\frac{d\mathbf{T}_{fj}}{d\mathbf{z}}\right|_{z=0} = (\mathbf{T}_{fj} - \mathbf{T}_{eij}) \times L_r{}^{Ramey} \qquad (a)$$

$$v_{initial} = \frac{2\pi\lambda_e}{\rho_w c_p f(t_d)} \times \left[\frac{(\mathbf{T}_{fj} - \mathbf{T}_{eij})}{\left.\frac{d\mathbf{T}_{fj}}{d\mathbf{z}}\right|_{z=0}}\right], \qquad (b)$$

Equation 4:11 – Linearization of the Ramey's equation

Equation (S-2) provides an initial solution to the problem. In a low flow regime and small flowing length, this solution can be very close to the final solution. The temperature gradient term in the denominator is calculated by simply doing a linear regression over the temperature data recorded in the zone of interest.

4.10.5 Inversion of Temperature data and flow profiling

The recorded distributed temperature data, thermal properties of fluid, and media are fed to the computer script. For each flowing region, the recorded temperature gradient is calculated and using linearized Ramey's equation, an initial fluid flow rate is estimated. Next, Hassan & Kabir Equations are used respectively to predict the fluid temperature profile. In the optimization step, the computer code starts minimization of the objective function defined as the misfit (normalized by value of error) between observed temperature profile and the predicted temperature profile (predicted by aforementioned equations) by varying the value of fluid flow rate. The optimization continues we reach a normalized root mean square error close to one. It is worth noting that in each iteration, due to change of the fluid flow rate and consequently the velocity, values of parameters depending on the fluid velocity will be updated as well. figure S-1, schematically shows the procedure used in this computer code.

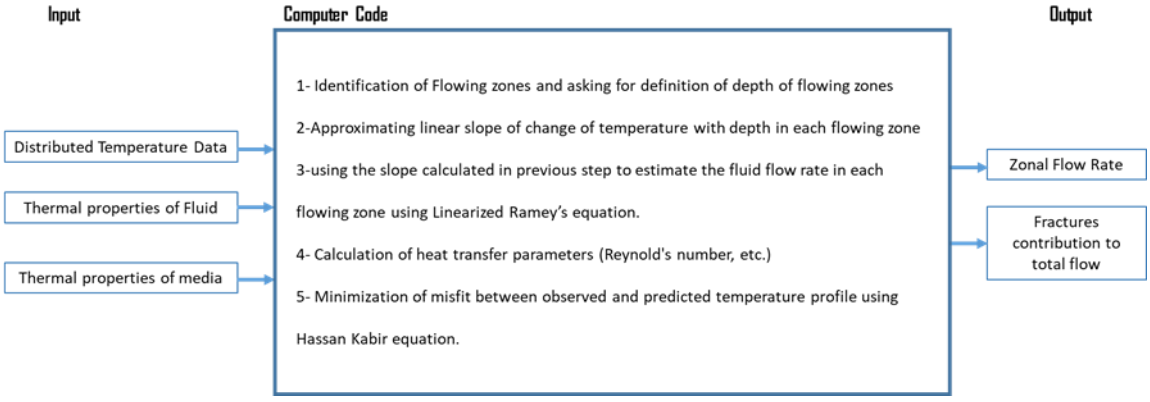

Figure S-1: Schematic of flow profiling procedure

4.10.6 Effect of the different parameters on temperature profile

4.10.6.1 Effect of geothermal gradient on the flowing water temperature

The geothermal gradient controls the original earth temperature with depth. It is one of the driving forces for the heat exchange of the flowing water in the borehole with surrounding media. High values of the geothermal gradient, results in more heat exchange of flowing water with the formation and consequently

higher temperature drop with respect to depth (vertical distance traveled by water in the borehole). This is presented in figure S1 which shows the temperature drop versus the depth traveled by water from the bottom of the borehole for different values of the geothermal gradient. An error of 20% in the geothermal gradient would result in 0.25°C of error in temperature for a 100 m long travel distance. This means that error in flow rate estimation increases as water travel distance increases.

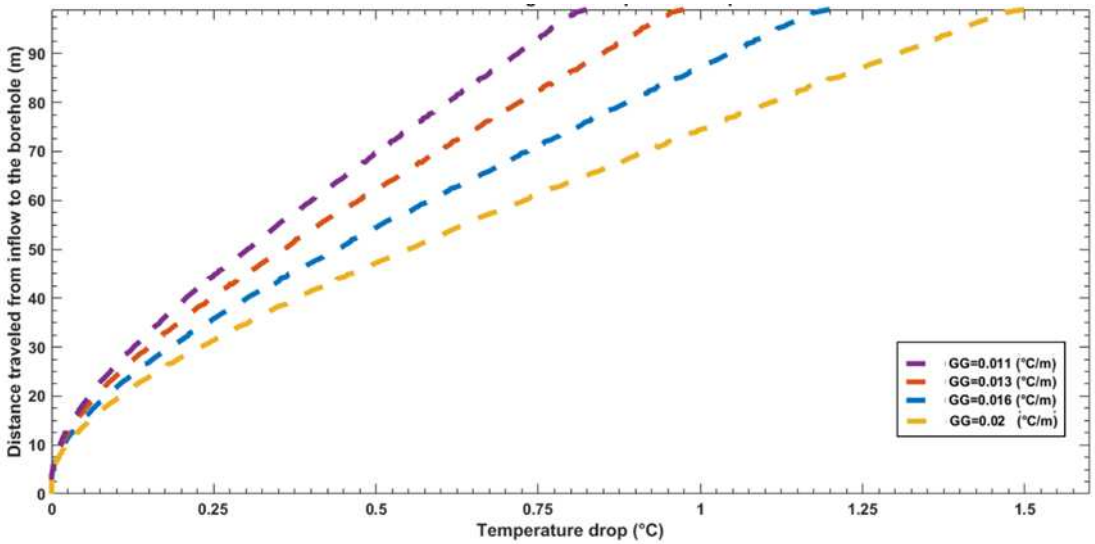

Figure S-2: Effect of geothermal gradient on flowing water temperature drop versus depth travelled in the borehole

4.10.6.2 Effect of rock thermal conductivity on the flowing water temperature

Another important parameter playing role in the temperature drop of flowing water is the thermal conductivity of the rock surrounding the borehole. Even though thermal conductivity does not define the driving force for heat exchange but higher values facilitate the heat transfer. Thus, increasing the thermal conductivity of rock surrounding the borehole increases the temperature drop versus depth travelled by the water (figure S2). This can be seen in figure 10. Here, a 30% uncertainty on rock thermal conductivity generates an apparent 0.06°C temperature change. On contrary to the geothermal gradient, this temperature bias appears on travel distances as short as 30 m, and constant afterward. Uncertainties in thermal conductivity will rather impact flow ratio among flowing zones when separated by more than 10s of meters.

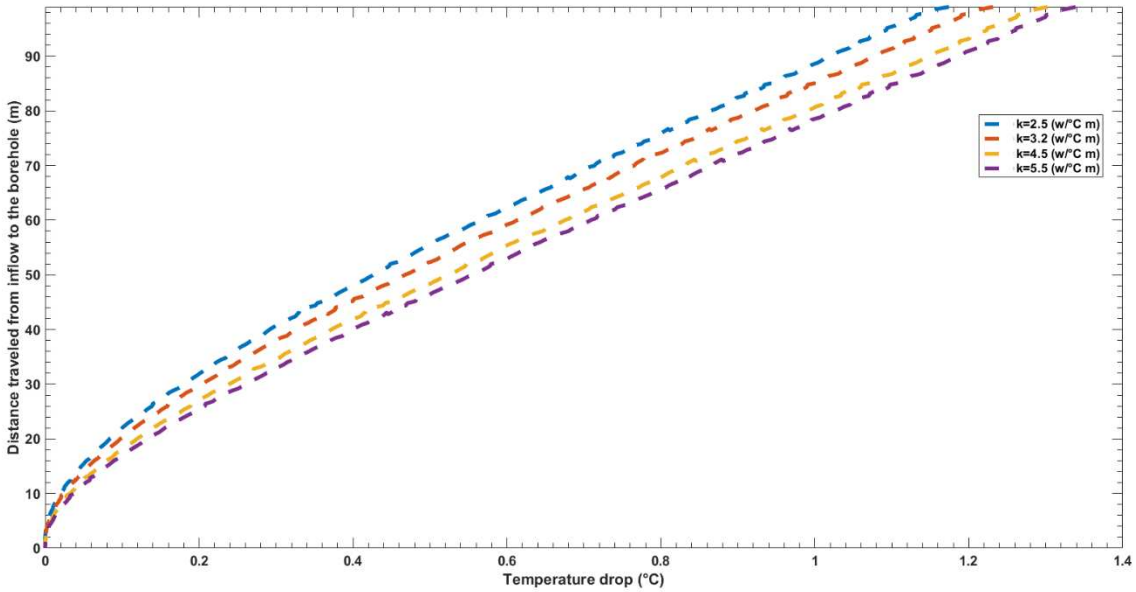

Figure S-3: Effect of rock thermal conductivity on flowing water temperature drop versus depth travelled in the borehole

4.10.6.3 Effect of flow time on flowing water temperature

Flow time implicitly defines the temperature in the rock around the borehole and thus the driving force for the heat exchange. In early times, the rock temperature equals almost to earth virgin temperature. As the flowing continues (flow time increases), the area around the borehole will tend to equilibrate with the flowing water temperature (tend toward water temperature) and consequently temperature difference between water and the surrounding rock will decrease. This results in diminishing heat exchange. This can be seen in figure S3. As flow time increases; we have a decrease in flowing water temperature drops versus depth travelled. The role of flow time is quite variable and the apparent temperature change can be as large as 0.4°C, over a travel distance of 100 m. It has a very high impact on the early times while the effect becomes negligible as the flow time increases. Therefore, borehole flowmeter at a given time requires knowledge of the dynamics of the flowing zones.

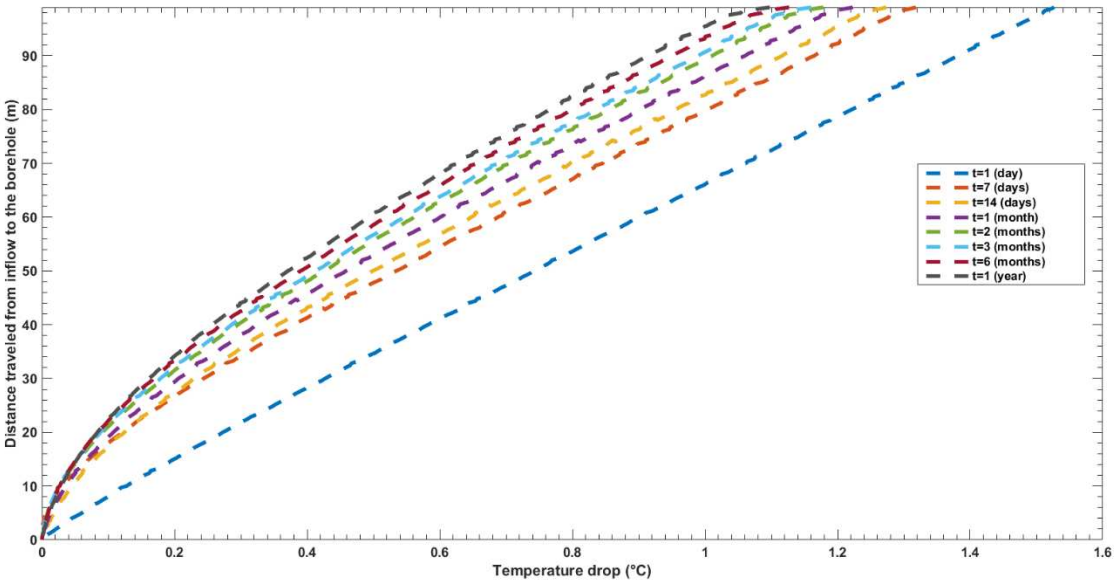

Figure S-4: Effect of flow time on flowing water temperature drop versus depth travelled in the borehole

4.10.7 Heat-Pulse flowmeter calibration curve

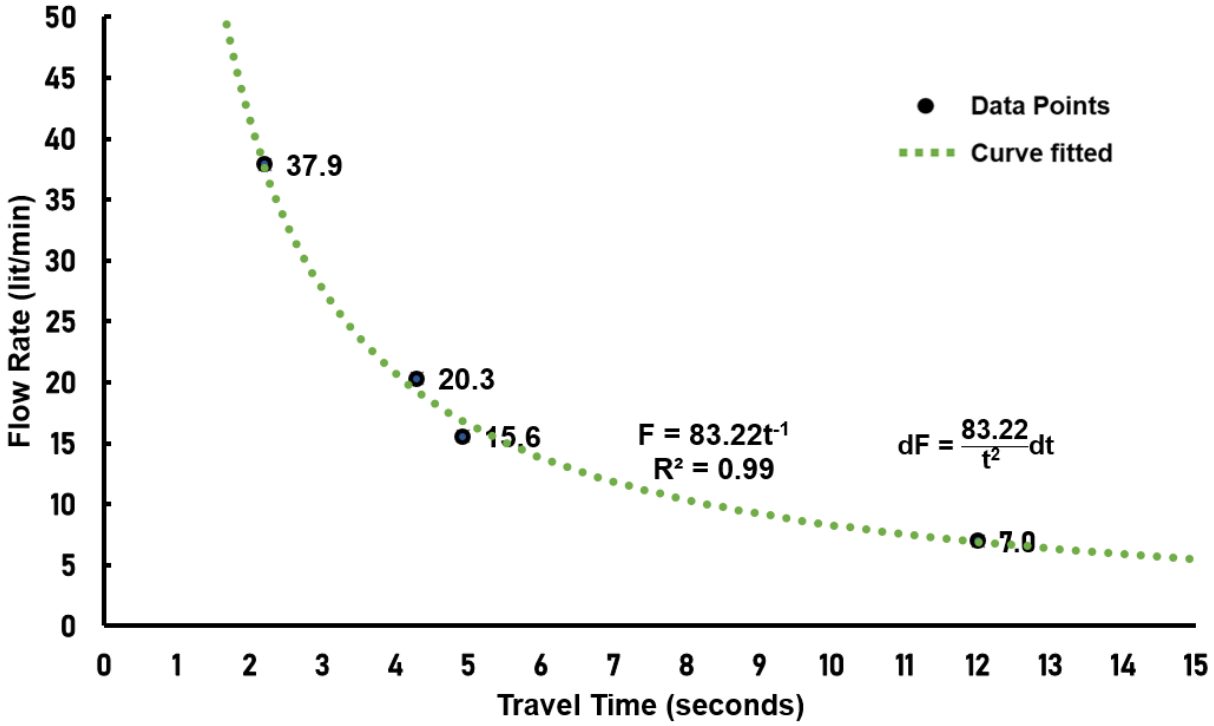

Figure S-5: Calibration curve obtained to calibrate the HPFM data

Chapter 5 Conclusions

5.1 Achieved results

The use of heat as a groundwater tracer has attained much attention in recent years as it is ubiquitous, easy to measure with inexpensive temperature sensors. In this thesis, we rely on using Fiber Optic Distributed Temperature Sensors (FO-DTS), a technology allowing to measure the temperature in space along the FO cable and with time. FO-DTS can be operated in passive and active modes. In the active mode, heat is added to the FO cable by heating element beside the cable inducing artificial temperature anomalies, while in the passive mode, natural variability of temperature is measured. FO cables can be hanged inside the boreholes or deployed vertically into the unconsolidated aquifer (in direct contact with the formation) using the direct-push method. The recorded temperature data along the FO cable can then be used to estimate the groundwater flow. This thesis aims to investigate and develop methods to use heat for quantifying the subsurface flow and further use the flow data to map and image the subsurface media heterogeneity. One of the most favourable techniques to reconstruct the aquifer heterogeneity is hydraulic tomography. In hydraulic tomography, the aquifer is subjected to a disturbance (classically pumping although heat and solute tracers are also popular), and the aquifer response is monitored at different points across the aquifer. The observed aquifer response with a numerical model undergoes an inversion process to reconstruct the aquifer heterogeneity.

In Chapter 2, a comparative numerical study is performed to assess the merit of flux data (which can be measured by Active FO-DTS) and head data (which is conventionally used in hydraulic tomography) in the reconstruction of the aquifer heterogeneity. A 2-D aquifer model with the gaussian distribution of the hydraulic conductivity is considered to simulate a hydraulic tomography test. The aquifer has five boreholes, arranged in a square pattern with four boreholes at the square's vertexes and one borehole in the middle. The aquifer is subjected to a series of pumping and head, and flux data are measured in non-pumping boreholes. In order to investigate the effect of the number of observations, additional observation points are considered. The minimum number of observation points are the four boreholes and the maximum number comprises the borehole and 28 additional observation points. The simulated head and flux data are then used solely and jointly to map the aquifer heterogeneity using geostatistical inversion. It is found that, for the small number of observations, flux data better captures the heterogeneity than the head data. As the number of observation points increases, both data perform the same, and the final inversion result will be independent of the data type. Considering the same number of observations, the joint inversion does not offer any advantage over the flux or head data. Nevertheless, for the same number of observation points, if we are able to measure the head and flux data at the same location, this will provide an improved estimate compared to the inversion of sole head or flux data due to double number of observation. We also found that the success of the inversion with solely head and flux data is dependent on the boundary condition imposed on the borehole. Head data performs the best with constant rate pumping at the borehole, while the flux data perform better with the constant head boundary condition at the borehole. Joint inversion of both data is independent of the type of boundary. It should be noted that the type of borehole boundary condition may be important just for steady-state hydraulic tomography. For the current techniques, steady-state flow condition is required to infer the flux data from active distributed temperature data.

Motivated by the results from Chapter 2, we designed a hydraulic tomography experiment in which head and flux data are measured simultaneously at few points across the aquifer. The Saint-Lambert site in the south of Quebec City, Canada, which hosts a sandy granular shallow aquifer and decommissioned sanitary landfill, is chosen to perform designed joint hydraulic tomography of head and flux data. The experimental site has 7 boreholes and two FO cables were deployed vertically into the ground by the direct-push method months before the start of the experiment to ensure that formation will surround the FO cables correctly. The borehole in the middle of the aquifer was chosen as the pumping borehole, and the head was observed

in four open boreholes and two boreholes equipped with the packers to measure the head at different isolated intervals. The flux was also measured by the A-FO DTS cable installed between the pumping borehole and two boreholes equipped with packers. The whole experiment took around 92 hours and started by pumping from the central borehole and recoding the passive temperature data by FO-cables and pressures in the surrounding borehole. After 19 hours of passive temperature data monitoring and ensuring of steady-state hydraulic condition, the heat was added to FO-cables. The effective heating period during the steady-state condition lasted for about 28 hours. It is worth mentioning that, to the best of our knowledge, this is one of the rare experiments in which FO cables were inserted in a sandy aquifer using direct-push method, and this is only the first time that hydraulic tomography is performed using groundwater flux data. The experiment was therefore very innovative but also very speculative since it required specific FO-splicing and FO cable insertion within the direct-push rods that were very uncertain. Despite these challenges, and some others incidence encountered in the field, the experiment has been a success since it has been possible to achieve active-DTS heat dissipation tests during a pumping experiment similar to most of classical hydraulic tomography experiments. Given the relative low permeability of the field site, it should be mentioned that a longer heating duration would certainly have provided a better estimation of groundwater fluxes. Nevertheless, the experiments provided some consistent data that could be used in the inversion process to test the added value of groundwater flux measurements to image subsurface hydraulic properties. The acquired head and flux data were used with a geostatistical inversion method to estimate the field's hydraulic conductivity. The geostatistical information about the site was obtained by analyzing the data from the cone penetration test previously conducted. The inversion was performed using recorded head data and joint inversion of head and flux data. The inversion with head data provides relative information about the distribution of the low and moderate hydraulic conductivity values. Obviously, there is a high uncertainty in the area where no or few head data are recorded. However, joint inversion of head and flux data provides more detailed hydraulic conductivity distribution map. Our results suggest that the Y-field estimate improvements are mainly due to the high density of FO measurements that provide a great number of observations in a single location. It is worth mentioning that the range of hydraulic conductivities obtained during the inversion are consistent with results from previous studies

The application of the approach mentioned above in the fractured aquifer would also be interesting. However, the deployment of the FO cable by direct push methods is only applicable to shallow unconsolidated media and can not be used for crystalline rock. Furthermore, there has been some attempts to quantify the flow in the fracture by using A-FO DTS between the borehole wall and a liner that keeps the A-FO DTS in close contact with the formation (Maldaner et al., 2019; Munn et al., 2020). However, the current spatial resolution of the DTS does not allow to measure precisely the flux coming from the fractures and such fluxes measurements in fractures are difficult to extrapolate at greater scale. To overcome this challenge, in Chapter 4, we developed a method to use the passive temperature profile (passive DTS data) of the water inside the borehole to quantify the vertical flow in different borehole segments and quantify the real-time contribution of each fracture to the total flow. The basic concept behind using the passive temperature profile for vertical flow quantification is based on the deviation from the geothermal gradient. If there is no flow in the borehole, the stagnant water temperature should follow the geothermal gradient, but as soon as the water starts flowing, the water temperature variations with depth will deviate from the geothermal gradient. The temperature profile of water inside the borehole can be described by analytical solutions provided by Ramey (1962) and Hassan & Kabir (2002, 2005), which are derived by considering the heat transfer model between water and the formation. The two above mentioned equations describe the water temperature profile as a function of the water velocity and thermal properties of the water and the formation (Geothermal gradient, thermal conductivity of the rock, flow time). Assuming proper knowledge of the thermal properties,

one can use the analytical solutions and passive temperature profile to estimate the velocity profile and thus the flow rate profile in the borehole.

Firstly, the accuracy of the analytical solutions was tested against a numerical model simulating the temperature of flowing water inside the borehole. The simulated temperature profile was used by the analytical solution to estimate the velocity assumed in the numerical model. Results show that velocity assumed in the numerical model was estimated with error of less than 10% which would certify the acceptable accuracy of the analytical solution. Next, a global sensitivity analysis was performed to assess sensitivity of the estimated flow to different parameters. We found that, geothermal gradient is the most sensitive parameter followed by thermal conductivity of the rock and also flow time. The geothermal gradient defines the heat transfer deriving force while the thermal conductivity acts as a controlling parameter on the heat transfer process. The flow time affects the near borehole region temperature and thus has an effect on the heat transfer deriving force but its effect will be minimum in large flow time. Next, the approach was tested on a fractured borehole in the Guidel site, Brittany, France. The passive temperature profile was measured in the borehole by FO-DTS for around 45 hours, comprising two ambient and one pumping flow condition. The vertical flow profile along the borehole was also measured by heat-pulse flow meter in all three hydraulic conditions. The passive temperature profile and analytical solutions were used to obtain the flow profile inside the borehole and were compared with the flow profile recorded by heat-pulse flowmeter. The results show that flow profile specially for ambient flow is in good accordance with results from heat-pulse flow meter. The flow profiling using passive temperature profile requires knowledge of the thermal properties of the media which may not be necessarily available. However, we showed that by measuring the flow at some points in the borehole or at the surface, we may estimate a set of thermal properties that may not necessarily represent the real thermal properties of the media but can be used for the purpose of the flow profiling using the passive temperature data.The passive temperature data by FO-DTS provides interesting dynamic behaviour of the fractured aquifer at borehole scale. The temperature data can be further used to analyse the fracture contribution and also the interaction with time. The fracture flow contribution with time can be insightful about the mixing that may occur at the borehole scale. It is worth also reminding that FO-DTS is operationally more convenient than other measurement methods due to narrow size of FO cables and hard covering material, making it suitable for minimum invasion inside the media and also for harsh conditions.

5.2 Future developments

The effect of number of observation points in the synthetic hydraulic tomography test revealed that as the number of observation increases, correlation coefficient between the estimated and real hydraulic conductivity field also increases up to a certain value after which no more significant improvement is observed. Bearing in mind that hydraulic tomography is quite time-consuming and also expensive operation, it would be interesting to perform numerical studies on hydraulic conductivity fields with different geostatistical features to answer the question of optimum design of hydraulic tomography test with optimum number of observations and also optimum observation locations.

Considering the practical feasibility of the subsurface flux measurement, it would be interesting to investigate the advantages of including the flux data in thermal/solute tracer tomography. To do so, Firstly, a numerical study must be conducted to assess the advantages or disadvantages of including the measured flux data into tracer experiment. Afterward, the field application might be investigated by performing a small scale experiment. Such groundwater fluxes measurements may be also particularly relevant to optimize site remediation operations.

Bearing in mind the geophysical approach advantages and the fact that Spontaneous potential is the only geophysical method directly related to the groundwater flow, it would be very interesting to compare the scale and relation of the groundwater flux measurement by A-FO DTS and also SP method. The first step would be using a laboratory sand box and measuring the water flux using both methods to enrich our understanding about the different aspects, scales and also the relationship between two measurements. Next step would be testing the hypothesis in a hydraulic tomography experiment in which A-FO DTS and SP are used for the measurement of the groundwater flux. Upon understanding the relationship between two measurements, the SP measurements can be used along the A-FO DTS measurement to obtain many observations and perform a high resolution hydraulic conductivity imaging. If this hypothesis works, it can probably reduce the cost and also the time of the hydraulic tomography experiments.

The proposed flux profile estimation method relies on the A-FO DTS data at Saint-Lambert site, but it should be possible to deduce some information about groundwater fluxes by using passive FO-DTS data. Thus, it should be interesting to use vertical temperature profile for better assessing natural fluxes or check that no-flow conditions are met before the beginning of pumping. A numerical study would be required to investigate the possibility of using passive temperature data and also dynamic temperature change to deduce the value of the flux. The data acquired in Saint-Lambert site also comprise the passive temperature data before the active heating was started. The flux data obtained by the passive could be then compared to those values obtained by active heating presented in this thesis. If the results agree well with each other, then it would be interesting to assess the possibility of using the passive temperature data in hydraulic tomography. It must be noted that using passive temperature profile, we may lose the advantage of the distributed flux measurement but at least it can be used to assess the consistency of the results with the flux from active measurement. It would also be interesting to plan for improvement of the current experiment by having a longer heating period. Furthermore, the current experiment could be expanded by obtaining more data. We may plan for employing additional FO cables or performing a series of pumping at all boreholes to obtain more data and perform a comprehensive tomography. The test performed was a preliminary successful hydraulic tomography test with relatively low groundwater flux values. However, it can be interesting to test the methodology on a site with higher value of hydraulic conductivity like the Valcartier site (near Quebec City) where groundwater flow is higher and the methodology could bring more interesting results.

The vertical flow profiling approach using passive temperature data presented in Chapter 4, could also be applied to tidal hydraulic tomography. In classical tidal hydraulic tomography, the head fluctuation data is used to infer the hydraulic properties of the aquifers (which are subjected to the tidal effect) while it would be interesting to use the flow data solely and jointly with head fluctuation in hydraulic tomography. However, this approach would be limited to artesian boreholes with tidal effect. Despite the hydraulic tomography with temperature data, it would be interesting to infer the flux fluctuation over depth and time. A very recent paper addresses the use of temperature in addition to the pressure of water in coastal sediments to quantify the exchanges between coastal sediments and overlaying coastal sediment bodies (LeRoux et al., 2020). A complementary application would be installing the Active FO cable in the beach to characterize how the flux varies over the depth (due to heterogeneities) and with time (due to tidal forces).

Even though, there has been numerous research conducted to develop the use of heat in hydrology but it is still an underused tool which requires further researches and developments. We should bear in mind that heat is more environmentally friendly tracer compared to other solute tracers and can be measured easily with great accuracy and over the time. The spatio-temporal recording of the temperature further allows to capture the dynamic of hydrology systems if the relation between the temperature and the system is well understood.

References

1- Alemán, D.I.O., 2018. Fracture Flow Rate Estimation Using Machine Learning On Temperature Data (Doctoral dissertation, Stanford University).

2- Alumbaugh, D., Chang, P.Y., Paprocki, L., Brainard, J.R., Glass, R.J., Rautman, C.A., 2002. Estimating moisture contents in the vadose zone using cross-borehole ground penetrating radar: A study of accuracy and repeatability. Water Resour. Res. 38, 41–45.

3- Alumbaugh, D.L., Newman, G.A., 2000. Image appraisal for 2-D and 3-D electromagnetic inversion. Geophysics 65, 1455–1467.

4- Anderson, M.P., 2005. Heat as a ground water tracer. Groundwater 43, 951–968.

5- Angermann, L., Krause, S., Lewandowski, J., 2012a. Application of heat pulse injections for investigating shallow hyporheic flow in a lowland river. Water Resour. Res. 48.

6- Angermann, L., Lewandowski, J., Fleckenstein, J.H., Nützmann, G., 2012b. A 3D analysis algorithm to improve interpretation of heat pulse sensor results for the determination of small-scale flow directions and velocities in the hyporheic zone. J. Hydrol. 475, 1–11.

7- Archie, G.E., 1942. The electrical resistivity log as an aid in determining some reservoir characteristics. Trans. AIME 146, 54–62.

8- Bakker, M., Caljé, R., Schaars, F., van der Made, K., de Haas, S., 2015. An active heat tracer experiment to determine groundwater velocities using fiber optic cables installed with direct push equipment. Water Resour. Res. 51, 2760–2772.

9- Ballard, S., 1996. The in situ permeable flow sensor: A ground-water flow velocity meter. Groundwater 34, 231–240.

10- Banks, E.W., Shanafield, M., Noorduijn, S., McCallum, J., Lewandowski, J., Batelaan, O., 2018. Active heat pulse sensing of 3-D-flow fields in streambeds.

11- Basinger, J.M., Kluitenberg, G.J., Ham, J.M., Frank, J.M., Barnes, P.L., Kirkham, M.B., 2003. Laboratory evaluation of the dual-probe heat-pulse method for measuring soil water content. Vadose Zo. J. 2, 389–399.

12- Bayless, E.R., Mandell, W.A., Ursic, J.R., 2011. Accuracy of flowmeters measuring horizontal groundwater flow in an unconsolidated aquifer simulator. Groundw. Monit. Remediat. 31, 48–62.

13- Bellin, A., Salandin, P., Rinaldo, A., 1992. Simulation of dispersion in heterogeneous porous formations: Statistics, first-order theories, convergence of computations. Water Resour. Res. 28, 2211–2227.

14- Bense, V.F., Read, T., Bour, O., Le Borgne, T., Coleman, T., Krause, S., Chalari, A., Mondanos, M., Ciocca, F., Selker, J.S., 2016. Distributed T emperature S ensing as a downhole tool in hydrogeology. Water Resour. Res. 52, 9259–9273.

15- Berg, S.J., Illman, W.A., 2015. Comparison of hydraulic tomography with traditional methods at a highly heterogeneous site. Groundwater 53, 71–89.

16- Berg, S.J., Illman, W.A., 2013. Field study of subsurface heterogeneity with steady-state hydraulic tomography. Groundwater 51, 29–40.

17- Berg, S.J., Illman, W.A., 2012. Improved predictions of saturated and unsaturated zone drawdowns in a heterogeneous unconfined aquifer via transient hydraulic tomography: Laboratory sandbox experiments. J. Hydrol. 470, 172–183.

18- Berg, S.J., Illman, W.A., 2011. Three-dimensional transient hydraulic tomography in a highly heterogeneous glaciofluvial aquifer-aquitard system. Water Resour. Res. 47.

19- Berg, S., 2011. Hydraulic Tomography: Field and Laboratory Experiments.

20- Berkowitz, B., 2002. Characterizing flow and transport in fractured geological media: A review. Advances in water resources, 25(8-12), pp.861-884.
21- Binley, A., Cassiani, G., Middleton, R., Winship, P., 2002. Vadose zone flow model parameterisation using cross-borehole radar and resistivity imaging. J. Hydrol. 267, 147–159.
22- Binley, A., Winship, P., Middleton, R., Pokar, M., West, J., 2001. High-resolution characterization of vadose zone dynamics using cross-borehole radar. Water Resour. Res. 37, 2639–2652.
23- Bochet, O., 2017. Caractérisation des hot spots de réactivité biogéochimique dans les eaux souterraines (Doctoral dissertation, Université Rennes 1).
24- Bochet, O., L. Bethencourt, A., Dufresne, J., Farasin, M., Pédrot, T., Labasque, E., Chatton, N., Lavenant, C., Petton, B.W., Abbott, L., Aquilina, and T. Le Borgne, 2020. Iron-oxidizer hotspots formed by intermittent oxic–anoxic fluid mixing in fractured rocks, Nature Geoscience 13(2), pp. 149-155
25- Bohling, G.C., Butler Jr, J.J., 2010. Inherent limitations of hydraulic tomography. Groundwater 48, 809–824.
26- Bohling, G.C., Butler Jr, J.J., Zhan, X., Knoll, M.D., 2007. A field assessment of the value of steady shape hydraulic tomography for characterization of aquifer heterogeneities. Water Resour. Res. 43.
27- Börner, F.D., Schopper, J.R., Weller, A., 1996. Evaluation of transport and storage properties in the soil and groundwater zone from induced polarization measurements1. Geophys. Prospect. 44, 583–601.
28- Bravo, H.R., Jiang, F., Hunt, R.J., 2002. Using groundwater temperature data to constrain parameter estimation in a groundwater flow model of a wetland system. Water Resour. Res. 38, 21–28.
29- Brauchler, R., Hu, R., Dietrich, P., Sauter, M., 2011. A field assessment of high-resolution aquifer characterization based on hydraulic travel time and hydraulic attenuation tomography. Water Resour. Res. 47.
30- Brauchler, R., Hu, R., Hu, L., Jiménez, S., Bayer, P., Dietrich, P., Ptak, T., 2013. Rapid field application of hydraulic tomography for resolving aquifer heterogeneity in unconsolidated sediments. Water Resour. Res. 49, 2013–2024.
31- Brauchler, R., Hu, R., Vogt, T., Al-Halbouni, D., Heinrichs, T., Ptak, T., Sauter, M., 2010. Cross-well slug interference tests: An effective characterization method for resolving aquifer heterogeneity. J. Hydrol. 384, 33–45.
32- Brauchler, R., Liedl, R., Dietrich, P., 2003. A travel time based hydraulic tomographic approach. Water Resour. Res. 39.
33- Bredehoeft, J.D., Papaopulos, I.S., 1965. Rates of vertical groundwater movement estimated from the Earth's thermal profile. Water Resour. Res. 1, 325–328.
34- Brewster, M.L., Annan, A.P., 1994. Ground-penetrating radar monitoring of a controlled DNAPL release: 200 MHz radar. Geophysics 59, 1211–1221.
35- Bristow, K.L., 1998. Measurement of thermal properties and water content of unsaturated sandy soil using dual-probe heat-pulse probes. Agric. For. Meteorol. 89, 75–84.
36- Brouyère, S., Batlle-Aguilar, J., Goderniaux, P., Dassargues, A., 2008. A new tracer technique for monitoring groundwater fluxes: The Finite Volume Point Dilution Method. J. Contam. Hydrol. 95, 121–140.
37- Campbell, G.S., Calissendorff, C. and Williams, J.H., 1991. Probe for measuring soil specific heat using a heat-pulse method. Soil Science Society of America Journal, 55(1), pp.291-293.
38- Cao, V., Schaffer, M., Taherdangkoo, R., Licha, T., 2020. Solute reactive tracers for hydrogeological applications: A short review and future prospects. Water 12, 653.

39- Cardiff, M., Bakhos, T., Kitanidis, P.K., Barrash, W., 2013. Aquifer heterogeneity characterization with oscillatory pumping: Sensitivity analysis and imaging potential. Water Resour. Res. 49, 5395–5410.
40- Cardiff, M., Barrash, W., 2011. 3-D transient hydraulic tomography in unconfined aquifers with fast drainage response. Water Resour. Res. 47.
41- Cardiff, M., Barrash, W., Kitanidis, P.K., 2013. Hydraulic conductivity imaging from 3-D transient hydraulic tomography at several pumping/observation densities. Water Resour. Res. 49, 7311–7326.
42- Cardiff, M., Barrash, W., Kitanidis, P.K., 2012. A field proof-of-concept of aquifer imaging using 3-D transient hydraulic tomography with modular, temporarily-emplaced equipment. Water Resour. Res. 48.
43- Cardiff, M., Barrash, W., Kitanidis, P.K., Malama, B., Revil, A., Straface, S., Rizzo, E., 2009. A potential-based inversion of unconfined steady-state hydraulic tomography. Groundwater 47, 259–270.
44- Carslaw, H. S., & Jaeger, J. C. (1959). Conduction of heat in solids, Oxford, UK: Oxford University Press. https://infoscience.epfl.ch/record/27427
45- Chatelier, M., Ruelleu, S., Bour, O., Porel, G. and Delay, F., 2011. Combined fluid temperature and flow logging for the characterization of hydraulic structure in a fractured karst aquifer. Journal of Hydrology, 400(3-4), pp.377-386.
46- Chen, J., 2007. Bin-nan San 56 block thermal analysis of steam injection well and estimation of insulation technology.
47- Chen, S., Beard, D., Gillen, M., Fang, S., Zhang, G., 2003. MR explorer log acquisition methods: Petrophysical-objective-oriented approaches, in: SPWLA 44th Annual Logging Symposium. Society of Petrophysicists and Well-Log Analysts.
48- Cheviron, B., Guérin, R., Tabbagh, A. and Bendjoudi, H., 2005. Determining long-term effective groundwater recharge by analyzing vertical soil temperature profiles at meteorological stations. Water resources research, 41(9).
49- Cleveland, W.S., 1979. Robust locally weighted regression and smoothing scatterplots. Journal of the American statistical association, 74(368), pp.829-836.
50- Coleman, T.I., Parker, B.L., Maldaner, C.H., Mondanos, M.J., 2015. Groundwater flow characterization in a fractured bedrock aquifer using active DTS tests in sealed boreholes. Journal of Hydrology, 528: 449-462.
51- Comsol multiphysics® v. 5.4. (2018). COMSOL AB, Stockholm, Sweden. (from www.comsol.com)
52- Conant Jr, B., 2004. Delineating and quantifying ground water discharge zones using streambed temperatures. Groundwater 42, 243–257.
53- Constantz, J., Niswonger, R.G., Stewart, A.E., 2008. Analysis of temperature gradients to determine stream exchanges with ground water. F. Tech. Estim. Water Fluxes Between Surf. Water Gr. Water 4-D2.
54- Constantz, J., Stewart, A.E., Niswonger, R., Sarma, L., 2002. Analysis of temperature profiles for investigating stream losses beneath ephemeral channels. Water Resour. Res. 38, 51–52.
55- Curtis, G.P., Roberts, P. V, Reihard, M., 1986. A natural gradient experiment on solute transport in a sand aquifer: 4. Sorption of organic solutes and its influence on mobility. Water Resour. Res. 22, 2059–2067.
56- Dagan, G., 1987. Theory of solute transport by groundwater. Annu. Rev. Fluid Mech. 19, 183–213.
57- Dagan, G., 1984. Solute transport in heterogeneous porous formations. J. Fluid Mech. 145, 151–177.
58- Davis, J.L., ANNAN, A.P., 1989. Ground-penetrating radar for high-resolution mapping of soil and rock stratigraphy 1. Geophys. Prospect. 37, 531–551.

59- Davy, P., Bour, O., De Dreuzy, J.R. and Darcel, C., 2006. Flow in multiscale fractal fracture networks. Geological Society, London, Special Publications, 261(1), pp.31-45.
60- Day-Lewis, F.D., Johnson, C.D., Paillet, F.L. and Halford, K.J., 2011. A computer program for flow-log analysis of single holes (FLASH). Groundwater, 49(6), pp.926-931.
61- Day-Lewis, F.D., Singha, K., Binley, A.M., 2005. Applying petrophysical models to radar travel time and electrical resistivity tomograms: Resolution-dependent limitations. J. Geophys. Res. Solid Earth 110.
62- Day-Lewis, F.D., Slater, L.D., Robinson, J., Johnson, C.D., Terry, N. and Werkema, D., 2017. An overview of geophysical technologies appropriate for characterization and monitoring at fractured-rock sites. Journal of environmental management, 204, pp.709-720.
63- de La Bernardie, J., Bour, O., Le Borgne, T., Guihéneuf, N., Chatton, E., Labasque, T., Le Lay, H. and Gerard, M.F., 2018. Thermal attenuation and lag time in fractured rock: theory and field measurements from joint heat and solute tracer tests. Water Resources Research, 54(12), pp.10-053.
64- de Dreuzy, Bodin, J., Le Grand, H., Davy, P., Boulanger D., Battais A., Bour O., Gouze P., Porel G., 2006. Groundwater database for site and processes studies : Point-like structure based on well, meteorological and hydrological platforms, Groundwater,44(5), pp 743-748.
65- De Lima, O.A.L., Niwas, S., 2000. Estimation of hydraulic parameters of shaly sandstone aquifers from geoelectrical measurements. J. Hydrol. 235, 12–26.
66- De Marsily, G., Delay, F., Gonçalvès, J., Renard, P., Teles, V., Violette, S., 2005. Dealing with spatial heterogeneity. Hydrogeol. J. 13, 161–183.
67- Delhomme, J.P., 1978. Kriging in the hydrosciences. Adv. Water Resour. 1, 251–266.
68- Deming, J., Investigators, N.S.C. and P., 1993. Northeast water polynya: Polar Sea cruise results. Eos, Trans. Am. Geophys. Union 74, 185–196.
69- Dentz, M., Le Borgne, T., Englert, A., Bijeljic, B., 2011. Mixing, spreading and reaction in heterogeneous media: A brief review. J. Contam. Hydrol. 120, 1–17.
70- des Tombe, B., Schilperoort, B. and Bakker, M., 2020. Estimation of Temperature and Associated Uncertainty from Fiber-Optic Raman-Spectrum Distributed Temperature Sensing. Sensors, 20(8), p.2235.
71- des Tombe, B.F., Bakker, M., Smits, F., Schaars, F., van der Made, K., 2019. Estimation of the variation in specific discharge over large depth using distributed temperature sensing (DTS) measurements of the heat pulse response. Water Resour. Res. 55, 811–826.
72- des Tombe, B., Schilperoort, B. and Bakker, M., 2020. Estimation of Temperature and Associated Uncertainty from Fiber-Optic Raman-Spectrum Distributed Temperature Sensing. Sensors, 20(8), p.2235.
73- Devlin, J.F., Tsoflias, G., McGlashan, M., Schillig, P., 2009. An inexpensive multilevel array of sensors for direct ground water velocity measurement. Groundw. Monit. Remediat. 29, 73–77.
74- De Vriendt, K., Pool, M. and Dentz, M., 2020. Heterogeneity-Induced Mixing and Reaction Hot Spots Facilitate Karst Propagation in Coastal Aquifers. Geophysical Research Letters, 47(10), p.e2020GL087529.
75- Domenico, P.A., Schwartz, F.W., 1998. Physical and chemical hydrogeology. Wiley New York.
76- Doro, K.O., Cirpka, O.A., Leven, C., 2015. Tracer tomography: Design concepts and field experiments using heat as a tracer. Groundwater 53, 139–148.
77- Doussan, C., Toma, A., Paris, B., Poitevin, G., Ledoux, E., Detay, M., 1994. Coupled use of thermal and hydraulic head data to characterize river-groundwater exchanges. J. Hydrol. 153, 215–229.

78- Drost, W., Klotz, D., Koch, A., Moser, H., Neumaier, F., Rauert, W., 1968. Point dilution methods of investigating ground water flow by means of radioisotopes. Water Resour. Res. 4, 125–146.
79- Dupuit, J., 1857. Mouvement de l'eau a travers le terrains permeables. CR Hebd. Seances Acad. Sci, 45, pp.92-96.
80- Dwarakanath, V., Dean, R.M., Slaughter, W., Alexis, D., Espinosa, D., Kim, D.H., Lee, V., Malik, T., Winslow, G., Jackson, A.C., 2016. Permeability reduction due to use of liquid polymers and development of remediation options, in: SPE Improved Oil Recovery Conference. Society of Petroleum Engineers.
81- Edwardson, M.J., Girner, H.M., Parkison, H.R., Williams, C.D., Matthews, C.S., 1962. Calculation of formation temperature disturbances caused by mud circulation. J. Pet. Technol. 14, 416–426.
82- Emsellem, Y., De Marsily, G., 1971. An automatic solution for the inverse problem. Water Resour. Res. 7, 1264–1283.
83- Fakhreddine, S., Lee, J., Kitanidis, P.K., Fendorf, S., Rolle, M., 2016. Imaging geochemical heterogeneities using inverse reactive transport modeling: An example relevant for characterizing arsenic mobilization and distribution. Adv. Water Resour. 88, 186–197.
84- Ferguson, G., Beltrami, H. and Woodbury, A.D., 2006. Perturbation of ground surface temperature reconstructions by groundwater flow?. Geophysical research letters, 33(13).
85- Ferguson, C., Husman, A.M. de R., Altavilla, N., Deere, D., Ashbolt, N., 2003. Fate and transport of surface water pathogens in watersheds.
86- Fienen, M.N., Clemo, T., Kitanidis, P.K., 2008. An interactive Bayesian geostatistical inverse protocol for hydraulic tomography. Water Resour. Res. 44.
87- Fienen, M., Hunt, R., Krabbenhoft, D., Clemo, T., 2009. Obtaining parsimonious hydraulic conductivity fields using head and transport observations: A Bayesian geostatistical parameter estimation approach. Water Resour. Res. 45.
88- Fiori, A., Jankovic, I., 2012. On preferential flow, channeling and connectivity in heterogeneous porous formations. Math. Geosci. 44, 133–145.
89- Fischer, P., Jardani, A., Lecoq, N., 2018. Hydraulic tomography of discrete networks of conduits and fractures in a karstic aquifer by using a deterministic inversion algorithm. Adv. Water Resour. 112, 83–94.
90- Fischer, P., Jardani, A., Cardiff, M., Lecoq, N. and Jourde, H., 2018. Hydraulic analysis of harmonic pumping tests in frequency and time domains for identifying the conduits networks in a karstic aquifer. Journal of Hydrology, 559, pp.1039-1053.
91- Fischer, P., Jardani, A., Soueid Ahmed, A., Abbas, M., Wang, X., Jourde, H., Lecoq, N., 2017. Application of Large-Scale Inversion Algorithms to Hydraulic Tomography in an Alluvial Aquifer. Groundwater 55, 208–218.
92- Francisca, F.M., Rinaldi, V.A., 2001. The potential application of the GPR to detect organic contaminants in sand, in: International Conference on Soil Mechanics and Geotechnical Engineering. pp. 405–408.
93- Freeze, R.A., 1975. A stochastic-conceptual analysis of one-dimensional groundwater flow in nonuniform homogeneous media. Water Resour. Res. 11, 725–741.
94- Freeze, R.A., Witherspoon, P.A., 1967. Theoretical analysis of regional groundwater flow: 2. Effect of water-table configuration and subsurface permeability variation. Water Resour. Res. 3, 623–634.
95- Frei, S., Fleckenstein, J.H., Kollet, S.J., Maxwell, R.M., 2009. Patterns and dynamics of river–aquifer exchange with variably-saturated flow using a fully-coupled model. J. Hydrol. 375, 383–393.

96- Freyberg, D.L., 1986. A natural gradient experiment on solute transport in a sand aquifer: 2. Spatial moments and the advection and dispersion of nonreactive tracers. Water Resour. Res. 22, 2031–2046.

97- Gaillardet, J., Braud, I., Hankard, F., Anquetin, S., Bour, O., Dorfliger, N., De Dreuzy, J.R., Galle, S., Galy, C., Gogo, S. and Gourcy, L., 2018. OZCAR: The French network of critical zone observatories. Vadose Zone Journal, 17(1), pp.1-24.

98- Gavalas, G.R., Shah, P.C., Seinfeld, J.H., 1976. Reservoir history matching by Bayesian estimation. Soc. Pet. Eng. J. 16, 337–350.

99- Greswell, R.B., Riley, M.S., Alves, P.F. and Tellam, J.H., 2009. A heat perturbation flow meter for application in soft sediments. Journal of hydrology, 370(1-4), pp.73-82.

100- Gelhar, L.W., Axness, C.L., 1983. Three-dimensional stochastic analysis of macrodispersion in aquifers. Water Resour. Res. 19, 161–180.

101- Gelhar, L.W., LW, G., 1976. Effects of hydraulic conductivity variations on groundwater flows.

102- Gelhar, Lynn W, Gelhar, L W, 1993. Stochastic subsurface hydrology. Prentice-Hall Englewood Cliffs, NJ.

103- Gottlieb, J., Dietrich, P., 1995. Identification of the permeability distribution in soil by hydraulic tomography. Inverse Probl. 11, 353.

104- Gutiérrez, M.G., Guimera, J., De Llano, A.Y., Benitez, A.H., Humm, J., Saltink, M., 1997. Tracer test at El Berrocal site. J. Contam. Hydrol. 26, 179–188.

105- Hagoort, J., 2004. Ramey's wellbore heat transmission revisited. SPE J. 9, 465–474.

106- Hall, S.H., 1993. Single well tracer tests in aquifer characterization. Ground Water Monit. Remediat. 13, 118–124.

107- Hasan, A.R., Kabir, C.S., 2007. A simple model for annular two-phase flow in wellbores, SPE Production & Operation. 22 (2): 168-175

108- Hasan, A.R., Kabir, C.S., 2005. A simple model for annular two-phase flow in wellbores, in: SPE Annual Technical Conference and Exhibition. Society of Petroleum Engineers.

109- Hasan, A.R., Kabir, C.S., 1994. Aspects of wellbore heat transfer during two-phase flow (includes associated papers 30226 and 30970). SPE Prod. Facil. 9, 211–216.

110- Hasan, A.R., Kabir, C.S., Sarica, C., 2002. Fluid flow and heat transfer in wellbores. Society of Petroleum Engineers Richardson, TX.

111- Hasan, A.R., Kabir, C.S., Wang, X., Hughes, B., 2009. A Robust Steady-State Model for Flowing-Fluid Temperature in Complex Wells.

112- Hatfield, K., Annable, M., Cho, J., Rao, P.S.C., Klammler, H., 2004. A direct passive method for measuring water and contaminant fluxes in porous media. J. Contam. Hydrol. 75, 155–181.

113- Heigold, P.C., Gilkeson, R.H., Cartwright, K., Reed, P.C., 1979. Aquifer transmissivity from surficial electrical methods. Groundwater 17, 338–345.

114- Heitman, J.L., Basinger, J.M., Kluitenberg, G.J., Ham, J.M., Frank, J.M., Barnes, P.L., 2003. Field evaluation of the dual-probe heat-pulse method for measuring soil water content. Vadose Zo. J. 2, 552–560.

115- Herckenrath, D., Auken, E., Christiansen, L., Behroozmand, A.A., Bauer-Gottwein, P., 2012. Coupled hydrogeophysical inversion using time-lapse magnetic resonance sounding and time-lapse gravity data for hydraulic aquifer testing: Will it work in practice? Water Resour. Res. 48.

116- Hess, A.E., 1986. Identifying hydraulically conductive fractures with a slow-velocity borehole flowmeter. Canadian Geotechnical Journal, 23(1), pp.69-78.

117- Hyndman, D.W., Harris, J.M. and Gorelick, S.M., 2000. Inferring the relation between seismic slowness and hydraulic conductivity in heterogeneous aquifers. Water Resources Research, 36(8), pp.2121-2132.

118- Hopmans, J.W., Šimunek, J., Bristow, K.L., 2002. Indirect estimation of soil thermal properties and water flux using heat pulse probe measurements: Geometry and dispersion effects. Water Resour. Res. 38, 1–7.

119- Horne, R.N., Shinohara, K., 1979. Wellbore Heat Loss in Production and Injection Wells. J. Pet. Technol. 31, 116–118. https://doi.org/10.2118/7153-PA

120- Hossain, M.E., Abu-Khamsin, S.A., 2012. Utilization of memory concept to develop heat transfer dimensionless numbers for porous media undergoing thermal flooding with equal rock and fluid temperatures. J. Porous Media 15.

121- Hsieh, P.A., 1998. Scale Effects in Fluid Flow Through Fractured Geological Media, Scale Dependence and Scale Invariance in Hydrology. Cambridge University Press , pp. 335–353

122- Huang, Y., Ferro-Famil, L., Reigber, A., 2011. Under-foliage object imaging using SAR tomography and polarimetric spectral estimators. IEEE Trans. Geosci. Remote Sens. 50, 2213–2225.

123- Huisman, J.A., Hubbard, S.S., Redman, J.D., Annan, A.P., 2003. Measuring soil water content with ground penetrating radar: A review. Vadose Zo. J. 2, 476–491.

124- Huisman, J.A., Snepvangers, J., Bouten, W., Heuvelink, G.B.M., 2002. Mapping spatial variation in surface soil water content: comparison of ground-penetrating radar and time domain reflectometry. J. Hydrol. 269, 194–207.

125- Illman, W.A., Berg, S.J., Alexander, M., 2012. Cost comparisons of aquifer heterogeneity characterization methods. Groundw. Monit. Remediat. 32, 57–65.

126- I Illman, W.A., Berg, S.J. and Yeh, T.C.J., 2012. Comparison of approaches for predicting solute transport: Sandbox experiments. Groundwater, 50(3), pp.421-431.

127- Illman, W.A., Berg, S.J., Zhao, Z., 2015. Should hydraulic tomography data be interpreted using geostatistical inverse modeling? A laboratory sandbox investigation. Water Resour. Res. 51, 3219–3237.

128- Illman, W.A., Craig, A.J., Liu, X., 2008. Practical issues in imaging hydraulic conductivity through hydraulic tomography. Groundwater 46, 120–132.

129- Illman, W. a, Liu, X., Craig, A., 2008. Evaluation of transient hydraulic tomography and common hydraulic characterization approaches through laboratory sandbox experiments. J. Environ. Eng. Manag. 18, 249–256.

130- Illman, W.A., Liu, X., Craig, A., 2007. Steady-state hydraulic tomography in a laboratory aquifer with deterministic heterogeneity: Multi-method and multiscale validation of hydraulic conductivity tomograms. J. Hydrol. 341, 222–234.

131- Illman, W.A., Liu, X., Takeuchi, S., Yeh, T.J., Ando, K., Saegusa, H., 2009. Hydraulic tomography in fractured granite: Mizunami Underground Research site, Japan. Water Resour. Res. 45.

132- Illman, W.A., Zhu, J., Craig, A.J., Yin, D., 2010. Comparison of aquifer characterization approaches through steady state groundwater model validation: A controlled laboratory sandbox study. Water Resour. Res. 46.

133- Imhoff, P.T., Pirestani, K., Jafarpour, Y., Spivey, K.M., 2003. Tracer interaction effects during partitioning tracer tests for NAPL detection. Environ. Sci. Technol. 37, 1441–1447.

134- Irvine, D.J., Simmons, C.T., Werner, A.D. and Graf, T., 2015. Heat and solute tracers: How do they compare in heterogeneous aquifers?. Groundwater, 53(S1), pp.10-20.

135- Izgec, B., Hasan, A.R., Lin, D., Kabir, C.S., 2010. Flow-rate estimation from wellhead-pressure and-temperature data. SPE Prod. Oper. 25, 31–39.

136- Jamin, P., Goderniaux, P., Bour, O., Le Borgne, T., Englert, A., Longuevergne, L., Brouyère, S., 2015. Contribution of the finite volume point dilution method for measurement of groundwater fluxes in a fractured aquifer. J. Contam. Hydrol. 182, 244–255.

137- Jardani, A., Revil, A., Boleve, A., Crespy, A., Dupont, J.P., Barrash, W. and Malama, B., 2007. Tomography of the Darcy velocity from self-potential measurements. Geophysical Research Letters, 34(24).

138- Jardani, A. and Revil, A., 2009. Stochastic joint inversion of temperature and self-potential data. Geophysical Journal International, 179(1), pp.640-654.

139- Jawitz, J.W., Annable, M.D., Demmy, G.G., Rao, P.S.C., 2003. Estimating nonaqueous phase liquid spatial variability using partitioning tracer higher temporal moments. Water Resour. Res. 39.

140- Jiménez, S., 2015. High resolution aquifer characterization using hydraulic tomography and tracer tomography.

141- Jiménez-Martínez, J., Longuevergne, L., Le Borgne, T., Davy, P., Russian, A. and Bour, O., 2013. Temporal and spatial scaling of hydraulic response to recharge in fractured aquifers: Insights from a frequency domain analysis. Water Resources Research, 49(5), pp.3007-3023.

142- Jiménez, S., Mariethoz, G., Brauchler, R., Bayer, P., 2016. Smart pilot points using reversible-jump Markov-chain Monte Carlo. Water Resour. Res. 52, 3966–3983.

143- Jouniaux, L., Maineult, A., Naudet, V., Pessel, M. and Sailhac, P., 2009. Review of self-potential methods in hydrogeophysics. Comptes Rendus Geoscience, 341(10-11), pp.928-936.

144- Kabir, C.S., Hasan, A.R., Kouba, G.E., Ameen, M., 1996. Determining circulating fluid temperature in drilling, workover, and well control operations. SPE Drill. Complet. 11, 74–79.

145- Kabir, C.S., Izgec, B., Hasan, A.R., Wang, X., Lee, J., 2008. Real-time estimation of total flow rate and flow profiling in dts-instrumented wells, in: International Petroleum Technology Conference. International Petroleum Technology Conference.

146- Kabir, C., Izgec, B., Hasan, A., Wang, X., 2012. Computing flow profiles and total flow rate with temperature surveys in gas wells. Journal of Natural Gas Science and Engineering, 4: 1-7.

147- Kang, P.K., Lee, J., Fu, X., Lee, S., Kitanidis, P.K., Juanes, R., 2017. Improved characterization of heterogeneous permeability in saline aquifers from transient pressure data during freshwater injection. Water Resour. Res. 53, 4444–4458.

148- Keery, J., Binley, A., Crook, N., Smith, J.W.N., 2007. Temporal and spatial variability of groundwater–surface water fluxes: Development and application of an analytical method using temperature time series. J. Hydrol. 336, 1–16.

149- Keys, W.S., 1990. Borehole geophysics applied to ground-water investigations (Vol. 6375). Dublin, Ohio: National Water Well Association.

150- Kitanidis, P.K., 1995. Quasi-linear geostatistical theory for inversing. Water Resour. Res. 31, 2411–2419.

151- Klammler, H.K.H., Annable, M., Agyei, E., Parker, B., Cherry, J., Rao, P.S.C., 2006. General analytical treatment of the flow field relevant for passive fluxmeter interpretation. Water Resour. Res.

152- Klepikova, M., Wildemeersch, S., Hermans, T., Jamin, P., Orban, P., Nguyen, F., Brouyère, S., Dassargues, A., 2016. Heat tracer test in an alluvial aquifer: Field experiment and inverse modelling. J. Hydrol. 540, 812–823.

153- Klepikova, M. V, Le Borgne, T., Bour, O., de Dreuzy, J., 2013. Inverse modeling of flow tomography experiments in fractured media. Water Resour. Res. 49, 7255–7265.

154- Klepikova, M. V, Le Borgne, T., Bour, O., Davy, P., 2011. A methodology for using borehole temperature-depth profiles under ambient, single and cross-borehole pumping conditions to estimate fracture hydraulic properties. J. Hydrol. 407, 145–152.

155- Klepikova, M., 2013. Imaging of fractured rock properties from flow and heat transport: field experiments and inverse modelling (Doctoral dissertation, Université Rennes 1).

156- Klepikova, M.V., Le Borgne, T., Bour, O., Gallagher, K., Hochreutener, R. and Lavenant, N., 2014. Passive temperature tomography experiments to characterize transmissivity and connectivity of preferential flow paths in fractured media. Journal of Hydrology, 512, pp.549-562.

157- Klotz, D., Seiler, K.P., Moser, H. and Neumaier, F., 1980. Dispersivity and velocity relationship from laboratory and field experiments. Journal of Hydrology, 45(3-4), pp.169-184.

158- Koltermann, C.E., Gorelick, S.M., 1996. Heterogeneity in sedimentary deposits: A review of structure-imitating, process-imitating, and descriptive approaches. Water Resour. Res. 32, 2617–2658.

159- Kowalsky, M.B., Finsterle, S., Rubin, Y., 2004. Estimating flow parameter distributions using ground-penetrating radar and hydrological measurements during transient flow in the vadose zone. Adv. Water Resour. 27, 583–599.

160- Kluth, R., Naldrett, G., 2009. Fiber-optic DTS flow profiling installed in advanced MRC well. Journal of Petroleum Technology, 61(04): 30-32.

161- Kuhlman, K.L., Hinnell, A.C., Mishra, P.K., Yeh, T.J., 2008. Basin-scale transmissivity and storativity estimation using hydraulic tomography. Groundwater 46, 706–715.

162- Kurylyk, B.L., Irvine, D.J., 2019. Heat: An overlooked tool in the practicing hydrogeologist's toolbox. Groundwater.

163- Kutun, K., Tureyen, O.I., Satman, A., 2014. Temperature behavior of geothermal wells during production, injection and shut-in operations, Proceedings, 39th Workshop on Geothermal Reservoir Engineering, Stanford University, Stanford, California, February, pp. 24-26.

164- Labaky, W., Devlin, J.F., Gillham, R.W., 2009. Field comparison of the point velocity probe with other groundwater velocity measurement methods. Water Resour. Res. 45.

165- Labaky, W., Devlin, J.F., Gillham, R.W., 2007. Probe for measuring groundwater velocity at the centimeter scale. Environ. Sci. Technol. 41, 8453–8458.

166- Leaf, A. T., D. J. Hart, and J. M. Bahr (2012), Active thermal tracer tests for improved hydrostratigraphic characterization, Ground Water, 50(5), 726–735,

167- Le Borgne, T., Paillet, F., Bour, O., Caudal, J.P., 2006. Cross-borehole flowmeter tests for transient heads in heterogeneous aquifers. Groundwater, 44(3): 444-452.

168- Lee, T.P., Chia, Y., Chen, J.S., Chen, H. and Liu, C.W., 2012. Effects of free convection and friction on heat-pulse flowmeter measurement. Journal of Hydrology, 428, pp.182-190.

169- Lee, J., Kitanidis, P.K., 2014. Large-scale hydraulic tomography and joint inversion of head and tracer data using the principal component geostatistical approach (PCGA). Water Resour. Res. 50, 5410–5427.

170- Lee, J., Kokkinaki, A., Kitanidis, P.K., 2018. Fast large-scale joint inversion for deep aquifer characterization using pressure and heat tracer measurements. Transp. Porous Media 123, 533–543.

171- Lee, J., Yoon, H., Kitanidis, P.K., Werth, C.J., Valocchi, A.J., 2016. Scalable subsurface inverse modeling of huge data sets with an application to tracer concentration breakthrough data from magnetic resonance imaging. Water Resour. Res. 52, 5213–5231.

172- Leray, S., De Dreuzy, J.R., Bour, O., Labasque, T. and Aquilina, L., 2012. Contribution of age data to the characterization of complex aquifers. Journal of Hydrology, 464, pp.54-68.

173- LeRoux, N.K., Kurylyk, B.L., Briggs, M.A., Irvine, D.J., Tamborski, J.J. and Bense, V.F., Using heat to trace vertical water fluxes in sediment experiencing concurrent tidal pumping and groundwater discharge. Water Resources Research, p.e2020WR027904.

174- Lesem, L.B., Greytok, F., Marotta, F., McKetta Jr., J.J., 1957. A Method of Calculating the Distribution of Temperature in Flowing Gas Wells. Trans. AIME 210, 169–176. https://doi.org/10.2118/767-G

175- Lewandowski, J., Angermann, L., Nützmann, G., Fleckenstein, J.H., 2011. A heat pulse technique for the determination of small-scale flow directions and flow velocities in the streambed of sand-bed streams. Hydrol. Process. 25, 3244–3255.

176- Lewis, D.C., Kriz, G.J., Burgy, R.H., 1966. Tracer dilution sampling technique to determine hydraulic conductivity of fractured rock. Water Resour. Res. 2, 533–542.

177- Li, E.Y.M., Mohamed, S., Leung, C.K.S., Rao, S.K., Cheng, A.C.K., Cheung, C.Y.L., Lam, D.S.C., 2007. Agreement among 3 methods to measure corneal thickness: ultrasound pachymetry, Orbscan II, and Visante anterior segment optical coherence tomography. Ophthalmology 114, 1842–1847.

178- Li, M.-L., Oh, J.-T., Xie, X., Ku, G., Wang, W., Li, C., Lungu, G., Stoica, G., Wang, L. V, 2008. Simultaneous molecular and hypoxia imaging of brain tumors in vivo using spectroscopic photoacoustic tomography. Proc. IEEE 96, 481–489.

179- Lie, K.-A., 2019. An introduction to reservoir simulation using MATLAB/GNU Octave: User guide for the MATLAB Reservoir Simulation Toolbox (MRST). Cambridge University Press.

180- Linde, N., 2005. Characterization of Hydrogeological Media using electromagnetic geophysics.

181- Liu, S., Yeh, T.J., Gardiner, R., 2002. Effectiveness of hydraulic tomography: Sandbox experiments. Water Resour. Res. 38, 1–5.

182- Liu, F., Yeh, T.J., Wang, Y., Hao, Y., Wen, J., Wang, W., 2020. Characterization of basin-scale aquifer heterogeneity using transient hydraulic tomography with aquifer responses induced by groundwater exploitation reduction. J. Hydrol. 588, 125137. https://doi.org/10.1016/j.jhydrol.2020.125137

183- Liu, S., Yeh, T.J., Gardiner, R., 2002. Effectiveness of hydraulic tomography: Sandbox experiments. Water Resour. Res. 38, 1–5.

184- Liu, X., Illman, W.A., Craig, A.J., Zhu, J., Yeh, T., 2007. Laboratory sandbox validation of transient hydraulic tomography. Water Resour. Res. 43.

185- Lochbühler, T., Doetsch, J., Brauchler, R., Linde, N., 2013. Structure-coupled joint inversion of geophysical and hydrological data. Geophysics 78, ID1–ID14.

186- Loke, M., Rucker, D.F., Chambers, J.E., Wilkinson, P.B. and Kuras, O., 2011. Electrical resistivity surveys and data interpretation.

187- Lowry, C.S., Walker, J.F., Hunt, R.J., Anderson, M.P., 2007. Identifying spatial variability of groundwater discharge in a wetland stream using a distributed temperature sensor. Water Resour. Res. 43.

188- Lu, N., Ge, S., 1996. Effect of horizontal heat and fluid flow on the vertical temperature distribution in a semiconfining layer. Water Resour. Res. 32, 1449–1453.

189- Luo, N., Illman, W.A., Zha, Y., Park, Y.-J., Berg, S.J., 2020. Three-dimensional hydraulic tomography analysis of long-term municipal wellfield operations: Validation with synthetic flow and solute transport data. J. Hydrol. 125438.

190- Luo, H., Li, H., Lu, Y., Li, Y. and Guo, Z., 2020. Inversion of distributed temperature measurements to interpret the flow profile for a multistage fractured horizontal well in low-permeability gas reservoir. Applied Mathematical Modelling, 77, pp.360-377.

191- Luo, H., Li, H., Tan, Y., Li, Y., Jiang, B., Lu, Y. and Cui, X., 2020. A novel inversion approach for fracture parameters and inflow rates diagnosis in multistage fractured horizontal wells. Journal of Petroleum Science and Engineering, 184, p.106585.

192- Maldaner, C.H., Munn, J.D., Coleman, T.I., Molson, J.W., Parker, B.L., 2019. Groundwater flow quantification in fractured rock boreholes using active distributed temperature sensing under natural gradient conditions. Water Resour. Res. 55, 3285–3306.

193- Mansure, A.J., Reiter, M., 1979. A vertical groundwater movement correction for heat flow. J. Geophys. Res. Solid Earth 84, 3490–3496.

194- Mao, D., Yeh, T.-C.J., Wan, L., Hsu, K.-C., Lee, C.-H., Wen, J.-C., 2013. Necessary conditions for inverse modeling of flow through variably saturated porous media. Adv. Water Resour. 52, 50–61.

195- Masciopinto, C. and Palmiotta, D., 2014. Estimation of water velocities in boreholes using a new passive flowmeter. Hydrological Sciences Journal, 59(9), pp.1738-1752.

196- Matheron, G., 1965. Les variables régionalisées et leur estimation: une application de la théorie des fonctions aléatoires aux sciences de la nature. Masson et CIE.

197- Mawer, C., Parsekian, A., Pidlisecky, A., Knight, R., 2016. Characterizing heterogeneity in infiltration rates during managed aquifer recharge. Groundwater 54, 818–829.

198- Meyzonnat, G. et al., 2018. High-Resolution Wellbore Temperature Logging Combined with a Borehole-Scale Heat Budget: Conceptual and Analytical Approaches to Characterize Hydraulically Active Fractures and Groundwater Origin. Geofluids, 2018, 19.

199- Michalski, A., Klepp, G.M., 1990. Characterization of transmissive fractures by simple tracing of in-well flow. Groundwater, 28(2): 191-198.

200- Molina-Giraldo, N., Blum, P., Zhu, K., Bayer, P., Fang, Z., 2011. A moving finite line source model to simulate borehole heat exchangers with groundwater advection. Int. J. Therm. Sci. 50, 2506–2513.

201- Molz, F.J., Boman, G.K., Young, S.C. and Waldrop, W.R., 1994. Borehole flowmeters: Field application and data analysis. Journal of Hydrology, 163(3-4), pp.347-371.

202- Molz, F.J., Morin, R.H., Hess, A.E., Melville, J.G. and Güven, O., 1989. The impeller meter for measuring aquifer permeability variations: evaluation and comparison with other tests. Water Resources Research, 25(7), pp.1677-1683.

203- Moore, Y.H., Stoessell, R.K., Easley, D.H., 1992. Fresh-water/sea-water relationship within a ground-water flow system, northeastern coast of the Yucatan Peninsula. Groundwater 30, 343–350.

204- Moreno, Á., García-Haro, F.J., Martínez, B., Gilabert, M.A., 2014. Noise reduction and gap filling of fapar time series using an adapted local regression filter. Remote Sensing, 6(9): 8238-8260.

205- Moss, J.T., White, P.D., 1959. How to calculate temperature profiles in a water-injection well. Oil Gas J 57, 174.

206- Munn, J.D., Maldaner, C.H., Coleman, T.I., Parker, B.L., 2020. Measuring Fracture Flow Changes in a Bedrock Aquifer Due to Open Hole and Pumped Conditions Using Active Distributed Temperature Sensing. Water Resour. Res. 56, e2020WR027229.

207- Naranjo, R.C., Turcotte, R., 2015. A new temperature profiling probe for investigating groundwater-surface water interaction. Water Resour. Res. 51, 7790–7797.

208- Neuman, S.P., 1973. Calibration of distributed parameter groundwater flow models viewed as a multiple-objective decision process under uncertainty. Water Resour. Res. 9, 1006–1021.

209- Neuman, S.P., 1987. Stochastic continuum representation of fractured rock permeability as an alternative to the REV and fracture network concepts. In Groundwater Flow and Quality Modelling (pp. 331-362). Springer, Dordrecht.

210- Ni, C.-F., Yeh, T.-C.J., Chen, J.-S., 2009. Cost-effective hydraulic tomography surveys for predicting flow and transport in heterogeneous aquifers. Environ. Sci. Technol. 43, 3720–3727.

211- Nian, Y.L. and Cheng, W.L., 2018. Insights into geothermal utilization of abandoned oil and gas wells. Renewable and Sustainable Energy Reviews, 87, pp.44-60..

212- Novakowski, K., Bickerton, G., Lapcevic, P., Voralek, J., Ross, N., 2006. Measurements of groundwater velocity in discrete rock fractures. J. Contam. Hydrol. 82, 44–60.

213- Novakowski, K.S., Lapcevic, P.A., Voralek, J., Bickerton, G., 1995. Preliminary interpretation of tracer experiments conducted in a discrete rock fracture under conditions of natural flow. Geophys. Res. Lett. 22, 1417–1420.

214- Nowak, W., Cirpka, O.A., 2006. Geostatistical inference of hydraulic conductivity and dispersivities from hydraulic heads and tracer data. Water Resour. Res. 42.

215- Nriagu, J.O., 2019. Encyclopedia of environmental health. Elsevier.

216- Nuñez-Lopez, V., Muñoz-Torres, J., Zeidouni, M., 2014. Temperature monitoring using distributed temperature sensing (DTS) technology. Energy Procedia, 63: 3984-3991.

217- Ouyang, L.-B., Belanger, D., 2004. Flow Profiling via Distributed Temperature Sensor (DTS) System-Expectation and Reality, SPE Prod &Oper 21 (1): 269-281. SPE-90541-PA.

218- Paillet, F.L., 1998. Flow modeling and permeability estimation using borehole flow logs in heterogeneous fractured formations. Water Resources Research, 34(5), pp.997-1010.

219- Paillet, F.L., Hess, A., Cheng, C., Hardin, E., 1987. Characterization of fracture permeability with high-resolution vertical flow measurements during borehole pumping. Groundwater, 25(1): 28-40.

220- Paillet, F.L., Pedler, W.H., 1996. Integrated borehole logging methods for wellhead protection applications. Eng. Geol. 42, 155–165.

221- Palmer, C.D., 1993. Borehole dilution tests in the vicinity of an extraction well. J. Hydrol. 146, 245–266.

222- Paradis, D., Gloaguen, E., Lefebvre, R., Giroux, B., 2015. Resolution analysis of tomographic slug test head data: Two-dimensional radial case. Water Resour. Res. 51, 2356–2376.

223- Paradis, D., Lefebvre, R., Gloaguen, E., Giroux, B., 2016. Comparison of slug and pumping tests for hydraulic tomography experiments: a practical perspective. Environ. Earth Sci. 75, 1159.

224- Paradis, D., Lefebvre, R., Gloaguen, E. and Rivera, A., 2015. Predicting hydrofacies and hydraulic conductivity from direct-push data using a data-driven relevance vector machine approach: Motivations, algorithms, and application. Water Resources Research, 51(1), pp.481-505.

225- Pehme, P.E., Parker, B.L., Cherry, J.A. and Greenhouse, J.P., 2010. Improved resolution of ambient flow through fractured rock with temperature logs. Groundwater, 48(2), pp.191-205.

226- Pianosi, F., Sarrazin, F., Wagener, T., 2015. A Matlab toolbox for global sensitivity analysis. Environmental Modelling & Software, 70: 80-85.

227- Piccinini, L., Fabbri, P. and Pola, M., 2016. Point dilution tests to calculate groundwater velocity: an example in a porous aquifer in northeast Italy. Hydrological Sciences Journal, 61(8), pp.1512-1523.

228- Pitrak, M., Mares, S., Kobr, M., 2007. A simple borehole dilution technique in measuring horizontal ground water flow. Groundwater 45, 89–92.

229- Preto, P., Stranne, C., Greenwood, S., Jakobsson, M., Näslund, J.O., Sundberg, J., Swärd, H. and O'Regan, M., 2019. Geothermal evidence for groundwater flow through Quaternary sediments overlying bedrock aquifers below Lake Vättern, Sweden. GFF, 141(2), pp.106-120.

230- Ptak, T., Schmid, G., 1996. Dual-tracer transport experiments in a physically and chemically heterogeneous porous aquifer: effective transport parameters and spatial variability. J. Hydrol. 183, 117–138.

231- Purvance, D.T., Andricevic, R., 2000. On the electrical-hydraulic conductivity correlation in aquifers. Water Resour. Res. 36, 2905–2913.

232- Racz, A.J., Fisher, A.T., Schmidt, C.M., Lockwood, B.S., Huertos, M.L., 2012. Spatial and temporal infiltration dynamics during managed aquifer recharge. Groundwater 50, 562–570.

233- Raman, C.V., 1928. A new radiation.

234- Ramey Jr., H.J., 1962. Wellbore Heat Transmission. J. Pet. Technol. 14, 427–435. https://doi.org/10.2118/96-PA

235- Rau, G.C., Andersen, M.S., McCallum, A.M., Acworth, R.I., 2010. Analytical methods that use natural heat as a tracer to quantify surface water–groundwater exchange, evaluated using field temperature records. Hydrogeol. J. 18, 1093–1110.

236- Read T., Bour O., Bense V., Le Borgne T., Goderniaux P., Klepikova , M.V., Hochreutener R., Lavenant N., and Boschero V., 2013. Characterizing groundwater flow and heat transport in fractured rock using Fibre-Optic Distributed Temperature Sensing, Geophysical Research Letters, vol. 40 (10), 2055–2059, doi:10.1002/grl.50397.

237- Read, T., Bour, O., Selker, J.S., Bense, V.F., Le Borgne, T., Hochreutener, R., Lavenant, N., 2014. Active-distributed temperature sensing to continuously quantify vertical flow in boreholes. Water Resour. Res. 50, 3706–3713.

238- Read T, Bense VF, Bour O, Le Borgne T, Lavenant N, Hochreutener R, Selker JS (2015) Thermal-plume fibre optic tracking (T-POT) test for flow velocity measurement in groundwater boreholes. Geoscientific Instrumentation, Methods and Data Systems Discussions 4, 197–202.

239- Reid, M.C., Jaffé, P.R., 2013. A push–pull test to measure root uptake of volatile chemicals from wetland soils. Environ. Sci. Technol. 47, 3190–3198.

240- Reiter, M., 2001. Using precision temperature logs to estimate horizontal and vertical groundwater flow components. Water Resour. Res. 37, 663–674.

241- Reiter, M., Costain, J.K., Minier, J., 1989. Heat flow data and vertical groundwater movement, examples from southwestern Virginia. J. Geophys. Res. Solid Earth 94, 12423–12431.

242- Ren, T., Kluitenberg, G.J., Horton, R., 2000. Determining soil water flux and pore water velocity by a heat pulse technique. Soil Sci. Soc. Am. J. 64, 552–560.

243- Ren, T., Noborio, K., Horton, R., 1999. Measuring soil water content, electrical conductivity, and thermal properties with a thermo-time domain reflectometry probe. Soil Sci. Soc. Am. J. 63, 450–457.

244- Revil, A., Karaoulis, M., Johnson, T., Kemna, A., 2012. Some low-frequency electrical methods for subsurface characterization and monitoring in hydrogeology. Hydrogeol. J. 20, 617–658.

245- Riemann, K., 2002. Aquifer parameter estimation in fractured-rock aquifers using a combination of hydraulic and tracer tests.

246- Rojstaczer, S.A., Ingebritsen, S.E. and Hayba, D.O., 2008. Permeability of continental crust influenced by internal and external forcing. Geofluids, 8(2), pp.128-139.

247- Ronen, D., Magaritz, M., Paldor, N., Bachmat, Y., 1986. The behavior of groundwater in the vicinity of the water table evidenced by specific discharge profiles. Water Resour. Res. 22, 1217–1224.

248- Roques, C., Bour, O., Aquilina, L., Dewandel, B., 2016. High-yielding aquifers in crystalline basement: insights about the role of fault zones, exemplified by Armorican Massif, France. Hydrogeology journal, 24(8): 2157-2170.

249- Roques C, Aquilina L., Boisson A., Vergnaud-Ayraud V., Labasque T., Longuevergne L., Laurencelle M., Dufresne A., de Dreuzy J.R, Pauwels H. and O. Bour, 2018. Autotrophic denitrification supported by biotite dissolution in crystalline aquifers: (2) transient mixing and denitrification dynamic during long-term pumping, Science of the Total Environment 619–620, 491–503.

250- Roshan, H., Rau, G.C., Andersen, M.S., Acworth, I.R., 2012. Use of heat as tracer to quantify vertical streambed flow in a two-dimensional flow field. Water Resour. Res. 48.

251- Ruelleu, S. F. Moreau, O. Bour, D. Gapais and G. Martelet 2010. Impact of gently dipping discontinuities on basement aquifer recharge: An example from Ploemeur (Brittany, France), J of Applied Geophysics, V 70, N° 2, pp 161-168, doi10.1016/j.jappgeo.2009.12.007.

252- Ruggeri, P., Gloaguen, E., Lefebvre, R., Irving, J. and Holliger, K., 2014. Integration of hydrological and geophysical data beyond the local scale: Application of Bayesian sequential simulation to field data from the Saint-Lambert-de-Lauzon site, Quebec, Canada. Journal of Hydrology, 514, pp.271-280.

253- Saar, M.O., 2011. Geothermal heat as a tracer of large-scale groundwater flow and as a means to determine permeability fields. Hydrogeol. J. 19, 31–52.

254- Sagar, R., Doty, D.R., Schmidt, Z., 1991. Predicting temperature profiles in a flowing well. SPE Prod. Eng. 6, 441–448.

255- Sale, T., Taylor, G.R., Iltis, G., Lyverse, M., 2007. Measurement of LNAPL flow using single-well tracer dilution techniques. Groundwater 45, 569–578.

256- Satman, A., Tureyen, O.I., 2016. Geothermal wellbore heat transmission: Stabilization times for “static” and “transient” wellbore temperature profiles. Geothermics, 64: 482-489.

257- Satter, A., 1965. Heat losses during flow of steam down a wellbore. J. Pet. Technol. 17, 845–851.

258- Sayde, C., Thomas, C.K., Wagner, J., Selker, J., 2015. High-resolution wind speed measurements using actively heated fiber optics. Geophys. Res. Lett. 42, 10–64.

259- Schmalholz, J., Stoffregen, H., Kemna, A., Yaramanci, U., 2004. Imaging of water content distributions inside a lysimeter using GPR tomography. Vadose Zo. J. 3, 1106–1115.

260- Schmalz, B., Lennartz, B., 2002. Analyses of soil water content variations and GPR attribute distributions. J. Hydrol. 267, 217–226.

261- Schmidt, C., Bayer-Raich, M., Schirmer, M., 2006. Characterization of spatial heterogeneity of groundwater-stream water interactions using multiple depth streambed temperature measurements at the reach scale.

262- Schneider, H.A., Jackson, W.A., Rainwater, K., Reible, D., Morse, S., Hatzinger, P.B., Garza-Rubalcava, U., 2019. Estimation of Interstitial Velocity Using a Direct Drive High-Resolution Passive Profiler. Groundwater 57, 915–924.

263- Selker, F. and Selker, J.S., 2018. Investigating water movement within and near wells using active point heating and fiber optic distributed temperature sensing. Sensors, 18(4), p.1023.

264- Sellwood, S.M., Hart, D.J. and Bahr, J.M., 2015. An in-well heat-tracer-test method for evaluating borehole flow conditions. Hydrogeology Journal, 23(8), pp.1817-1830.

265- Sharma, P.V., 1997. Environmental and engineering geophysics. Cambridge university press.

266- Silliman, S. and Robinson, R., 1989. Identifying fracture interconnections between boreholes using natural temperature profiling: I. Conceptual basis. Groundwater, 27(3), pp.393-402.

267- Silva, W.L., Lima, V.S., Fonseca, D.A., Salazar, A.O., Maitelli, C.W. and Echaiz E, G.A., 2019. Study of Flow Rate Measurements Derived from Temperature Profiles of an Emulated Well by a Laboratory Prototype. Sensors, 19(7), p.1498.

268- Simon, N., Bour, O., Lavenant, N., Porel, G., Nauleau, B., Pouladi, B., Longuevergne, L. and Crave, A., 2021. Numerical and experimental validation of the applicability of active-DTS experiments to estimate thermal conductivity and groundwater flux in porous media. Water Resources Research, p.e2020WR028078.

269- Simon, N., Bour, O., Lavenant, N., Porel, G., Nauleau, B., Pouladi, B. and Longuevergne, L., 2020. A Comparison of Different Methods to Estimate the Effective Spatial Resolution of FO-DTS Measurements Achieved during Sandbox Experiments. Sensors, 20(2), p.570.

270- Slater, L., 2007. Near surface electrical characterization of hydraulic conductivity: From petrophysical properties to aquifer geometries—A review. Surv. Geophys. 28, 169–197.

271- Slater, L., Lesmes, D.P., 2002. Electrical-hydraulic relationships observed for unconsolidated sediments. Water Resour. Res. 38, 31.

272- Snodgrass, M.F., Kitanidis, P.K., 1997. A geostatistical approach to contaminant source identification. Water Resour. Res. 33, 537–546.

273- Sommer, T., Carpenter, J.R., Schmid, M., Lueck, R.G., Schurter, M., Wüest, A., 2013. Interface structure and flux laws in a natural double-diffusive layering. J. Geophys. Res. Ocean. 118, 6092–6106.

274- Somogyvári, M., Bayer, P., 2017. Field validation of thermal tracer tomography for reconstruction of aquifer heterogeneity. Water Resour. Res. 53, 5070–5084.

275- Somogyvári, M., Bayer, P., Brauchler, R., 2016. Travel-time-based thermal tracer tomography. Hydrol. Earth Syst. Sci. 20, 1885–1901.

276- Song, X., Shi, Y., Li, G., Shen, Z., Hu, X., Lyu, Z., Zheng, R. and Wang, G., 2018. Numerical analysis of the heat production performance of a closed loop geothermal system. Renewable Energy, 120, pp.365-378.

277- Soueid Ahmed, A., Jardani, A., Revil, A., Dupont, J.-P., 2016. Joint inversion of hydraulic head and self-potential data associated with harmonic pumping tests. Water Resour. Res. 52, 6769–6791.

278- Stallman, R.W., 1965. Steady one-dimensional fluid flow in a semi-infinite porous medium with sinusoidal surface temperature. J. Geophys. Res. 70, 2821–2827.

279- Straface, S., Yeh, T., Zhu, J., Troisi, S., Lee, C.H., 2007. Sequential aquifer tests at a well field, Montalto Uffugo Scalo, Italy. Water Resour. Res. 43.

280- Sudicky, E.A., 1986. A natural gradient experiment on solute transport in a sand aquifer: Spatial variability of hydraulic conductivity and its role in the dispersion process. Water Resour. Res. 22, 2069–2082.

281- Sun, R., Yeh, T.J., Mao, D., Jin, M., Lu, W., Hao, Y., 2013. A temporal sampling strategy for hydraulic tomography analysis. Water Resour. Res. 49, 3881–3896.

282- Sutton, D.J., Kabala, Z.J., Schaad, D.E., Ruud, N.C., 2000. The dipole-flow test with a tracer: a new single-borehole tracer test for aquifer characterization. J. Contam. Hydrol. 44, 71–101.

283- Tabbagh, A., Cheviron, B., Henine, H., Guérin, R. and Bechkit, M.A., 2017. Numerical determination of vertical water flux based on soil temperature profiles. Advances in Water Resources, 105, pp.217-226.

284- Taniguchi, M., Burnett, W.C., Smith, C.F., Paulsen, R.J., O'rourke, D., Krupa, S.L., Christoff, J.L., 2003. Spatial and temporal distributions of submarine groundwater discharge rates obtained from various types of seepage meters at a site in the Northeastern Gulf of Mexico. Biogeochemistry 66, 35–53.

285- Theis, C. V, 1935. The relation between the lowering of the piezometric surface and the rate and duration of discharge of a well using ground-water storage. Eos, Trans. Am. Geophys. Union 16, 519–524.

286- Thiem, A., 1906. Hydrogeological methods. Gebhardt, Leipzig.

287- Tosaka, H., Masumoto, K., Kojima, K., 1993. Hydropulse tomography for identifying 3-D permeability distribution, in: High Level Radioactive Waste Management: Proceedings. Volume 1.

288- Touchard, F., 1998. Caractérisation hydrogéologique d'un aquifère en socle fracturé: Site de Ploemeur (Morbihan) (Doctoral dissertation, Université Rennes 1).

289- Tremblay, L., Lefebvre, R., Paradis, D. and Gloaguen, E., 2014. Conceptual model of leachate migration in a granular aquifer derived from the integration of multi-source characterization data (St-Lambert, Canada). Hydrogeology journal, 22(3), pp.587-608.

290- Tsang, C., Hufschmied, P., Hale, F. V, 1990. Determination of fracture inflow parameters with a borehole fluid conductivity logging method. Water Resour. Res. 26, 561–578.

291- Tso, Michael C., Zha, Y., Jim Yeh, T., Wen, J., 2016. The relative importance of head, flux, and prior information in hydraulic tomography analysis. Water Resour. Res. 52, 3–20.

292- Vandenbohede, A., Louwyck, A., Lebbe, L., 2009. Conservative solute versus heat transport in porous media during push-pull tests. Transp. Porous Media 76, 265–287.

293- Vanderborght, J., Kemna, A., Hardelauf, H., Vereecken, H., 2005. Potential of electrical resistivity tomography to infer aquifer transport characteristics from tracer studies: A synthetic case study. Water Resour. Res. 41.

294- Van De Giesen, N. et al., 2012. Double-ended calibration of fiber-optic Raman spectra distributed temperature sensing data. Sensors, 12(5): 5471-5485.

295- Vitale, S.A., Robbins, G.A., 2017. Measuring flow rate in crystalline bedrock wells using the dissolved oxygen alteration method. Groundwater, 55(4): 588-592.

296- Vogt, T., Schneider, P., Hahn-Woernle, L., Cirpka, O.A., 2010. Estimation of seepage rates in a losing stream by means of fiber-optic high-resolution vertical temperature profiling. J. Hydrol. 380, 154–164.

297- Walter, K., Devlin, J.F., 2017. Application of 3D printing to the manufacturing of groundwater velocity probes. Groundw. Monit. Remediat. 37, 71–77.

298- Walton, W.C., 1962. Selected analytical methods for well and aquifer evaluation. Bull. (Illinois State Water Surv. no. 49.

299- Wang, X., Lee, J., Thigpen, B., Vachon, G.P., Poland, S.H., Norton, D., 2008. Modeling flow profile using distributed temperature sensor (DTS) system, in: Intelligent Energy Conference and Exhibition. Society of Petroleum Engineers.

300- Wang, Q., Ochsner, T.E. and Horton, R., 2002. Mathematical analysis of heat pulse signals for soil water flux determination. Water resources research, 38(6), pp.27-1.

301- Wang, Z., 2012. The uses of distributed temperature survey (DTS) data (Doctoral dissertation, Stanford University).

302- Welch, S.M., Kluitenberg, G.J., Bristow, K.L., 1996. Rapid numerical estimation of soil thermal properties for a broad class of heat-pulse emitter geometries. Meas. Sci. Technol. 7, 932.

303- West, L.J., Odling, N.E., 2007. Characterization of a multilayer aquifer using open well dilution tests. Groundwater 45, 74–84.

304- Wilson, J.T., 2001. An evaluation of borehole flowmeters used to measure horizontal ground-water flow in limestones of Indiana, Kentucky, and Tennessee, 1999 (No. 1). US Department of the Interior, US Geological Survey.

305- Wurzel, P., 1983. A comparison of classical and radio isotope methods in the determination of safe yield in the Sabi alluvial plain in Zimbabwe. In Papers of the international conference on groundwater and man. Volume 1: The investigation and assessment of groundwater resources.

306- Yeh, T.-C., Khaleel, R., Carroll, K.C., 2015. Flow through heterogeneous geologic media. Cambridge University Press.

307- Yeh, T.J., Liu, S., 2000. Hydraulic tomography: Development of a new aquifer test method. Water Resour. Res. 36, 2095–2105.

308- Yeh, T., 1992. Stochastic modelling of groundwater flow and solute transport in aquifers. Hydrol. Process. 6, 369–395.

309- Yeh, T.J., Zhang, J., 1996. A geostatistical inverse method for variably saturated flow in the vadose zone. Water Resour. Res. 32, 2757–2766.

310- Yin, D., Illman, W.A., 2009. Hydraulic tomography using temporal moments of drawdown recovery data: A laboratory sandbox study. Water Resour. Res. 45.

311- Young, S.C. and Pearson, H.S., 1995. The electromagnetic borehole flowmeter: Description and application. Groundwater Monitoring & Remediation, 15(4), pp.138-147.

312- Zha, Y., Yeh, T.-C.J., Illman, W.A., Tanaka, T., Bruines, P., Onoe, H., Saegusa, H., 2015. What does hydraulic tomography tell us about fractured geological media? A field study and synthetic experiments. J. Hydrol. 531, 17–30.

313- Zha, Y., Yeh, T.-C.J., Mao, D., Yang, J., Lu, W., 2014. Usefulness of flux measurements during hydraulic tomographic survey for mapping hydraulic conductivity distribution in a fractured medium. Adv. Water Resour. 71, 162–176.

314- Zha, Y., Yeh, T.J., Illman, W.A., Zeng, W., Zhang, Y., Sun, F., Shi, L., 2018. A reduced-order successive linear estimator for geostatistical inversion and its application in hydraulic tomography. Water Resour. Res. 54, 1616–1632.

315- Zhao, Z., Illman, W.A., Berg, S.J., 2016. On the importance of geological data for hydraulic tomography analysis: Laboratory sandbox study. J. Hydrol. 542, 156–171.

316- Zhu, J., Yeh, T.-C.J., 2005. Characterization of aquifer heterogeneity using transient hydraulic tomography. Water Resour. Res. 41.

317- Zhu, J., Yeh, T.J., 2006. Analysis of hydraulic tomography using temporal moments of drawdown recovery data. Water Resour. Res. 42.

L'utilisation de la chaleur comme traceur des eaux souterraines a attiré beaucoup d'attention ces dernières années car elle est omniprésente et facile à mesurer avec des capteurs de température peu coûteux. Dans cette thèse, nous nous appuyons sur l'utilisation de capteurs de température distribués à fibre optique (FO-DTS), une technologie permettant de mesurer la température dans l'espace, le long du câble FO, et dans le temps. Les capteurs FO-DTS peuvent être utilisés en modes passif et actif. En mode actif, de la chaleur est ajoutée au câble FO par un élément chauffant à côté du câble induisant des anomalies artificielles de température, tandis qu'en mode passif, la variabilité naturelle de la température est mesurée. Les câbles FO peuvent être suspendus à l'intérieur des trous de forage ou déployés verticalement dans l'aquifère non consolidé (en contact direct avec la formation) en utilisant la méthode de poussée directe. Les données de température enregistrées le long du câble FO peuvent ensuite être utilisées pour estimer le débit des eaux souterraines. Cette thèse vise à étudier et à développer des méthodes d'utilisation de la chaleur pour quantifier l'écoulement souterrain et à utiliser davantage les données d'écoulement pour cartographier et imager l'hétérogénéité des milieux souterrains. L'une des techniques les plus favorables pour reconstruire l'hétérogénéité de l'aquifère est la tomographie hydraulique. En tomographie hydraulique, l'aquifère est soumis à une perturbation (pompage classique bien que les traceurs de chaleur et de soluté soient également populaires), et la réponse de l'aquifère est surveillée à différents points de l'aquifère. La réponse de l'aquifère observée avec un modèle numérique subit un processus d'inversion pour reconstruire l'hétérogénéité de l'aquifère.

Dans le chapitre 2, une étude numérique comparative est réalisée pour évaluer la qualité des données de flux (qui peuvent être mesurées par Active FO-DTS) et des données de charge hydraulique (qui sont classiquement utilisées en tomographie hydraulique) dans la reconstruction de l'hétérogénéité de l'aquifère. Un modèle aquifère 2D doté d'une distribution gaussienne de conductivités hydrauliques est considéré pour simuler un test de tomographie hydraulique. L'aquifère est accessible via cinq forages, disposés en carré, avec quatre forages aux sommets du carré et un forage au milieu. L'aquifère est soumis à une série de pompages et de refoulement, et les données de flux sont mesurées dans des forages sans pompage. Afin d'étudier l'effet du nombre d'observations, des points d'observation supplémentaires sont considérés. Le nombre minimum de points d'observation correspond aux quatre forages et le nombre maximum comprend le forage et 28 points d'observation supplémentaires. Les données de charge et de flux simulées sont ensuite utilisées seules et conjointement pour cartographier l'hétérogénéité de l'aquifère en utilisant l'inversion géostatistique. On constate que, pour le petit nombre d'observations, les données de flux capturent mieux l'hétérogénéité que les données de charge hydraulique. À mesure que le nombre de points d'observation augmente, les deux données tendent à fonctionner de la même manière, et le résultat final de l'inversion sera indépendant du type de données. Compte tenu du même nombre d'observations, l'inversion conjointe n'offre aucun avantage sur les données de flux ou de charge. Néanmoins, pour le même nombre de points d'observation, si nous sommes capables de mesurer les charges hydrauliques et les flux au même endroit, cela fournira une estimation améliorée par rapport à l'inversion des données de charge ou de flux de seules en raison du nombre doublé d'observations. Nous avons également constaté que le succès de l'inversion avec uniquement les données de charge ou de flux dépend de la condition aux limites imposée au forage. Les données de charge fonctionnent le mieux avec un pompage à débit constant au niveau du trou de forage, tandis que les données de flux fonctionnent mieux avec une condition aux limites de charge constante au puits de forage. L'inversion conjointe des

deux données est indépendante du type de limite. Il convient de noter que le type de condition aux limites du forage est important uniquement pour la tomographie hydraulique en régime permanent. Pour les techniques actuelles, des conditions de débit en régime permanent sont nécessaires pour déduire les flux à partir des données de température réparties actives.

Motivés par les résultats du chapitre 2, nous avons conçu une expérience de tomographie hydraulique dans laquelle les données de charge et de flux sont mesurées simultanément en quelques points à travers l'aquifère. Le site de Saint-Lambert dans le sud de la ville de Québec, au Canada, qui abrite un aquifère sableux granulaire peu profond et une décharge sanitaire déclassée, est choisi pour effectuer une tomographie hydraulique conjointe à partir des données de charge et de flux. Le site expérimental comporte 7 forages, et deux câbles FO ont été déployés verticalement dans le sol par la méthode de la poussée directe des mois avant le début de l'expérience pour s'assurer que la formation entourera correctement les câbles FO. Le forage au milieu de l'aquifère a été choisi comme forage de pompage, et la charge hydraulique a été mesurée dans quatre trous de forage ouverts et deux trous de forage équipés de packers pour mesurer la hauteur à différents intervalles isolés. Le flux a également été mesuré par le câble A-FO DTS installé entre le forage de pompage et deux forages équipés de packers. L'expérience entière a duré environ 92 heures et a commencé par le pompage du forage central et le recodage des données passives de température par des câbles FO et des pressions dans le trou de forage environnant. Après 19 heures de surveillance passive des données de température et de vérification de l'état hydraulique en régime permanent, de la chaleur a été ajoutée aux câbles FO. La période de chauffage efficace pendant l'état d'équilibre a duré environ 28 heures. Il est à noter qu'à notre connaissance, il s'agit de l'une des rares expériences dans lesquelles des câbles FO ont été insérés dans un aquifère sableux à l'aide de la méthode de poussée directe, et ce n'est que la première fois que la tomographie hydraulique est réalisée dans une nappe souterraine avec données de flux. L'expérience était donc très innovante mais aussi très spéculative car elle nécessitait des épissures FO spécifiques et l'insertion de câbles FO dans les tiges de poussée directe qui étaient très incertaines. Malgré ces défis, et quelques autres incidents rencontrés sur le terrain, l'expérience a été un succès car il a été possible de réaliser des tests de dissipation thermique active-DTS au cours d'une expérience de pompage similaire à la plupart des expériences de tomographie hydraulique classiques. Compte tenu de la faible perméabilité relative du site sur le terrain, il convient de mentionner qu'une durée de chauffage plus longue aurait certainement fourni une meilleure estimation des flux des eaux souterraines. Néanmoins, les expériences ont fourni des données cohérentes qui pourraient être utilisées dans le processus d'inversion pour tester la valeur ajoutée des mesures de flux des eaux souterraines pour imager les propriétés hydrauliques souterraines. Les données de charge et de flux acquises ont été utilisées avec une méthode d'inversion géostatistique pour estimer la conductivité hydraulique du champ. Les informations géostatistiques sur le site ont été obtenues en analysant les données du test de pénétration de cône réalisé précédemment. L'inversion a été réalisée en utilisant les données de charge enregistrées seules, et l'inversion conjointe à partir des données de charge et de flux. L'inversion avec les données de charge fournit des informations relatives sur la distribution des valeurs de conductivité hydraulique faible et modérée. De toute évidence, il existe une forte incertitude dans la zone où peu ou pas de données de charge sont enregistrées. Cependant, l'inversion conjointe des données de charge et de flux fournit une carte de distribution de conductivité hydraulique plus détaillée. Nos résultats suggèrent que les améliorations de l'estimation du champ de

conductivité hydraulique sont principalement dues à la densité élevée des mesures de FO qui fournissent un grand nombre d'observations en un seul endroit. Il est à noter que les gammes de conductivités hydrauliques obtenues lors de l'inversion sont cohérentes avec les résultats des études précédentes.

L'application de l'approche mentionnée ci-dessus dans un aquifère fracturé serait également intéressante. Cependant, le déploiement du câble FO par des méthodes de poussée directe n'est applicable qu'aux milieux non consolidés peu profonds et ne peut pas être réalisé dans des roches cristallines. De plus, il y a eu quelques tentatives pour quantifier l'écoulement dans la fracture en utilisant l'A-FO DTS entre la paroi du trou de forage et un revêtement qui maintient l'A-FO DTS en contact étroit avec la formation (Maldaner et al., 2019; Munn et al., 2020). Cependant, la résolution spatiale actuelle du DTS ne permet pas de mesurer précisément le flux provenant des fractures et de telles mesures de flux dans les fractures sont difficiles à extrapoler à plus grande échelle. Pour surmonter ce défi, dans le chapitre 4, nous avons développé une méthode pour utiliser le profil de température passif (données DTS passives) de l'eau à l'intérieur du forage pour quantifier l'écoulement vertical dans différents segments de forage, et quantifier la contribution en temps réel de chaque fracture au débit total. Le concept de base derrière l'utilisation du profil de température passif pour la quantification de l'écoulement vertical est basé sur l'écart par rapport au gradient géothermique. S'il n'y a pas d'écoulement dans le forage, la température de l'eau stagnante doit suivre le gradient géothermique, mais dès que l'eau commence à couler, les variations de température de l'eau avec la profondeur s'écarteront du gradient géothermique. Le profil de température de l'eau à l'intérieur du forage peut être décrit par des solutions analytiques fournies par Ramey (1962) et Hassan & Kabir (2002, 2005), qui sont dérivées en considérant le modèle de transfert de chaleur entre l'eau et la formation. Les deux équations mentionnées ci-dessus décrivent le profil de température de l'eau en fonction de la vitesse de l'eau et des propriétés thermiques de l'eau et de la formation (gradient géothermique, conductivité thermique de la roche, temps d'écoulement). En supposant une bonne connaissance des propriétés thermiques, on peut utiliser les solutions analytiques et le profil de température passif pour estimer le profil de vitesse et donc le profil de débit dans le forage.

Tout d'abord, la précision des solutions analytiques a été testée par rapport à un modèle numérique simulant la température de l'eau qui coule à l'intérieur du forage. Le profil de température simulé a été utilisé par la solution analytique pour estimer la vitesse supposée dans le modèle numérique. Les résultats montrent que la vitesse supposée dans le modèle numérique a été estimée avec une erreur inférieure à 10%, ce qui assurerait une bonne description de la solution analytique. Ensuite, une analyse de sensibilité globale a été réalisée pour évaluer la sensibilité du débit estimé à différents paramètres. Nous avons constaté que le gradient géothermique est le paramètre le plus sensible suivi de la conductivité thermique de la roche et également du temps d'écoulement. Le gradient géothermique définit la force dérivant du transfert de chaleur tandis que la conductivité thermique agit comme un paramètre de contrôle sur le processus de transfert de chaleur. Le temps d'écoulement affecte la température de la région proche du trou de forage et a donc un effet sur la force de transfert de chaleur dérivant, mais son effet sera minimal dans un temps d'écoulement important. Par la suite, l'approche a été testée sur un forage fracturé du site de Guidel, Bretagne, France. Le profil de température passif a été mesuré dans le forage par FO-DTS pendant environ 45 heures, comprenant deux conditions de débit ambiant et une condition de débit de pompage. Le profil d'écoulement vertical le long du forage a

également été mesuré par un débitmètre à impulsions de chaleur dans les trois conditions hydrauliques. Le profil de température passif et les solutions analytiques ont été utilisés pour obtenir le profil d'écoulement à l'intérieur du trou de forage et ont été comparés au profil d'écoulement enregistré par un débitmètre à impulsion thermique. Les résultats montrent que le profil d'écoulement, particulièrement pour le débit ambiant, est en bon accord avec les résultats du débitmètre à impulsions de chaleur. Le profil d'écoulement à l'aide d'un profil de température passif nécessite une connaissance des propriétés thermiques du milieu qui peut ne pas être nécessairement disponible. Cependant, nous avons montré qu'en mesurant le débit en certains points du forage ou en surface, nous pouvons estimer un ensemble de propriétés thermiques qui ne représentent pas nécessairement les propriétés thermiques réelles du milieu mais peuvent être utilisées afin de décrire l'écoulement profilage à l'aide des données de température passives. Les données de température passive de FO-DTS fournissent un comportement dynamique intéressant de l'aquifère fracturés à l'échelle du forage. Les données de température peuvent en outre être utilisées pour analyser la contribution d'une fracture à l'écoulement et également son interaction avec le milieu dans le temps. La contribution de l'écoulement de fracture au cours du temps peut être révélatrice du mélange qui peut se produire à l'échelle du forage. Il convient également de rappeler que FO-DTS est opérationnellement plus pratique que les autres méthodes de mesure en raison de la taille étroite des câbles FO et du matériau de revêtement dur, ce qui le rend approprié pour une invasion minimale à l'intérieur du support et également pour des conditions difficiles.

UNIVERSITÉ DE RENNES 1

Titre : Utilisation de la chaleur pour la quantification des flux souterrains et la compréhension de l'hétérogénéité souterraine

Mots clés : Chaleur, DTS, Flux et écoulements souterrains, Hétérogénéité, Tomographie hydraulique

Résumé : L'hétérogénéité des milieux souterrains et la variabilité de conductivité hydraulique contrôlent l'écoulement des eaux souterraines et le transport de contaminants dans les aquifères. Ici, plusieurs approches complémentaires sont développées pour utiliser la chaleur pour mieux contraindre les flux souterrains et reconstruire l'hétérogénéité du sous-sol. Une approche typique pour reconstruire les valeurs de conductivité hydraulique et leur distribution spatiale est la tomographie hydraulique qui repose en général sur une l'inversion de données de charge hydraulique.
Dans ce travail, une première approche a consisté à évaluer sur des cas synthétiques, l'intérêt des données de flux d'écoulement (déduites en utilisant des mesures distribuées de température par fibre optique active (A-FO DTS)) –pour des expériences de tomographie hydraulique. Nous concevons ensuite et mettons en œuvre la première expérience de tomographie hydraulique mesurant à la fois les charges hydrauliques et les flux dans un aquifère granulaire peu profond du site de Saint-Lambert au Québec, Canada. Les résultats des études numériques révèlent que les données de flux sont plus contraignantes que les données de charge hydraulique pour un petit nombre d'observations, tandis que pour un nombre élevé d'observations, l'hétérogénéité reconstruite est indépendante du type de données. Les résultats de l'expérience de tomographie hydraulique montrent l'intérêt d'inclure un nombre élevé de mesures de flux, obtenues par A-FO DTS conduisant à une réduction de l'incertitude des estimations.
Enfin, le DTS passif est utilisé pour surveiller l'écoulement des eaux souterraines dans un forage fracturé artésien sur le site de Ploemeur en Bretagne. Les résultats révèlent le potentiel du DTS passif pour capturer la dynamique des eaux souterraines dans les milieux fracturés.

Title : The use of heat for subsurface flow quantification and understanding the subsurface heterogeneity

Keywords : Heat, DTS, Flux and Subsurface Flow, Heterogeneity, Hydraulic tomography

Abstract : The heterogeneity of subsurface media and variability of hydraulic conductivity controls groundwater flow and contamination transport in aquifers. Here, several complementary approaches are developed to used heat to better constrain subsurface flow and reconstruct the subsurface heterogeneity. A typical approach for reconstruction of hydraulic conductivity values and their spatial distribution is hydraulic tomography relying on the inversion of hydraulic head data.
In this work, we first assess the advantages of groundwater flux data (inferred by using Active Fiber Optic Distributed Temperature Sensors (A-FO DTS)) in a synthetic hydraulic tomography test. Next, we design and implement the first hydraulic tomography experiment measuring groundwater head and flux data simultaneously in a shallow granular aquifer at Saint-Lambert site close to Québec city, Canada. The results from numerical studies reveal that flux data outperforms the head data for a small number of observations while for the high number of observations, the reconstructed heterogeneity is independent of the data type. The results from the hydraulic tomography experiment show the advantage of including a high number of measured flux obtained by A-FO DTS leads to a reduction of estimation uncertainty.
Finally, the passive DTS is used to monitor groundwater flow in an artesian fractured borehole at Ploemeur site in Brittany. The results unveil the potential of passive DTS for capturing the groundwater dynamics in fractured media.